LEABHARLANN CHOLÁISTE NA TRÍONÓIDE, BAILE ÁTHA CLIATH | TRINITY COLLEGE LIBRARY DUBLIN
Ollscoil Átha Cliath | The University of Dublin

Terms and Conditions of Use of Digitised Theses from Trinity College Library Dublin

Copyright statement

All material supplied by Trinity College Library is protected by copyright (under the Copyright and Related Rights Act, 2000 as amended) and other relevant Intellectual Property Rights. By accessing and using a Digitised Thesis from Trinity College Library you acknowledge that all Intellectual Property Rights in any Works supplied are the sole and exclusive property of the copyright and/or other IPR holder. Specific copyright holders may not be explicitly identified. Use of materials from other sources within a thesis should not be construed as a claim over them.

A non-exclusive, non-transferable licence is hereby granted to those using or reproducing, in whole or in part, the material for valid purposes, providing the copyright owners are acknowledged using the normal conventions. Where specific permission to use material is required, this is identified and such permission must be sought from the copyright holder or agency cited.

Liability statement

By using a Digitised Thesis, I accept that Trinity College Dublin bears no legal responsibility for the accuracy, legality or comprehensiveness of materials contained within the thesis, and that Trinity College Dublin accepts no liability for indirect, consequential, or incidental, damages or losses arising from use of the thesis for whatever reason. Information located in a thesis may be subject to specific use constraints, details of which may not be explicitly described. It is the responsibility of potential and actual users to be aware of such constraints and to abide by them. By making use of material from a digitised thesis, you accept these copyright and disclaimer provisions. Where it is brought to the attention of Trinity College Library that there may be a breach of copyright or other restraint, it is the policy to withdraw or take down access to a thesis while the issue is being resolved.

Access Agreement

By using a Digitised Thesis from Trinity College Library you are bound by the following Terms & Conditions. Please read them carefully.

I have read and I understand the following statement: All material supplied via a Digitised Thesis from Trinity College Library is protected by copyright and other intellectual property rights, and duplication or sale of all or part of any of a thesis is not permitted, except that material may be duplicated by you for your research use or for educational purposes in electronic or print form providing the copyright owners are acknowledged using the normal conventions. You must obtain permission for any other use. Electronic or print copies may not be offered, whether for sale or otherwise to anyone. This copy has been supplied on the understanding that it is copyright material and that no quotation from the thesis may be published without proper acknowledgement.

UNDERSTANDING LEAKAGE FROM A FAULT-SEALED CO_2 RESERVOIR IN EAST-CENTRAL UTAH: A NATURAL ANALOGUE APPLICABLE TO CO_2 STORAGE

by

BEN DOCKRILL

A thesis submitted for the degree of Doctor of Philosophy

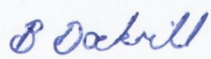
Department of Geology, University of Dublin, Trinity College.

September 2005.

TRINITY COLLEGE
12 MAY 2006
LIBRARY DUBLIN
THESIS
7841

DECLARATION

This thesis is entirely the work of the author, except where otherwise stated. All references are duly acknowledged. It has not been previously submitted as an exercise for a degree at this or any other university. Permission is granted for the library of the University of Dublin to lend or copy the thesis upon request, provided the source is acknowledged.



Ben Dockrill

SUMMARY

This thesis investigates a natural CO_2 reservoir to define the factors that can cause leakage and determine the rates and consequences of CO_2 leakage on the surrounding environment. Situated at the northern end of the Paradox Basin in east-central Utah, faulting of the north-plunging Green River Anticline has created structural highs in the footwalls of the west-north-west trending Little Grand Wash Fault and northern fault of the Salt Wash Graben. Focussed surface leakage of CO_2 is prevalent in the immediate footwalls of both faults with the presence of CO_2-charged geysers and springs and travertine deposits. The CO_2-rich waters erupting from the geysers and springs are a product of CO_2 produced from clay-carbonate reactions in Triassic and sub-Permian source beds rising and mixing with a series of overlying stacked aquifers (Heath, 2004). Geochemical investigations of active and ancient travertines along both faults indicate that this hydrologic system has been prevalent for at least the last 78,000 years.

Factors causing leakage from these aquifers were identified by field and geochemical investigations of the CO_2 leak products and faults at the surface combined with fault seal assessment of both faults in the subsurface. Regional dips indicate that the CO_2 charging the aquifers migrates up-dip to pool in the footwall structural highs. Both faults provide effective lateral seals to prevent across-fault flow from these traps due to lithological juxtapositions and/or development of continuous argillaceous smears. Conversely, fracture networks developed in the damage zones of both faults provide vertical conduits in the footwall for CO_2 to migrate through overlying, argillaceous-rich cap rocks and charge shallower fault-bound aquifers. Spatial associations between CO_2 leak products and additional fluid regimes suggest this is a common migration pathway for fluids through this faulted stratigraphy. Furthermore, uncapped and corroded boreholes that penetrate the footwall aquifers also provide direct conduits for CO_2 to migrate from the aquifers to the surface.

Quantifying the proportion of CO_2 that has leaked from these fault-bound aquifers was approximated by calculating the storage capacities of aquifers sealed by the Little Grand Wash Fault and comparing these capacities with surface leak estimates derived from travertine volumes. Volumetric estimates from travertine deposits indicate at least 1.9 million tonnes of CO_2 have leaked to the surface along the Little Grand Wash Fault over the last 78,000 years. Storage capacities for all aquifers sealed by the Little Grand Wash Fault are between 0.6 and 6.3 million tonnes. Thus, this system is being constantly recharged at depth with the aquifers leaking between 3.9% and 37.9% of their total CO_2 capacity every 10,000 years. The consequences of this leakage on the surrounding environment are minimal due to the reservoir's remoteness and geological setting, though leakage could be a significant issue in other settings. The results of this thesis highlight the roles faults and boreholes play in trapping and transmitting CO_2 and should influence the selection and design of future CO_2 geologic storage sites.

ACKNOWLEDGEMENTS

There are numerous groups and people I need to thank for helping me with this PhD. To start with, I would like to thank my official and unofficial supervisors:

- Zoe Shipton at Trinity/Glasgow University and Jim Evans at Utah State University for giving me the opportunity and resources to do this PhD. I would also thank Zoe for her friendship and unending enthusiasm, support and advice towards the cause that kept this project ticking over.
- David Kirschner at Saint Louis University for his assistance in the field, use of stable isotope equipment and guidance in all aspects related to travertines. I am also grateful to David and his wife, Carol, for proving me with a home for the month of isotope work in Saint Louis.
- John Walsh, Conrad Childs, Tom Manzocchi and Julian Strand of the Fault Analysis Group at University College Dublin for providing constructive advice and assistance on all aspects of faults and fluid flow. I am also indebted to them for making software available and assistance with three-dimensional model construction and utilisation.

For funding, I would like to thank:

- The Carbon Capture Project (http://www.co2capture project.org/index.htm) for providing funds to start this PhD.
- The Broad Curriculum Initiative at Trinity for allowing me to continue and finish this PhD.

For geochemical aspects of this thesis, I would like to thank:

- Mark Wilkinson, Stuart Hazeldine and Gavin England at Edinburgh University for use of equipment and helpful discussions on diagenesis.
- George Sevastopulo at Trinity for many discussions on geochemistry and carbonates and reviewing early chapters of this thesis.
- Robbie Goodhue at Trinity for assistance with XRD and stable isotope analyses.
- Kathy Keefe and Rob Ellam at Scottish Universities Environmental Research Centre for coming through at the last moment and providing invaluable travertine dates.
- Steven Bryant at the Univeristy of Texas, Karsten Pruess at the Lawrence Berkeley National Laboratory and Sean Brennan at the USGS for helpful discussions on CO_2 behaviour in the subsurface and reservoir volumetrics.

For modelling aspects of this thesis, I would like to thank:

- Midland Valley for generously providing 2DMove and 3DMove and Noah Jaffey and Colin Zimmer for assistance with the software.
- Badley Geoscience for generously providing Traptester and Pete Bretan and Steven Dee for assistance with the software.
- Mike Cunningham currently at the University of Cambridge for assistance with GIS.
- Stuart Clarke at the British Geological Survey for helpful discussions on the study area, faulting and three-dimensional model construction.
- Rob Hardy at Trinity for assistance with the modelling software and insightful discussions on rugby, the oil industry and Australia's dominance in sport.

In Utah, I would like to thank:

- Jason Heath and Tony Williams for assistance in the field and helpful discussions on the field area.
- The Utah Geological Survey for providing the well database and Rick Allis for helpful discussions on CO_2 storage and the geology of the field area.
- Justin Ericsson for helping out with all the little things in Utah and Dublin.

In Trinity, I would like to thank:

- The can do people in the geology department Neil, Declan, Maura and Frank. Special thanks to Declan for helping me with countless computer and software issues throughout the years.
- John Graham and Mags Duncan for helping me out with all admin nightmares.
- The rest of the academic staff for helping me out with all the little questions I have had over the year.
- The postgrads at Trinity, especially Aileen, Stuart, Rory, Catherine and Brian for their friendship and having someone to shoot to shit with.

On a personal note, I would like to thank:

- My parents for their support and faith in me
- Oon and Fionn for putting up with all the crap that comes with doing a PhD and still being there for me at the other end.

TABLE OF CONTENTS

SUMMARY

ACKNOWLEDGEMENTS

CHAPTER 1: INTRODUCTION 1

1.1 CO_2 AND CLIMATE CHANGE 1

1.2 GEOLOGIC STORAGE OF CO_2 3

1.3 ISSUES WITH GEOLOGICAL STORAGE 4

1.4 AIM OF THESIS 7

1.5 STRUCTURE OF THESIS 7

CHAPTER 2: GEOLOGICAL FRAMEWORK 9

2.1 INTRODUCTION 9

2.2 GEOLOGICAL SETTING 9

2.3 STRATIGRAPHY 11

2.3.1 Introduction 11

2.3.2 Stratigraphic Units 11

2.4 TECTONIC HISTORY OF THE PARADOX BASIN 18

CHAPTER 3: STRUCTURE 20

3.1 INTRODUCTION 20

3.2 STRUCTURAL COMPONENTS OF THE STUDY AREA 20

3.2.1 Folds 20

3.2.2 Faults 21

3.3 FAULT ZONE ARCHITECTURE 23

3.3.1 Introduction 23

3.3.2 Fault Core 24

3.3.3 Damage Zone 26

3.3.4 Summary 30

3.4 SEDIMENTATION PATTERNS OF THE REGION 31

3.4.1 Introduction 31

3.4.2 Permian 31

3.4.3 Triassic 31

3.4.4 Lower Jurassic 32

3.4.5 Mid Jurassic 32

3.4.6 Late Jurassic 33

3.5 TECTONIC HISTORY OF THE STUDY AREA 33

3.6 CONCLUSIONS 34

CHAPTER 4: FAULT-RELATED MINERALIZATION AND DIAGENESIS . 36

4.1 Introduction 36

4.2 Travertine Review 36

4.3 Field Relationships 38
4.3.1 Introduction *38*
4.3.2 Travertines *38*
4.3.3 Fault-Related Diagenesis *50*

4.4 Geochemistry 53
4.4.1 Methodology *53*
4.4.2 Mineralogy *54*
4.4.3 Stable Isotopes *58*
4.4.4 Radiometric Dating *69*

4.5 Discussion 70
4.5.1 Conceptual Model of Travertine Mound Evolution *70*
4.5.2 Origin, Timing and Quantity of CO_2 Leakage Based on Travertines *72*
4.5.3 Origin and Timing of Fault-Related Diagenesis *74*
4.5.4 Migration Pathways of Fluids in the Study Area *77*

4.6 Conclusions 79

CHAPTER 5: MODELLING 81

5.1 Introduction 81

5.2 Model Construction and Validation 82
5.2.1 Introduction *82*
5.2.2 Model Construction *83*
5.2.3 Model Components *88*
5.2.4 Model Validation *88*

5.3 Fault Seal Analysis 90
5.3.1 Introduction *90*
5.3.2 Fault Seal Review *91*
5.3.3 Model Appendages *98*
5.3.4 Fault Seal Assessment *99*
5.3.5 Uncertainty *101*
5.3.6 Fault-Associated Migration of Carbon Dioxide *104*
5.3.7 Fault Seal Summary *106*

5.4 Volumetrics 107
5.4.1 Introduction *107*
5.4.2 Method *107*
5.4.3 Results *110*
5.4.4 Discussion *111*
5.4.5 Volumetric Summary *113*

5.5 Conclusions 113

CHAPTER 6: DISCUSSION, CONCLUSIONS AND FUTURE WORK 115

6.1 DISCUSSION 115
6.1.1 CO_2 Flow Pathways 115
6.1.2 Factors Affecting Seal Integrity 116
6.1.3 Applications to CO_2 Storage 118

6.2 CONCLUSIONS 127

6.3 FUTURE WORK 130

REFERENCES 132-165

APPENDICIES

I. Outcrop fault data

II. Scanline fracture data

III. X-ray diffraction data

IV. Stable isotope data

V. Methodology for U-Th dating of travertines

LIST OF FIGURES

Chapter 2

Figure 2.1 Distribution of sedimentary basins and CO_2 fluxes throughout the Colorado Plateau and Southern Rocky Mountain region.
Figure 2.2 Geological features of the Paradox Basin and surrounding area.
Figure 2.3 Generalised stratigraphic section for the Green River area.
Figure 2.4 Field photographs of stratigraphy outcropping in the study area.

Chapter 3

Figure 3.1 Geological map displaying the main structural features of the region surrounding the town of Green River.
Figure 3.2 Detailed structure and stratigraphy of the Little Grand Wash Fault and the Salt Wash and Ten Mile Grabens
Figure 3.3 Throw profiles of the Little Grand Wash Fault and bounding faults of the Salt Wash and Ten Mile Grabens.
Figure 3.4 Schematic transects across fault zone outcrops at three locations along the Little Grand Wash Fault and Salt Wash Graben.
Figure 3.5 Fracture analyses at two locations along the Little Grand Wash Fault.
Figure 3.6 Isopach map of the Permian Cutler Group.
Figure 3.7 Isopach map of the Triassic Chinle and Moenkopi Formations.
Figure 3.8 Isopach map of the lower Jurassic Glen Canyon Group.
Figure 3.9 Isopach map of the mid Jurassic Carmel Formation.
Figure 3.10 Isopach map of the mid Jurassic Entrada Sandstone.
Figure 3.11 Isopach map of the combined upper Jurassic Curtis, Summerville and Morrison Formations.

Chapter 4

Figure 4.1 Distribution of fault-related mineralization and diagenesis along the Little Grand Wash Fault and Salt Wash Graben.
Figure 4.2 Field photographs of the active Crystal Geyser travertine mound.
Figure 4.3 Field photographs of active travertines along the northern fault of the Salt Wash Graben.
Figure 4.4 Lithofacies of an ancient travertine deposit.
Figure 4.5 Field photographs and photomicrographs of ancient travertine lithofacies.
Figure 4.6 Field photographs and photomicrographs of banded veins.
Figure 4.7 Estimated thicknesses, areas and volumes of travertines along the Little Grand Wash Fault.
Figure 4.8 Aspects of iron-oxide reduction along the Little Grand Wash Fault.
Figure 4.9 Aspects of hydrocarbon staining along the Little Grand Wash Fault.
Figure 4.10 Aspects of iron-oxide reduction along the northern fault of the Salt Wash Graben.
Figure 4.11 Field photographs of fractures surrounded by reduction haloes and infilled with either aragonite, gypsum or celestine.

Figure 4.12 Isotopic composition of active travertines from the Little Grand Wash Fault and northern fault of the Salt Wash Graben.
Figure 4.13 Variation in carbon and oxygen isotopes relative to topography and distance from Crystal Geyser vent along two separate flow paths.
Figure 4.14 Isotopic composition of the differing lithofacies within each ancient travertine deposit.
Figure 4.15 $\delta^{13}C$ and $\delta^{18}O$ boxplots of banded veins from travertine deposit.
Figure 4.16 Isotopic comparison of banded veins from ancient travertines.
Figure 4.17 Variation in carbon and oxygen isotopes between an aragonite vein infilling a fracture and carbonate cements from reduced and unreduced Entrada sandstones surrounding the fracture.
Figure 4.18 Isotopic comparison of spring-fed travertine deposits from several localities around the world.
Figure 4.19 Isotopic variability of ancient travertine surface lithofacies and altered host rock relative to order of deposition.
Figure 4.20 Variations in isotopic trends of white-banded veins from vein rim to centre.
Figure 4.21 $\delta^{13}C$ and $\delta^{18}O$ comparisons between layered mats from ancient deposits and active travertine.
Figure 4.22 Sampling areas of ancient travertine on Ten Mile butte.
Figure 4.23 Isotopic comparison of white-banded veins from three separate travertine deposits at Ten Mile butte.
Figure 4.24 Isotopic comparison of ancient travertines with carbonate veins from several localities in the northern half of the Paradox basin.
Figure 4.25 Isotopic comparison of fracture infill and carbonate cements from Entrada Sandstone with overlying travertine deposit.
Figure 4.26 Linear relationship between travertine age and erosion in the study area.
Figure 4.27 Schematic diagram showing different stages in the development of fault-associated travertine deposits of this study.

Chapter 5

Figure 5.1 Distribution of boreholes used for modelling at the northern end of the Paradox basin and surrounding area.
Figure 5.2 Structure contours for the top of the lower Jurassic Navajo Sandstone.
Figure 5.3 Structure contours for the top of the Pennsylvanian Honaker Trail Formation.
Figure 5.4 Structure contours for the top of the lower Cretaceous Dakota Formation.
Figure 5.5 Development of the Navajo Sandstone structure map.
Figure 5.6 Distribution of cross sections generated in 2DMove.
Figure 5.7 2DMove section construction in map view.
Figure 5.8 2DMove section construction in section view.
Figure 5.9 Balanced cross sections of the Little Grand Wash Fault, Salt Wash Graben, Ten Mile Graben and San Rafael Swell.
Figure 5.10 3DMove surface construction.
Figure 5.11 Completed three-dimensional model of the Green River area.

Figure 5.12 Comparison of original cross sections constructed and balanced in 2DMove with cross sections generated from the completed three-dimensional model in 3DMove.
Figure 5.13 Principles of Allan diagrams.
Figure 5.14 Principles of Juxtaposition diagrams.
Figure 5.15 Published algorithms used to predict the likelihood of argillaceous smear developing along a fault surface.
Figure 5.16 Generation of a V_{shale} curve.
Figure 5.17 Footwall and hanging wall cutoffs for the Little Grand Wash Fault and northern fault of the Salt Wash Graben in Traptester.
Figure 5.18 Fault sealing properties of the Little Grand Wash Fault.
Figure 5.19 Fault sealing properties of the northern fault of the Salt Wash Graben.
Figure 5.20 Juxtaposition diagram of the modelled stratigraphy showing the minimal effects of vertical fault throw changes on fault seal behaviour.
Figure 5.21 Potential leakage caused by structural complexities.
Figure 5.22 Influence of temperature and pressure on CO_2 phase.
Figure 5.23 Workflow to calculate volume of a trap filled with CO_2 in 3DMove.

Chapter 6

Figure 6.1 Schematic north-south cross-section through the Little Grand Wash Fault used to illustrate the conceptual model of CO_2 migration developed from this study.
Figure 6.2 Burial and thermal history of the Green River area accompanied with the timing of CO_2 generation and fault activity from the Cretaceous (100 Ma) to present.
Figure 6.3 Map of the study area showing the direction of groundwater flow based on potentiometric data for the Navajo Sandstone aquifer.

LIST OF TABLES

Chapter 1

Table 1.1	Summary of worldwide storage capacity estimates for CO_2	2

Chapter 4

Table 4.1	Mineralogical composition of travertine determined from XRD analyses	50
Table 4.2	Mineralogical composition of samples from transects of reduction haloes surrounding fractures along the northern fault of the Salt Wash Graben.	50
Table 4.3	One-way ANOVA of $\delta^{13}C$ between ancient travertines.	52
Table 4.4	One-way ANOVA of $\delta^{18}O$ between ancient travertines.	52
Table 4.5	Tukey HSD test of $\delta^{13}C$ between ancient travertines.	53
Table 4.6	Tukey HSD test of $\delta^{18}O$ between ancient travertines.	53
Table 4.7	Calculated and predicted ages of ancient travertines deposits based on U-Th dating.	55

Chapter 5

Table 5.1	Properties and storage capacities of CO_2 in aquifers sealed by the Little Grand Wash Fault.	108

Chapter 1: Introduction

1.1 CO_2 and Climate Change

Human activity over the last several hundred years since the industrial revolution has resulted in atmospheric CO_2 concentrations rising from a pre-industrial level of 280ppm to about 380ppm today (Chadwick et al., 2004; Brook, 2005). Current global anthropogenic emissions are estimated at about 23 billion tonnes of CO_2 per year (Chadwick et al., 2004). This increase is largely attributed to fossil fuel combustion for domestic and industrial use (i.e. electricity and transportation). There is a growing consensus that this rise in CO_2 concentrations has altered the global climate leading to irregular weather patterns, sea level rises and damage to sensitive ecosystems (IPCC, 2001). To address these problems, the Kyoto Protocol was drafted in 1997 and called on the developed countries to reduce their greenhouse gas emissions, of which CO_2 constitutes 63.5%, by an average of 5.2% below 1990 levels by 2012. While the protocol was not ratified by all countries, with Australia and the United States being notable exceptions, there has been universal acknowledgement that emissions must be reduced (Lee et al., 2005).

Measures to reduce greenhouse gas emissions include improving energy efficiency, switching to alternate (natural gas, hydrogen, nuclear) or renewable (solar, wind, biomass) energy sources with lower or negligible CO_2 emissions and CO_2 capture and storage. To achieve large emission reductions that would meet the targets set by the Kyoto Protocol, wide-scale changes in the world's energy usage are required (i.e. energy efficiency and fuel switching). These changes are possible but not realistically achievable for at least another decade or more (Edmonds et al., 2000; Gale, 2004). In the meantime, CO_2 capture and storage offers the best, large-scale option to reduce CO_2 anthropogenic emissions until other technologies are available.

Carbon dioxide storage is achievable through the enhancement of natural sinks (i.e. forests or soils) or injection into deep oceans or geologic reservoirs. The use of forests and soils to capture and store CO_2 is considered an environmentally attractive option for reducing emissions (Gale, 2004). However, large land masses are required to store modest amounts of CO_2 (Chadwick et al., 2004) and there is uncertainty about the permanence of CO_2 in these natural sinks (Lewis and Shinn, 2001; Gale, 2004). The oceans are the largest natural sink of CO_2, having absorbed approximately one third of all anthropogenic CO_2 emissions since the start of the industrial revolution

(Siegenthaler and Joos, 1992). Injection of CO_2 into the deep ocean (>1500m) has the potential to store large quantities of CO_2 for periods greater than 500 years (Orr, 2002). However, there are large uncertainties over the environmental impact of deep ocean storage (Omerod et al., 1999) as well as current international law prohibiting disposal of waste into the ocean. Therefore, storage of CO_2 in forests, soils and oceans is possible and is occurring passively but is too unreliable and controversial to contribute significantly towards large reductions in CO_2 emissions.

A final option is the use of geologic reservoirs for the injection and storage of CO_2. There are multiple advantages of geologic storage over ocean storage or terrestrial sinks with one main aspect being that CO_2 is potentially removed from the biosphere for very long periods of time (10^2 to 10^6 years; Chadwick et al., 2004). Geologic reservoirs have repeatedly shown the ability to store various fluids (i.e. oil, natural gas and groundwater) in the subsurface for many millions of years. Specifically, many geologic reservoirs have naturally stored CO_2 for thousands to millions of years (Baines and Worden, 2004a; Stevens et al., 2001; Stevens, 2005). Thus, careful selection of geologic reservoirs could ensure the storage of CO_2 beyond the age of fossil fuel dependence and high CO_2 emissions. Another main advantage of geologic reservoirs is the potentially vast capacities available for CO_2 storage. Capacity estimates for these reservoirs show that geological storage of CO_2 can make a substantial impact on global emissions with saline aquifers offering the largest storage potential (see Table 1.1). Finally, large scale injection of CO_2 into oil fields has been occurring since the mid 1980's for enhanced oil recovery (EOR). Thus, much of the infrastructure and knowledge required to inject CO_2 into reservoirs is already available resulting in a technology that could significantly reduce anthropogenic CO_2 emissions in the near future.

Table 1.1 Summary of worldwide geological storage capacity estimates for CO_2

Reservoir Type	**Global Estimates**[1]	
	Gt CO_2	**% of emissions to 2050**
Depleted Oil and Gas Reservoirs	450-920	22-45
Unmineable Coal Seams	20-150	<7
Saline Aquifers	300-10 000	15-500

1 – Estimates from Gale (2004) and Benson (2005).

1.2 Geologic Storage of CO_2

Based on availability and storage capacity, the main geologic reservoir types that could store CO_2 captured from power and industrial plants include saline aquifers, depleted oil and gas fields and unmineable coal seams. Other potential reservoirs that may provide storage options in niche opportunities include marine and arctic hydrates, salt dome cavities and oil shales (Benson, 2005).

Saline aquifers are geologic formations that do not have any potential to act as a source for potable water. The global storage capacity of saline aquifers is huge, accounting for between 15% and 500% of the projected total CO_2 emissions up to 2050 (Table 1.1; Davidson et al., 2001). Economically, saline aquifers are less desirable than the other main reservoir options due to no resource recovery from CO_2 injection (see below). However, government incentives could offset costs through tax credits and/or carbon trading systems (Baines and Worden, 2004b). There is one commercial CO_2 storage project (Sleipner) that has been injecting CO_2 into a saline aquifer since 1996. The Sleipner gas field in the North Sea strips CO_2 from produced gas and reinjects it into a deep saline aquifer, known as the Utsira Formation (Zweigel et al., 2000; Arts et al., 2004; Zweigel et al., 2004). Further storage projects involving CO_2 injection into saline aquifers have or are about to commence in Algeria (In Salah), Australia (Gorgon) and Norway (Snohvit) (Benson, 2005).

Depleted oil and gas fields provide another geologic option for CO_2 storage with the additional benefit of increased hydrocarbon production. CO_2 injection for enhanced oil recovery (EOR) has been occurring for the last two decades with current EOR operations injecting 33 million tonnes of CO_2 per annum into oil fields in the United States alone (Gale, 2004). The benefit of this operation is improved oil recovery, which commonly extends the life of a field. Previously, EOR operations have not generally considered the long term storage of CO_2, with average residence times of CO_2 in reservoirs being in the order of months to years (Worden and Smith, 2004). Refined objectives for CO_2 storage in EOR operations could ensure greater retention times (10^2 to 10^4 years) for CO_2 in oil fields after they cease to be economic. One such operation that combines CO_2 storage with EOR is the Weyburn field in Canada. Commencing in 2000, 1.7 million tonnes of CO_2 are injected annually into the reservoir to increase oil production by an expected 170 million barrels and extend the field life by 25 years (Baines and Worden, 2004b; Wilson and Monea, 2004). In

addition, CO_2 injected into the reservoir over a 33 year period will result in approximately 56 million tonnes of CO_2 stored in the depleted oil field post production (Wilson and Monea, 2004).

Enhanced gas recovery through CO_2 injection is also a possibility. Instances of use are limited because primary production without CO_2 flooding can recover up to 95% of in-situ gas (Oldenburg, 2000; Wildenborg and van der Meer, 2002). However, disused or depleted gas and oil fields can also provide an attractive option for CO_2 storage as the reservoirs are generally well characterised, have pre-existing infrastructure and are proven storage sites. Therefore, depleted oil and gas fields provide an attractive storage option as they can either enhance the production of a field or at a minimum reduce costs through established geological characterisation and infrastructure.

Deep unmineable coal seams are the other main geologic option that combines CO_2 storage with enhanced recovery of a resource (i.e. methane). Coal seams typically contain economic quantities of methane-rich gas absorbed onto the surfaces of the coal (Gale and Freund, 2001). As CO_2 is more absorbent than methane, injection of CO_2 into coal seams will displace the methane for recovery and retain CO_2 on the coal surfaces (Reeves, 2003). In the United States alone, coal seams have the potential to store 90 billion tonnes of CO_2 resulting in the recovery of approximately 4 trillion cubic metres of methane (Reeves, 2003). So far, there have only been pilot-scale projects of CO_2 injection into coal seams in the San Juan Basin in the United States and the Alberta Basin in Canada (Gale and Freud, 2001; Reeves et al., 2001; Reeves, 2003). In addition, the technology for injection and retention of CO_2 in deep unmineable coal seams is at an earlier stage of development than storage in saline aquifers or depleted oil and gas fields. However, economic benefits will probably ensure commercial-scale development and utilisation of this reservoir type for CO_2 storage in the near future.

1.3 Issues with Geological Storage

While there has been rapid progress in the development of geologic CO_2 storage in recent years, further technical and economic issues need to be resolved before widespread implementation of this technology can occur (Gale, 2004; Benson, 2005). Many of these issues are outlined by Gale (2004), though specific geology-

related topics include additional knowledge on the processes that contribute to long term geologic storage of CO_2 and better assessment of the risks and consequences of CO_2 leakage from storage sites. Previous and on-going studies aimed at understanding the impact of CO_2 in the subsurface have commonly used forward modelling with geochemical software and/or short term experiments to simulate conditions expected during CO_2 injection and storage (i.e. Czernichowski-Lauriol et al., 1996; Gunter et al., 1997; Pruess et al., 2001; Pruess and Garcia, 2002; Johnson et al., 2004, 2005; Rochelle et al., 2004; Kumar et al., 2005; White et al., 2005; Wo and Liang, 2005). These investigations provide insight into CO_2-fluid-rock interactions but are limited by the complexity of the system, incomplete datasets and short time spans (months to years) relative to the retention periods required for CO_2 storage (hundreds to thousands of years; Baines and Worden, 2004a). Other studies are monitoring current CO_2 storage projects (i.e. Sleipner and Weyburn) to demonstrate the viability of the technology (i.e. Zweigel et al., 2000, 2004; Moberg et al., 2003; Arts et al., 2004; Wilson and Monea, 2004). These projects, however, are only in their infancy and provide little information on the long-term fate of CO_2 in the subsurface.

A third approach to overcome uncertainties associated with CO_2 storage is to investigate sites where large volumes of CO_2 have naturally accumulated and been stored in geologic reservoirs for thousands to millions of years (Stevens, 2005). These naturally occurring CO_2 accumulations have been studied worldwide (i.e. Pearse et al., 1996, 2004; Allis et al., 2001; Stevens et al., 2001; Baines and Worden, 2004a; Shipton et al., 2004 2005; Moore et al., 2005; Stevens, 2005), as they provide analogues for studying long-term storage and migration of CO_2 in geologic reservoirs. In particular, reservoirs that have trapped CO_2 for geological timescales can aid in identifying dominant CO_2 reservoir- and cap rock-interaction processes as well as constrain criteria for selecting storage sites. Conversely, where CO_2 is or has leaked to the surface there are opportunities to investigate migration pathways (i.e. faults and fractures), leakage rates and fluxes and effects of leakage on the subsurface and surface environment.

The Paradox Basin, located in the Colorado Plateau region of the United States, is one such area that contains a number of natural CO_2 reservoirs that are being investigated as analogues for future engineered CO_2 geologic storage sites (Fig. 2.1; Allis et al., 2001; 2005; Shipton et al., 2004; 2005; Moore et al., 2005; Stevens, 2005; White et al., 2005). Many of these reservoirs have contained CO_2 for extended periods

of time and are currently being exploited, predominantly for EOR (i.e. Bravo, Farnham and McElmo; Allis et al., 2001). Other reservoirs leak CO_2 due to the influence of faults (Springerville-St Johns; Moore et al., 2005; Stevens, 2005) and/or boreholes (Woodside; Doelling, 1994).

The study presented in this thesis examines a leaking reservoir at the northern end of the Paradox Basin in east-central Utah. The reservoir consists of a sequence of siliciclastic rocks folded into the open, gently north-plunging Green River Anticline and cut by the west-north-west trending Little Grand Wash Fault, Salt Wash Graben and Ten Mile Graben. Carbon dioxide discharges from sandstone aquifers cut by the Little Grand Wash Fault, the northern fault of the Salt Wash Graben and certain boreholes to erupt as a series CO_2-charged geysers and springs and precipitate travertine deposits. Work by Heath (2004) has focused on characterising the CO_2-charged waters that erupt from the geysers and springs to define the current source and characterise the hydrologic regime associated with the migrating CO_2 in the study area. This thesis focuses on the travertine deposits and dominant structural features of the study area to define the migration pathway of the CO_2 through the faulted stratigraphy and elucidate the CO_2 leakage history of the reservoir.

Research into this leaking CO_2 reservoir was funded by, and forms part of, the Carbon Capture Project (CCP). Initiated in 2000 by eight of the world's leading energy companies and various government agencies (see http://www.co2capture project.org/index.htm), the CCP's aim is to develop technologies that will reduce anthropogenic carbon emissions in the short- to medium-term future. As previously stated, geologic storage is currently considered the best short-term option to reduce CO_2 emissions and efforts have been directed towards developing this technology. This study contributed towards the storage integrity theme of the CCP, which was concerned with developing a better understanding of natural (faults, cap rocks, reservoirs) and engineered (boreholes and associated materials) features that permit safe and effective geologic storage of CO_2. To date the research in this thesis has resulted in two publications entitled "Internal structure and evolution of fault-related active and ancient travertine deposits in east-central Utah, U.S.A." (Dockrill et al., Submitted) and "Natural leaking CO_2-charged systems as analogues for failed geologic storage reservoirs" (Shipton et al., 2005).

1.4 Aim of Thesis

The aim of this thesis is to use a naturally failed CO_2 geologic reservoir to define the factors that influence the integrity of potential geologic storage sites and determine the rates and consequences of CO_2 leakage in the subsurface and surface environments. Using an integrated field and geochemical approach to investigate the fault zones and leak products at the surface combined with three-dimensional modelling of the reservoir in the subsurface, a comprehensive model of the CO_2 flow system from source to surface has been developed. Furthermore, the multidisciplinary study enabled the structural and hydraulic properties of the fault zones to be characterised, the migration pathways of CO_2 and earlier fluid regimes through the faulted stratigraphy to be identified, the volume of CO_2 contained and leaked from the reservoir to be approximated and the long-term consequences of CO_2 leakage on the surrounding environment to be documented. Results from this thesis have implications for future studies on the interaction of CO_2 with both fault and cap-rock seals. Additionally, this thesis highlights the potential risks of CO_2 storage in certain geologic settings and may influence selection and design of future CO_2 geologic storage sites.

1.5 Structure of Thesis

This thesis is divided into six chapters that cover a range of topics related to investigating the controls and effects of CO_2 leakage from a fault-bounded reservoir. Due to the range of techniques used and subjects covered in this study, each chapter contains detailed introduction, methodology and literature review sections where needed. Chapter 2 provides an overview of the structural and stratigraphic characteristics of the study area and reviews the tectonic events that shaped it. Chapter 3 details the main structural features in the study area that appear to be controlling the leakage of CO_2, focussing on the composition and architecture of the fault zones and their potential influence on fluid flow. Chapter 4 describes all fault-related mineralization and diagenesis in the study area, using it to constrain the migration pathways of various fluid regimes including CO_2. In addition, travertine deposits precipitated from CO_2-rich waters are used to highlight spatial and temporal variations in leakage and approximate the amount of CO_2 that has leaked to the surface from the reservoir. Chapter 5 uses three-dimensional modelling to predict

subsurface migration pathways, trapping structures and storage capacities of CO_2 in the faulted stratigraphy. Chapter 6 summarises the findings of the previous chapters, discusses the major implications of the research and proposes future work based on this research.

Chapter 2: Geological Framework

2.1 Introduction

This chapter provides an overview of the geology and tectonic events that shaped the region around the Little Grand Wash Fault, Salt Wash Graben and Ten Mile Graben at the northern end of the Paradox Basin. The Paradox basin has been extensively studied due to its hydrocarbon (Baker, 1933; Bryant, 1987; Hansley, 1995; Huntoon et al., 1999) and mineral resources (Doelling and Trimble, 1978; Morrison and Parry, 1986; Breit and Meunier, 1990; Huffman et al., 1996) and anomalous flux of CO_2 (Cappa and Rice, 1995; Allis et al., 2001, 2005; Shipton et al., 2004, 2005; Moore et al., 2005; Stevens, 2005; White et al., 2005). The chapter is subdivided into describing the geological setting of the study area (section 2.2), outlining the sedimentary characteristics of the faulted stratigraphy (section 2.3) and documenting the tectonic history of the Paradox Basin (section 2.4). New information on the timing of fault growth and salt movement in the study area will be presented in Chapter 3 and will be used in the modelling phase in Chapter 5.

2.2 Geological Setting

The Little Grand Wash Fault, Salt Wash Graben and Ten Mile Graben are located at the northern end of the Paradox Basin in east-central Utah. The Paradox Basin forms part of the Colorado Plateau and is a late Palaeozoic to Mesozoic intracratonic basin infilled with a thick sequence of evaporite, carbonate and clastic sediments (Fig. 2.1; Hintze, 1993). The basin is defined by the extent of evaporites in the middle Pennsylvanian Paradox Formation (Baars and Stevenson, 1981), which cover an extensive area of southern Utah and western Colorado (Fig. 2.2a). The shape and topography of the basin has been influenced by several tectonic events cumulating in the present-day uplift of the Colorado Plateau and downcutting by the Colorado River and its tributaries. These events are summarised in section 2.4.

The Paradox Basin is bordered by a series of monoclines and structural highs (Fig. 2.2a). To the northwest, the San Rafael Swell is an arcuate anticline with a broad west limb and a steep east limb. To the northeast, the Uncompahgre uplift is a near rectangular, northwest-trending anticline cored by Precambrian basement rocks that has 200 to 300km long thrust faults along its southwest and northeast margins (Barbeau, 2003). In between, the Paradox Basin merges with the southern edge of the

Uinta basin, with strata gently dipping to the north. The southeastern and southern borders are defined by the San Juan Dome structural high and the Hogback monocline, respectively, while the southwest border is bounded by the broad Monument uplift anticline.

The structural and topographic features of the Paradox Basin can be subdivided into three provinces (Fig. 2.2a): the Paradox Fold and Fault Belt (Kelley, 1958) in the north and the Blanding basin and Four Corners Platform in the south. The Paradox Fold and Fault Belt province consists of a series of roughly parallel, northwest-trending faults, anticlines and synclines related to the migration and dissolution of evaporites from the Paradox Formation that has been occurring since shortly after deposition to the present day (Doelling, 1988). Rocks that crop out in the basin range in age from the Pennsylvanian in some exposed anticline cores to Cretaceous in synclines. To the south, the Blanding basin is a relatively undeformed area with Jurassic and Cretaceous rocks. The Four Corners Platform is a structurally high bench capped by Cretaceous rocks that separates the Paradox Basin from the San Juan basin to the south (Condon, 1992).

At the northern end of the Paradox Basin, the Little Grand Wash Fault and Salt Wash/Ten Mile Graben systems cut the open, north plunging Green River anticline (Fig. 2.2b). The Green River Anticline is most likely related to evaporite movement in the Paradox Formation (Fig. 2.2b; section 3.5). The Little Grand Wash Fault is a 30km long, south-dipping, arcuate normal fault. The Salt Wash and Ten Mile Grabens are a set of WNW-trending, dip-slip grabens linked by a complex relay zone. CO_2-charged groundwater effuses from a series of geysers and springs that precipitate carbonates (travertine) along or immediately to the north (footwall) of both fault systems (see chapter 4). Additional CO_2-charged geysers (Woodside, Tumbleweed and Chaffin Ranch geysers) are found in the surrounding region where water and petroleum wells have tapped carbonate-rich groundwaters (Fig. 2.2; Doelling, 1994).

Numerous natural CO_2-rich gas accumulations have been discovered throughout other parts of the Colorado Plateau-Southern Rocky Mountain region (Fig. 2.1). The accumulations commonly have CO_2 concentrations in excess of 90% with the remainder a mixture of nitrogen, helium and/or hydrocarbon gases (Bryant, 1987; Morgan and Chidsey, 1991; Cappa and Rice, 1995; Allis et al, 2001). Around a dozen CO_2 fields have been exploited for enhanced oil recovery, dry ice and industrial uses.

Five of these (Bravo Dome, McElmo Dome, Sheep Mountain, Big Piney-LaBarge and McCallum) are currently being produced to supply CO_2 for enhanced oil recovery. Most of the CO_2 reservoirs have accumulated in fault-bounded anticlines with either four-way anticlinal closure or fault seal along one margin of the field. The dominant reservoir lithologies are sandstone, dolomite and fractured basement, while the overlying sealing lithologies are low permeability mudstones and/or anhydrite (Allis et al, 2001). Many CO_2 fields have multiple, stacked reservoirs indicating vertical migration of CO_2 through the stratigraphy primarily via fault and fracture systems (Allis et al, 2001).

2.3 Stratigraphy

2.3.1 Introduction

Strata offset by the Little Grand Wash Fault, Salt Wash Graben and Ten Mile Graben range in age from at least the mid-Pennsylvanian to Cretaceous, though mid-Jurassic to Cretaceous rocks outcrop at the surface in the study area. Figure 2.3 presents a generalised section of the lithological formations offset by these faults. The average thickness of the deposited formations in the study area is ~2900m. The Palaeozoic section is more than 1600m thick and was mainly deposited in marine environments. The Mesozoic sediments were primarily terrestrial or marginal marine, except for the Mancos Shale. Cretaceous sediment is unconformably overlain by Quaternary sediments, though the presence of Tertiary strata in the Book Cliffs to the north suggests that these strata were once present in the study area as well. The following section provides an introduction of the stratigraphic units involved in the generation or migration of fluids through the study area.

2.3.2 Stratigraphic Units

2.3.2.1 Paradox Formation

The Paradox Formation is a diverse unit composed of halite, anhydrite and dolomite with subordinate amounts of black shale (Fig. 2.3). The unit was deposited in the middle Pennsylvanian as a series of cycles that represented the desiccation and marine flooding of a restricted basin (Condon 1992). Halite is the most abundant constituent, representing 75 to 90 percent of the total thickness of the formation (Doelling, 1988). The other lithologies define internal marker beds, with the organic-

rich black shale constituting an important source rock for some of the hydrocarbons that have been extracted from the basin. The formation was initially deposited as a tabular sheet around 1500m thick (Doelling, 1988). Subsequent basement faulting and sedimentary loading induced salt flowage and the development of salt-cored anticlines with the formation locally thickening to more than 4000m within the anticlines and partially to completely withdrawing from adjacent synclines (Cater, 1970).

2.3.2.2 Honaker Trail Formation

The Late Pennsylvanian Honaker Trail Formation is composed of fossiliferous and micritic limestones interbedded with siltstones and sandstones (Fig. 2.3). The siliclastic content increases towards the northeastern side of the basin. The formation represents a return to normal marine conditions following a period of restricted, evaporitic marine conditions (Condon, 1992). The thickness of the formation varies significantly throughout the basin due to salt flowage in the underlying Paradox Formation during deposition.

2.3.2.3 Cutler Formation

In the northeastern part of the Paradox Basin, the Cutler Formation is composed of a thick Permian sequence of arkosic sandstones with subordinate amounts of conglomerates, siltstones and mudstones (Fig. 2.3). The formation was deposited from large, coalescing alluvial fans that were derived from uplift of the Uncompahgre block in the late Pennsylvannian to early Permian (Nuccio and Condon, 1996). The thickness of this formation also varies significantly due to syn-depositional salt flowage in the underlying Paradox Formation. In the western and southern parts of the basin, the Cutler is raised to Group status, with formations present in the study area consisting of the Elephant Canyon Formation, Organ Rock Formation and White Rim Sandstone.

The Elephant Canyon Formation is composed of limestone beds interbedded with marine sandstones and fluvial and aeolian siliclastics (Baars, 1962; Condon, 1992). The Organ Rock Formation is composed of interbedded sandstones, siltstones, mudstones and limestone-nodule conglomerates. The formation was deposited in sabhka and aeolian environments (Stanesco and Dubiel, 1992). The White Rim Sandstone is composed of thick aeolian sandstones modified by coastal marine processes (Steele, 1987; Chan, 1989). The sandstones are fine- to medium-grained,

moderately-sorted quartz arenites (Chan, 1989). In the Canyonlands region of southeastern Utah, the White Rim sandstones contain the largest accumulation of heavy oil (tar) in North America (Demaison, 1977). This formation is also a major regional aquifer (Hood and Patterson, 1984).

2.3.2.4 Kaibab Limestone

The Late Permian Kaibab Limestone, also known as the Black Box Dolomite (Welsh et al, 1979), is composed of interbedded dolomite and limestone and is only present as a thin veneer (0 to 40m thick) in the western part of the Paradox Basin (Condon, 1992). Pre-Triassic erosion combined with onlapping relationships with the White Rim Sandstone has left scattered outcrops only in the adjacent San Rafael Swell. The unit is a shallow marine shelf deposit that represents the maximum eastward marine transgression (Irwin, 1971). Around the flanks of the San Rafael Swell, wells that penetrate the Kaibab have produced hydrocarbons (Irwin, 1971; Kiser, 1976).

2.3.2.5 Moenkopi Formation

The Early to Middle Triassic Moenkopi Formation is a mixed unit of interbedded siltstones and fine- grained sandstones with subordinate amounts of limestone and mudstone (Fig. 2.3). The formation is regionally extensive and has been divided, based on lithology and weathering characteristics, into several members (with different names in various parts of the basin). In the northwestern part of the basin, Blakey (1974) divided the Moenkopi into the Black Dragon Member, Sinbad Limestone Member, Torrey Member and Moody Canyon Member. The lower, slope-forming Black Dragon beds are composed of fluvial siltstone and fine-grained sandstone shed eastward from a highland west of the Paradox Basin (Huntoon et al, 1994). The ledge-forming Sinbad Limestone is composed of marine limestone and dolomite with minor amounts of siltstone and sandstone. Most beds within this unit are saturated with hydrocarbons (Trimble and Doelling, 1978). The two upper members are composed of siltstone with lesser amounts of fine grained sandstone and mudstone that were deposited from a combination of sabhka, mudflat and fluvial environments (Stewart et al, 1972). Blakey (1974) differentiated the two members on the basis of one being a slope-former (Torrey Member) and the other a cliff-former (Moody Canyon Member).

2.3.2.6 Chinle Formation

The Late Triassic Chinle Formation was deposited in fluvial and lacustrine environments with the siliclastic sediments primarily derived from the Uncompahgre Uplift (Hazel, 1994). Similar to the Moenkopi, the formation has been divided into several members in various parts of the basin. In the northwestern part of the basin, based on topographic habit and lithology, Trimble and Doelling (1978) divided the formation into the Temple Mountain Member, Moss Back Member and Church Rock Member. The lower Temple Mountain is a thin floodplain siltstone with laterally discontinuous channel sands and conglomeritic lenses. The cliff-forming Moss Back is composed of well-connected fluvial channel sands with minor amounts of conglomerate and siltstone. The upper, slope-forming Church Rock is an interbedded siltstone and fine-grained sandstone floodplain deposit with subordinate amounts of mudstone and conglomerate. Continued salt flow in the Paradox Fomation during deposition of the unit has significantly altered the thickness of the formation throughout the basin. Hazel (1994) indicated that channel sands would be less abundant and continuous over topographic highs produced by the rising salt-cored anticlines.

2.3.2.7 Glen Canyon Group

The oldest Jurassic rocks in the study area are the Early Jurassic Glen Canyon Group, which is composed of the Wingate Sandstone, Kayenta Formation and Navajo Sandstone (Fig. 2.3). Contact between the terrestrial formations is gradational with unconformities at the base and top of the group (Pipiringos and O'Sullivan, 1978).

The Wingate Sandstone is a prominent cliff-forming aeolian deposit. The massive, cross-bedded unit is dominated by clean, aeolian dune and interdune sandstones with six major erg sequences identified (Clemmensen et al, 1989). The sandstones are typically well-sorted, fine-grained quartz arenites with mainly calcareous cementation. There are occasional partings of sandy siltstones, especially towards the base of the unit. The Wingate is identified as a regional aquifer throughout the Colorado Plateau (Hood and Patterson, 1984).

The Kayenta Formation is composed of arkosic sandstones with subordinate siltstones and mudstones deposited from a fluvial system. It is micaceous with medium to thick beds. The stream-deposited sandstones are lenticular, cross-bedded and fine to medium grained with occasional conglomeritic lenses. The siltstones and

mudstones form sporadic partings representing overbank fines deposited over and between the lenticular channel sands. Bromley (1991) indicated that the south-west flowing Kayenta fluvial system was episodically channelled through the northwest-trending salt withdrawal synclines leading to thickening of the formation in these areas.

The Navajo Sandstone is an aeolian-dominated sequence that formed part of an extensive Jurassic erg system (Blakey et al, 1988). The unit is a well-sorted, fine-grained quartzarenite dominated by large-scale aeolian cross-stratification. Sporadic, thin interdune playa limestone beds occur through the deposit. The thickness of the unit is locally modified in areas around salt movement. The formation is generally a highly porous and permeable unit resulting in it being a major regional aquifer (Hood and Patterson, 1984; Spangler et al, 1996).

2.3.2.8 San Rafael Group

Unconformably overlying the Glen Canyon Group is the Middle Jurassic San Rafael Group consisting of the Carmel Formation, Entrada Sandstone, Curtis Formation and Summerville Formation (Fig. 2.3). These formations were deposited in and on the margins of an inland sea that transgressed from the north during at least two transgressive-regressive cycles (Nuccio and Condon, 1996).

The Carmel Formation is a mixed marine sequence of limestone, sandstone, siltstone and gypsum. Within the study area, Trimble and Doelling (1978) have identified two distinct members based on lithology. The lower member is composed of interbedded limestone and sandstone with subordinate amounts of siltstone. The upper member is composed of siltstone and gypsum with minor amounts of interbedded sandstone and siltstone. East of the Green River, Doelling (2001) interpreted the Carmel to change facies to a sabhka deposit and integrated it as the lowest member (Dewey Bridge) of the Entrada Sandstone.

The Entrada Sandstone is a dune-sea deposit that displays facies variations on a regional scale (Kocurek, 1981). In the San Rafael Swell, the Entrada is a shallow marine silty sandstone, while to the east it changes facies to an aeolian deposit (Trimble and Doelling, 1978). In the study area, the Entrada is a wet-aeolian dune system with alternating thin to massive cross-bedded and horizontal layers. The red sandstone is a predominantly fine to medium-grained, moderately sorted quartzarenite (Fig. 2.4a) with numerous soft sedimentation deformation features. Sporadic, thin

sabhka siltstone layers are intercalcated throughout the unit. Hood and Patterson (1984) identified this unit as the highest major aquifer in the region. Towards the Moab region, this unit is demoted to member status and is known as the Slick Rock Member within a revised Entrada Sandstone (Doelling, 2001).

The Curtis Formation is a shallow marine deposit that resulted from a marine transgression across the Entrada erg (Escher and Kocurek, 1986). The formation changes facies eastward and pinches out between the Green and Colorado rivers (Nuccio and Condon, 1992). In the study area, the Curtis Formation is composed of sandstones, siltstones and shales that can be divided into a lower cliff-forming member and an upper slope-forming member (Trimble and Doelling, 1988). The lower member consists of fine to medium-grained, poorly sorted quartz arenites with basal beds representing the reworking of Entrada sediments (Fig. 2.4b). The upper member is predominantly glauconitic sandstone that becomes increasingly clay-rich up sequence (Fig. 2.4c). A zone of limestone beds with distinctive jasper nodules caps the top of the formation.

The Summerville Formation is composed of thinly-bedded siltstone and mudstone with minor amounts of fine-grained sandstone and limestone (Fig. 2.4c). In the top half of the formation, there are a series of gypsum beds that become thicker and more frequent up sequence. The Summerville represents a marginal marine, tidal-flat environment that was deposited at the margin of the retreating Curtis Sea (Trimble and Doelling, 1978).

2.3.2.9 Morrison Formation

The Late Jurassic Morrison Formation is a widespread unit outcropping throughout the Rocky Mountain and Colorado Plateau regions. In the study area, the Morrison was deposited in fluvial and lacustrine environments and is subdivided into three members: the Tidwell Member, Salt Wash Member and Brushy Basin Member (Fig. 2.3). The basal Tidwell Member is composed of thin bedded calcareous mudstone with sporadic, thin limestone beds and chert concretions deposited in a marginal marine, tidal environment (Fig.2.4c). The Salt Wash Member is a sandstone-dominated, stacked fluvial channel deposit interbedded with discontinuous siltstone and fine-grained overbank mudstones (Fig.2.4c). The medium to coarse-grained sandstones are lenticular and generally low-sinuosity, braided river deposits that were sourced from the west and southwest of the basin (Peterson and Turner-Peterson,

1987). The upper Brushy Basin Member is composed of multicoloured, banded mudstone and siltstone with occasional thin limestone beds (Fig. 2.4d). Isolated channel sandstones are present towards the base, while a significant component of volcanic ash is present in the upper two thirds of the unit. The unit was deposited in a combination of lacustrine and floodplain environments with periodic supply of ash from nearby volcanoes (Turner and Fishman, 1991).

2.3.2.10 Cedar Mountain Formation

The Lower Cretaceous Cedar Mountain Formation consists of the lower Buckhorn Conglomerate and an upper shale member (Fig. 2.3). The Buckhorn Conglomerate is composed of conglomeritic sandstones deposited in a fluvial environment, which are discontinuous throughout the study area. The sandstones are immature, lithic arenites that are commonly silicified and have abundant chert and quartzite pebbles and cobbles. The upper shale member is composed of multicoloured, banded mudstone, siltstone and subordinate limestone. The limestone zones commonly weather out brown nodules that litter the lower slopes of hillsides comprised of this member. The unit was deposited in similar floodplain and lacustrine conditions to the Brushy Basin Member of the Morrison Formation (Trimble and Doelling, 1988).

2.3.2.11 Dakota Formation

The Late Cretaceous Dakota Formation is thin and discontinuous in the region and consists of conglomerate with occasional thin sandstone lenses (Fig. 2.4e; Trimble and Doelling, 1988). The immature conglomerates are composed of chert and quartzite pebbles and cobbles and are partly silicified. The Dakota was deposited in a coastal plain environment, in front of transgressing intracratonic sea (the Mancos Sea of Molenaar, 1981).

2.3.2.12 Mancos Formation

The Late Cretaceous Mancos Formation is a thick marine sequence of mudstones and siltstones with minor amounts of sandstones. In the study area, the Mancos is divided into three members: the Tununk Shale Member, Ferroan Sandstone Member and Upper Mancos Shale Member. The Tununk Shale is a blue grey marine shale with occasional thin sandy limestone beds (Fig. 2.4f). The Ferroan Sandstone is

a thin, fine-grained, thin bedded marine sandstone interbedded with grey shale. The Upper Mancos Shale is a thick grey shale with several thin, fine-grained sandstone beds and occasional limestone lenses. The Mancos was deposited as part of the extensive Western Interior Cretaceous seaway (Nuccio and Condon, 1992).

2.4 Tectonic History of the Paradox Basin

The Paradox Basin developed along the southwestern flank of the Uncompahgre uplift during the mid Pennsylvanian to Permian Ancestral Rocky Mountain orogeny (Stevenson and Baar, 1986). The uplift of the crystalline Uncompahgre block by northwest-trending reverse faults induced crustal flexure to create an asymmetric depressed basin closest to the uplift, as well as a peripheral uplift-parallel bulge ~200km southwest of the uplift (Barbeau, 2003). This bulge restricted the flow of marine waters into the basin, promoting deposition of thick evaporite-shale-carbonate successions (Paradox Formation; Fig. 2.3). Nearshore carbonates (Honaker Trail Formation) and terrestrial siliclastic sediments (Cutler Formation) infilled and breached the basin during the later stages of subsidence (300-260Ma) as sedimentation exceeded the rate of subsidence in the basin (Barbeau, 2003).

Reactivation of basement faults below the Paradox Basin combined with sedimentary loading are thought to have initiated flowage of the mid Pennsylvanian evaporites in the Desmoinesian (~310-305Ma), to form a series of northwest-trending, salt-cored anticlines and pillows (Shoemaker et al, 1958; Doelling, 1988). Drilling and geophysical surveys have identified northwest-striking, high angle basement faults beneath several of the salt-cored anticlines (Case et al, 1963, Parker, 1981; Woodward-Clyde Consultants, 1983). Movement of the evaporites continued until the late Triassic (Doelling, 1988), with voluminous arkosic sediments, sourced from the Uncompahgre uplift, burying the rising salt anticlines. This caused significant variation in the thickness of the overlying sediments with upper Pennsylvanian to mid Jurassic formations being thin to absent over some salt anticlines, but significantly thicker in the synclines that developed adjacent to the anticlines from evaporite withdrawal (Cater, 1970; Doelling, 1988; Condon, 1992).

Major tectonic activity resumed with the onset of the Laramide orogeny from the late Cretaceous to the early Tertiary. This orogeny reactivated and uplifted pre-

existing structures (Uncompahgre uplift), as well as forming a series of basement fault-cored monoclines bordering the Paradox Basin (Fig. 2.2a; Davis, 1978; Baars and Stevenson, 1981; Heyman et al, 1986). In addition, regional north to northwest-trending broad folds are suggested to have formed during this period (Cater, 1970). These broad folds are believed to have superimposed on the salt-induced anticlines and adjacent synclines to accentuate folding in the region (Cater, 1970; Doelling, 1988). Prominent faults (Moab Fault, Lisbon Fault, and Salt Valley Graben) within the sedimentary cover were also formed or reactivated during this period (McKnight, 1940; Doelling, 1988; Foxford et al, 1996). Although these faults are related to the compressive Laramide Orogeny, the positions of the faults were influenced by the evaporites, preferentially rupturing along the margins of thick salt bodies (Doelling, 1988).

Following the Laramide orogeny, a number of laccolithic complexes (La Sal Mountains) were intruded at shallow depths (1.9 to 6km) into the sedimentary sequence in the northeastern part of the Paradox Basin (Fig. 2.2a; Ross, 1998). Similar laccolithic complexes are present further south in the Paradox Basin (Abajo Mountains) and to the west of the basin (Henry Mountains). K-Ar dating of the complexes indicates that the intrusions were emplaced in the late Oligocene (Nelson et al, 1992). The igneous intrusions consisted of trachytes and rhyolite porphyries. The elliptical shape of the La Sal Mountains indicates that magma emplacement was partially controlled by the pre-existing salt-core structures (Ross, 1998).

From the late Cenozoic, the Colorado Plateau has undergone epeirogenic uplift (Hunt, 1956; Lucchitta, 1979). This has been accompanied by regional erosion causing salt-cored anticlines to be brought close to the surface or exhumed. Infiltration of groundwaters through fractures and joints has caused salt dissolution and collapse of some of the anticline crests (Doelling, 1988). The collapsed crests transform most anticlines into valleys or grabens, infilled with Quaternary deposits and bordered by escarpments.

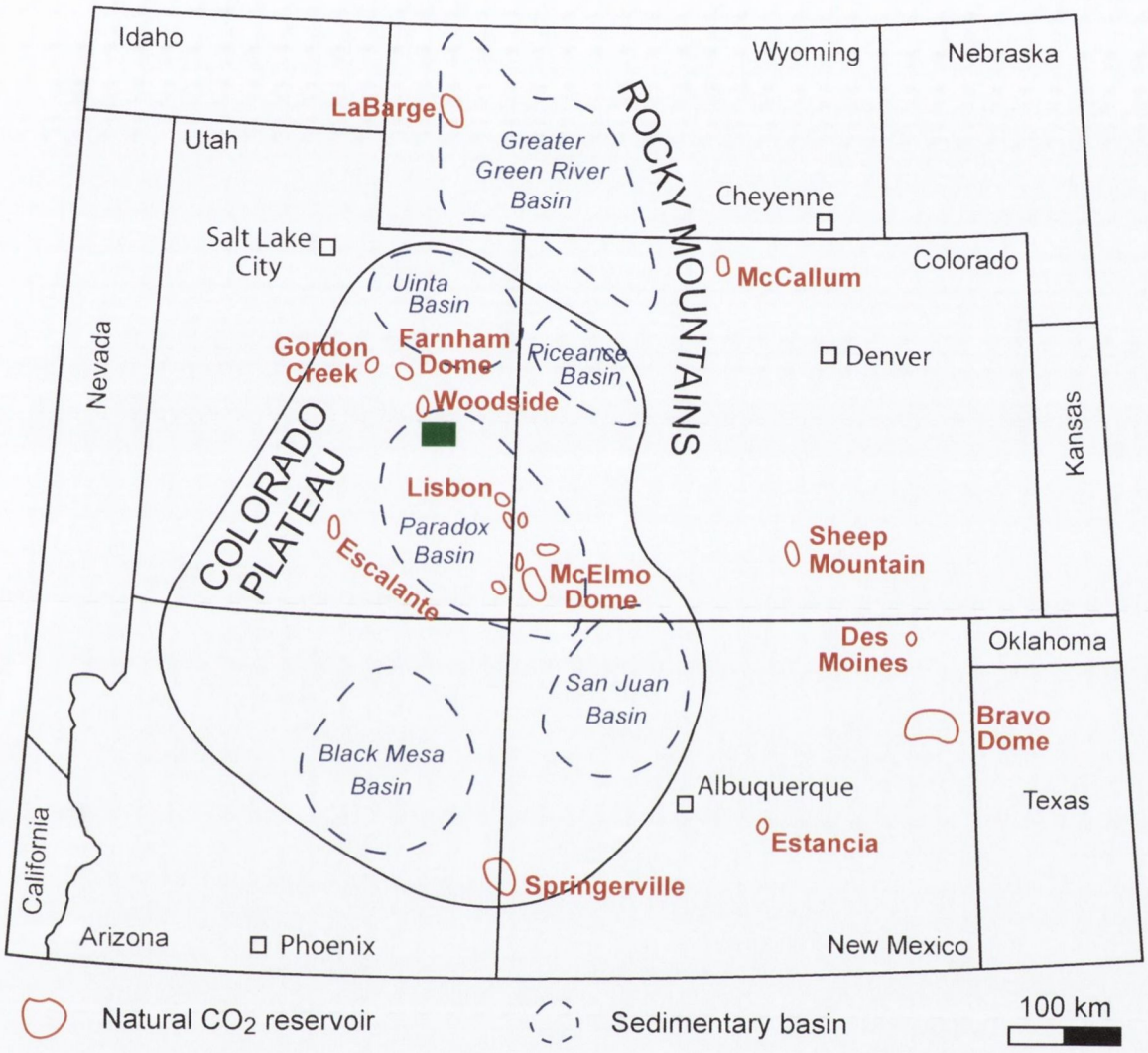


Figure 2.1: Distribution of sedimentary basins and CO_2 reservoirs throughout the Colorado Plateau and Southern Rocky Mountain region (after Allis et al, 2001). Green box indicates field area.

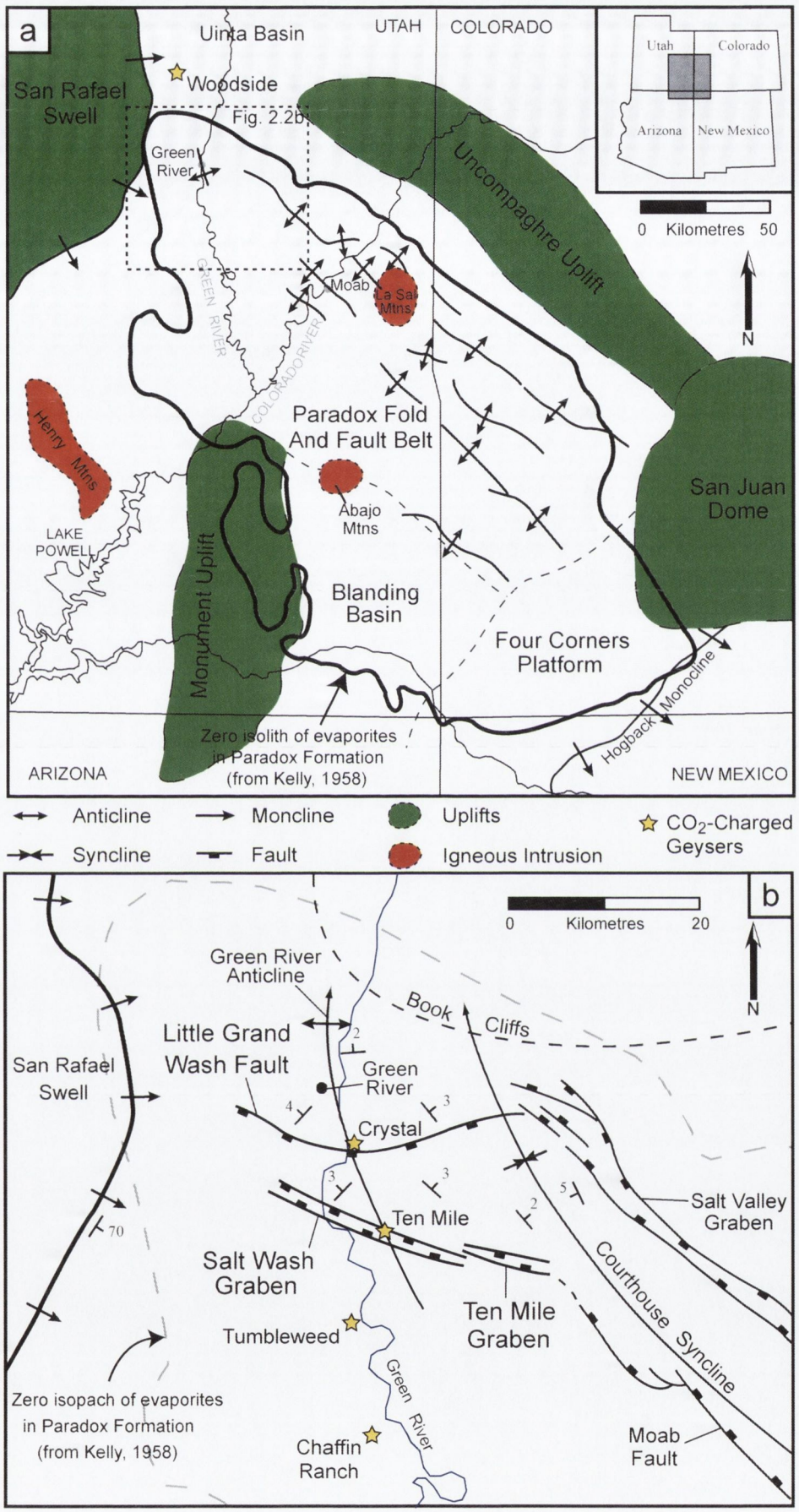


Figure 2.2: Geological features of the Paradox basin and surrounding region. (a) Structural provinces of the Paradox basin and bordering uplifts (after Condon, 1997). Inset shows location of basin in cenral west USA. (b) Main structural features at the northern end of the Paradox Basin. Fault positions from Doelling (2001).

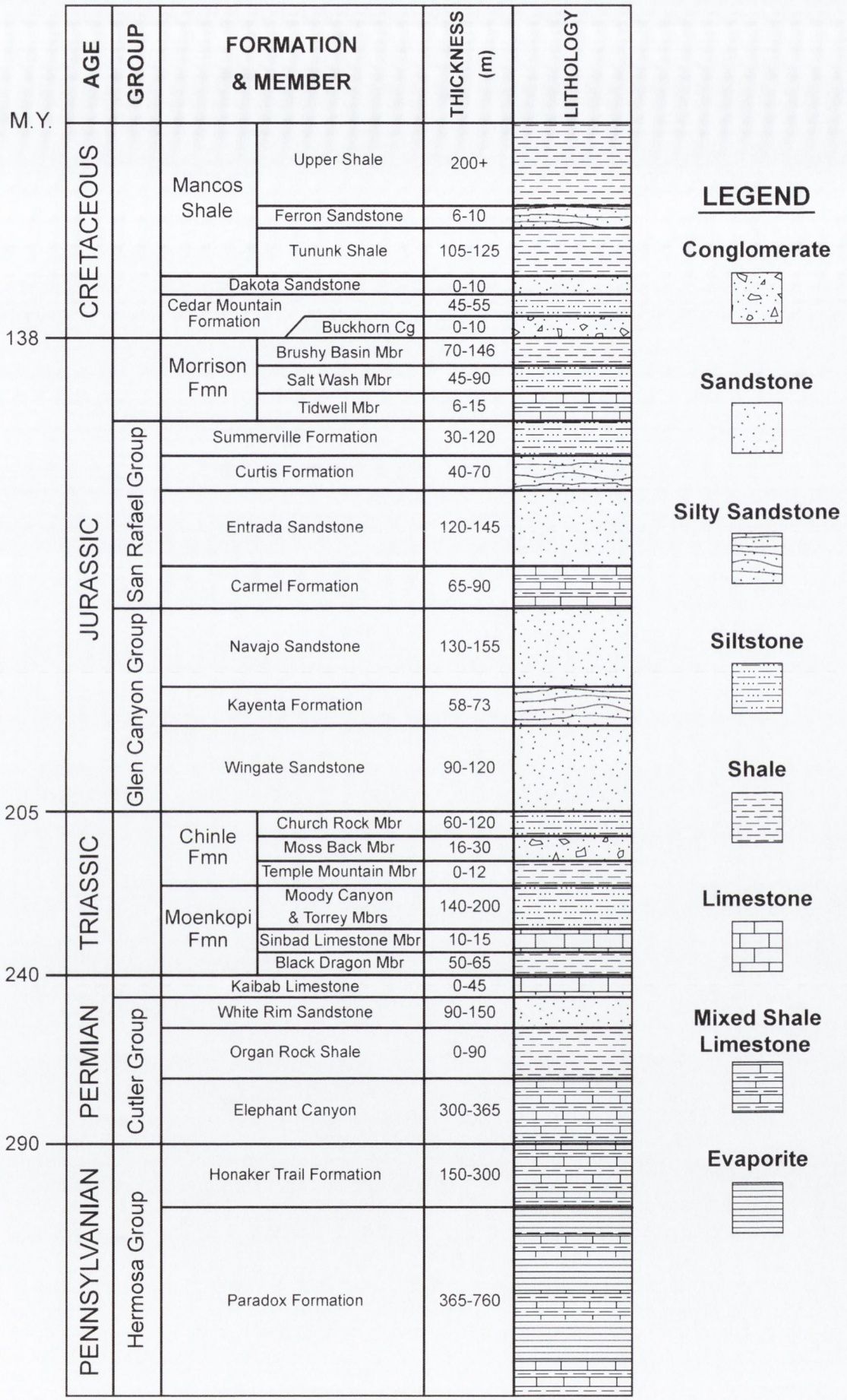


Figure 2.3: Generalised stratigraphic section for the Green River area. Thickness data compiled from Trimble and Doelling (1978) and Hintze (1993).

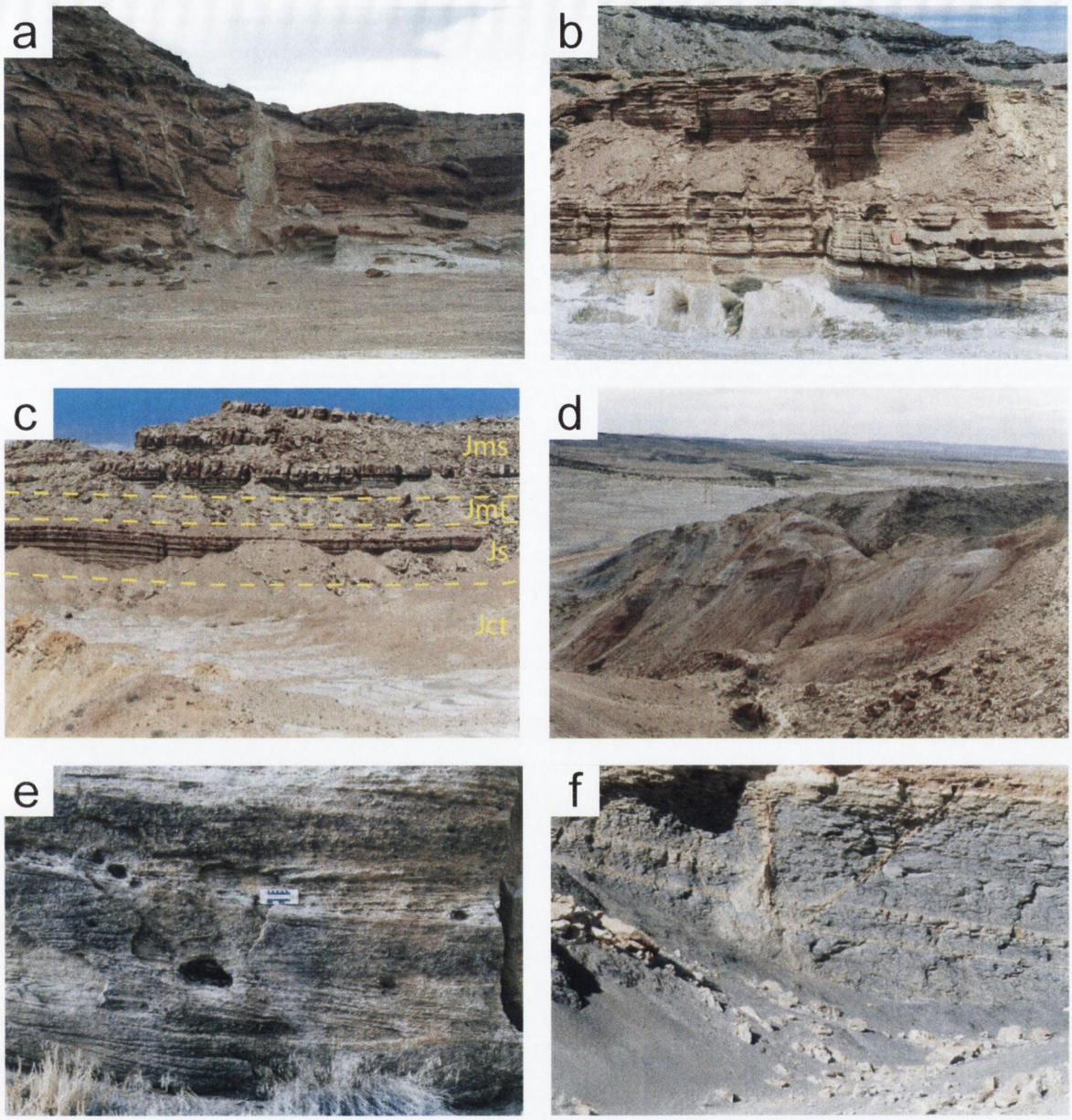


Figure 2.4: Field photographs of stratigraphy outcropping in study area. (a) Red Entrada Sandstone with zones of bleaching around sub-vertical fractures. (b) Lower, cliff-forming sandstone member of the Curtis Formation. (c) Panoramic view displaying the upper slope-forming member of the Curtis Formation (Jct), the thinly-bedded Summerville Formation (Js) and the Tidwell (Jmt) and Salt Wash (Jms) Members of the Morrison Formation (Jms). (d) Dipping, clay-rich Brushy Basin Member of the Morrison Formation. (e) Coarse-grained river channel conglomerate from the Dakota Formation. (f) Typical grey shales from the Tununk Shale Member of the Mancos Formation.

Chapter 3: Structure

3.1 Introduction

The northwest-trending Little Grand Wash Fault and kinematically-linked Salt Wash and Ten Mile Grabens outcrop to the south of the town of Green River and cut the north-plunging Green River Anticline. Structural highs created by the faulting of the anticline have focused multiple phases of fluid flow in the footwalls of the Little Grand Wash Fault and the northern fault of the Salt Wash Graben (see Chapter 4). This chapter characterises these structures to enable assessment of fluid migration through the faulted stratigraphy in subsequent chapters. The chapter is subdivided into three sections, which: (1) document the geometry and characteristics of the Little Grand Wash Fault, Salt Wash Graben, Ten Mile Graben and Green River Anticline; (2) describe the composition of the faults and variability in their accompanying damage zones; and (3) identify temporal changes in sedimentation associated with the development of the Green River Anticline. These studies clarify the structural characteristics of the study area to provide the framework for the generation of conceptual and three-dimensional models for fluid flow, as well as supplying a platform for fault seal assessment in later chapters.

3.2 Structural Components of the Study Area

The main structural features of the study area are documented in the following section. Structural characteristics were elucidated from a combination of field mapping, a well summary database supplied by the Utah Geological Survey, wire-line logs donated by Rileys Electric Logs Inc and published geological maps (Baker, 1933; Condon, 1997; Doelling, 2001; 2002; Hood and Patterson, 1984).

3.2.1 Folds

3.2.1.1 Green River Anticline

The Green River Anticline is a broad, open fold cut by the Little Grand Wash Fault and Salt Wash Graben (Fig. 3.1). The fold has a wavelength of 30km, an amplitude of 320m and a fold axis in excess of 25km. The anticline trends north to northwest, plunging 3 to 5° in the same direction. Both limbs of the open fold have similar dips of 2 to 6° but are of unequal length with the eastern limb being significantly longer.

3.2.2 Faults

3.2.2.1 Little Grand Wash Fault

The Little Grand Wash Fault is an east-west trending, south-dipping normal fault, which crops out about 5km to the south of the town of Green River (Fig. 3.1). At the surface, the fault trace is approximately 30km long and juxtaposes a mid Jurassic to Cretaceous sedimentary sequence. Quaternary sediments overlying sections of the fault remain undisturbed. In the subsurface, the down-dip extent of the fault is uncertain, though drilling records for two exploration wells (Amerada Hess 1 and 2; Fig. 3.1) that intersect the fault at depth suggest that the fault may offset sediments as old as Pennsylvanian in age. To the west, the fault appears structurally linked to the Saleratus (Cottonwood) Graben, while eastward, the fault may connect with northern extensions of the Salt Valley Graben (Fig. 3.1).

The fault has an arcuate surface trace that splits into two main fault strands in the central part of the structure, extending from 3.2km east to 0.1km west of the Green River (Fig. 3.2a). The two sub-parallel fault strands introduce structural complexities to the fault with a series of prominent fault bends, branch points and relay ramps. Between the two main strands, a complicated array of minor faults has created structural terraces with varying dips (Fig. 3.2a). Away from the central zone, a single fault strand is present.

The dip of the fault planes along the Little Grand Wash Fault varies but is generally steep, averaging 70^{o} to the south (stereonets in Fig. 3.2a; Appendix 1). Conversely, shallow (Exxon) and deep (Amerada Hess 1 and 2) well data indicate more moderate fault dips, averaging 58^{o} in the subsurface (Appendix 1). Slip indicators show that the fault is mostly dip-slip with some oblique right and left lateral movement (stereonets in Fig. 3.2a; Appendix 1).

Displacement is predicted to vary in both the horizontal and vertical directions along a fault with maximum displacement in the centre and zero displacement at the fault tips (Childs et al., 1996; Mansfield and Cartwright, 1996; Nicol et al., 1996). The horizontal throw profile of the Little Grand Wash Fault (Fig. 3.3) was calculated from locally derived stratigraphic cutoffs and thickness data extrapolated from exploration wells and published data (Trimble and Doelling, 1978; Hintze, 1993; Doelling, 2001). However, a scarcity of subsurface data, only provided by two exploration wells

(Amerada Hess 1 and 2) that penetrate the fault at depth, limited calculation of the vertical throw profile of the fault. Juxtaposition of the mid Jurassic Curtis Formation against Cretaceous Mancos Shale occurs at the maximum surface throw of 260m immediately east of the Green River (Fig. 3.3). Throw decreases systematically, though the resolution of throw towards the fault tips becomes limited where the thick Mancos Shale (>300m) is juxtaposed against itself. A horizontal throw gradient of c.0.01 agrees well with published data on other studied normal faults (cf. Walsh and Watterson, 1989; Nicol et al., 1996; Shipton and Cowie, 2001).

3.2.2.2 Salt Wash and Ten Mile Grabens

This 31km-long structure consists of the northwest-trending Salt Wash and Ten Mile Grabens, which are linked by a left-stepping relay ramp (Fig. 3.1). The grabens overlap for a kilometre, resulting in a steep, east-dipping ramp connecting the northern and southern footwalls between the two down-dropped structures (Williams, 2005). Both grabens are bound by sub-parallel, inward-dipping normal faults that offset a mid Jurassic to Cretaceous sequence at the surface. Quaternary sediments overlying sections of these faults remain undisturbed. The depth that the faults extend to is unknown due to the lack of subsurface data. However, reservoir-scale faults (Moab Fault and Salt Valley Graben) commonly penetrate the Pennsylvanian Paradox Formation in the immediate region (Doelling et al., 1988; Foxford et al., 1996) suggesting these faults may also sole into the Pennsylvanian Paradox Formation at depth.

The Salt Wash Graben is a 20km long, trough-shaped feature with an average width of 800m. Bed dips within the graben range from sub-horizontal in the centre of the graben to up to 25° towards the bounding faults. The northern fault is a single strand that dips steeply to the south, averaging 73° (Fig. 3.2b). Sporadic complexities are encountered along the fault trace in the form of relay ramps and branch points. The southern fault dips steeply to the north, averaging 75° and displays rare relay ramps and branch points along strike. To the east, the southern fault bends eastward, truncating the northern fault and terminating against the southern fault of the Ten Mile Graben, which accommodates the partial breaching of the relay ramp. Slickensides are rare but are found bordering shaley gouge along both faults, as well as along minor faults within the footwalls and indicate dominantly dip-slip movement.

The Ten Mile Graben is a 12km-long, trough-shaped feature that widens eastward from 250m to 1000m. Bedding dips within this graben also vary from sub-horizontal in the centre to moderate towards the bounding faults and further steepen westward in the overlap zone. Both bounding faults are relatively simple, single fault strands that dip steeply towards the graben, averaging 73° (Fig. 3.2b). Polished slickensides located on sand-rich, footwall beds bordering both faults indicate dip-slip movement (Fig. 3.2b). Lineaments on aerial photos suggest the southern fault of the Ten Mile Graben may be structurally linked to the Moab Fault to the southeast, though Quaternary deposits obscure the area where potential linkage occurs.

Horizontal throw profiles of the faults bounding each graben were calculated from locally determined stratigraphic cutoffs and the same thickness data used for the Little Grand Wash Fault profile. No vertical throw profiles could be established due to the lack of subsurface fault data. The northern and southern faults bounding the Salt Wash Graben have maximum throws of 366m and 210m, respectively; while the northern and southern faults of the Ten Mile Graben have maximum throws of 165m and 154m, respectively (Fig. 3.3). The variation in throw along strike of all the faults is not constant. There is a rapid change in throw along all faults approaching, and within, the overlap zone. Abrupt decreases in throw occur at a breached relay ramp on the northern fault of the Salt Wash Graben and at the branch point on the southern fault of the Ten Mile Graben where the southern fault of the Salt Wash Graben terminates. Considering the northern and southern faults combined, a cumulative throw profile displays an irregular, bell-shaped distribution interrupted by discrete throw reductions around the overlap zone. This decrease in throw is common in overlapping fault segments (Peacock and Sanderson, 1991; Dawers and Anders, 1995) and it is suggested that displacement is transferred to the relay ramp in the form of bed rotation and minor faulting. As such, these throw profiles indicate that the two overlapping grabens and bounding faults represent a geometrically and kinematically coherent graben system.

3.3 Fault Zone Architecture

3.3.1 Introduction

A fault zone is typically composed of a fault core, where most of the slip is accommodated, surrounded by a zone of smaller structures in the host rock that is

called the damage zone (Chester and Logan, 1986; Caine et al, 1996). The fault core may consist of a single slip surface, argillaceous-rich gouge, brecciated and/or cataclasitic rock or a combination of all of the above (Engelder, 1974; Caine et al., 1996, Yielding et al, 1997; Foxford et al., 1998; Ngwenya et al,, 2000). Depending on the amount of slip and faulting in the stratigraphic sequence, this can result in the fault core behaving as a conduit or seal to fluid flow (see section 5.3.2 for further details). A damage zone can consist of small faults, joints, deformation bands and/or veins that evolve during the growth of the fault (Caine et al., 1996; Sibson, 1996; Knipe et al., 1997; Gudmundsson et al., 2001). The complexity and density of structures within the damage zone increases around bends, jogs, tips and relay zones along the fault (Peacock and Sanderson, 1991; Trudgill and Cartwright, 1994; Sibson, 1996; Ferrill and Morris, 2001; Gartell et al., 2004). The damage zones can also influence fluid flow around the fault zone depending on the characteristics of the smaller structures (Caine et al., 1996).

This section provides a preliminary description of the fault core and damage zone for faults in the study area. By characterising the architecture of these fault zones, a preliminary assessment on the hydraulic behaviour of these structures can be established. This is subsequently combined with field relationships for CO_2 surface leak points (Chapter 4) and fault seal assessments (Chapter 5) to define the migration pathways of CO_2 from the source to the reservoir and eventually the surface.

3.3.2 Fault Core

3.3.2.1 Introduction

Characterisation of the fault core was conducted along sections of the Little Grand Wash Fault and northern fault of the Salt Wash Graben. These sections were selected as dry stream channels running at high angles to both faults providing good exposures of the fault core. Selected exposures were enhanced by digging shallow trenches and cleaning the outcrop with brushes. Detailed transects at these exposures characterised the composition and lateral variability of the fault cores. X-ray powder diffraction (XRD) analyses of selected samples aided in the identification of gouge mineralogy. The location of these transects are shown in Fig. 3.1.

3.3.2.2 Composition

The fault core can be defined as a brittle shear zone that separates fault rocks from relatively undeformed host lithologies (Fig. 3.4). The fault cores are typically 1 to 3m wide, have a complex internal structure and are variable from one outcrop to the next. Based on the transects, the fault core can be divided into three principal components consisting of: (1) argillaceous-rich gouge; (2) entrained sections of host rock; and (3) slip zones.

The argillaceous-rich gouge forms centimetre to metre thick sheets with a highly foliated, fault-parallel fabric that locally forms an S-C fabric adjacent to slip zones. The gouge is composed of mixtures of quartz and clay minerals including illite, illite-smectite and kaolinite minerals. Sporadic amounts of halite, calcite, feldspar and hematite are also found in the gouge. An increase in the illite content in illite/smectite minerals commonly occurs from wall rock to fault gouge (Fig. 3.4a/b). This increase has been previously reported in other argillaceous-rich faults with mixed-layer illite/smectite assemblages (Vrolijk and van der Pluijm, 1999). The cause of this increase is attributed to faulting providing additional energy to overcome kinetic barriers in the smectite to illite mineral reaction without appreciable addition of heat (Vrolijk and van der Pluijm, 1999).

The entrained sections of sand-rich host rock vary from small, isolated pods to coherent, highly-fractured slabs. These pods and slabs are most evident where mid to late Jurassic sandstones are located in the footwall. The slabs are thick blocks of sandstone and siltstone that are highly fractured with occasional deformation bands and rare calcite veining. The pods are fractured, elongated lenses of sandstone and siltstone that range in size from a few centimetres to 20cm thick. The isolated pods are enveloped by gouge with their long axis orientated sub-parallel to the gouge foliation.

The slip zones define the limit of the fault core separating fault rock from host rock. The intensely foliated argillaceous-rich slip zones are 5 to 100mm thick and have highly polished striated surfaces. They occasionally contain angular, sand-rich, pebble-sized clasts. Additional slip zones are also common within the fault zone, where they separate gouges and sandstone pods delivered from different lithologies. The striated surfaces and highly foliated nature of these zones suggest they accommodate most of the slip in the fault core.

3.3.2.3 Hydraulic Conductivity of the Fault Core

The sealing properties of a fault core are dependant on either the across-fault juxtaposition of reservoir (i.e. sandstone) and non-reservoir (i.e. shale) rocks or the presence of fault rocks that form a membrane seal or a combination of both (Yielding et al., 1997; Foxford et al., 1998; Knipe et al., 1998). Fault rocks that can provide an effective membrane seal include argillaceous gouge, cataclasites or cemented fault rock (Yielding et al., 1997; Knipe et al., 1998; Ngwenya et al., 2000). Multiple studies have demonstrated that a continuous argillaceous gouge is the most effective seal in preventing across-fault fluid flow (Smith, 1980; Gibson, 1994; Gibson, 1998; Yielding et al., 2002). The most significant feature of the fault core examined along the Little Grand Wash Fault and northern fault of the Salt Wash Graben is the universal presence of a thick, continuous argillaceous gouge. The presence of this gouge is due to the multiple argillaceous source beds present in the Upper Jurassic footwall and Lower Cretaceous hanging wall (see Fig. 2.3) and indicates the fault core forms an effective seal to across-fault fluid flow at the surface. Additionally, nonreservoir rocks in the hanging walls of both faults would also prevent across-fault fluid flow. However, this approach at the surface can not be extrapolated to the subsurface due to changes in the stratigraphy and the presence of more sand-rich beds in the Lower Jurassic sequence (Fig. 2.3). Therefore, an empirical approach predicting across-fault juxtapositions (Allen, 1989; Knipe, 1992; 1997) and argillaceous gouge development (Yielding et al., 1997) is needed to elucidate the sealing behavior of the fault core in the subsurface. This approach is taken in section 5.3 and results in the characterization of the across-fault conductivity for the Little Grand Wash Fault and northern fault of the Salt Wash Graben.

3.3.3 Damage Zone

3.3.3.1 Introduction

Networks of fractures are prevalent in the host rocks surrounding both the Little Grand Wash Fault and bounding faults of the Salt Wash and Ten Mile Grabens. The density of these fractures decreases with distance from the faults and is most intense in zones of structural complexity (i.e. fault intersections and relay zones). Occasionally, fractures are infilled with carbonates or sulphates. These structures can be considered to represent a damage zone as defined in section 3.3.1.

A preliminary investigation of fracture orientations and distributions surrounding the Little Grand Wash Fault was undertaken to characterise variations of the damage zone, both along strike and within different lithologies. Fracture analyses were limited to the Little Grand Wash Fault due to good, continuous outcrop exposures and varying degrees of structural complexity along the fault. A series of scanlines were focussed in two areas along the central part of the Little Grand Wash Fault (Fig. 3.1 and 3.5). Area 1 consisted of five scanlines along the Salt Wash sandstones of the Morrison Formation at intervals within and away from a partially breached relay ramp (Fig. 3.5a). The ramp is located in the footwall, adjoining the northern strand of two main fault strands with a combined throw of 245m. Area 2 consists of two scanlines in the immediate footwall and hanging wall of the master fault along silty sandstones of the Curtis Formation and shales of the Mancos Formation, respectively (Fig. 3.5b).. The Little Grand Wash Fault has a more simple structure in this area consisting of two closely-spaced fault strands with a combined throw of 255m. Further scanlines could not be conducted in this area due to a lack of outcrop.

A potential problem with fracture analyses is that one-dimensional scanlines are subject to sampling bias depending on the orientation of the transect compared to the fracture orientations (Park and West, 2002). To limit this bias, nearly all of the scanlines were locally orientated perpendicular to the master fault, where most fractures were expected to be intersected (Fig. 3.5). An additional fault-parallel scanline was taken within the relay ramp due to the diverse range of orientations observed in the fault-perpendicular scanlines. Each scanline measured and recorded the orientation and spacing of all fractures along the tape. Fracture data were then plotted on rose diagrams and frequency distribution histograms to compare orientations and changes in fracture density.

3.3.3.2 Results

3.3.3.2.1 Area 1

Most fault-perpendicular scanlines show a dominant east-west trending set of fractures that roughly parallel the strike of the master fault (Fig. 3.5a). Within the relay ramp, scanline 4 shows an additional complex array of subordinate fractures with diverse orientations that are highlighted by the fault-parallel scanline (5). Alternatively, scanline 3 located at the top edge of the ramp, has a dominant

northwest-trending set of fractures as well as the more common east-west fracture set. The fracture density of the fault-perpendicular scanlines progressively decreases with increasing distance from the relay ramp. Within the relay ramp, the fault-parallel scanline has a lower fracture density compared to the equally frequent perpendicular scanlines but a greater density than other scanlines further into the footwall.

3.3.3.2.2 Area 2

Fracture orientations and clustering differ from footwall to hanging wall (Fig. 3.5b). The footwall is populated by northwest-trending fractures that are sub-parallel to the northern strand of the master fault. The hanging wall has a main east-west fracture set as well as subordinate northwest and northeast-trending fractures. Both sides of the fault are equally intensely fractured regardless of the varied lithologies. The hanging wall shows a slight decrease in fracture density away from the fault. The footwall is more complicated with no discernable density decrease away from the fault but rather local increases around some minor faults.

3.3.3.3 Damage Zone Characteristics

The damage in the host rock surrounding the Little Grand Wash Fault has been characterised by analysing variations in fracture orientation and density distribution at two areas along the fault. These areas were chosen due to variations they exhibited in lithology and structural complexity as well as good outcrop exposures. Overall, the fracture orientations in the host rock were dominated by a broad, east-west trending set of fractures that locally reflect the strike of the Little Grand Wash Fault. Variations from this trend are observed in the relay ramp (scanlines 3-5) and in the hanging wall shales (scanline 7). The relay ramp contains a diverse array of fracture orientations that are considered a function of the complicated three-dimensional strain experienced during the development of the ramp. Furthermore, distinct northwest-trending fractures at the top of the ramp (scanline 3) are inferred to be the result of rotation and steepening of strata into the structure. The varied fracture orientations in the hanging wall shales (scanline 7) may represent: (1) pre-existing fractures overprinted by later fault-associated fractures or (2) differing forms of strain accommodation in the clay-rich strata compared to the sand-rich footwall strata. Further analyses are needed to validate either of these hypotheses.

A clear relationship exists with fracture density decreasing with increasing distance from the Little Grand Wash Fault. The decrease in density is evident over hundreds of metres spanning several scanlines (area 1) but difficult to resolve over tens of metres (area 2). This relationship is well documented by other researchers (Chester and Logan, 1986; Fowles and Burley, 1994; Antonellini and Aydin, 1995; Knott et al., 1996; Beach et al., 1999) and is related to the diminishing influence of the fault on the adjacent host rock. Comparisons of scanlines adjacent to the main fault in both areas show an increase in fracture density from relatively simplistic (scanlines 6 and 7) to structurally complex (scanline 4) sections of the fault. Furthermore, comparisons of the scanlines in differing lithologies (scanlines 6 and 7) show no significant variation in fracture density. This suggests that fracture density in the damage zone is primarily controlled by the proximity of the fault and degree of structural complexity and less by changes in lithology. This concurs with Hanks et al (1997) who suggests that locally, structure plays a more important role than lithology in determining fracture intensity.

The width of the damage zone around the Little Grand Wash Fault was not clearly defined because continuous scanlines could not be taken from the fault to unaffected host rock. Damage zone width is commonly defined by a background level of fracture density (Knott et al., 1996; Beach et al, 1999).The cumulative scanlines in area 1 (Fig. 3.5a) suggest that the fracture density possibly drops off to a background level at scanline 1. This would represent a damage zone half-width between 100 to 150m. However, further scanlines extending farther into the footwall in this area would be needed to confirm the background level. Damage zone half-widths for area 2 could not be estimated as there was no appreciable decrease in fracture density for scanlines 6 and 7. Therefore, more extensive scanline program would be needed to better define the width of the damage zones along the Little Grand Wash Fault.

3.3.3.4 Hydraulic Conductivity of the Damage Zone

The damage zones hydraulic conductivity is dependant on the characteristics of the fracture population. Potential fluid flow within the damage zone will be focused where the fracture aperture, density and connectivity are greatest (Sibson, 1996; Cox et al., 2001). Though apertures were not recorded, scanlines in this study demonstrate that fracture density and orientation (i.e. connectivity) are greatest around a relay ramp, such as that along the Little Grand Wash fault. This corroborates with other

studies that show fracture intensity to be greatest around structurally complex sections of a fault, which include fault intersections, fault bends, fault tips and relay ramps (McGrath and Davidson, 1995; Sibson, 1996; Curewitz and Karson, 1997). Structural complex areas are also proven sites for enhanced fluid flow due to the increased permeability resulting from fracture development (Curewitz and Karson, 1997, Hancock et al., 1999; Cox et al., 2001; Gartell et al., 2004). Thus, a conceptual model for fluid flow in the damage zone would assume localized fault-parallel flow in structural complex sections of the fault zone. This model is tested in the following chapter by comparing the location of fluid-related diagenesis and mineralization in relation to the fault zone components mapped at the surface.

3.3.4 Summary

Faults in the study area consist of a fault core surrounded by a zone of damage in the adjacent host rock. At the surface, the fault core consists of an argillaceous-rich gouge, with or without sand-rich, host rock pods and slabs that are bound and internally separated by two or more slip zones. The adjacent damage zone consists of an array of minor structures that extend for at least 150m from the fault and are most extensively developed around structural complexities along the fault (e.g. relay ramp). The hydraulic conductivity of a fault zone must consider the fault core and damage zone components. A conceptual model for fluid migration associated with the studied fault zones would predict across-fault fluid flow where reservoir-reservoir rocks are juxtaposed and argillaceous gouge is absent in the fault core. Fault-parallel flow would preferentially occur in structurally complex sections of the damage zone and wouldbe the dominant migration pathway when reservoir-nonreservoir rocks are juxtaposed and/or continuous argillaceous gouge is present in the fault core. Prediction of the subsurface fluid migration pathways in the study area requires extra evidence, which is provided by field mapping of fault-related diagenesis and mineralization and empirical fault seal assessments carried out in Chapters 4 and 5, respectively.

3.4 Sedimentation Patterns of the Region

3.4.1 Introduction

During the construction of the three-dimensional model of the study area, six isopach maps of the stratigraphy were generated in ArcView, based on borehole and wire-line log data (see section 5.2.2.2). The variation in thickness of these stratigraphic units aided in identifying the timing and extent of certain tectonic events related to faulting and salt migration. Stratigraphic units in formation or group packages were calculated from the Permian Cutler Group through to the late Jurassic Morrison Formation. Data quantity and quality restricted further subdivision of the stratigraphy, but this data enabled broad, temporal trends in sedimentation to be identified. A well summary database from the Utah Geological Survey and wire-line logs donated by Rileys Electric Logs Inc were used to construct the isopach maps. The absence of wells penetrating either the Salt Wash or Ten Mile Grabens preclude these structures from this analysis.

3.4.2 Permian

The Permian is represented by the Cutler Group (Elephant Canyon Formation, Organ Rock Formation and White Rim Sandstone), unconformably overlain by the Kaibab Limestone. In the study area, the Kaibab Limestone is thin (0-10m) and discontinuous and is not considered further. The Cutler Group is thick, with an average thickness of 450m around the studied faults (Fig. 3.6). A broad eastward thickening of the group corresponds to increasing proximity to its source, the Uncompahgre Uplift. The limited number of wells in this dataset meant that no thickness changes associated with fault movement or salt flow were detected. However, various authors (Doelling et al., 1988; Condon, 1997) have indicated that salt migration was active during the deposition of the Cutler Group in the northern end of the Paradox Basin.

3.4.3 Triassic

The Triassic is represented by the Moenkopi and Chinle Formations in the study area. The average thickness of the combined formations is approximately 300m around the studied faults (Fig. 3.7). Sediment significantly thickens along the Courthouse syncline and thins to the west along the Green River Anticline to

demonstrate that folding was active and probably related to salt flowage in the Triassic as observed in other locations in the northern Paradox Basin at that time (Doelling et al., 1988; Condon, 1997). A decrease in sediment thickness into the hanging wall of the Little Grand Wash Fault may represent early fault movement, which would be contemporaneous with incipient movement along the Moab Fault (Foxford et al, 1996). However, this thinning into the hanging wall is the opposite of what is expected with syn-sedimentary deposition associated with normal faulting and probably represents a thickness variation related to the development of the Green River Anticline or the sparseness of the borehole data.

3.4.4 Lower Jurassic

The lower Jurassic stratigraphy comprises the Glen Canyon Group (Wingate Sandstone, Kayenta Formation and Navajo Formation) in the study area. The group regionally thickens from the northeast to the southwest and has an average thickness around the studied faults of 293m (Fig. 3.8). Sediments are again seen to thicken into the Courthouse syncline and thin along the axis of the adjacent Green River Anticline suggesting the continued migration of salt in the region. However, no across-fault variations in sediment thickness suggest that the Little Grand Wash Fault was inactive during this period.

3.4.5 Mid Jurassic

The mid Jurassic stratigraphy in the study area is represented by the Carmel Formation and Entrada Sandstone. The Carmel regionally thins to the east and has an average thickness of 50m around the studied faults (Fig. 3.9). No localised variations in sediment thickness of the Carmel are evident in the region. The Entrada thins along a northwest-trending axis that parallels the Green River Anticline, thickening either side of the feature and has an average thickness of 100m around the studied faults (Fig. 3.10). Limited data indicate no thickening associated with the Courthouse syncline. The lack of localised sediment thickness variations in the Carmel combined with limited changes in the Entrada suggest that salt migration was slow to absent, with only possible upwelling associated with the Green River Anticline. Additionally, limited across-fault sediment variations suggest the Little Grand Wash Fault was inactive during this period.

3.4.6 Late Jurassic

The remaining mid to late Jurassic stratigraphy consists of the Curtis, Summerville and Morrison Formations. Due to significant facies changes within the formations and varied interpretations of this sequence from the exploration wells, the formations were grouped together. The combined formations thicken to the west and have an average thickness of 250m (Fig. 3.11). No significant variations in sediment thickness indicate a period of no salt migration. Subsequent partial to complete erosion of this stratigraphy against the faults prevented any detection of fault movement during the late Jurassic.

3.5 Tectonic History of the Study Area

Outcrop and well data reveal a protracted tectonic history involving salt tectonism and faulting for the area surrounding the town of Green River. Regional investigations have indicated that salt migration commenced in the Permian and continued to the mid Jurassic (Doelling et al., 1988; Condon, 1997). Sedimentation patterns derived from this study suggest salt migration was locally active from the Triassic (Fig. 3.7) to the mid Jurassic (Fig. 3.10) resulting in the development of the Green River Anticline and adjacent Courthouse Syncline through salt upwelling and withdrawal, respectively. Cenozoic salt dissolution and anticlinal collapse experienced by neighbouring structures (Moab Anticline and Salt Valley Graben) did not affect the Green River Anticline, possibly due to the greater depth below the surface of the rising salt compared to other salt-induced anticlines in the region.

No significant thickness changes were detected across any of the studied faults from outcrop or well data for the Permian to Cretaceous sequence (Figs. 3.6-3.11). Furthermore, Quaternary travertine deposits and river terrace sediments covering sections of the studied faults are also undeformed. The only direct evidence for the timing of fault movement in the study area is unpublished radiometric ($^{40}Ar/^{39}Ar$) dates of recrystallised clay-rich gouge from the Little Grand Wash Fault performed by Exxon in the late 1990's. Based on the assumption that new (authigenic) fine-grained clays are generated during fault movement (see section 3.3.2.2), the $^{40}Ar/^{39}Ar$ technique requires the separation and dating of this fine-grained authigenic component. To have confidence in this technique, two obstacles must be overcome:

(1) recoil-induced redistribution and loss of ^{39}Ar during $^{40}Ar/^{39}Ar$ chronology; and (2) contamination of authigenic, fault-related clays with older, detrital clays (Muller, 2003). Vacuum encapsulation overcomes the recoil problem by monitoring ^{39}Ar loss during neutron irradiation and enables accurate $^{40}Ar/^{39}Ar$ dating for clay-rich samples (Dong et al., 1995; Foland et al., 1992; Onstott et al., 1997). A mixed age resulting from the contribution of detrital and authigenic clay components can be resolved through quantitative X-ray analysis of clay size populations. By quantifying the ratio of authigenic to detrital clay in each size fraction, the age of both end members and hence faulting can be extrapolated (van der Pluijm et al., 2001). An $^{40}Ar/^{39}Ar$ dating methodology that attempts to overcomes these obstacles when dating clay-rich fault rocks is presented by van der Pluijm et al. (2001).

Using the van der Pluijm et al. (2001) methodology, Exxon dated fault movement on the Little Grand Wash Fault at 40Ma ± 10. This corresponds with early Tertiary Laramide tectonism; a period attributed to the formation of most relatively large displacement faults in the region (McKnight, 1940; Doelling et al., 1988). Additionally, Foxford et al. (1996) suggested an earlier Triassic to early Jurassic phase of movement on the nearby Moab Fault. Generated isopach maps (Figs. 3.6-3.11) combined with the Exxon dates suggest the Little Grand Wash Fault did not rupture until the early Tertiary. However, the paucity of data means an early (Triassic) phase of movement could not be totally dismissed. Additionally, a complete absence of data associated with the Salt Wash and Ten Mile Grabens preclude any direct evidence of fault movement along these structures. Timing of movement for the Little Grand Wash Fault and other large-scale faults in the region (see Doelling et al., 1988; Foxford et al., 1996;1998) implies the grabens probably also developed from the early Tertiary. The undisturbed Quaternary travertine deposits and river terrace sediments overlying the studied faults suggest there has been no fault movement in the study area for the last 80,000 years (see section 4.4.4).

3.6 Conclusions

The Little Grand Wash Fault, Salt Wash and Ten Mile Grabens cut the open, shallowly north plunging Green River Anticline, which formed from Triassic to mid Jurassic salt tectonism. The Little Grand Wash Fault is a steeply-dipping, arcuate normal fault with a maximum throw of 260m. The central part of the fault splits into

two main fault strands that produces a series of fault bends, branch points, structural terraces and relay ramps. The Salt Wash and Ten Mile Grabens are linked by a left-stepping relay ramp and are bound by steep, inward-dipping normal faults. Throw profiles of the bounding faults indicate the grabens are kinematically linked with maximum throws of 366m and 210m for the northern and southern faults, respectively. Sharp decreases in throw occur at overlap zones and relay ramps. Dating and indirect evidence indicate that the Little Grand Wash Fault, Salt Wash and Ten Mile Grabens probably formed during the early Tertiary Laramide orogeny but have been recently inactive. All fault zones consist of a fault core composed of an argillaceous-rich gouge, with or without sand-rich host rock slabs and pods that are bound and internally separated by two or more slip zones. This is bordered by a damage zone consisting of an array of minor structures that extend at least 150m from the fault and are most extensively developed around zones of structural complexity (i.e. relay ramps). A conceptual model of fault-associated fluid migration suggests that across-fault flow will occur when argillaceous gouge is absent and reservoir rocks are juxtaposed, while dominant fault-parallel flow will occur in structurally complex sections of the damage zone when argillaceous gouge is present and/or reservoir-nonreservoir rock is juxtaposed. Defining these migration pathways in the study area is resolved in subsequent chapters through fluid-related field relationships (Chapter 4) and fault seal assessment (Chapter 5).

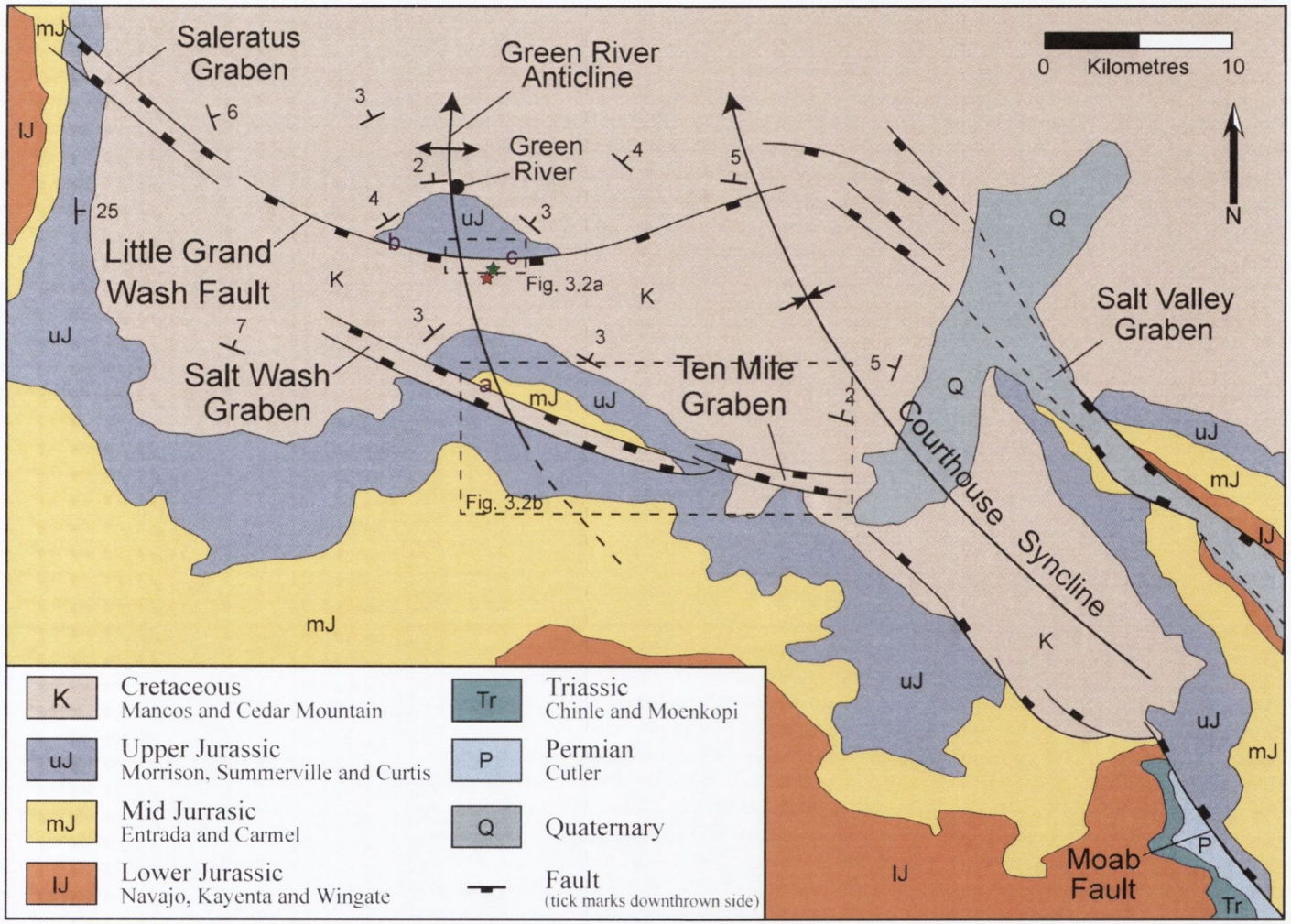


Figure 3.1: Geological map displaying the main structural features of the region surrounding the town of Green River. Structural data from authors own field work and McKnight (1940). Dashed boxes show the positions of Fig. 3.2. Purple lower case letters indicate position of the fault zone strip maps displayed in Fig. 3.4. The green and red stars indicate the location of exploration wells Amerada Hess 1 and 2, respectively.

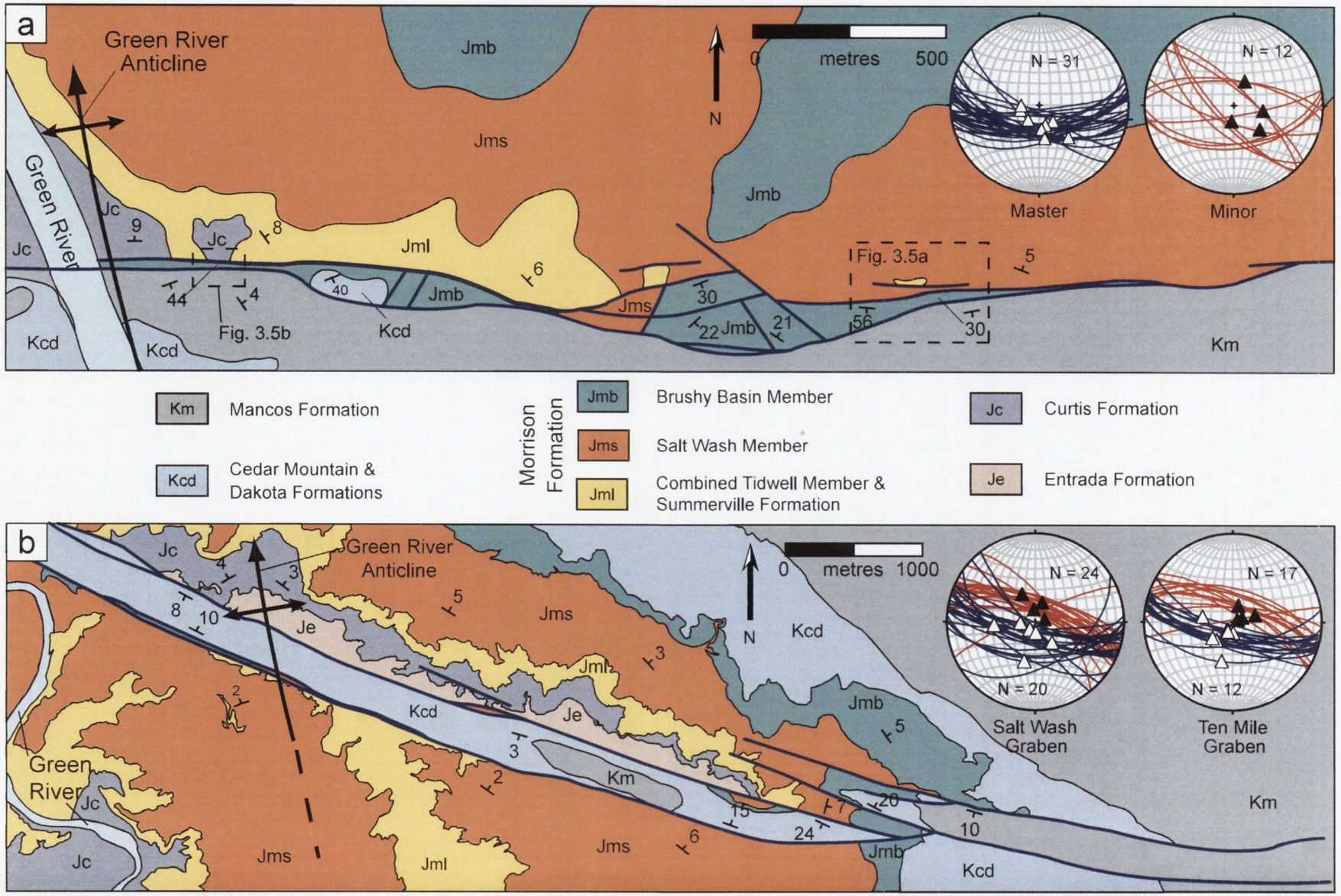

a
Green River Anticline
Green River
Jmb
Jms
Jml
Jc
Kcd
Km
N
0
metres
500
N = 31
Master
N = 12
Minor
Fig. 3.5a
Fig. 3.5b
b
Green River Anticline
Je
Salt Wash Graben
Ten Mile Graben
N = 24
N = 20
N = 17
N = 12
1000
Morrison Formation
Brushy Basin Member
Salt Wash Member
Combined Tidwell Member & Summerville Formation
Curtis Formation
Entrada Formation
Mancos Formation
Cedar Mountain & Dakota Formations

Figure 3.2: Detailed structure and stratigraphy of the Little Grand Wash Fault and the Salt Wash and Ten Mile Grabens (after McKnight, 1940; Doelling, 2002). Equal angle stereonets show strike and dip of fault strands within the main fault zone with triangles representing lineations to indicate direction of fault movement. N is the number of faults measured. (a) Central part of the Little Grand Wash Fault where it splits into two main strands and cuts the hinge of the Green River Anticline. Stereonets show the trend of the Little Grand Wash Fault (master) and variation in minor faults between the two main strands (minor). Dashed boxes show the two locations for the fracture analysis display in Fig. 3.5. (b) Detailed structure of the Salt Wash and Ten Mile Grabens. Stereonets display the trend of the northern (red) and southern (blue) bounding faults of both grabens. Closed triangles correspond to northern fault lineations, while open triangles indicate southern fault lineations.

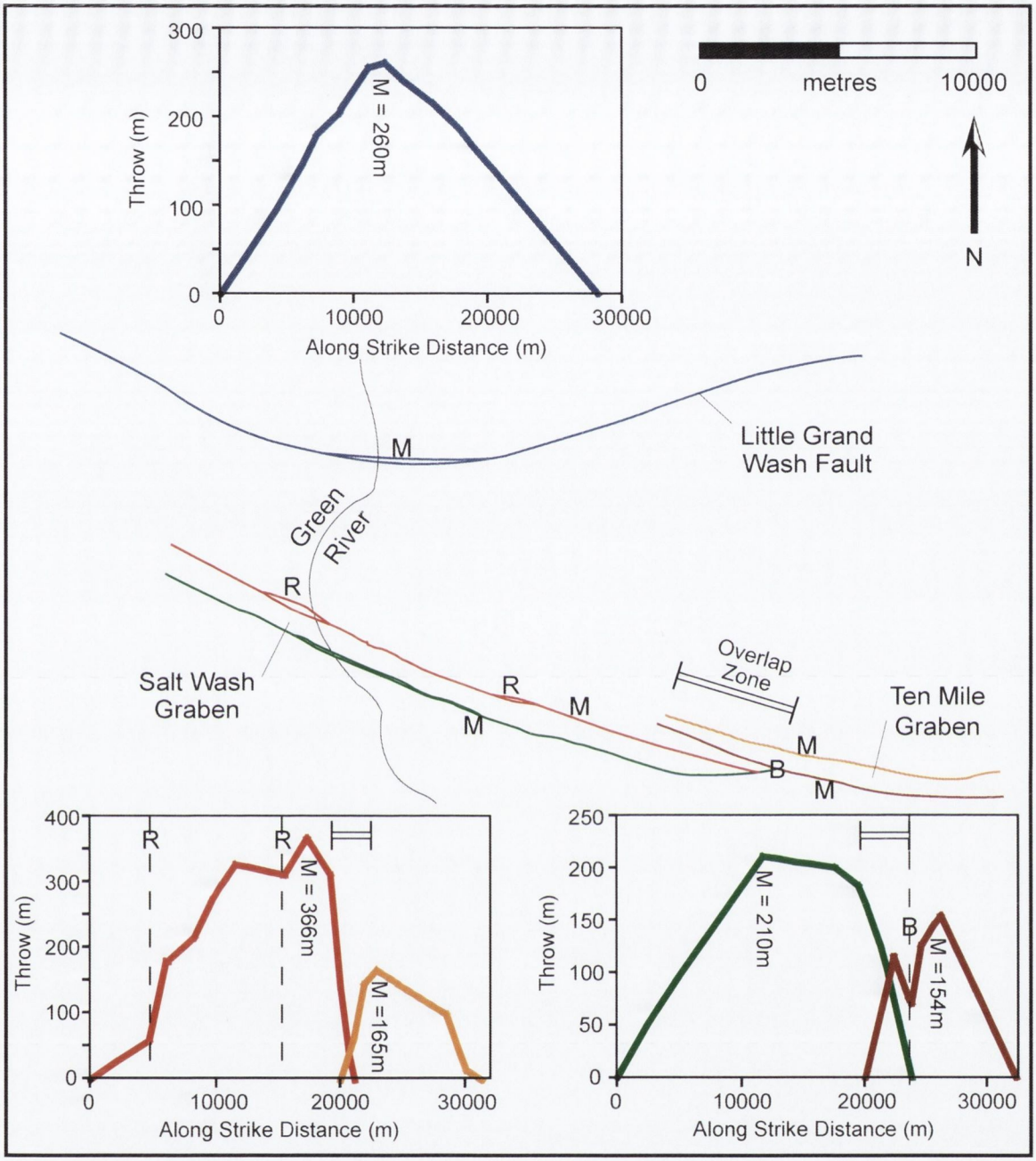


Figure 3.3: Throw profiles for the Little Grand Wash fault and bounding faults of the Salt Wash and Ten Mile grabens. Colours in throw charts correspond to fault in map. Sharp changes in throw are observed at relay ramps (R), branch points (B) and overlap zones. M is the location for maximum throw along each fault.

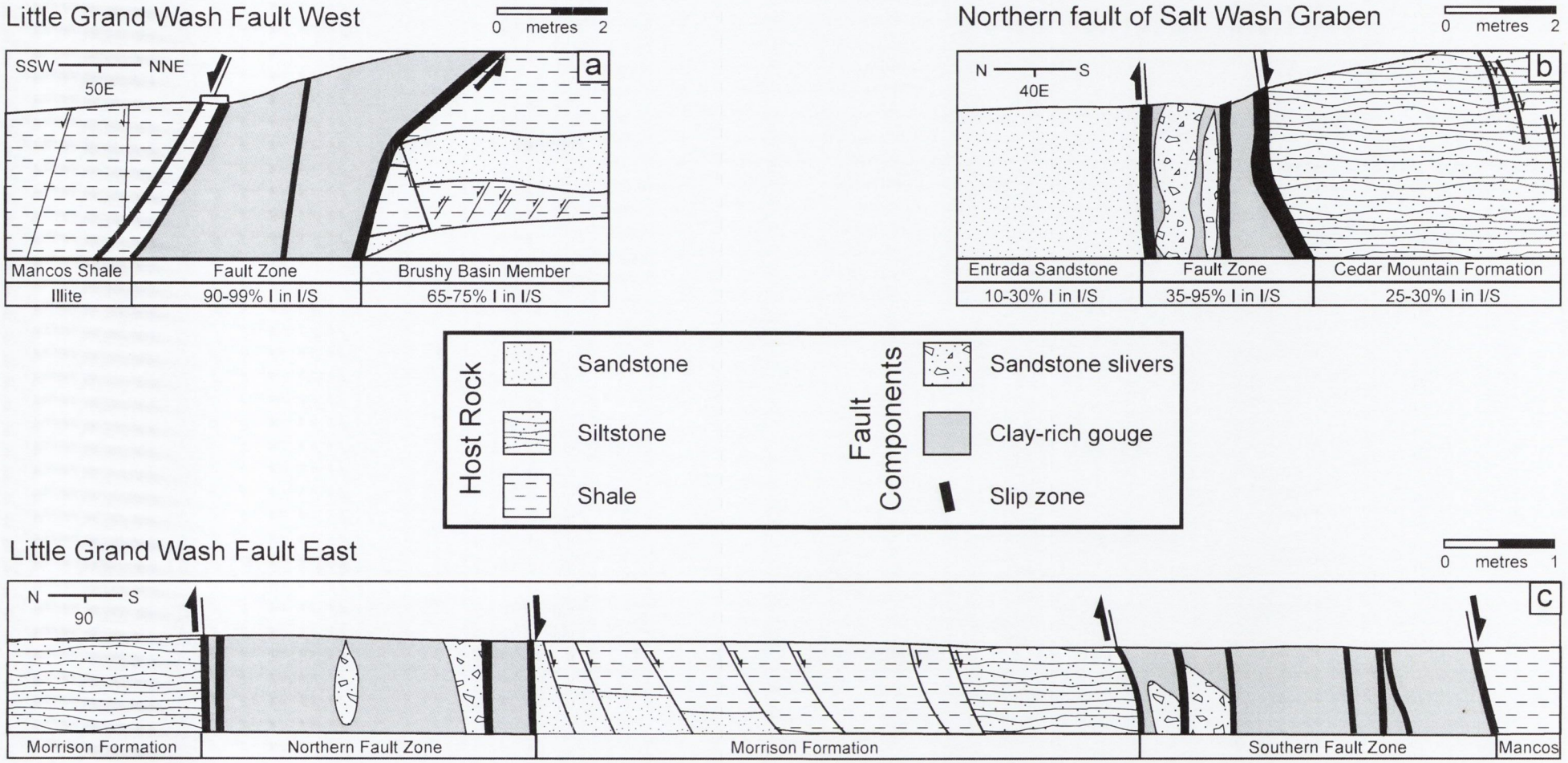


Fig. 3.4: Schematic transects across fault zone outcrops at three locations along the Little Grand Wash Fault and Salt Wash Graben. The location of transects are shown in Fig. 3.1. Variation in illite in mixed layer illite/smectite clays across the fault zone are shown for two transects along the Little Grand Wash fault (a) and northern fault of the Salt Wash graben (b).

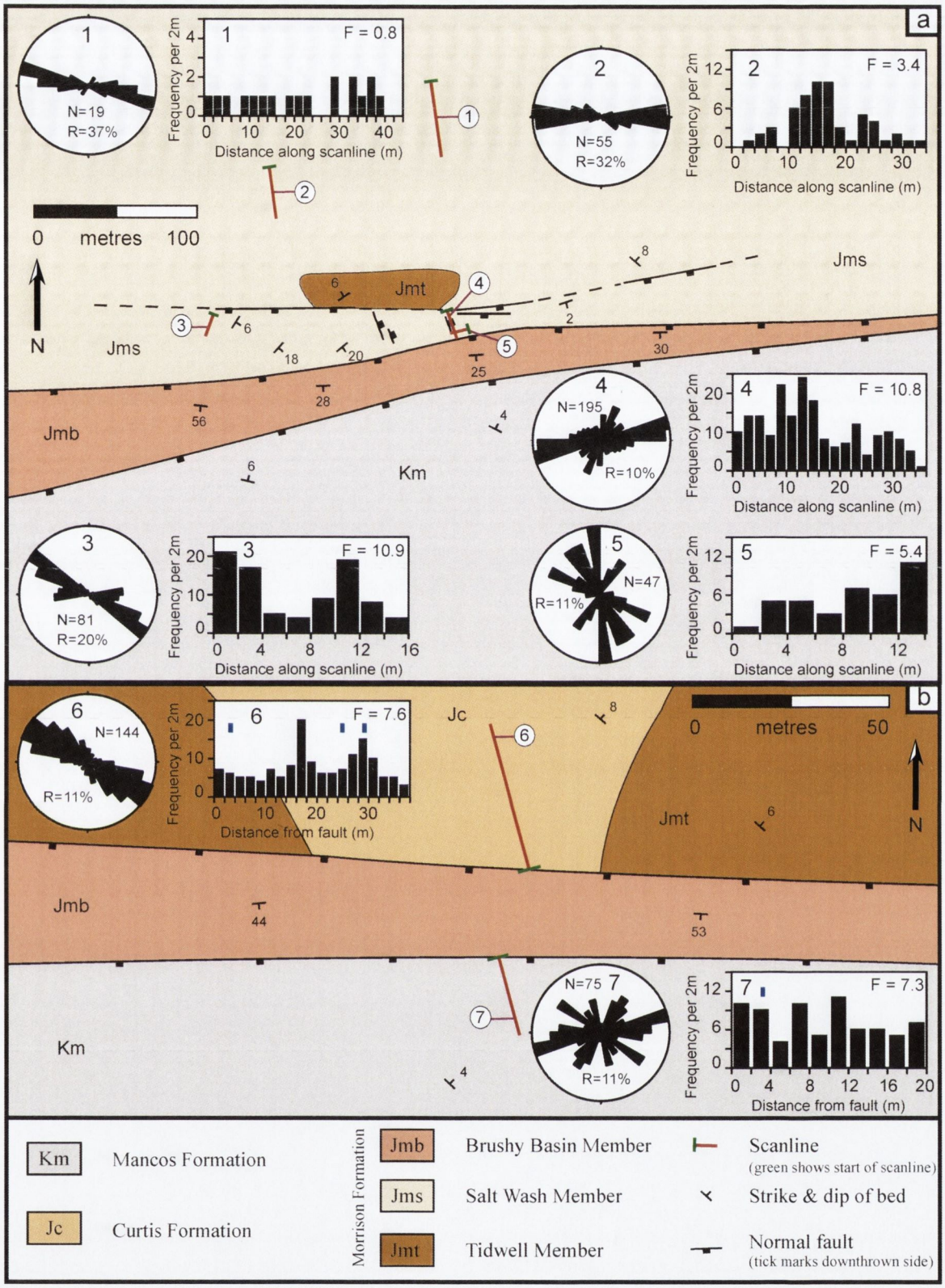


Figure 3.5: Fracture analyses at two locations along the Little Grand Wash fault. Each location contains a series of scanlines that show variations in fracture orientation (rose diagrams) and frequency (histograms). All structural data derived from field work. N is the number of fractures measured; R indicates the approximate size (as a percentage of the total fracture population) of the largest petal in the rose diagram; F is the average number of fractures per 2m for the length of the scanline. (a) Fracture analysis within and away from a footwall relay ramp consisting of one parallel and four perpendicular scanlines relative to the main fault strands. (b) Fracture analysis consisting of two scanlines in the immediate footwall and hanging wall of a simplistic section of the Little Grand Wash fault. Blue lines in histograms represent position of minor faults.

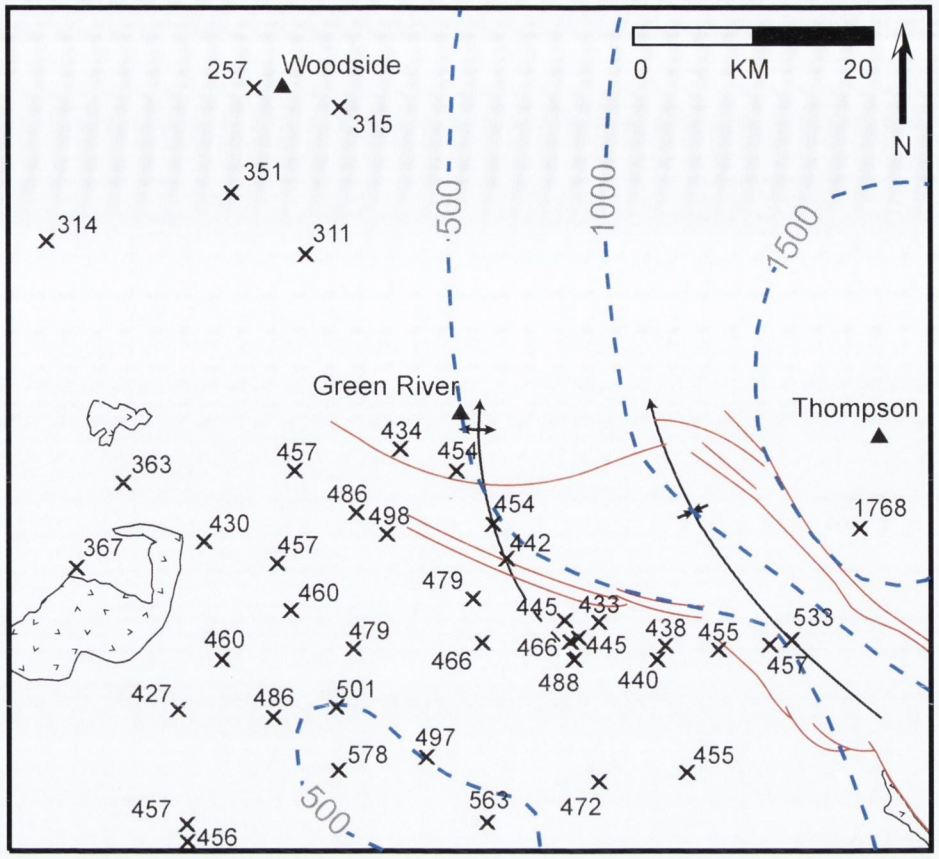


Figure 3.6: Isopach map of the Permian Cutler Group constructed from borehole and published data (Condon, 1997). Crosses indicate position of boreholes with accompanying thicknesses in metres. Stippled areas indicate regions where the sequence is outcropping.

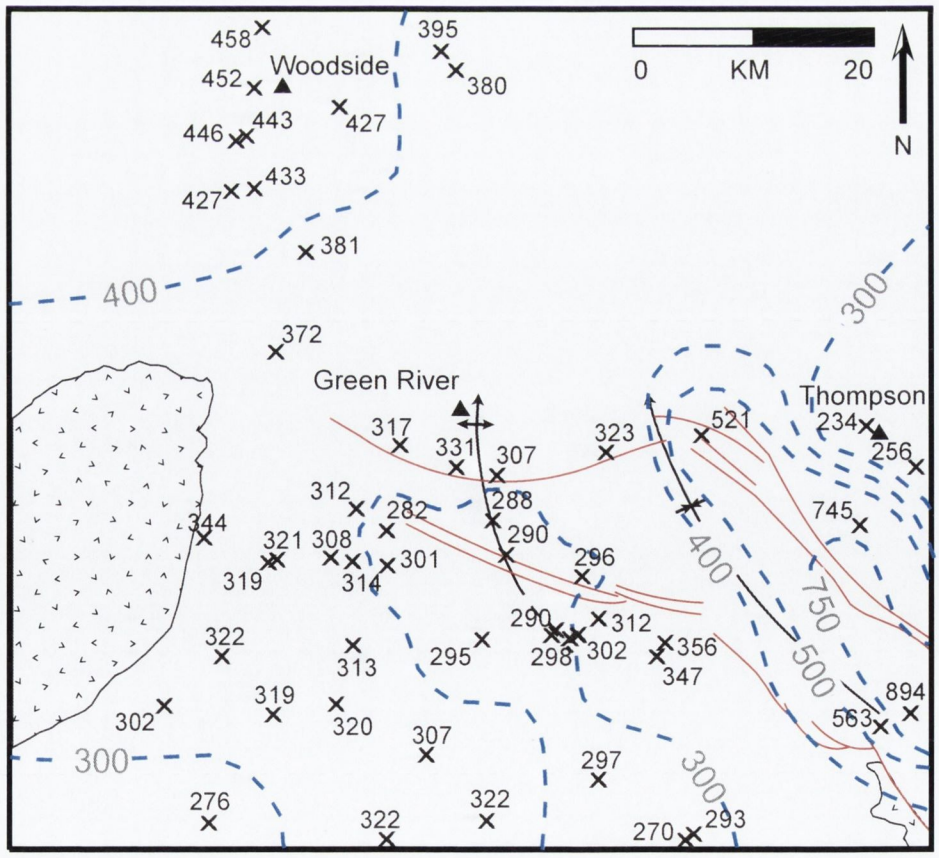


Figure 3.7: Isopach map of the Triassic Chinle and Moenkopi Formations, constructed from borehole data. Crosses indicate position of boreholes with accompanying thicknesses in metres. Stippled areas indicate regions where the sequence is outcropping or removed.

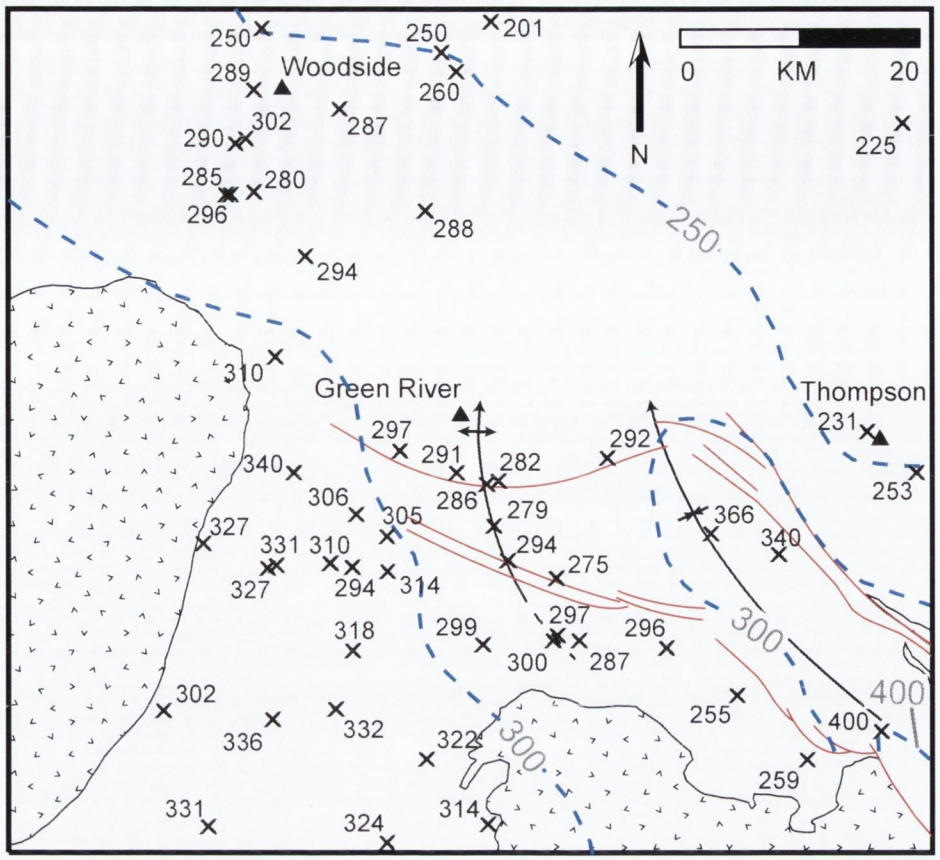


Figure 3.8: Isopach map of the lower Jurassic Glen Canyon Group, constructed from borehole data. Crosses indicate position of boreholes with accompanying thicknesses in metres. Stippled areas indicate regions where the sequence is outcropping or removed.

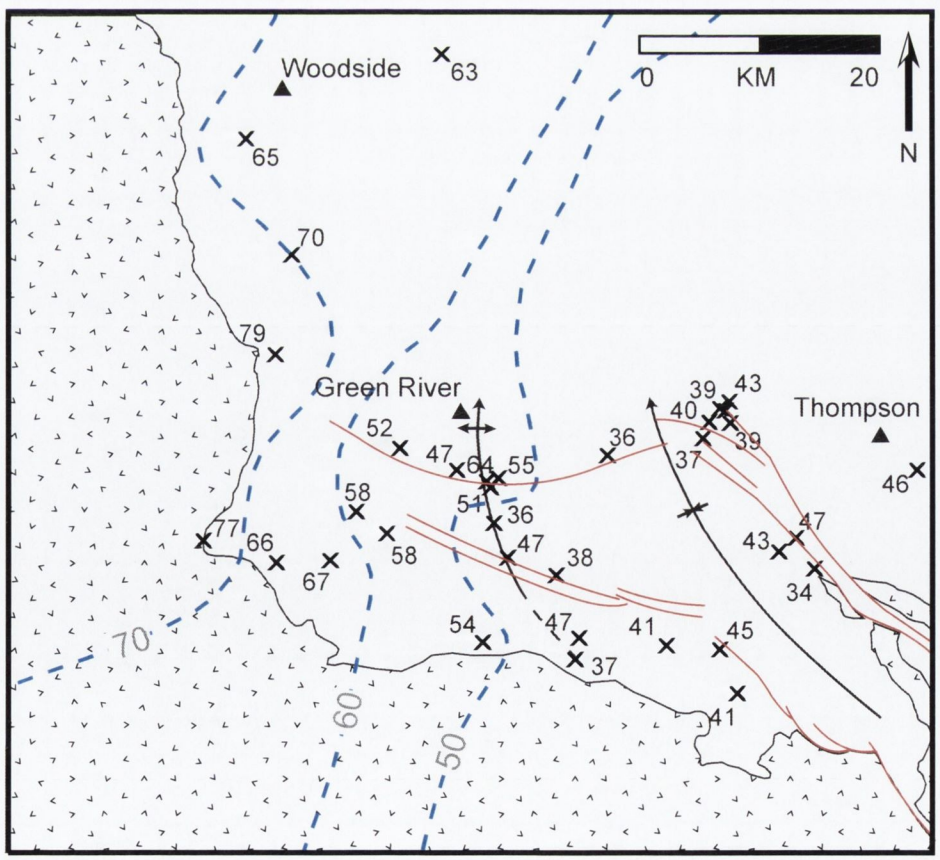


Figure 3.9: Isopach map of the mid Jurassic Carmel Formation, constructed from borehole data. Crosses indicate position of boreholes with accompanying thicknesses in metres. Stippled areas indicate regions where the sequence is outcropping or removed.

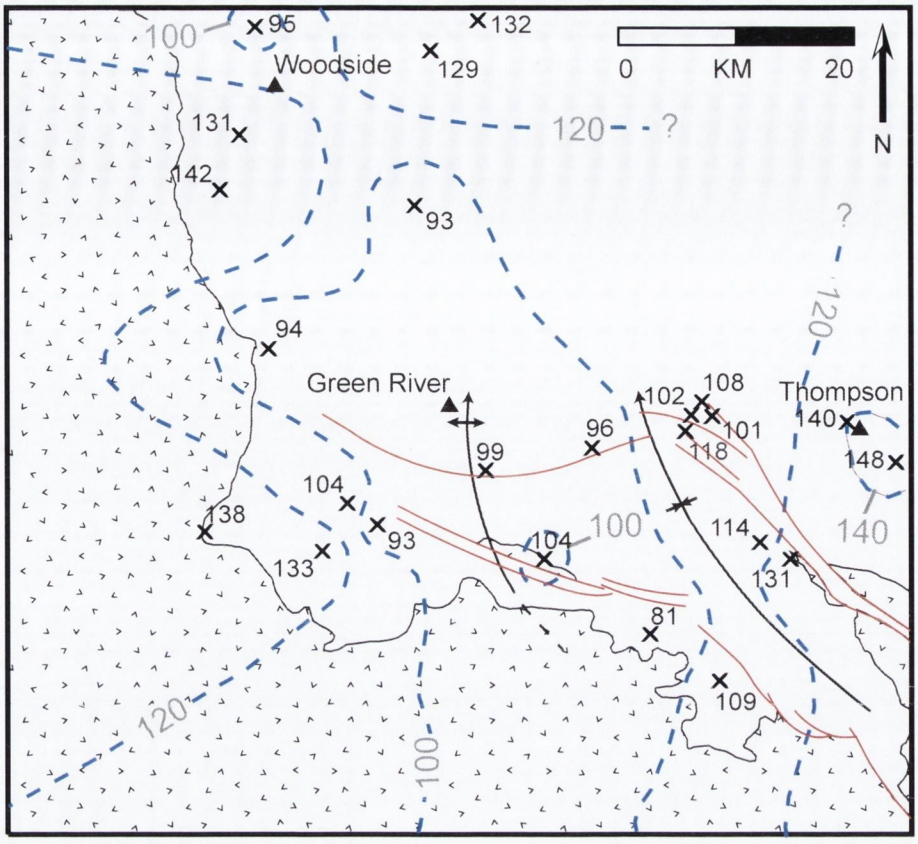


Figure 3.10: Isopach map of the mid Jurassic Entrada Sandstone, constructed from borehole data. No data in the northeast area limit interpretation of isopachs. Crosses indicate position of boreholes with accompanying thicknesses in metres. Stippled areas indicate regions where the sandstone is outcropping or removed.

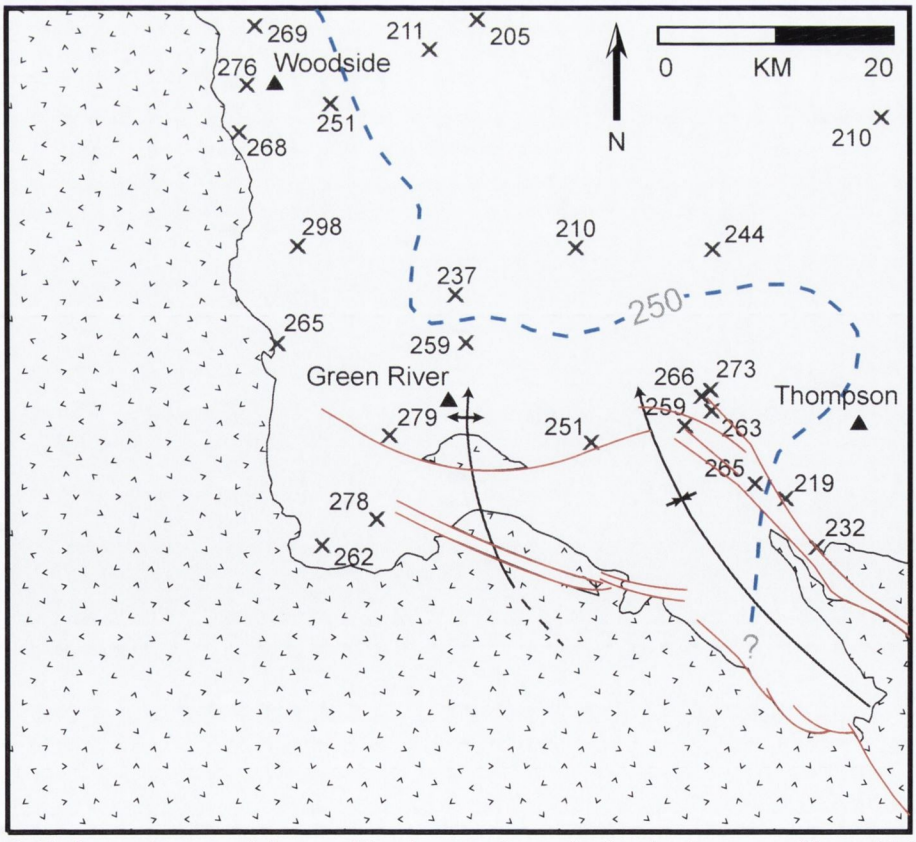


Figure 3.11: Isopach map of the combined upper Jurassic Curtis, Summerville and Morrison Formations, constructed from borehole data. Crosses indicate position of boreholes with accompanying thicknesses in metres. Stippled areas indicate regions where the sequence is outcropping or removed.

Chapter 4: Fault-Related Mineralization and Diagenesis

4.1 Introduction

Faults can act either as conduits or as seals to subsurface fluid migration (Caine et al., 1996). Instances of faults acting as conduits to migrating fluids have been identified by the presence of springs (Curewitz and Karson, 1997), precipitation of veins and mineral deposits (e.g. Kerrich, 1986; Hancock et al., 1999; Rohrlach et al., 1999; Micklethwaite and Cox, 2004) or diagenetic alteration of adjacent host rocks (e.g. Chan et al., 2000; Garden et al., 2001; Labaume et al., 2001). In the study area, fault-associated fluid flow is recognised in the footwalls of the Little Grand Wash Fault and northern fault of the Salt Wash Graben through the presence of mineral deposits (travertines) as well as fluid-related diagenetic alteration of Jurassic sandstones (iron-oxide reduction, sporadic hydrocarbon staining and carbonate and sulphate veining). The travertines are direct products of past and present leakage of CO_2 along both fault zones. As such, the chapter focuses on the actively-forming and ancient deposits to characterise CO_2 leakage at the surface along both faults. Preliminary investigations of the diagenetic features are also undertaken to gain an understanding of fluid regimes associated with this faulted system. Diagenesis in this study is defined as any chemical or physical change undergone by the sandstones at relatively low temperatures and pressures that was instigated by a migrating fluid.

To investigate these fault-associated fluid flow features, field mapping coupled with petrological and geochemical analyses were undertaken. The resulting data enable the: (1) establishment of a facies model documenting the origin and evolution of a travertine deposit (manuscript currently under review in Sedimentary Geology); (2) characterisation of spatial and temporal variations in travertine precipitation and hence CO_2 leakage; (3) calculation of CO_2 flux and local erosion rates; (4) definition of migration pathways and leak points of fluids through the faulted stratigraphy; and (5) preliminary identification of fluid regimes that have migrated through the faulted system. The results of these findings provide an insight into the interaction of faults and fluid flow at a reservoir scale.

4.2 Travertine Review

A non-marine, low-Mg carbonate deposit that forms in or near terrestrial springs, lakes, rivers or caves is commonly known as travertine (Sanders and

Friedman, 1967). Depending on temperature and location, travertines can be subdivided into hot spring travertine (precipitates from hydrothermal springs), tufa (precipitates from ambient springs, lakes and waterfalls) or speleothems (precipitates from waters in subterranean caves and fracture systems; Pentecost, 1995; Ford and Pedley, 1996; Fouke et al., 2000). To avoid confusion within this study, all terrestrial carbonate deposits precipitated from carbonate-rich effusions will be termed travertine.

Travertines precipitate from carbonate-rich waters due to the removal of CO_2 via the reaction (Clark and Fritz, 1997):

$$2HCO_3^-{}_{(aq)} + Ca^{2+}{}_{(aq)} \Rightarrow CaCO_{3\,(s)} + CO_{2\,(g)} + H_2O_{\,(l)}$$

CO_2 degassing is initiated by a decrease in hydrostatic pressure as carbonate-rich ground waters rise to shallow depths and is continued at the surface by abiotic (e.g. turbulence, evaporation and temperature changes) and biotic (e.g. photosynthesis, respiration, trapping, nucleation and secretion) processes (Barnes, 1965; Gonfiantini et al., 1968; Turi, 1986; Lorah and Henmann, 1988; Ford and Pedley, 1996; Guo et al., 1996; Chen et al., 2004). Dominant surface degassing processes vary widely and are dependant on local conditions such as water chemistry (Chafetz and Folk, 1984; Sant'Anna et al., 2004), temperature (Gonfiantini et al., 1968; Janssen et al., 1999; Fouke et al., 2000), flow rates (Chen et al., 2004) and surface topography (Turi, 1986; Guo et al., 1996; Chen et al., 2004). As such, travertine deposition in hydrothermal conditions is greatly influenced by evaporation and temperature changes (Fouke et al., 2000) while biotic influences are more prevalent in ambient conditions (Janssen et al., 1999).

An important aspect of travertine deposits is their association with tectonically and seismically active areas (Barnes et al, 1978). Numerous authors have noted that travertine deposits are precipitated along or close to fault traces, generally being concentrated in high-flow, structurally complex zones (i.e. relay zones or fault tips; Hancock et al., 1999; Minisalle et al., 2002; Morratti et al., 2003, Trancos et al., 2003). This structural affinity combined with a poor preservation potential has resulted in travertine being utilised principally in neotectonic studies (Hancock et al., 1999; Hancock et al., 2000; Cello et al, 2001; Brogi et al, 2004). In addition, precipitation of terrestrial carbonate deposits from meteoric or surface waters has

enabled travertines to be utilised for paleohydrology (Szabo and Winograd, 1995; Rihs et al., 2000; Minisalle et al., 2002) and paleoclimatology (Clark and Fontes, 1990; Magnin et al., 1990; Sturchio et al., 1994; Auler and Smart, 2001) studies.

4.3 Field Relationships

4.3.1 Introduction

Field evidence of fault-associated mineralization or diagenesis is limited primarily to the footwalls of the Little Grand Wash Fault and northern fault of the Salt Wash Graben (Fig. 4.1). Within these footwalls, fault-associated fluid flow is mainly defined by travertine precipitation and iron-oxide reduction of mid Jurassic sandstones, though the spatial distribution and minor diagenetic products vary between faults. Outside this localised area, only thin (up to 5cm wide) gypsum, calcite and quartz veins fill fractures within varied lithologies. Detailed below are the main fluid flow features mapped within the footwalls of both faults. Special emphasis is placed on the travertine deposits, as they are the product of CO_2 leakage at the surface. Based on this, the travertine deposits are also used to approximate the amount of CO_2 that has leaked to the surface over time.

4.3.2 Travertines

4.3.2.1 Active Travertines

4.3.2.1.1 Little Grand Wash Fault

The only actively forming travertine deposit on the Little Grand Wash Fault is associated with the CO_2-charged Crystal Geyser (Fig. 4.2a). Situated in the immediate footwall of the Little Grand Wash Fault at the point where it cuts the east bank of the Green River (Fig. 4.1a), the geyser erupts from an exploration hydrocarbon well (Glen Ruby #1-X) drilled in 1935. The cold-water geyser (~18°C) is powered by CO_2-charged waters that erupt to heights of 25 m at intervals of 12 to 18 hours, though local people have reported more frequent and intense eruptions in the past. In conjunction with the erupting geyser, two small springs immediately north and northeast of the geyser erupt periodically throughout one eruption cycle and are assumed to be related to the same plumbing system (Fig. 4.2b). Drilling records for the exploration well document a 21 m thick, pre-existing travertine mound at the surface, indicating the spring system was active prior to drilling (McKnight, 1940).

The Crystal Geyser eruptions have resulted in the development of a large, ochre-coloured, terraced deposit. The deposit is approximately 70 m wide by 80 m long and has a total relief of about 7 m from the emergence point of the geyser to the base of the outcrop, where the waters flow directly into the Green River. The travertine is devoid of any conspicuous plant growth, except for some bushes and grasses that have been encroached by the aggrading mound. During an eruption, waters cover the entire travertine surface though the majority of downstream flow is contained in a series of channels.

A series of downstepping travertine lobes radiate out downslope of the geyser (Fig. 4.2c), similar to the terraced mound example of Chafetz and Folk (1984). Hemispherical carbonate ponds (2 mm to 5 cm wide), each with an undulating pool and raised rim, build on the surface of the travertine to form the terrace morphology (Fig. 4.2c-d). The size of the ponds are roughly proportional to the gradient of the surface with microterraces (1 to 5 mm wide) forming on steeper surfaces, while larger terraces form on gentler to subhorizontal surfaces. In cross section, the ponds are generally 5 to 20 mm deep and are vertically stacked to give a porous, sinuous texture. Within each pond, abiotic carbonate precipitation occurs mainly on the rims and in some cases in the pools with circular masses termed pisoids (Chafetz and Folk, 1984) generally growing up to 2 mm in diametre. Green algae are seen in some of the deeper pools where waters are retained longer before evaporating, and these algae may assist in the growth of the travertine mound (Fig. 4.2d-e). At the edge of some of the lobate mounds, a change in relief has induced speleothems to precipitate underneath the protruding mounds (Fig 4.2f). The speleothems are 2 to 10 cm long and conically layered.

4.3.2.1.2 Salt Wash Graben

There are six actively-forming travertine mounds spatially associated with the northern fault of the Salt Wash Graben that are the result of natural or drilling-induced, CO_2-charged, cold water (13 to 17°C) effusions (Fig. 4.1b). All but one of the mounds is situated in the footwall close to where the Green River Anticline crest is cut by the fault. The final mound is associated with an abandoned drill hole (Ten Mile geyser), 200 m into the hanging wall that likely penetrates the footwall at depth. The travertine mounds are generally low, thin and poorly-developed compared to the Crystal Geyser deposit. Halite (NaCl) and thenardite (Na_2SO_4) commonly form thin

salt crusts around drier sections of the developing mounds. The mounds are located in three broad locations along the northern fault, which are Torrey's, Ten Mile and Three Sisters.

Torrey's spring is situated 350 m into the footwall of the northern fault and is possibly the result of an exploration well drilled in 1949 (Delaney Petroleum Corporation Well #1), though no well casing or other onsite evidence is visible. CO_2-charged waters constantly emanate from the spring to precipitate a low, flaky travertine mound approximately 12 m in diametre (Fig. 4.3a). The orange mound has limited terrace development concentrated along downstream flow channels. Sporadic green algae occur in terrace pools generally submerged within the flow channels. At the edge of the mound, a series of speleothems form an impressive 1 m long frozen waterfall structure where the carbonate-rich waters descend into an adjacent dry river bed. Extensive salt staining occurs in areas of the travertine infrequently covered by the erupting fluids.

The Ten Mile geyser is located at an abandoned exploration well, 200 m into the graben and infrequently erupts to heights of 1 to 1.5 m (Doelling, 1994). No drilling records have been found for the well but it is assumed to penetrate the footwall at depth due to the dearth of any other travertine deposits within the graben, its proximity to the south-dipping northern fault and geochemical similarities between the erupting carbonate-rich waters and other CO_2-charged effusions associated with the fault (Heath, 2004). A low travertine mound has developed around the geyser and is approximately 15 m long by 3 m wide with a total relief of 0.5 m. The ochre-coloured mound contains well-developed terraces that generally increase in width downstream from the geyser (Fig. 4.3b). The deposit has encroached and encrusted low lying sections of a nearby tree and grasses and there are limited amounts of green algae observed within terrace pools. A second CO_2-charged effusion (Ten Mile spring) is located 100 m into the opposing footwall. The travertine surrounding the spring has been partially excavated leaving a cavity (2 m wide by 1.5 m long by 0.5 m deep) filled with a pool of brines. A continual stream of carbonate-rich waters discharge from three vents at the base of the pool causing the reprecipitation of the partially excavated travertine deposit.

The Three Sisters area consists of the CO_2-charged Big Bubbling spring and two smaller springs (northern and southern Small Bubbling springs) located 400 m to the west (Fig. 4.1b). The Big Bubbling spring is composed of an algae-rich shallow

pool (0.4 m deep) with an approximate radius of 1 m that continuously discharges carbonate-rich waters through a series of vents at its base. The fluids are constantly expelled from the pool via two main channels to precipitate a surrounding low-lying travertine mound that extends up to 40 m to the west (Fig. 4.3c). Close to the pool, the orange-coloured mound contains well-developed terraces (up to 20 cm wide) that diminish in frequency and relief downstream. Toward the middle and outer sections of the mound, travertine is thin and brittle with sporadic coatings of a salt crust up to 1 cm thick. Further west, smaller travertine deposits have precipitated from two close but distinct effusions (Small Bubbling Springs). The northern spring consists of carbonate-rich waters infrequently erupting along a sparse network of open fissures to heights of 15 cm. The connected fissures are 0.5 to 5 m long and are orientated roughly parallel and perpendicular to the main fault trace (Fig. 4.3d). A low, travertine mound extends up to 20 m from the fissures and consists of infrequent, poorly developed terraces proximal to the fissures as well as a pervasive salt crust, up to 3 cm thick, sporadically covering sections of the mound (Fig. 4.3d). The southern spring is composed of a small cylindrical cavity, 10 cm in diametre, which frequently expels CO_2-charged fluids as well as occasionally erupting to heights of 0.6 m. Surrounding the cavity is a compact, flat-lying travertine mound that extends outward for 15 m (Fig. 4.3e). The orange-coloured mound consists of well-developed terraces, 5 to 30 cm wide that increase in width away from the spring. The deposit has encroached surrounding bushes and grasses as it has aggraded though no algae were observed within the terrace pools.

4.3.2.2 Ancient Travertines

4.3.2.2.1 Distribution

Along the Little Grand Wash Fault and northern fault of the Salt Wash Graben there are a series of partial to complete remnants of ancient travertine deposits that parallel the fault trace (Fig. 4.1). The travertine deposits form resistant caps on top of numerous buttes (Fig. 4.4a) and are topographically higher than the actively-forming travertines. All deposits originate in the footwall proximal to where the fold axis of the Green River Anticline is cut by both faults. However, there are variations in the distribution and development of the ancient deposits between the two faults. The Little Grand Wash Fault contains a series of discrete, well-developed, thick (1 to 10 m) deposits that are located in various footwall lithologies from the sand-rich Curtis

Formation to clay-rich sections of the Morrison Formation (Fig. 4.1a). The deposits form in the immediate footwall but generally drape over the fault into the hanging wall. Additionally, the deposits are confined to sections where the two main fault strands are close together and/or there are pronounced structural complexities such as fault bends and relay ramps. The northern fault of the Salt Wash Graben contains mainly thinner (0.5 to 4 m) and less well-developed deposits compared to the Little Grand Wash Fault. They are located in the sand-rich Entrada and Curtis Formations. The deposits are predominantly confined to the immediate footwall, occasionally draping into the adjacent graben. However, around the Green River fold axis deposits increase in number and form further into the footwall (Fig. 4.1b). The easternmost travertine deposits are associated with a breached relay ramp.

4.3.2.2.2 Morphology

Erosion of the surrounding host rock has created excellent cross-sectional exposures of the ancient deposits. Based on field observations and detailed strip maps of the best preserved ancient mounds from both faults, four distinct lithofacies in addition to altered host rock have been identified, which are: (1) conglomerate, (2) layered mats, (3) white-banded veins, and (4) brown-banded veins (Fig. 4.4b). Descriptions of each lithofacies are discussed in detail below.

Altered Host Rock

The host rock at the base of the ancient travertine mounds are generally altered along fractures and bedding planes. Within sandstone-dominated lithologies, the host rock is crosscut by thick white-banded veins (4 to 15 cm thick) with associated yellow to white iron-oxide reduction haloes (1 to 5 cm wide). In mud-dominated lithologies, networks of thin boxwork veins (5 to 10 mm thick) are more common than the thicker white-banded veins, locally destroy the host rock fabrics, and have thinner reduction haloes (1 to 5 mm; Fig. 4.5a).

Conglomerate

Calcite-cemented conglomerates are found at the base of the deposits (Fig. 4.4b). In places, the conglomerate extends up to 200 m from the main travertine deposit. The conglomerate is poorly sorted with sand- to cobble-size detrital clasts (2 mm to 15 cm) surrounded by calcite cement (Fig. 4.5b). The clasts are sub-angular to

sub-rounded and consist of rock fragments and quartz grains derived locally from the surrounding stratigraphy. Sub-angular clasts of white-banded veins and layered mats also occur but are uncommon. There are limited sedimentary structures within this unit with a few horizons containing imbricated lenticular clasts and/or planar cross-bedding. More distal conglomerate deposits generally define palaeochannels for spring water that flowed off the travertine mound.

Layered Carbonate Mats

A subhorizontal, layered carbonate deposit with moderate to high visible porosity is situated above the conglomerate (Fig. 4.5c). This unit is poorly preserved on top of the ancient deposits and generally only a thin, weathered crust (0.5 to 2 m thick) remains. Layering in the carbonate dips gently away from the central area of the mounds, which are usually the present-day topographic high point of the ancient deposits (Fig. 4.4b). The morphology of the layered mats varies considerably in texture and packing, but is generally composed of layered, subhorizontal alternating porous and dense horizons. The porous horizons, generally 5 to 50 mm thick, consist of multiple, vertically stacked layers. Each layer contains subvertical, dendritic precipitates that branch out from a thin, laminated substrate. The substrate commonly has an irregular, sinuous shape similar to the pool-and-rim geometries of microterraces on the present-day travertine (Fig. 4.5d). The dendritic precipitates contain aggregates of elongate blocky calcite that branch out to form shrub-like structures (Fig. 4.5e), similar to those reported by Chafetz and Folk (1984) and Guo and Riding (1994). Large proportions of the blocky calcites are partially to completely obscured by micritic rims, which give the horizons a mottled to dark appearance under the plane polarized light microscope (Fig. 4.5e). Conversely, the dense horizons generally consist of sporadic angular to sub-rounded clasts engulfed in a dominant micritic matrix (Fig. 4.5f). The clasts range from fine- to medium-grained detrital quartz grains to fine-grained blocky calcites and detached pieces of substrate from the porous horizons. Occasionally, a dense horizon consists solely of locally-derived detrital clastic sediments. Many pore spaces and cavities are filled with euhedral, elongate crystals that form a drusy texture.

The boundary between the layered mats and the underlying conglomerate is a transitional zone that thickens away from the central part of the deposit (Fig. 4.4b). Within this transitional zone, the lithofacies are initially well-defined and alternate

repeatedly in 5 to 30 cm thick packets. Farther from the central part of the deposit, the boundary between the two units is harder to define and the layered mat packets are thinner and more discontinuous, while the conglomerate layers are thicker. The layered mats pinch out near the margins of the mound and only conglomerate remains.

White-Banded Veins

This unit consists of a series of dense, banded, white veins that cut through the mound. The veins range in thickness from 5 to 80 cm. Individual veins grew primarily from the fracture walls toward a central cavity (Fig. 4.6a). The carbonate lining the fracture walls are usually equidimensional and occasionally separated by a central cavity. The cavities are normally only a few centimetres wide and commonly contain speleothems (Fig. 4.6b). While the number and size of speleothems infilling the cavities vary widely, all are subvertical and range in length from 2 to 80 mm (Fig. 4.4b). In some instances, an outer layer of white-banded vein material has precipitated over the speleothems (Fig. 4.6b).

Each vein consists of a series of bands, generally 5 to 30 mm thick, containing acicular to columnar crystals orientated perpendicular to the depositional surface (Fig. 4.6c). Within each band, the acicular to columnar crystals radiate out in a fan pattern to form a mammilated surface (Fig. 4.6d). Crystal size increases in the growth direction of each band. Most veins contain a few thin, orange to dark brown laminations that parallel the growth surface.

Both horizontal and vertical veins are present throughout the ancient mounds and crosscut the host rock, conglomerate, and layered mat units (Fig. 4.4b). The more common subhorizontal veins are thicker and tend to form along lithologic contacts, though some clearly crosscut contacts. Most vertical veins are thinner, infill fractures and minor faults, and terminate at the bottom of horizontal veins. Exceptions are some thicker veins that are vertical at depth (in altered host rock) and rotate to be subhorizontal at shallower levels.

Brown-Banded Veins

Thinly banded, brown veins crosscut all the other lithofacies and therefore are the last facies to form in the deposit. The veins are generally subvertical, thin downwards, and tend to have dendritic terminations (Fig. 4.6e). The veins are 2 to 20

cm thick and contain alternating brown, orange, and white bands that are 1 to 30 mm thick (Fig. 4.6f). Each band consists of acicular crystals that form radial fans similar to those in the white-banded veins.

4.3.2.3 Interpretation of Travertine Lithofacies

The following section will outline where each of the four identifed lithofacies forms and how they are related to each other within a travertine deposit.

4.3.2.3.1 Conglomerate

There is a paucity of references in the literature to travertine-related conglomerates, with only Ford and Pedley (1996) mentioning surface-cemented screes and alluvium associated with thin tufa deposits. It is unknown whether this lithofacies is absent or ignored in other studies, but it is an integral component of the ancient travertines located in this field area.

The conglomerates are positioned between the host rock and layered mats and consist of locally derived sediment cemented by carbonate. These relations are consistent with colluvium surrounding the travertine having been cemented by carbonate precipitated from the erupting spring waters to form the conglomerate. Furthermore, the conglomerates extend laterally farther than any of the other lithofacies and, in a few cases, preserve palaeochannels that show the flow paths of spring waters away from the deposit.

The conglomerate and layered mat units are both surface expressions of a travertine deposit, with the difference being that the layered mats are almost entirely comprised of carbonate precipitation from the spring water, while only the pore-filling cements in the conglomerates are from the spring water. The relative positions of the two units are consistent with vertical and lateral cementation of the conglomerate that eventually produced a relatively impermeable substrate for subsequent growth of the layered mats.

The presence of a transitional zone between the conglomerate and layered mats could be due to extended periods of spring and non-spring activity or episodic flooding of the travertine by non-spring waters. Though neither of these causes can be ruled out, the presence of sedimentary structures (e.g. imbrication and cross bedding) within the conglomerate and the proximity of the Green River to the ancient deposits is consistent with episodic flooding, resulting in the alternation between the two units.

4.3.2.3.2 Layered Carbonate Mats

The layered mats are interpreted to be the product of precipitation on the surface of the travertine deposits for three reasons. First, this lithofacies is at the top of every ancient mound in the field area. Second, locally derived clastic sediments are dispersed in some of the fine-grained layers of the layered carbonate mats. Third, the layered mat texture is similar to the microterraces of the active travertine and as such, this lithofacies is interpreted to be an ancient version of the active surface deposit.

The dendritic precipitates, which alternate with the micritic-dominated layers, are texturally similar to the shrub facies of travertines documented in many studies (Julia, 1983; Chafetz and Folk, 1984; Casanova, 1986; Pentecost, 1990 and 1993; Guo and Riding, 1994; Ford and Pedley, 1996; Fouke et al., 2000). This shrub facies is one of the most common and widely discussed travertine lithologies due to it being the dominant surface precipitate of a travertine deposit, though the factors controlling the formation of this unit are still speculative. Chafetz and Folk (1984) in their study of shrubs suggested that their formation is controlled solely by bacterial activity. Later work by Guo and Riding (1994) subdivided the shrubs into micritic and spar-rhomb components and concluded that the two components probably formed by biotic and abiotic precipitation, respectively. Other authors have found no evidence for microbial precipitation and concluded that shrubs form by abiotic precipitation (Pentecost, 1990). The fundamental difference in each study was the identification of organic and/or inorganic materials that made up the shrub facies, which led to differing suggestions on how the shrubs formed. Due to petrological similarities between the blocky calcites with micritic rims in this study and the spar-rhomb and micritic components of Guo and Riding (1994), we infer that the layered mats precipitate from a combination of abiotic and biotic processes. The vertical alternation of dendritic precipitates (shrubs) and fine-grained layers of the layered mats would indicate depositional cyclicity in the system. One cycle of the layered mats contains dendritic precipitates that grew on a basal substrate, overlain by a fine-grained layer with or without clastic material. The dendritic precipitates need a very shallow-water environment in a lake or a terrace pool to grow (Chafetz and Folk, 1984). Using the active travertine as an analogue, these conditions are only maintained during an eruption, and for several hours after, depending on how quickly the supersaturated waters are evaporated from the pools. Therefore, a continual supply of supersaturated waters is needed to replenish or refill the pools and provide the environment needed

for shrub growth. It is inferred that the micrite and clastic sediments are deposited during extended periods of little or no flow of supersaturated waters, which could occur from periodic non-spring activity. Furthermore, the clastics may have been transported to the growing lithofacies by flooding of the Green River or by sheet flooding during periods of high rainfall. Finally, the onset of a new cycle was controlled by the precipitation of a basal substrate, which must develop a rim-and-pool geometry to provide a suitable environment for shrubs to grow. Therefore, the alternation between dendritic precipitates and fine-grained layers is likely a function of spring and non-spring activity, combined with occasional flooding of the deposit by non-spring waters.

4.3.2.3.3 White-Banded Veins

The white-banded veins are interpreted to be a subsurface feature of the travertine deposits as the veins crosscut both the cemented conglomerate and layered mat facies. In previous travertine studies, units with a similar morphology to the white-banded veins have been documented as a surficial feature that forms by rapid loss of CO_2 in areas of extremely agitated waters, such as close to a spring vent or on steep slopes. These were termed ray-crustal crusts by Folk et al. (1985) and crystalline slope crusts by Guo and Riding (1994). No deposits with the white-banded vein morphology are present on the surface of the active travertine in this study, even in areas of extreme water agitation. It is probable that rapid degassing of CO_2 from highly agitated subsurface waters is also the mechanism for the precipitation of these veins.

The radiating crystal fans, mammilated texture, and paired symmetry of the white-banded veins are consistent with these veins having precipitated in sub-aqueous, open fractures. The presence of vertically oriented speleothems in the central cavities of some subhorizontal white-banded veins is consistent with carbonate precipitation in air-filled fractures, potentially due to a lowering of the water table. In addition, the rare occurrence of alternating banded layers and speleothems in the same veins is consistent with there having been alternating periods of growth in flooded and drained fractures.

The significance of this unit can be understood when considering the position and relationship between the vertical and horizontal white-banded veins. The majority of the vertical veins are observed to infill fractures or minor faults and terminate at the

base of thick horizontal veins, consistent with the vertical veins being the primary conduits through which supersaturated waters travelled into the evolving travertine mound. Once the supersaturated waters reach the interior of the travertine mound through vertical feeder veins, the waters preferentially use subhorizontal lithologic contacts/fractures to reach the surface. This results in lateral movement of waters, which in turn precipitate numerous thick subhorizontal veins.

4.3.2.3.4 Brown-Banded Veins

The veins within the ancient travertine deposit have been divided into white- and brown-banded veins on the basis of colour, crosscutting relations, and meso- to macroscale textural differences. Microscopic comparisons of the two vein types reveal that both have similar radiating crystal fan morphologies; however, the brown-banded veins have significantly thinner bands and a much higher proportion of iron-rich laminations. These differences appear to be related since iron-rich laminations terminate the underlying crystal growth and promote the precipitation of finer-grained crystals on top of the lamination. Iron is known to inhibit carbonate growth due to the adsorption of the iron onto crystal surfaces, thus effectively blocking nucleating and growth sites (Meyer, 1984; Dromgoole and Walter, 1990; Sumner and Grotzinger, 1996). A higher proportion of iron-rich laminations will continually inhibit crystal growth and result in a series of thinner, finer-grained carbonate bands. The fundamental difference between the white and brown-banded veins is therefore the presence or lack of iron-rich horizons.

The variation in the number of iron-rich laminations may reflect a change in conditions between the precipitation of the two vein sets. More specifically, the higher proportion of iron-rich laminations in the brown-banded veins could indicate more episodic fluid-flow conditions supplying the deposit during emplacement. It is postulated that aragonite precipitates when there is continual recharge of CO_2-charged groundwater to the deposit. In subsequent periods of no recharge of CO_2-charged groundwater to the deposit, incompatible elements precipitate out of the waters to form the iron oxide in the laminations. It is suggested that these fluctuations in recharge correspond to periods of spring and non-spring activity. If this is the case, then the brown-banded veins may represent the terminal stages of travertine formation, when the final discharges of supersaturated waters were being sporadically

channelled and released through the deposit before the main migration pathway of the supersaturated waters changed at depth and the deposit became inactive.

4.3.2.4 Travertine Volumetrics

Estimating the volume of travertine precipitated in the footwall of the Little Grand Wash Fault enables the calculation of CO_2 leaked to the surface provided the ratio between CO_2 precipitated as travertine and CO_2 vented into the atmosphere is known and constant. Volumetric calculations for travertine in the northern footwall of the Salt Wash Graben were not performed due to the absence of thickness data for the active deposits. Volumes were calculated by computing travertine areas from digitised outcrop maps in ArcView and multiplying with their respective thicknesses estimated in the field. The subsurface thickness of the active Crystal Geyser travertine was taken directly from the Glen Ruby #1-X well record (McKnight, 1940), which drilled through the deposit in 1935. Estimated thicknesses, areas and resultant volumes for the travertines along the Little Grand Wash Fault are shown in Fig. 4.7. The total volume of travertine along the fault is $1.5 \times 10^5 m^3$, with the Crystal Geyser travertine ($6.5 \times 10^4 m^3$) and Travertine 3 ($7.0 \times 10^4 m^3$) contributing the greatest proportion.

To convert the volumes into CO_2 mass leaked to the surface, a series of basic calculations need to be conducted. Firstly, the total mass of travertines along the Little Grand Wash Fault is calculated by:

$$M_{CaCO3} = \rho_{CaCO3} V_{CaCO3}$$

where ρ_{CaCO3} is the average density of calcium carbonate ($2800 kg/m^3$;) and V_{CaCO3} is the total volume of travertine ($1.5 \times 10^5 m^3$). Next, the proportion of CO_2 within this total mass is calculated by:

$$M_{CO2} = M_{CaCO3}\left(\frac{MM_{CO2}}{MM_{CaCO3}}\right)$$

where M_{CaCO3} is the mass of travertine ($4.3 \times 10^8 kg$), MM_{CO2} is the molar mass of carbon dioxide (44g) and MM_{CaCO3} is the molar mass of calcium carbonate (100.1g).

Finally, the total mass of CO_2 that has leaked to the surface along the Little Grand Wash Fault is calculated by:

$$M_{TCO2} = \frac{M_{CO2}}{X_{CO2}}$$

where M_{TCO2} is the mass of CO_2 precipitated in the travertines ($1.9x10^8$kg) and X_{CO2} is the proportion of CO_2 leaked to the surface that is precipitated as travertine (10%). This X_{CO2} value was based on geochemical modelling by Heath (2004) using measured water chemistry from the Crystal Geyser. Based on the assumptions that there was no free CO_2-gas phase and no solid calcite in the solution, Heath (2004) used Phreeqc 2.8 to model the solution equilibrating with respect to calcite and atmospheric CO_2 ($P_{CO2} = 10^{-3.5}$atm). The modelling indicated that approximately 10% of the CO_2 is precipitated, while the remaining CO_2 is either vented as a free gas into the atmosphere or retained in solution (Heath, 2004).

Using these calculations, the total amount of CO_2 calculated to have leaked to the surface along the Little Grand Wash Fault since the precipitation of the oldest remaining travertine deposit is $1.9x10^9$kg ($4.3x10^{10}$mol). This is a conservative estimate of leakage as all the ancient deposits have been eroded to varying degrees. In addition, the presence of white-banded vein and layered mat remnants in ancient travertine conglomerates (see section 4.3.2.2.2) suggest that further travertine deposits were once present but have been subsequently removed through erosion by the down cutting of the Green River. However, this estimate of CO_2 mass leaked to the surface along the Little Grand Wash Fault enables the calculation of leakage flux (section 4.4.4) and assessment of sealing integrity for subsurface, fault-sealed traps (section 5.4) later in the thesis.

4.3.3 Fault-Related Diagenesis

4.3.3.1 Little Grand Wash Fault

Fault-associated diagenesis within the footwall of the Little Grand Wash Fault consists of iron-oxide reduction and hydrocarbon staining with minor aragonite and calcite veining (Fig. 4.1a). Iron-oxide reduction is characterised by the loss of haematite rims around sand grains (Fig, 4.8a-b) resulting in a colour change from

ubiquitous red to yellow or white in the footwall sandstones. The reduction is confined to either host rocks at the base of ancient travertine deposits or sections of the Curtis Formation. At the base of the ancient deposits, reduction is characterised by thin haloes (1 to 20 cm wide) around subvertical fractures, commonly infilled with aragonite or calcite veins (Fig. 4.8c) and subhorizontal tabular reduction bodies (5 to 200 cm thick) that extend laterally up to 200 m from the fault (Fig. 4.8d). The tabular bodies thin to dendritic stringers into the footwall and subparallel bedding, though occasionally cross bedding contacts. The thicknesses of the reduction haloes and tabular bodies are dependant on the lithology with clay-rich, lower porosity units (i.e. Morrison Formation) having thinner reduction zones relative to the sand-rich, higher porosity units (i.e. Curtis Formation).

Reduction away from the travertines is limited to lower sections of the Curtis Formation, where it outcrops next to the Crystal Geyser. The bottom 2 m of outcropping sandstone is partially to completely reduced, with an upper contact that is subconformable to bedding. Above this zone, there are sporadic, thin reduction horizons (1 to 10 cm thick) subparallel to bedding and thin reduction haloes (1 to 5 cm thick) surrounding steeply-dipping fractures sporadically infilled with calcite or rarely gypsum veins (Fig. 4.8e). These reduced horizons and haloes are sporadic for the next 4 m above of the completely reduced zone and are rare above this within the Curtis Formation.

Hydrocarbon staining is evident in the sandstones of the Curtis Formation and in the Salt Wash Member of the Morrison Formation close to or between the main fault strands of the Little Grand Wash Fault. Hydrocarbon-stained sandstones are identified by a greyish colour, petroleum odour when freshly broken and occasional presence of bitumen veins. The greyish colour results from numerous, microscopic oil globules that coat sand grains and fill porosity (Fig. 4.9a).

Hydrocarbon-staining in the Curtis Formation is rare, with 5 to 20 cm thick horizons of grey sandstone bordered by 1 to 5 cm thick, yellow to white reduction haloes (Fig. 4.9b). The horizons are limited to the same stratigraphic section that contains iron-oxide reduction. Alternatively, hydrocarbon staining in the Salt Wash Member is more abundant with a 10 m thick sequence of stained beds immediately north of the southern fault strand (Fig. 4.1a). Towards the top of the sequence, the sandstones are dark grey and inundated with bitumen veins to indicate heavy staining of hydrocarbons (Fig. 4.9c). Towards the base, the sandstones are light and lack the

bitumen veins but many subvertical fractures are stained with a hydrocarbon coating (Fig. 4.9d). At the base of the sequence, a hydrocarbon seep has been active at least since the beginning of the 20th century (Lupton, 1914; Fig. 4.9e). A shallow pit contains fresh oil floating on surface water indicating active flow of hydrocarbons to the surface.

4.3.3.2 Salt Wash Graben

Fault-related diagenesis in the footwall of the northern fault of the Salt Wash Graben consists of iron-oxide reduction and precipitation of gypsum, carbonate and celestine veins within the Entrada and Curtis sandstones (Fig. 4.1b). In an area centred about the faulted fold axis of the Green River Anticline, red Entrada sandstones are extensively reduced to pale yellow (Fig. 4.10a). Within this area, lower sections of Entrada sandstone (up to 8 m thick) are completely reduced (Fig. 4.10b), though reduction is not confined to specific beds nor limited by bedding contacts (Fig. 4.10c). Above this section, reduction is confined to clusters of steeply-dipping fractures with reduction haloes up to 5 m wide (Fig. 4.10b). The local, shallowly-north plunging dip results in the disappearance of the Entrada sandstone and pervasive reduction around 300m into the footwall. Beyond this area, reduced sandstones are only seen at the base of ancient travertine deposits and around steeply-dipping fractures.

Below the travertine deposits, reduction is characterised mainly by reduction haloes (up to 50 cm wide) around fractures (Fig. 4.10d) and limited subhorizontal tabular reduction bodies (up to 2 m thick). Additional reduction is observed around steeply-dipping fracture clusters up to 400 m into the footwall. Close to the fault, a significant proportion of the fractures within the Entrada and Curtis sandstones are accompanied with reduction haloes, 5 to 200 cm wide. Further into the footwall, sporadic clusters of fractures, generally oblique to the fault, contain thinner reduction haloes (1 to 100 cm wide) that continue as far as the Curtis sandstones outcrop at the surface (Fig. 4.10e).

Fractures with reduction haloes located between the peripheral travertine deposits and up to 200m from the fault are commonly infilled with aragonite, calcite, gypsum or celestine veins (Fig. 4.11). The aragonite and calcite veins infill fractures mainly at or near the base of travertine deposits (Fig. 4.11a).The gypsum veins are the most extensive fracture infill being distributed throughout Entrada and Curtis

sandstones (Fig. 4.11b-c). Celestine veins are rare, observed at only one locality in the Curtis sandstones immediately next to the northern fault (Fig. 4.11d).

4.4 Geochemistry

4.4.1 Methodology

Sampling for geochemical analyses focussed on active and ancient travertines deposits and iron-oxide reduction of host rocks. For the active deposits, similar-sized, surface travertine terraces were extracted with a chisel and hammer proximal and distal from the geyser or spring vent. At the Crystal Geyser, a more detailed sampling regime collected travertine every 4 m along two flow paths from the geyser vent to the end of the mound to characterise CO_2 surface degassing processes. For the ancient deposits, all available lithofacies were collected at each deposit with particular emphasis on the universal, white-banded veins. For iron-oxide reduction, three transects perpendicular to subvertical fractures with reduction haloes sampled fracture infill (sulphate or carbonate veins), reduced and unreduced sandstones from the Entrada Sandstone along the northern fault of the Salt Wash Graben (Fig. 4.1b).

After field and hand sample descriptions, selected samples were slabbed and mounted as polished thin sections. Each thin section was analysed under plane-polarised light to characterize the travertine lithofacies and define any variations between reduced and unreduced sandstones. The mineralogical content of both fluid flow features were subsequently confirmed by X-ray powder diffraction (XRD). Whole rock samples were ground and analysed as powder cavity mounts at Trinity College Dublin on a Phillips PW1720 diffractometre using CuK_α radiation over a range of 2 to 46° 2θ.

Active and ancient travertine samples and carbonate cements of reduced and unreduced sandstone were analysed for $\delta^{13}C$ and $\delta^{18}O$ using continuous-flow mass spectrometres at Saint Louis University and Trinity College Dublin. Travertine samples were slabbed and micro-drilled to obtain pure, well-characterized, powdered samples. Whole rock reduced and unreduced sandstone samples were ground directly into powder. Submilligram aliquots of powder were reacted with orthophosphoric acid at 90°C for several hours to produce CO_2 that was then analyzed in the mass spectrometre via an automated extraction device. Duplicate and some triplicate analyses were made for most samples. A combination of in-house and international

carbonate standards analyzed with every five samples had an analytical precision of 0.09‰ for carbon and 0.22‰ for oxygen at Saint Louis University (1σ, N=34 standard analyses) and 0.06‰ for carbon and 0.19‰ for oxygen at Trinity College Dublin (1σ, N=12 standard analyses), relative to PDB and VSMOW standards, respectively.

U-Th radiometric dating of white-banded veins from selected ancient travertine deposits was performed at the Scottish Universities Environmental Research Centre (SUERC) to define the timing of CO_2 leakage along both faults. Samples of dense aragonite, free from vegetal detritus, was crushed and altered or weathered material removed. Aliquots of the crushed carbonate were reacted with nitric acid and uranium and thorium were separated from the solution using the first step of the methodology of Yokoyama et al. (1999). Separated U and Th solutions were diluted with 5% nitric acid and analysed on a Micromass GV Isoprobe multiple collector (ICP-MS) to ascertain uranium and thorium isotopic ratios. ^{230}Th and ^{238}U concentrations were calculated and $^{234}U/^{238}U$ was corrected using an iterative procedure and exponential fractionation laws. Ages were subsequently calculated from the concentrations and ratios using Isoplot/Ex rev. 2.49 (Ludwig, 2001). A more detailed methodology of this procedure is outlined in Appendix 5.

4.4.2 Mineralogy

4.4.2.1 Travertines

4.4.2.1.1 Results

The mineralogy of samples from active and ancient travertine are presented in Table 4.1. Active travertine is composed of a mixture of calcite and aragonite close to the geyser vent and calcite far from the vent. In the ancient travertine, the white-banded veins are composed of aragonite, and the brown-banded veins contain a mixture of aragonite and goethite with minor amounts of calcite. The goethite is present in the dark laminations, which are numerous in the brown-banded veins and rare in the white-banded veins. The layered mats are composed of calcite, minor amounts of aragonite, and quartz, which presumably comes from detrital material from the surrounding host rock deposited on top of the growing mound. The conglomerate cement is composed of calcite with detrital quartz.

Table 4.1: Mineralogical composition of travertine determined from XRD analyses.

Sample Location [a]	**Lithofacies**	**Mineralogy**			
		aragonite	calcite	quartz	goethite
Crystal Geyser	Active Travertine (8m from geyser vent)	x	x		
Crystal Geyser	Active Travertine (55.7m from geyser vent)		x		
Travertine 2	Layered Carbonate Mat	x	x	x	
Travertine 2	Layered Carbonate Mat	x	x	x	
Travertine 6	Layered Carbonate Mat	x	x	x	
Travertine 2	White Banded Vein	x			
Travertine 2	White Banded Vein	x			
Travertine 4	White Banded Vein	x			
Travertine 6	White Banded Vein	x			
Travertine 2	Vertical Banded Vein Brown Band	x	x		x
Travertine 2	Vertical Banded Vein White Band	x	x		
Travertine 2	Conglomerate Cement		x	x	

a – See Fig. 4.1 for location of the samples

4.4.2.1.2 Interpretation

In low-Mg waters similar to the waters that discharge from Crystal Geyser, low-Mg calcite is the dominant cement mineralogy and aragonite is exceedingly rare (Tucker and Wright, 1996). This is not the case for the studied travertine deposits with aragonite being a major carbonate constituent (Table 4.1). Therefore, other factors controlling carbonate mineralogy need to be considered. Two important physical factors that influence carbonate mineralogy are temperature and the rate of supply of CO_3^{2-} ions. With increasing temperature, there is a greater increase in the precipitation rate of aragonite over that of calcite (Burton and Walter, 1987). Fouke et al. (2000) reported a temperature control on the mineralogy of carbonates precipitated at the Angel Spring travertine deposit with temperatures above 44°C precipitating aragonite, those below 30°C precipitating calcite, and those in between, a mixed aragonite-calcite assemblage. However, the spring water from Crystal Geyser does not significantly change its temperature during flow and precipitation of the carbonates, thus indicating temperature has little or no role in determining the carbonate mineralogy of the travertine deposits.

High rates of carbonate ion supply could also account for aragonite precipitation and acicular crystal growth (Given and Wilkinson, 1984). Within the studied travertine deposits, aragonite is the primary mineral in the white-banded veins and calcite is the primary mineral in the layered mats at the distal margin of the modern travertine mound and in the carbonate cements of the conglomerates. Elsewhere, mixed aragonite-calcite mineralogies are present. This variation in mineralogy is interpreted to reflect the varying concentration of CO_3^{2-} ions along the migration pathway(s) of the precipitating carbonate-rich waters in and across the mounds. The subsurface white-banded veins with acicular aragonite precipitated first from the CO_3^{2-} rich waters. After discharging to the surface, the concentration of CO_3^{2-} ions in the water decreased downstream, resulting first in a mixed aragonite-calcite mineralogy and then in a pure calcite precipitate at the distal margin of the mound.

4.4.2.2 Reduction Zones

The mineralogy of samples from three transects across reduction zones are presented in Table 4.2. These reduction zone transects sampled fracture infill, reduced and unreduced sandstones (Fig. 4.11a-c). Material infilling the fractures is composed of gypsum or aragonite with quartz and minor amounts of calcite. Aragonite is limited to the base of a travertine deposit while the quartz represents detrital material derived from surrounding sandstones. All the sandstones are composed of quartz, feldspars and clays and generally carbonates. The clays are a mixture of muscovite, kaolinite, illite and smectite. There are no common variations in mineralogy between the reduced and unreduced sandstones. Calcite is added to the reduced sandstones in transect 1, removed with dolomite in transect 3 and consistent between reduced and unreduced sandstones in transect 2. These mineralogical variations are suggested to represent local heterogeneities sampled within the sandstones.

Table 4.2: Mineralogical composition of samples from transects of reduction haloes surrounding fractures along the northern fault of the Salt Wash Graben.

TRANSECT [a]	FRACTURE INFILL	SANDSTONE	
		REDUCED	UNREDUCED
1	ARAGONITE QUARTZ CALCITE [d]	QUARTZ, FELDSPARS [b] CLAYS [c] ,DOLOMITE CALCITE	QUARTZ, FELDSPARS [b] CLAYS [c] ,DOLOMITE
2	GYPSUM QUARTZ CALCITE [d]	QUARTZ, FELDSPARS [b] CLAYS [c] ,DOLOMITE CALCITE	QUARTZ, FELDSPARS [b] CLAYS [c] ,DOLOMITE CALCITE
3	GYPSUM QUARTZ	QUARTZ, FELDSPARS [b] CLAYS [c]	QUARTZ, FELDSPARS [b] CLAYS [c] DOLOMITE CALCITE

a - see Fig. 4.1b for location of transects
b - combination of plagioclase and alkali-feldspars
c - combination of muscovite, kaolinite, illite and smectite
d - minor amounts of mineral in sample

4.4.3 Stable Isotopes

4.4.3.1 Results

The isotopic values for the active travertine deposits are presented in Fig. 4.12 and range from 5.2 to 11.3‰ for $\delta^{13}C$ and 18 to 22.2‰ for $\delta^{18}O$. The Salt Wash Graben travertines have similar to slightly heavier $\delta^{13}C$ values and predominantly heavier $\delta^{18}O$ values relative to the Crystal Geyser travertine (Fig. 4.12). The detailed analysis of the Crystal Geyser travertine shows that the $\delta^{13}C$ values are constant (flow path 1; Fig. 4.13a) to slightly decreasing (flow path 2; Fig. 4.13.b) downslope of the geyser vent while the $\delta^{18}O$ values decrease slightly along both flow paths (Fig. 4.13). Substantial $\delta^{18}O$ variations occur along steep to vertical sections of flow path 2 (Fig. 4.13b).

The isotopic composition of the ancient travertine deposits and their respective altered host rocks are shown in Fig. 4.14. The host rock at the base of the deposits exhibit fluctuating $\delta^{13}C$ and $\delta^{18}O$ values, dependant on lithology that range between -3.9 to 3.7‰ and 16.2 to 23.9‰, respectively. The travertines have values of 3.3 to 7.8‰ for $\delta^{13}C$ and 16.6 to 24.8‰ for $\delta^{18}O$. Within each deposit in $\delta^{13}C$ - $\delta^{18}O$ space, the banded veins form tight clusters, while the layered mats and conglomerates plot over a wide range having comparable to lighter $\delta^{13}C$ values and heavier $\delta^{18}O$ values (Fig. 4.14).

Graphical comparisons of the universal banded veins (white and brown) from each ancient deposit show significant overlap in $\delta^{13}C$ and $\delta^{18}O$ values (Fig. 4.15). To assess whether any of the deposits are isotopically distinct, the banded veins underwent statistical analysis with the ancient deposits treated as the independent variable and the $\delta^{13}C$ or $\delta^{18}O$ values treated as the dependant variables. A one-way analysis of variance (ANOVA) test was run for both the $\delta^{13}C$ and $\delta^{18}O$ values to find if there were any significant differences between the deposits. If statistically significant differences were observed at the 0.05 alpha level, a post-hoc Tukey test was run to identify subsets of ancient deposits that do not differ significantly based on means. The results of the tests are summarised in Table 4.3, 4.4, 4.5 and 4.6. From the one-way ANOVA, significant differences between ancient deposits were detected for

Table 4.3: One-way ANOVA of $\delta^{13}C$ between ancient travertines. There are significant differences between travertines with $F(6) = 10.268$, $p < 0.001$.

Source	Type III Sum of Squares	df	Mean Square	F	Sig.
Intercept	2687.539	1	2687.539	14852.969	.000
Travertine	11.148	6	1.858	10.268	.000
Error	22.980	127	.181		
Total	3835.685	134			
Corrected Total	34.128	133			

Table 4.4: One-way ANOVA of $\delta^{18}O$ between ancient travertines. There are significant differences between travertines with $F(6) = 34.387$, $p < 0.001$.

Source	Type III Sum of Squares	df	Mean Square	F	Sig.
Intercept	32001.510	1	32001.510	88490.503	.000
Travertine	74.613	6	12.436	34.387	.000
Error	45.928	127	.362		
Total	44976.940	134			
Corrected Total	120.541	133			

Table 4.5: Tukey HSD test of $\delta^{13}C$ between ancient travertines. Subsets indicate isotopically similar subgroups of travertine deposits.

Travertine [a]	N [b]	Subset for alpha = 0.05		
		1	2	3
1	8	4.778		
5	9	5.100	5.100	
2	49	5.121	5.121	
6	24		5.335	5.335
4	21			5.643
3	13			5.701
7	10			5.804
Sig.		.368	.786	.074

a - Location of the travertine deposits are shown in Fig. 4.1

b - Number of data per travertine

Table 4.6: Tukey HSD test of $\delta^{18}O$ between ancient travertines. Subsets indicate isotopically similar subgroups of travertine deposits.

Travertine [a]	N [b]	Subset for alpha = 0.05			
		1	2	3	4
2	49	17.502			
1	8	17.706	17.706		
3	13		18.346	18.346	
6	24			18.553	
7	10			18.824	
5	9			18.841	
4	21				19.566
Sig.		.975	.094	.341	1.000

a - Location of the travertine deposits are shown in Fig. 4.1

b - Number of data per travertine

both $\delta^{13}C$ and $\delta^{18}O$ values (Table 4.3 and 4.4). The Tukey test grouped the isotopically non-significant deposits together, though the grouping of deposits varied between the $\delta^{13}C$ and $\delta^{18}O$ tests (Table 4.5 and 4.6). However, travertines 1 and 2 and travertines 3, 6 and 7 formed isotopically similar groups for both the $\delta^{13}C$ and $\delta^{18}O$ tests.

Non-travertine related, carbonate veins sampled within the fault zone and south side of both faults have distinct isotopic values compared to the travertines with $\delta^{13}C$ values of -7.1 to 1.6‰ and $\delta^{18}O$ values of 15 to 22.3‰ (Fig. 4.16).

Isotopic comparison of carbonate cements from reduced and unreduced sandstones with fracture fill (aragonite) for transect 1 are presented in Fig. 4.17. The carbon values for the reduced and unreduced sandstones are consistent, ranging from -2.8 to -1.5‰ and distinct from the aragonite vein (5‰; Fig. 4.17a). The oxygen values for the sandstones vary, ranging from 19.7 to 23.6‰ but are similar between reduced and unreduced sections and slightly heavier that the aragonite vein (18.3‰; Fig. 4.17b).

4.4.3.2 Interpretation

4.4.3.2.1 Introduction

Carbon and oxygen isotopic compositions of travertines provide insight into the source of the fluid and the precipitation conditions (Friedman and O'Neil, 1977; Turi, 1986). Analysis of both ancient and active travertines can indicate any possible temporal or spatial changes to the hydrological system, while comparison of the travertines with other local carbonate veins and carbonate cements from reduced sandstones can constrain the extent of this system. In the following discussion, carbon and oxygen isotopes are used to (1) evaluate the chemical, physical and biological processes that are controlling precipitation of the travertines; (2) document any spatial or temporal changes to the hydrologic system; and (3) define the flow pathways for the leaking system.

4.4.3.2.2 Variations within a Travertine Deposit

A detailed analysis of isotopic variations within and between the fundamental components of the best developed active (Crystal Geyser) and ancient (Travertine 3; Fig. 4.1) travertine deposits provide information to characterise the processes

precipitating a travertine. The following section investigates reasons for isotopic variability within a travertine deposit.

Active Surface

Analysis of downstream $\delta^{13}C$ and $\delta^{18}O$ variations along two flow paths from the Crystal geyser vent to the edge of the travertine provide insight into the processes controlling surface carbonate precipitation. Apart from the first two samples of flow path 1, the $\delta^{13}C$ values along both flow paths of the active travertine are constant (flow path 1; Fig. 4.13a) to slightly decreasing (flow path 2; Fig. 4.13b). Most studies examining the variation of carbon isotopes downstream of a spring vent have found increasing isotopic values presumably due to CO_2 degassing (Fig. 4.18; Gonfiantini et al., 1968; Friedman, 1970; Amundsen and Kelly, 1987). In contrast, Gou et al. (1996) reported negative downstream trends in $\delta^{13}C$ values that were attributed to microbial activity. The presence of algae within deeper terrace pools of the active travertine (Fig. 4.2e) combined with the ambient temperatures of the erupting waters is consistent with biotic processes having played a role in the precipitation of the travertine in this study. However, the flat trends displayed by both flow paths indicate that the precipitation of travertine downstream of the geyser vent is a complex process that probably involves a combination of competing abiotic (CO_2 degassing) and biotic (microbial respiration) processes to form the overall trend. The anomalous $\delta^{13}C$ for the first two samples of flowpath 1 are considered to be contaminated, due to the large difference in values from the rest of the data. Though uncertain, the source of the contamination could be anthropogenic, caused by numerous tourists continually walking and driving over this section of the travertine to watch the Crystal Geyser erupt.

There are several differences in the oxygen isotope trends between the two flowpaths on the active travertine mound (Fig. 4.13). For flowpath 1, $\delta^{18}O$ values change by ~1.5‰ during the first 20 m of flow, and then are nearly constant for the last 50 m of flow. The variations do not correlate strongly with distance from vent or changes in surface topography. In contrast for flow path 2, $\delta^{18}O$ values are nearly constant within ~30 m of the vent, decreases ~1‰ in the region of several small waterfalls, and then varies somewhat until it enters the Green River. This decrease at the waterfalls is most easily understood in terms of more vigorous CO_2 degassing due to increased turbulent flow (cf. Turi, 1986). The anomalously light oxygen isotope

values of two samples (13 to 17m) along flowpath 1 might be due to anthropogenic contamination.

Ancient Surface

The isotopic composition of the layered mats is characterised by a wide range of $\delta^{13}C$ and a generally limited range of $\delta^{18}O$ (Fig. 4.14). The conglomerate cements have the lowest $\delta^{13}C$ of any lithofacies and $\delta^{18}O$ similar to the layered mats (Fig. 4.14). The $\delta^{13}C$ values for the layered mats are the highest in some deposits and can be attributed to CO_2 degassing at the effusion vents causing enrichment of $\delta^{13}C$ in the spring waters and subsequently precipitated layered mats. In the better preserved deposits, no systematic change in $\delta^{13}C$ is observed downstream of the inferred paleo-vents, though differentiation of this lithofacies show that pure layered mats have relatively constant, high $\delta^{13}C$, while transitional zone layered mats have more variable, similar to lower $\delta^{13}C$ (Fig. 4.19). This variation probably represents the degree of clastic material captured within the transitional zone layered mats, with increasingly larger proportions of clastics giving progressively lower $\delta^{13}C$ due to the isotopic characteristics of the host rocks. This contamination of the layered mats by the host rock is also inferred for the conglomerate cements with the low $\delta^{13}C$ reflecting a proportion of clastics within the sampled cements.

The similar $\delta^{18}O$ for the layered mats and conglomerate cements indicate stable surface precipitation conditions. These values are similar to ranges reported by Shipton et al (2004), who concluded that surface carbonates were precipitated at low temperatures from supersaturated meteoric waters, consistent with contemporary conditions in the study area. The isotopically heavy $\delta^{18}O$ outliers recorded at some ancient deposits may reflect diagenetic changes in the surface carbonates from post-deposition fluids such as rain, river or meteoric waters. This is probable as oxygen isotopes are much more easily affected than carbon isotopes by meteoric or interstitial fluids (Fairchild et al., 1990).

Ancient Subsurface

Detailed transects through the thickest white-banded veins at the best developed ancient deposits indicate there are possible isotopic trends from vein rim to centre (Fig. 4.20). However, the trends vary between and within deposits. This is demonstrated with travertine 1 having a negative covariant isotopic trend, travertine 3

having constant isotopic values and travertine 2 having positive covariant and constant isotopic trends from vein rim to centre (Fig. 4.20). Furthermore, the later, crosscutting brown-banded veins in all three deposits have isotopic values similar to the earlier white-banded veins (Fig. 4.14a-c). This indicates that the carbonate-rich water supplying each ancient deposit did not evolve but remained stable throughout the precipitation of the travertine with minor perturbations during individual vein emplacement.

Comparison of the banded veins with the layered mats and conglomerate cements show that the surface lithofacies have similar to lighter $\delta^{13}C$ and heavier $\delta^{18}O$ (Fig. 4.14). The similar $\delta^{13}C$ values support stable carbonate-rich waters supplying each deposit with the lighter values indicating a degree of mixing between the surface carbonates and the isotopically light host rocks. An average $\delta^{18}O$ increase of 1.2‰ from the banded veins to the surface carbonates in each ancient deposit indicates a decrease in precipitation temperatures between lithofacies. To quantify the temperature change, the fractionation factor (α) and fractionation equation for inorganic aragonite at low temperatures (Zhou and Zheng, 2003) can be used:

$$10^3 \ln\alpha = 20.44 \times 10^3/T - 41.48$$

$$\alpha = (\delta^{18}O_{CaCO3} + 1000)/(\delta^{18}O_{H2O} + 1000)$$

where $\delta^{18}O_{CaCO3}$ is the carbonate value, $\delta^{18}O_{H2O}$ is the fluid value from the carbonate-rich effusion and T is in degrees Celsius. Using a $\delta^{18}O_{CaCO3}$ value of 1.2‰ to represent the mean difference in subsurface and surface carbonate values and a $\delta^{18}O_{H2O}$ value of -14‰ measured from the erupting Crystal Geyser waters (Heath, 2004) a temperature difference of 4.9°C is calculated. Thus, the layered mats and conglomerate cements are precipitated, on average, at temperatures 5°C less than the subsurface banded veins.

4.4.3.2.3 Variations Between Travertine Deposits

The isotopic record for the active and ancient travertines document the hydrological history of carbonate-rich waters leaking along both faults. The following section investigates possible spatial and temporal changes to this hydrological system.

Spatial Trends

The active travertines along the northern fault of the Salt Wash Graben have similar to slightly heavier $\delta^{13}C$ and predominantly heavier $\delta^{18}O$ compared to the Crystal Geyser travertine (Fig. 4.12). All $\delta^{13}C$ values fall within the range of the Crystal Geyser travertine except for the Small Bubbling Spring South travertine and one value from the Ten Mile Geyser travertine. This indicates a common fluid is currently responsible for precipitating travertine along both fault systems. The slight increase in $\delta^{13}C$ for some Salt Wash Graben travertines could reflect additional evolution of the fluid between the faults possibly due to variations in the source(s) supplying the CO_2. The variation in $\delta^{18}O$ between active deposits is directly related to the emergence temperatures of the carbonate-rich waters precipitating the travertines with relatively warm effusions (Crystal Geyser) precipitating lighter $\delta^{18}O$ compared to colder effusions (Ten Mile Geyser; Fig. 4.12).

Isotopic comparisons of the ancient travertines were limited to the white-banded veins due to being universally present and free from clastic contamination. Statistical testing based on means and variances indicate significant differences in $\delta^{13}C$ and $\delta^{18}O$ values between deposits with smaller isotopically-similar subgroups that vary between $\delta^{13}C$ and $\delta^{18}O$. The $\delta^{13}C$ subgroups consist of travertines 1, 2 and 5, travertines 2, 5 and 6 and travertines 3, 4, 6 and 7. The subgroups are not confined to individual faults nor do they vary strongly along strike of either fault. This suggests the variation between subgroups may represent temporal fluctuations in the source/s of the CO_2. The $\delta^{18}O$ subgroups consists of travertines 1 and 2, travertines 1 and 3, travertines 3, 5, 6 and 7 and travertine 4. These subgroups indicate variability of $\delta^{18}O$ along the Little Grand Wash Fault and stability along the Salt Wash Graben. Utilising the Zhou and Zheng (2003) fractionation of aragonite equation with a $\delta^{18}O_{CaCO3}$ value of 2.1‰ (difference between minimum and maximum $\delta^{18}O$ means) and a $\delta^{18}O_{H2O}$ value of -14‰ (Crystal Geyser fluids; Heath, 2004) a temperature of 7.7°C is calculated. This indicates that a variation of ~ 8°C in precipitation temperature between deposits would generate the observed $\delta^{18}O$ range. As the active geysers and springs have variations in emergence fluid temperatures of up to 4°C, it is feasible that changes in temperature are controlling the $\delta^{18}O$ range in the white-banded veins. However, the common grouping of travertines 1 and 2 and travertines 3, 6 and 7 for both $\delta^{13}C$ and $\delta^{18}O$ statistical tests suggest a variation in source may also contribute to $\delta^{18}O$ variability between travertines.

Studies of waters and gases emanating from the geysers and springs along both faults indicate the erupting waters consist of CO_2 from an inorganic upper crustal source that mixes with shallow meteoric waters to precipitate the travertine deposits (Mayo et al, 1991; Heath, 2004). Research by Heath (2004) indicated there are two possible sources for the CO_2 which are clay-carbonate reactions that occurred during the burial of the Colorado Plateau and/or metamorphic reactions of Palaeozoic limestones near Tertiary igneous intrusions. The clay-carbonate reactions occur at temperatures between 100-200°C (Hutcheon and Abercombie, 1990), potentially sourcing CO_2 from Pennsylvanian to Cretaceous carbonates. The most likely source beds are from the Sinbad Limestone Member of the Moenkopi Formation, Elephant Canyon Formation and/or Honaker Trail Formation (see Fig. 2.3). Isotopic variations in the multiple carbonate source rock will translate to variations in the $\delta^{13}C$ for the generated CO_2. The metamorphic reactions require temperatures above 450°C (Mayo and Muller, 1997) limiting CO_2 generation to locations where Permian and Pennsylvanian carbonate rocks are close to Tertiary intrusions. The closest intrusions are 45km to the southwest (Robbers Roost lamproite) and 100km to the southeast (La Sal laccolith), requiring the CO_2 to migrate large lateral distances. As such, the most likely source for the CO_2 is from clay-carbonate reactions with isotopic variations reflecting changes in the source rock (Heath, 2004). Additional CO_2 may come from metamorphic reactions though it is less likely due to the large migration distances.

Temporal Trends

The active travertines have heavier $\delta^{13}C$ and similar $\delta^{18}O$ relative to their ancient-equivalent layered mats (Fig. 4.21). Small fluctuations between active and ancient $\delta^{13}C$ values were anticipated due to varied clastic contamination in some of the layered mat samples. However, significant shifts in $\delta^{13}C$ between the ancient and active deposits suggest a temporal change of the CO_2 sources with an isotopically heavier carbonate source being recently introduced or becoming more volumetrically significant in supplying CO_2 to the system. Due to the two potential sources and multiple available source rocks it is difficult to define specific changes to the CO_2 source apart from indicating that a relatively isotopically heavy carbonate source has recently become influential. The similar $\delta^{18}O$ values indicate precipitation conditions (i.e. low temperature meteoric fluid) have remained stable throughout the generation of all travertines.

Temporal isotopic variations between ancient travertine deposits can be assessed at Ten Mile Butte on the northern fault of the Salt Wash Graben (Travertine 6 on Fig. 4.1), where three discrete phases of travertine precipitation occur at varying elevations (Fig. 4.22). As all the deposits have the same drainage level, this variation in elevation represents travertine development at three separate periods at the same location from $5.9x10^5$years ago (see section 4.4.4). Comparing the isotopic values of the white-banded veins, all three deposits overlap in $\delta^{13}C$ - $\delta^{18}O$ space (Fig. 4.23). The middle and younger deposits have a large range of isotope values to indicate local fluctuations in source and precipitation conditions during precipitation of each deposit. The older deposit has a more limited isotopic range that may reflect the smaller dataset or more stable isotopic conditions during this period. Overall, the carbonate-rich waters erupting from this location have remained stable through time with isotopic variations related to individual travertine development.

Based on radiometric dating and vertical separation between deposit and drainage level, the travertine deposits on Ten Mile butte represent some of the oldest and youngest ancient deposits preserved in the study area (see section 4.4.4). Therefore, the carbonate-rich fluids have remained broadly isotopically consistent over time with variations possibly reflecting the influence of multiple source rocks in CO_2 generation.

4.4.3.2.4 Comparison with Non-Travertine Carbonate Veins

The isotopic comparison of banded veins from ancient deposits with other local and regional carbonate veins will geochemically constrain the surficial extent of the carbonate-rich waters, which precipitate travertine in the immediate footwalls of both the Little Grand Wash Fault and northern fault of the Salt Wash Graben. Carbonate veins within the fault zone and on the south side of both faults have significantly lighter $\delta^{13}C$ and similar $\delta^{18}O$ compared to the banded veins (Fig. 4.16). The different $\delta^{13}C$ values indicate that the non-travertine-related veins are generated from different sources and fractionation processes. The carbonate-rich waters that precipitate the travertine therefore appear to have not crossed the fault zone. The similar $\delta^{18}O$ values indicate the precipitation of all the carbonate veins occurred at comparable low temperatures from meteoric waters.

A similar situation is observed regionally, with published data on carbonate veins (Morrison and Parry, 1986; Breit and Meunier, 1990; Chan et al, 2000; Garden

et al, 2001) from the northern half of the Paradox Basin being isotopically distinct from the banded veins (Fig. 4.24). Therefore, the Little Grand Wash Fault and northern fault of the Salt Wash Graben represent the only identified locations where isotopically unique and temporally stable carbonate-rich waters are naturally leaking to the surface and precipitating travertine in east-central Utah.

4.4.3.2.5 Variation in Reduced Zones

The isotopic comparison of carbonate cements from reduced and unreduced sandstones with carbonate veins from adjacent fracture infill and overlying travertine deposits can indicate the generic or contrasting nature of the fluids precipitating the carbonates. Differences in $\delta^{13}C$ between the carbonate cements from the sandstones and the aragonite vein infilling the adjacent fracture indicate the carbonates were derived from two different sources. Consistent $\delta^{13}C$ between the reduced and unreduced sandstones show the reducing fluids responsible for bleaching sections of the sandstone did not alter the isotopic composition of the carbonate cements. Similar $\delta^{18}O$ between the aragonite vein and carbonate cements indicate all the carbonates were precipitated from cool meteoric waters, though the lower $\delta^{18}O$ of the aragonite suggest the vein was precipitated in slightly warmer waters.

An isotopic comparison of the aragonite vein and carbonate cements with white banded veins from the overlying travertine deposit is presented in Fig. 4.25. Isotopic similarities between the aragonite vein and travertine carbonates indicate they were all precipitated from a similar carbonate-rich fluid. The isotopically distinct carbonate cements indicate that they were precipitated from a separate fluid probably relating back to the formation of the sandstones. Therefore, the stable isotopes indicate that the carbonate-rich fluids responsible for precipitating travertines at the surface also precipitated aragonite in fractures as the fluids migrated to the surface. However, a separate reducing fluid responsible for causing the reduction haloes around fractures did so without introducing additional carbonates into the system and has left no trace in the stable isotope signatures.

4.4.4 Radiometric Dating

Radiometric ages of five ancient travertine deposits along with their respective elevations above adjacent drainage levels are presented in Table 4.7. The travertine ages vary significantly and strongly correspond with vertical separations between deposit and drainage level. Assuming the travertines represent paleo-surfaces, vertical separation (i.e. eroded material) divided by travertine age (i.e. time) will indicate the erosion rates of the area. A regression analysis of these two parametres show a strong correlation ($r^2 = 0.98$) and a well-constrained local erosion rate of 0.5m every thousand years (Fig. 4.26).

Of more importance to this study, a maximum travertine age of 7.8×10^5years along the Little Grand Wash Fault combined with the calculated leaked mass for CO_2 of 1.9×10^6tonnes (see section 4.3.2.4) indicates an average leak rate of 24.1tonnes/year along this fault. An alternate measurement of CO_2 leakage that is commonly used in risk assessment is flux. Flux is a measure of the rate at which CO_2 passes out of the ground per unit area and is calculated by (Oldenburg and Unger, 2005):

$$FLUX = M / A / t$$

where M is the calculated leaked mass of CO_2 (1.9×10^9kg), A is the area of emissions at the surface defined by the areal extent of travertine deposits ($2.9 \times 10^5 m^2$; Fig. 4.7) and t is the duration of leakage (7.8×10^5years). The average CO_2 flux calculated for the Little Grand Wash Fault is $0.84 kg/m^2/yr$ or $0.60 \mu mol/m^2/s$. Unfortunately, CO_2 leak rates and flux could not be determined for the northern fault of the Salt Wash Graben as the absence of thickness data for active deposits prevented calculation of volumes for all travertines (see section 4.3.2.4). In addition, the flux value is considered an underestimate due to the forced assumption that all travertine sites were active after initiation. Further dating would be needed to constrain periods of activity for each travertine deposit to allow a better constraint on CO_2 flux along the Little Grand Wash Fault.

Table 4.7 Calculated and predicted ages of ancient travertines deposits based on U-Th dating. Elevation data is included to demonstrate the dependence between erosion (vertical separation) and travertine age.

Travertine [a]	Elevation (m)		Vertical Separation (m)	Radiometric Age (years)	Predicted Age (years)[d]
	Deposit	Drainage Level [b]			
1	1231	1229	2	6072 ± 209	
2	1284	1243	41	78378 ± 4347	
3	1284	1254	30		59694
4	1283	1267	16	26701 ± 1163	
5	1295	1278	17		33827
6.1[c]	1285	1257	28	59335 ± 2927	
6.3[c]	1262	1257	5		9949
7	1272	1249	23	50455 ± 2555	

a – see figure 4.1 for location of travertine deposits

b – Drainage level is the lowest immediate elevation in a wash or drainage channel around each travertine deposit.

c – Highest and lowest elevations of separate travertine deposits at Ten Mile Butte (Travertine 6 in Fig. 4.1).

d – ages predicted from the linear relationship between vertical separation and travertine age displayed in Fig. 4.26.

4.5 Discussion

4.5.1 Conceptual Model of Travertine Mound Evolution

Field observations coupled with petrological and geochemical analyses indicate that travertine deposits are composed of four distinct lithofacies, which are: (1) cemented conglomerate, (2) layered carbonate mats, (3) white-banded veins, and (4) brown-banded veins. Documented below and illustrated in Figure 4.27 is a preliminary facies model that indicates how these lithofacies interact and the steps involved in the initiation and development of a travertine deposit based on interpretations from this study.

1. Supersaturated carbonate-rich waters migrate to the surface via a fault-related fracture network and initiate a cold-water spring. The carbonate-rich waters erupt from the spring vent and flow into the surrounding colluvium, progressively infilling open pore spaces with a carbonate cement during degassing to form a conglomerate (Fig. 4.27a).
2. As the conglomerate develops around the spring vent, it forms a relatively impermeable horizon enabling the waters to flow across the surface and precipitate layered carbonate mats by abiotic and biotic processes (Fig. 4.27b). The layered mats gradually prograde from the spring vent, limited by the

development of the underlying conglomerate, to form a surficial terraced deposit with hemispherical ponds. Contemporaneously, highly agitated, warmer waters migrating through conduits to the spring vent, precipitate bands of radiating aragonite crystals on the conduit walls. Each isopachous set of bands grows perpendicular to the substrate, increasing in crystal grain size to produce a white-banded vein morphology.

3. Continued eruption and precipitation of carbonates in the distal colluvium and proximal mound expand and thicken the travertine mound (Fig. 4.27c). This thickening results in waters having to migrate through the mound, preferentially along subvertical fractures and subhorizontal lithological contacts, to reach the spring vent. White-banded veins form along these pathways. Through time, the migration pathways of the fluids in the mound alternate due to fluid flow being inhibited by precipitating banded veins that decrease flow.
4. Towards the later stages of activity for the spring system, the supply of carbonate-rich waters to the spring becomes episodic, leading to unstable and alternating environmental conditions reflecting periods of spring and non-spring activity. These variable conditions result in the development of a late set of brown-banded veins characterised by numerous iron-rich laminations interspersed between thinner bands of radial aragonite crystals (Fig. 4.27d).
5. Eventually, the spring system dries up and the travertine deposit becomes inactive. Subsequent erosion can remove the deposit, though in the study area they have tended to provide a resistant cap to form a series of buttes that display cross-sectional exposures of the internal and external components of ancient deposits.

This model offers a new perspective on the formation of travertine deposits by describing the physical and geochemical evolution as well as the interaction of surface and subsurface components of the system. Though the model is derived from fault-associated travertine deposits, it is anticipated that the model could be extrapolated to describe how travertines evolve in other terrestrial, point-fed environments.

4.5.2 Origin, Timing and Quantity of CO_2 Leakage Based on Travertines

Travertines are a direct product of carbonate-rich waters leaking to the surface. Field mapping coupled with geochemical analyses of the travertines provide information on the source, timing and quantity of CO_2 that has naturally leaked to the surface along the Little Grand Wash Fault and northern fault of the Salt Wash Graben. The following discussion highlights results of this chapter that characterise these aspects of CO_2 leakage in the study area.

Present-day, carbonate-rich waters precipitating travertine in the footwalls of both faults originate from a common fluid that is the product of CO_2, generated from clay-carbonate reactions at depth, charging shallow aquifers and mixing with low-temperature meteoric waters (Heath, 2004). Isotopic comparison of active and ancient travertine deposits indicate the same fluid has effused along both faults throughout the precipitation history of the surface carbonates. Minor isotopic variations between the travertine deposits reflect the influence of multiple source rocks supplying CO_2 as well as fluctuations in the emergence temperatures of the carbonate-rich waters. Regional isotopic comparisons between travertines and other types of carbonate veins (Morrison and Parry, 1986; Breit and Meunier, 1990; Chan et al, 2000; Garden et al, 2001) indicate the natural leakage of these carbonate-rich waters is limited to the study area in the northern half of the Paradox Basin.

Radiometric dating of ancient travertine deposits from both faults indicate leakage of carbonate-rich waters has occurred for at least 7.8×10^5 years, though remnants of white-banded vein and layered mat cemented into some of the oldest deposits suggests CO_2 leakage could have started significantly earlier. Based on the assumption that travertine age is proportional to the amount of eroded material around each deposit, regional erosion rates were used in previous studies to estimate the maximum age of the deposits along both faults (190,000 to 200,000 years; Doelling, 1994). Although an overestimate, a linear relationship between travertine age and erosion was apparent in this study and gave a local erosion rate of 0.5m every thousand years (Fig. 4.26). This is significantly larger than regional erosion rates (0.15m every thousand years; Deither, 2001) and indicates the reason for the disparity in maximum travertine age between studies. The variation in local and regional erosion rates may reflect the influence of the Green River in accelerating erosion in the area, though further investigation is beyond the limits of this study. However, the

relationship between travertine age and erosion does offer a novel approach to determining the erosion rates of an area.

The distribution of travertine ages along the Little Grand Wash Fault suggest CO_2 leakage has been consistent, though the leak sites have alternated through time. This alternation of leakage along the fault probably represents the self-sealing nature of these systems with carbonate mineralization gradually clogging the feeder conduits to the leak site until the permeability is sufficiently reduced to initiate a new leak site at a different location. The clustering of travertine deposits at varied elevations in discrete areas (Crystal Geyser and Travertine 3 areas; Fig 4.1) suggest the carbonate-rich waters migration pathways do not generally alter significantly with the initiation of a new leak site. Though travertine deposits are more numerous and dispersed in the footwall of the northern fault of the Salt Wash Graben, a similar, consistent CO_2 leakage pattern is apparent with clustering of travertine deposits at varied elevations around the fold axis of the Green River Anticline. Further dating would confirm or reject this leakage pattern and allow comparison between the two faults.

Quantifying the proportion and rates of CO_2 that has leaked to the surface was approximated through the mapping and dating of travertine deposits along the Little Grand Wash Fault. Data gaps prevented calculation of these parametres for the northern fault of the Salt Wash Graben (see section 4.3.2.4). Determination and manipulation of travertine volumes indicate approximately 1.9×10^6tonnes of CO_2 have leaked to the surface along the Little Grand Wash Fault over a 7.8×10^5 year period. This translates to a CO_2 leakage rate of 24.1tonnes per year along the fault. In contrast, a contemporary study using aerometric measurements to quantify the mass of CO_2 emitted from the Crystal Geyser estimated that the geyser solely discharges approximately 12000 tonnes of CO_2 per year (Gouveia et al., 2005). This large discrepancy could be due to various factors, though the two most likely reasons are: (1) a recent increase in CO_2 emissions related to the drilling and penetration of subsurface reservoirs by the Glen Ruby well that feeds the Crystal Geyser; or (2) an overestimation of the proportion of CO_2 that is trapped in travertine deposits (10% from Shipton et al., 2005) when it leaks to the surface. Clarification of this discrepancy could be solved through high resolution dating of the active and ancient travertine deposits along the Little Grand Wash Fault. This would isolate periods and rates of CO_2 leakage associated with individual deposits, which should highlight any variations in leakage through time. Unfortunately, time constraints prevented any

further dating of the travertine deposits, though it should be continued to better constrain leakage patterns along this fault.

Assuming the leak rates from this study are correct, the impact of CO_2 leakage on the surrounding surface environment is minimal. To put the leakage into perspective, the natural CO_2 flux from a forest floor is 2 to 20μmol/m^2/s (Janssens et al., 2001; Drewitt et al., 2002), while the tree kill at Mammoth Mountain in the early 1990's had an average flux of 400μmol/m^2/s (Benson and Hepple, 2005). At a flux rate of 0.6μmol/m^2/s along the Little Grand Wash Fault, CO_2 should not pose any threat to the local ecosystem or humans. This is supported by local observations that witnessed no plant mortality around any of the leak sites. Furthermore, anecdotal evidence has reported no casualties due to CO_2 leakage, even though the area is frequented by locals and tourists (Shipton et al., 2005). However, as stated above, further dating of the travertines is needed to constrain periods of activity for each deposit, which would better constrain spatial and temporal changes to CO_2 leakage along the Little Grand Wash Fault and northern fault of the Salt Wash Graben.

4.5.3 Origin and Timing of Fault-Related Diagenesis

Preliminary investigations of fault-related diagenesis along the Little Grand Wash Fault and northern fault of the Salt Wash Graben were conducted to identify the source(s) and timing of fluids that have migrated through and subsequently altered the faulted stratigraphy. Field mapping indicated that iron-oxide reduction of the mid Jurassic sandstones was the dominant fault-related diagenetic feature along both faults, though hydrocarbon-staining and carbonate and sulphate veining were also encountered. The following discussion reviews the main aspects of each diagenetic feature resolved from this study and attempts to define the source and timing of the responsible fluid(s).

Iron-oxide reduction of mid-Jurassic sandstones in the footwalls of both faults are a product of the host sediments interacting with one or more extra-formational fluids. Petrographic investigations indicated the removal of iron oxide (haematite) rims around quartz and feldspar grains was the only diagenetic feature involved in the creation of the reduction zones. This is supported by isotopic and mineralogical data that reveal no systematic variations in carbonates or other minerals between the reduced and unreduced sediments. To remove the haematite rims, the ferric iron

(Fe^{3+}) within the haematite must be mobilised as ferrous iron (Fe^{2+}) by an iron-reducing fluid (Chan et al., 2000). Several studies on iron-oxide reduction in the region (Hansley, 1995; Chan et al., 2000; Parry et al., 2004) have reported the mobile ferrous iron is removed after being reduced and reprecipitated elsewhere as an oxide (i.e. haematite) or sulphide (i.e. pyrite), depending on the local conditions. Sites of concentrated iron oxide or sulphide precipitation were not found in the study area. Therefore, it is suggested that the iron was mobilised by an extra-formational fluid but the ferrous iron remained in-situ, being absorbed by surrounding iron-rich minerals such as dolomite or smectite.

Potential extra-formational fluids capable of reducing ferric iron include hydrocarbons, organic acids, methane and hydrogen sulphide (Surdam et al., 1993; Chan et al., 2000; Garden et al., 2001). Identifying the specific fluid responsible for iron-oxide reduction is difficult and reliant on distinguishing diagenetic features specifically related to the migrating fluid. All previous studies of iron-oxide reduction in the Paradox Basin have attributed the iron-reducing fluid to hydrocarbons (Hansley, 1995; Chan et al., 2000; Garden et al., 2001; Beitler et al., 2003; Parry et al., 2004). The presence of oil-stained sandstones in reduced sections of the Curtis Formation adjacent to the Little Grand Wash Fault indicates hydrocarbons could also be causing iron-oxide reduction in the study area. However, the absence of hydrocarbons or associated features in the more extensively reduced northern footwall of the Salt Wash Graben suggests hydrocarbons may not be the iron-reducing fluid or multiple fluids may contribute to iron-oxide reduction in the footwalls of both faults. Therefore, further petrological and geochemical investigations of iron-oxide reduction in the footwalls of both faults are needed to identify the source and timing.

If hydrocarbons were responsible for iron-oxide reduction, in addition to staining sandstones along the Little Grand Wash Fault, the most likely hydrocarbon source would be organic-rich black shales from the Pennsylvanian Paradox Formation (Nuccio and Condon, 1996). Other potential source rocks include the Pennsylvanian Honaker Trail Formation, the Permian Kaibab Limestone and the Triassic Sinbad Limestone (Peterson, 1989; Huffman et al., 1996). The timing of hydrocarbon migration in the region has been confined to the early Tertiary along the Moab Fault to the east (Garden et al., 2001) and to the mid Tertiary in the Tar Sand Triangle to the south (Hansley, 1995; Huntoon et al., 1999). The hydrocarbons that migrated along the Moab Fault have also been linked to the Paradox Formation source (Garden et al.,

2001), indicating that hydrocarbon migration in the study area probably also started in the early Tertiary. The presence of an active seep on the Little Grand Wash Fault suggests that hydrocarbon migration has continued to the present day or one or more subsequent pulses of hydrocarbons have charged the system from different sources. As such, further characterisation of hydrocarbons and hydrocarbon-related features is needed to constrain the number of hydrocarbon regimes that have migrated through this faulted system and clarify the source and timing each regime.

The final fault-related fluid flow feature in the study area, apart from travertines, is the sporadic precipitation of carbonate and sulphate veins. Field and isotopic evidence indicates the carbonate veins were precipitated from the same carbonate-rich fluids that currently precipitate travertine at the surface. In contrast, the precipitation of gypsum ($CaSO_4.2H_2O$) and celestine ($SrSO_4$) veins in the same formations required different hydrological conditions (Hanor, 2000). Gypsum commonly precipitates in fractures close to significant gypsum deposits due to dissolution, migration and reprecipitation by meteoric waters (Warren, 1999). Thick gypsum beds within the Carmel Formation, stratigraphically below the gypsum-filled fractures in the Entrada Sandstone are a probable source for the sulphates with local meteoric waters dissolving, transporting and precipitating gypsum within fractures in the overlying formation. Precipitation of celestine is more complicated, with a Sr^{2+}-rich fluid needing to mix with a SO_4^{2-}-rich fluid or replace calcium sulphate minerals (i.e. gypsum or anhydrite) in-situ (Scholle et al., 1990). The most common source of strontium is from coastal evaporite deposits (Hanor, 2000), which are locally prevalent in the Pennsylvanian Paradox and Honaker Trail Formations. As such, precipitation of celestine probably results from Pennsylvanian-derived, Sr^{2+}-rich fluids rising through the stratigraphy and mixing with shallow SO_4^2-rich meteoric waters or directly replacing gypsum precipitated in fractures.

The timing of the sulphate precipitation is speculative. Analysis of meteoric waters erupting from geysers and springs along both faults by Heath (2004) indicate the present-day waters are undersaturated in respect to sulphate. Thus, sulphate precipitation must predate the current fluid regime. Alternatively, the presence of reduction haloes around fractures infilled with sulphate suggests sulphate precipitation was during or after iron-oxide reduction as fracture pathways needed to be open to allow the migration of iron-reducing fluids. Unfortunately, uncertainty in the source and timing of iron-oxide reduction restricts placing temporal constraints on

sulphate precipitation. However, if hydrocarbons were responsible for iron-oxide reduction, sulphate precipitation commenced during or after the early Tertiary and ceased before start of the present-day meteoric conditions.

Therefore, the study area has experienced a protracted history of fault-related fluid flow along the Little Grand Wash Fault and northern fault of the Salt Wash Graben. Field evidence indicates hydrocarbons have and are migrating along the Little Grand Wash Fault with regional studies indicating migration commenced from the early Tertiary (Garden et al., 2001). Iron-oxide reduction in the footwalls of the Little Grand Wash Fault and northern fault of the Salt Wash Graben may be the result of this hydrocarbon migration, though the absence of hydrocarbons or hydrocarbon-related features in the northern footwall of the Salt Wash Graben suggests alternate or multiple fluid regimes could be responsible. Sporadic sulphate veins derived from SO_4^{2-}-rich meteoric waters (gypsum) and rising Pennsylvanian brines (celestine) were precipitated during or after iron-oxide reduction and before the start of present-day meteoric water conditions. Precipitation of subsurface carbonate veins accompanied precipitation at the surface of travertine from present-day carbonate-rich meteoric waters. Further investigations of iron-oxide reduction and hydrocarbons along both faults are needed to elucidate the sources and timing of fluids that have caused fault-related diagenesis in the study area.

4.5.4 Migration Pathways of Fluids in the Study Area

Multiple fluids have migrated through the faulted stratigraphy in the study area, directly precipitating minerals or diagenetically altering host rocks. While travertines have been the focus of this chapter due to being direct products of CO_2 leakage, consideration of all fluid flow products constrain the migration pathways of fluids through this faulted system.

Field mapping combined with isotopic analysis indicate that all travertine precipitation and diagenesis is confined to the footwalls of the Little Grand Wash Fault and northern fault of the Salt Wash Graben, at or close to the fold axis of the Green River Anticline (Fig. 4.1). One exception is the active Ten Mile Geyser travertine, which is supplied with carbonate-rich waters from an exploration well that probably penetrates the footwall at depth. Close spatial associations between the two dominant fluid flow products are evident with iron-oxide reduction commonly at or

surrounding the base of travertine deposits. Spatial associations between the diagenetic products have also been documented (see section 4.5.3). This indicates the multiple fluids responsible for travertine precipitation and diagenesis use the same shallow migration pathways through the faulted stratigraphy.

The spatial distribution of mineralization and diagenesis in varied footwall lithologies define the migration pathways of fluids in the faulted stratigraphy. In sand-rich formations (Entrada and Curtis) prevalent in the northern footwall of the Salt Wash Graben, pervasive iron-oxide reduction and numerous travertine deposits extend into the footwall around the fold axis of the Green River Anticline. This distribution is consistent with fluids migrating up-dip and pooling at the crest of the faulted anticline. Distal to this area, iron-oxide reduction and travertine precipitation is limited to the immediate footwall suggesting fracture networks developed in the damage zone of the fault play a role in the migration of fluids. This is readily evident in the clay-rich formations (Summerville and Morrison) of the Little Grand Wash Fault footwall, where travertine precipitation and diagenesis (i.e. iron-oxide reduction and hydrocarbon staining) is restricted to the immediate footwall, preferentially around structural complexities (i.e. relay zones and fault bends) where the fracture network is most intense (see section 3.3). Therefore, upon the migration of fluids to the crest of the fault anticline, fluids vertically migrate through low-porosity, clay-rich units by utilising the fracture network developed in the damage zone of the fault. This localisation of flow in fracture networks associated with the damage zone is well documented (Kerrich, 1986; Caine et al., 1996; Sibson, 1996; Curewitz and Karson, 1997; Gudmundsson et al., 2001) and reiterates the risks of fluid leakage involved with fault-sealed systems.

Based on the field relationships, a conceptual model of fluid migration through the faulted stratigraphy can be established (see Fig. 6.1). A fluid will initially charge and diffuse through a sand-rich carrier bed, migrating up-dip to pool in the structural high created by the faulted, north-plunging Green River Anticline. The fault forms an effective lateral seal, while overlying clay-rich cap rocks provide a transient top seal. Fractures formed as part of the damage zone to the fault comprise the sealing integrity of this top seal and enable vertical migration of fluids, preferentially around structurally complexities where the fracture network is most intense. The fluids subsequently charge a shallower sand-rich carrier bed and the process continues through the faulted sequence. The dependence of folding and fault-associated fracture

permeability is paramount in controlling fluid flow in the study area and emphasizes the influence structure plays on the migration of fluids in sedimentary basins.

4.6 Conclusions

Field mapping illustrates that fault-related mineralization and diagenesis from fluid flow is restricted to the immediate footwalls of the Little Grand Wash Fault and northern fault of the Salt Wash Graben around the fold axis of the faulted Green River Anticline. Investigations have focussed on the travertines, as they are the direct products of CO_2 leakage at the surface along both faults. Field and petrological observations indicate travertine deposits have four distinct lithofacies, which are: (1) a cemented, colluvium conglomerate that forms a relatively impermeable, basal substrate; (2) layered carbonate mats that develop terrace mounds on top of the conglomerates; (3) sub-surface, white-banded veins that crosscut buried sections of the two surface lithofacies and represent the primary migration pathways of supersaturated waters through the deposit to the effusion vent; and (4) a later set of brown-banded veins that crosscut all lithofacies to represent the migration pathways of supersaturated waters through the deposit associated with the terminal stages of spring activity for the travertine deposit.

Field observations coupled with geochemical analyses indicate the travertines are precipitated from carbonate-rich waters that erupt from geysers and springs and are sourced from deep crustal CO_2 mixing with shallow meteoric waters. The carbonate-rich waters have remained isotopically stable for at least a 7.8×10^5 year period of travertine precipitation apart from minor variations related to the influence multiple source rocks supplying CO_2 and fluctuations in emergence temperatures of the erupting waters. Estimates on leakage indicate approximately 1×10^6tonnes of CO_2 have leaked to the surface over the last 7.8×10^5 years to give an average flux of $0.6 \mu mol/m^2/s$. This flux rate combined with personal observations and anecdotal evidence suggest CO_2 leakage has not caused any adverse effects to the local ecosystem or humans.

Additional fault-associated fluid flow in the footwalls of both faults was identified by the presence of hydrocarbon staining, iron-oxide reduction and sulphate and carbonate veins. Hydrocarbon stained sandstones close to or between fault strands of the Little Grand Wash Fault suggest hydrocarbon migration along this fault from

the early Tertiary to present. Iron-oxide reduction prevalent in the footwalls of both faults may be related to this hydrocarbon migration or a separate, yet-to-be identified fluid. Sulphate veins accompanied or followed iron-oxide reduction and precipitated from sulphate-rich meteoric waters (gypsum) or rising Pennsylvanian-source brines (celestine). Carbonate veins were precipitated from the same carbonate-rich fluids that precipitated the travertines at the surface.

Spatial associations between the fault-related mineralization and diagenetic features suggest all the fluids used the same migration pathways through the faulted stratigraphy. In sand-rich carrier beds, fluids would migrate up-dip and pool in structural highs created by the faulting of the Green River Anticline. The faults would form a lateral seal and fluids would vertically migrate through overlying low-porosity lithologies via fracture networks developed by the damage zone of the fault in the immediate footwall. This process is repeated to enable the vertical migration of fluids through the faulted stratigraphic sequence.

Future work identified from this chapter include the further dating of travertine deposits to better characterise temporal and spatial variations in CO_2 leakage along both faults and more importantly constrain the CO_2 flux along the Little Grand Wash Fault. In addition, a detailed paradiagenetic investigation focussing on iron-oxide reduction should be performed to isolate the fluid(s) responsible for fault-related diagenesis of sandstones in the footwalls of both faults.

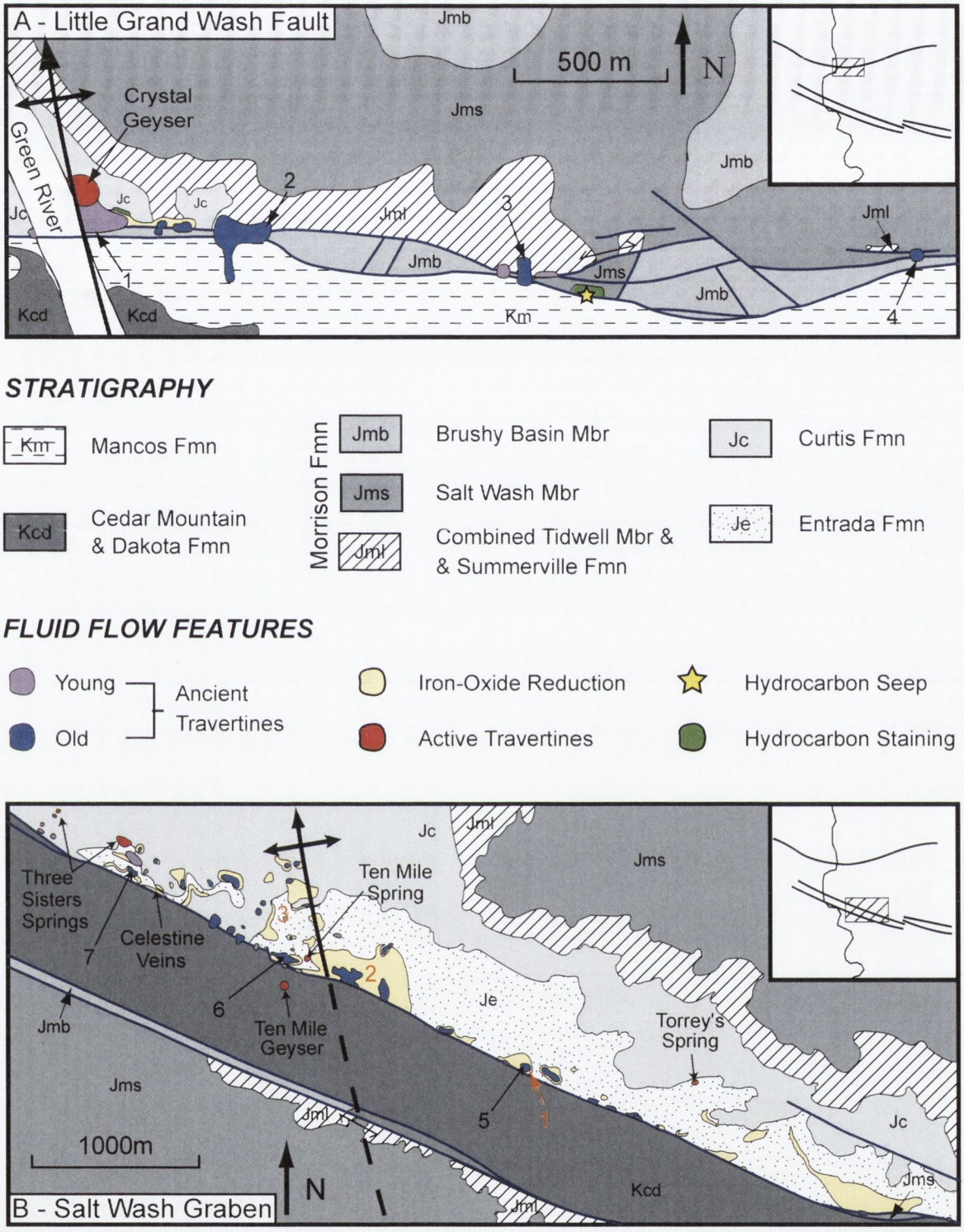


Figure 4.1: Distribution of fault-related mineralization (travertines) and diagenesis (iron-oxide reduction, hydrocarbon staining) along the (a) Little Grand Wash Fault and (b) Salt Wash Graben (stratigraphic basemap from Doelling, 2001). Insets show the relative location of the maps along each fault. Black numbers and arrows indicate travertines sampled for geochemical analyses. Orange numbers indicate the position of the iron-oxide reduction transects.

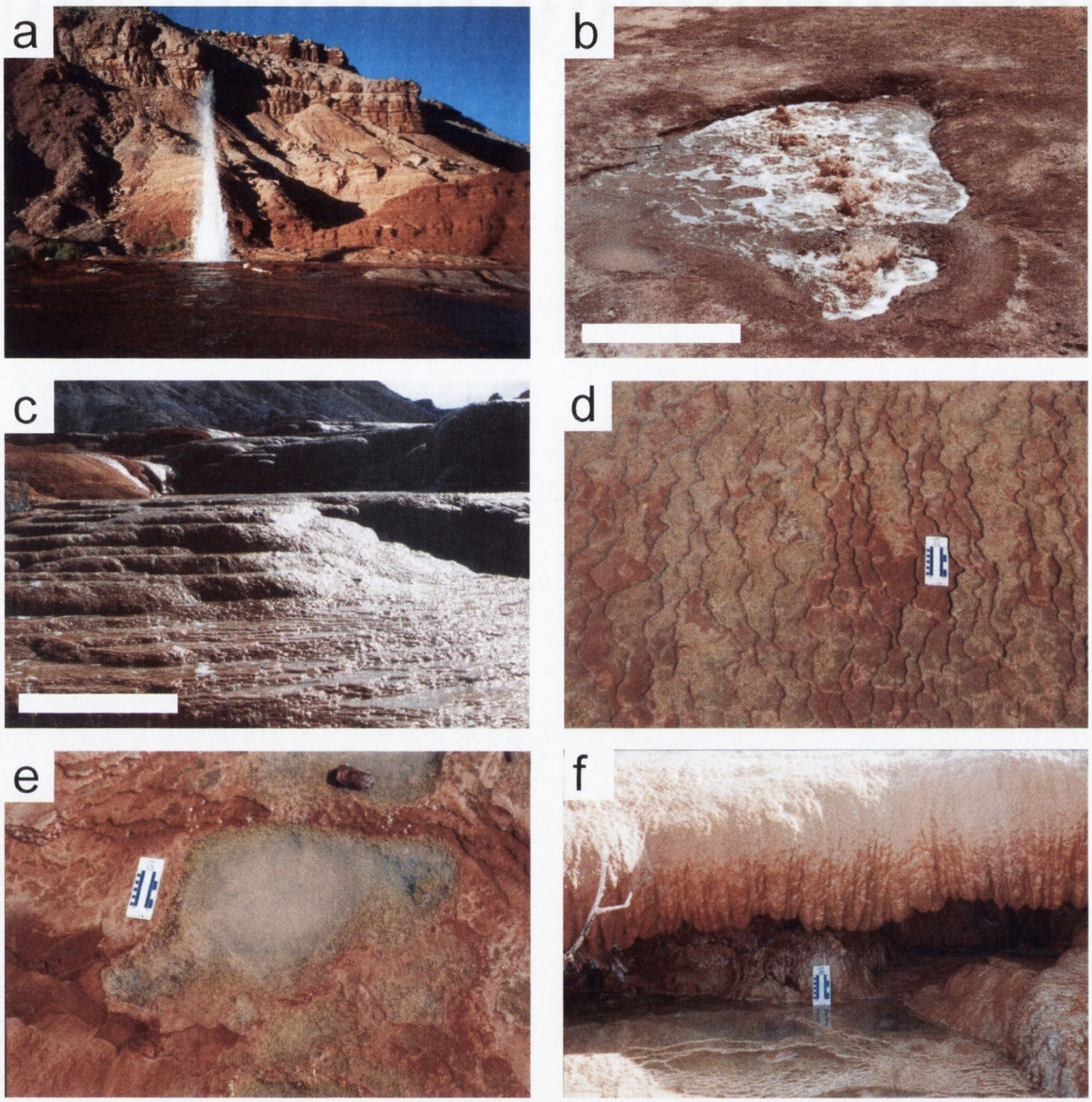


Figure 4.2: Field photographs of active Crystal Geyser travertine mound. Scale card is 15cm long (d-f). (a) Eruption of the Crystal Geyser onto travertine mound, looking north. Erupting waters reach heights of 20m. (b) One of two springs located approximately 20 m north of Crystal Geyser vent. The scale bar is 2 m long. (c) Downstepping lobate mounds that radiate out from geyser vent. The scale bar is 3 m long. (d) Plan view of the hemispherical pools that form the terrace morphology on travertine surface. (e) Algae occupying the deeper hemispherical pools (to the right of the scale card) that retain water for longer periods. (f) Conically shaped speleothems on sub-vertical surfaces of the mound.

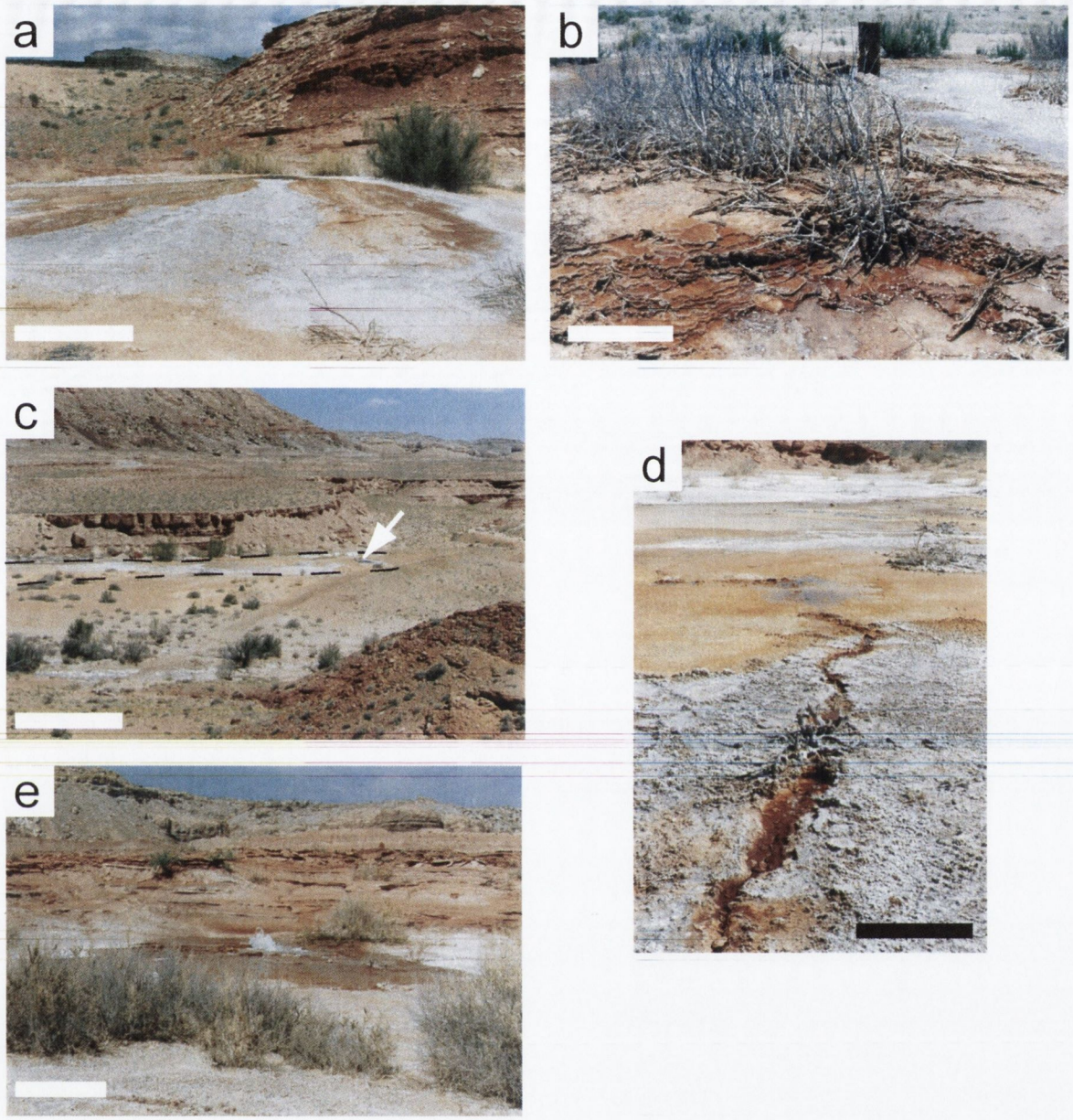


Figure 4.3: Field photographs of active travertines along the northern fault of the Salt Wash Graben. See figure 4.1 for location of travertines. (a) Low travertine mound surrounding the central Torrey's spring looking northwest. Scale bar is 1m. (b) Ten Mile Geyser with remaining well casing and surrounding travertine. Scale bar is 1m. (c) Big Bubbling Spring looking to the north. Dashed black lines indicate extent of travertine with white arrow showing brine pool. Scale bar is 10m. (d) Fracture controlled Small Bubbling spring (north) with surrounding travertine partially covered with salt crust. Scale bar is 1m. (e) Eruption of the Small Bubbling spring (south) onto a low travertine mound looking north. Scale bar is 2m.

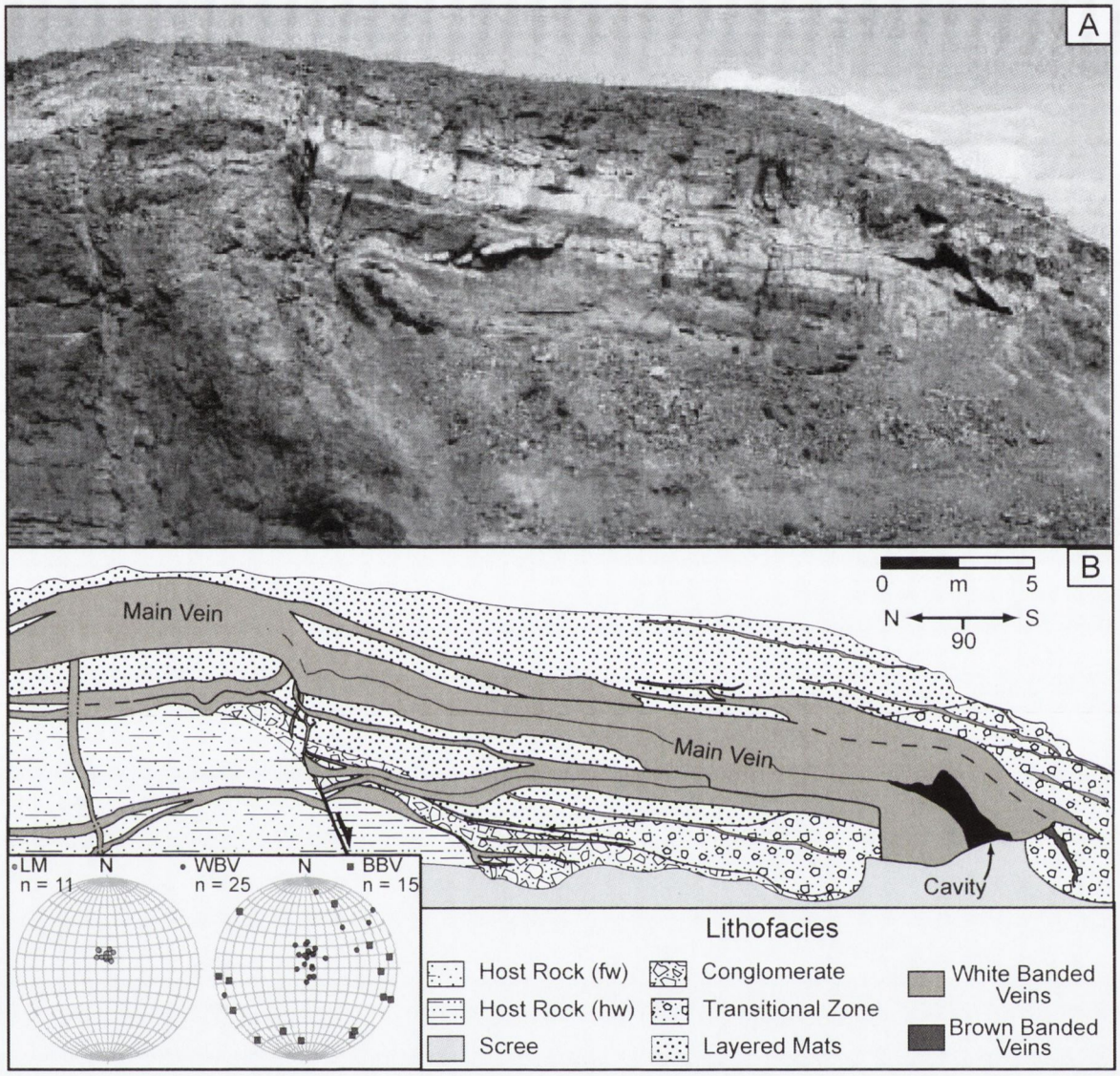


Figure 4.4: (a) Field photograph of best-exposed ancient travertine deposit (Travertine 2) in the field area. See figure 4.1 for location of deposit. (b) Annotated section of outcrop displaying the distribution of lithofacies and south-dipping normal fault. Transitional zone consists of layered mats interbedded with cemented conglomerates. Equal-area stereoplots contain poles to layered mats (LM), white-banded veins (WBV), and brown-banded veins (BBV). The layered mats and white-banded veins are predominantly sub-horizontal, while brown-banded veins are steeply dipping and form a radial pattern about the paleo-vent.

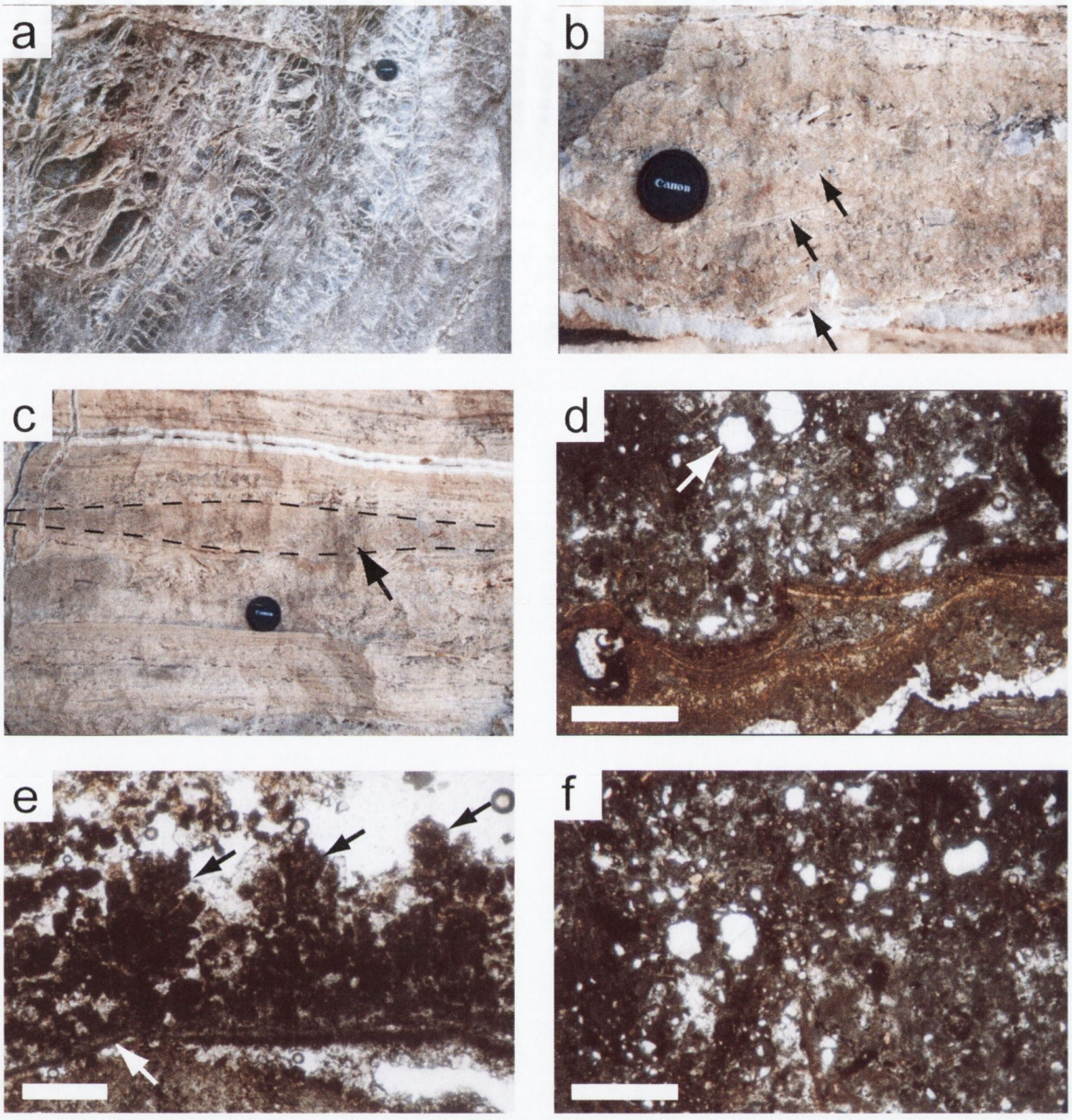


Figure 4.5: Field photographs and photomicrographs of ancient travertine 2 on the Little Grand Wash fault. (a) Boxwork veins in a clay-rich siltstone beneath the ancient travertine deposit (lens cap is 8 cm in diameter). (b) Conglomerate with imbricated clasts (black arrows) crosscut by a white-banded vein towards the base of the photograph. (c) Layered carbonate mats with a small lens of cross-bedded sediment (black arrow) crosscut by thin white-banded vein. (d) Thin section view of layered mat with rim and pool morphology, overlain by a micritic layer containing detrital quartz grains (white arrow). Scale bar is 5 mm. (e) Basal substrate (white arrow) overgrown with shrub-like dendritic precipitates. Micritic rims obscure the precipitates and give a mottled appearance (black arrows). Scale bar is 2 mm. (f) Dense micritic layer containing large proportions of detrital quartz grains. Scale bar is 5 mm.

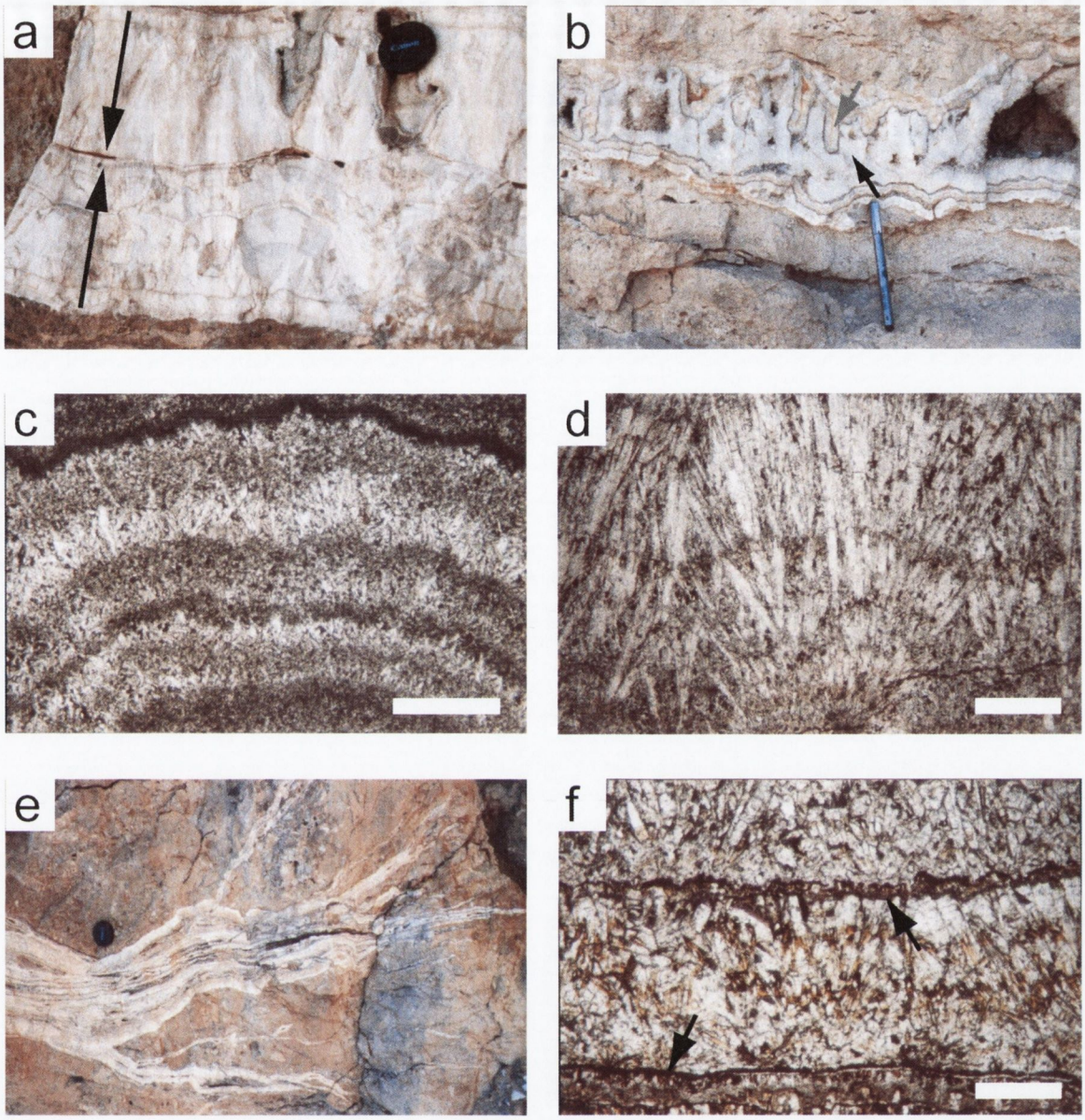


Figure 4.6: Field photographs and photomicrographs of banded veins from ancient travertine 2 on the Little Grand Wash fault. (a) White-banded vein with aragonite bands that radiate towards a central cavity (lenses cap is 8 cm in diameter). Black arrows indicate direction of growth for the vein. (b) Speleothems (grey arrow) infilling the cavity of a white-banded vein. An outer rim of white-banded vein material (black arrow) encapsulates the speleothems (pen is 14 cm long). (c) Multiple bands of radiating columnar to acicular aragonite crystals in white-banded vein. Scale bar is 5 mm. (d) Single aragonite band with acicular crystals that form radial fans with compromise boundaries. Scale bar is 2 mm. (e) Brown-banded vein crosscut the conglomerate lithofacies (lenses cap is 8 cm in diameter). (f) Brown-banded vein with dark-colored laminations (black arrows) that terminated growth of the underlying aragonite crystals. Scale bar is 2 mm.

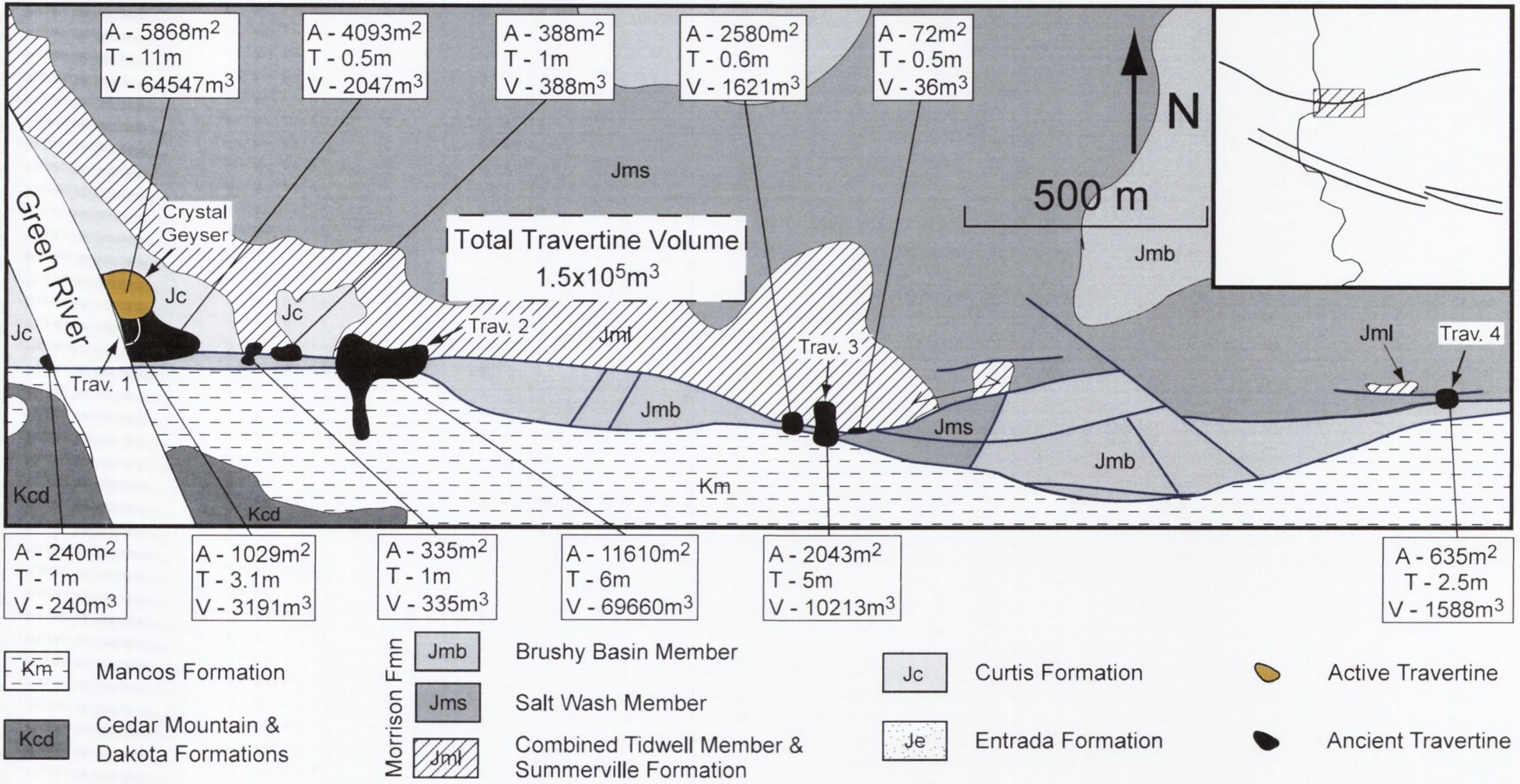


Figure 4.7: Estimated thicknesses (T), areas (A) and volumes (V) of travertines in the footwall of the Little Grand Wash Fault. Values calculated from field mapping with the thickness of the active Crystal Geyser travertine taken from Glen Ruby #1-X well (McKnight, 1940). Inset shows relative location along the fault.

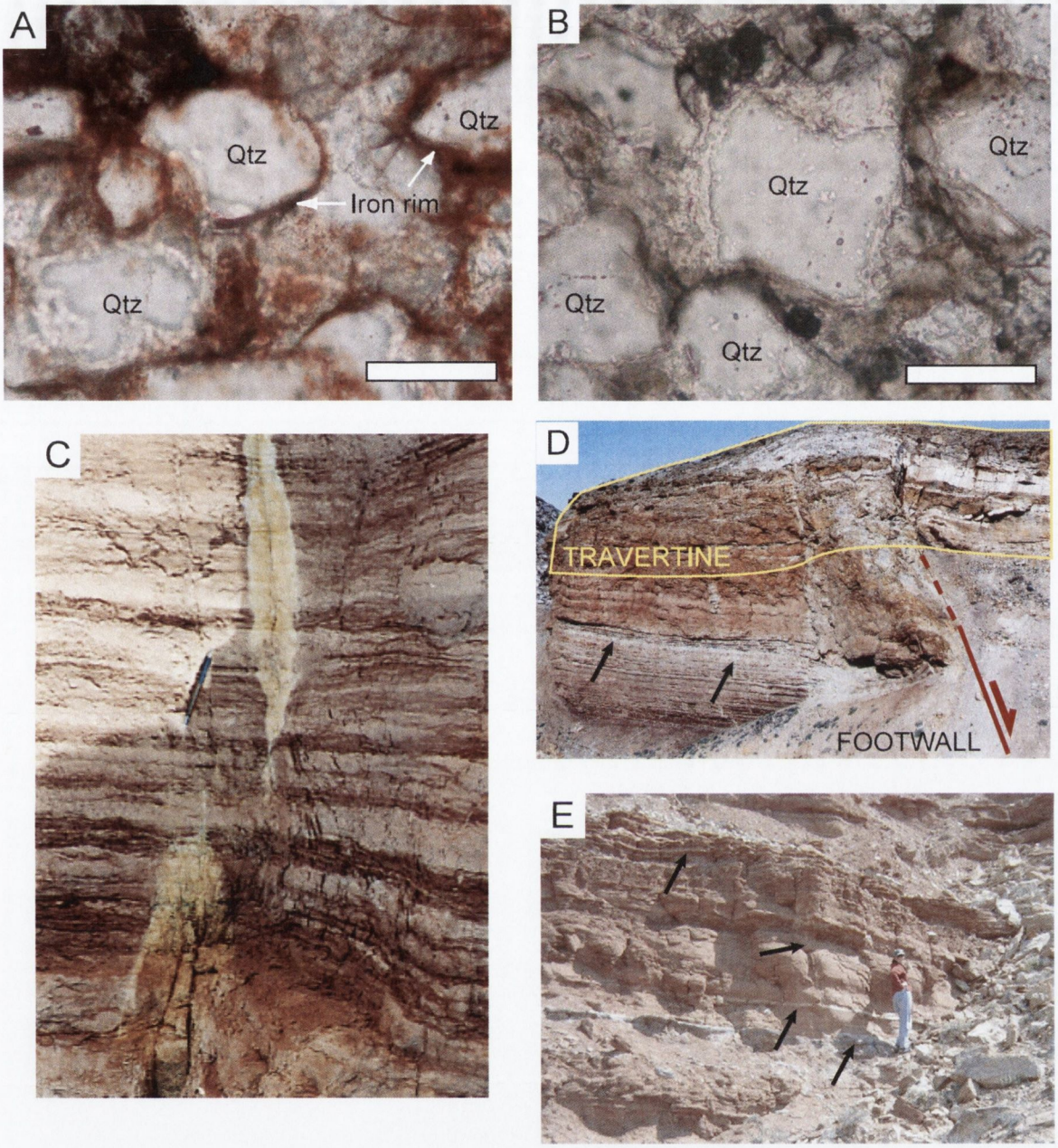


Figure 4.8: Aspects of iron-oxide reduction along the Little Grand Wash Fault. (a) Photomicrograph of Curtis Sandstone with quartz (Qtz) grains rimmed by haematite. Scale bar is 0.5mm. (b) Photomicrograph of haematite rims removed from quartz (Qtz) grains. Scale bar is 0.5mm. (c) Reduction haloes surrounding sub-vertical fractures in the Curtis Formation (pen is 15cm long). (d) Tabular reduction bodies (black arrows) extending into the Curtis Formation footwall. Yellow outline shows extent of overlying travertine deposit; red line indicates location and direction of the fault. (e) Sporadic reduction horizons within the Curtis sandstone above the zone of complete reduction.

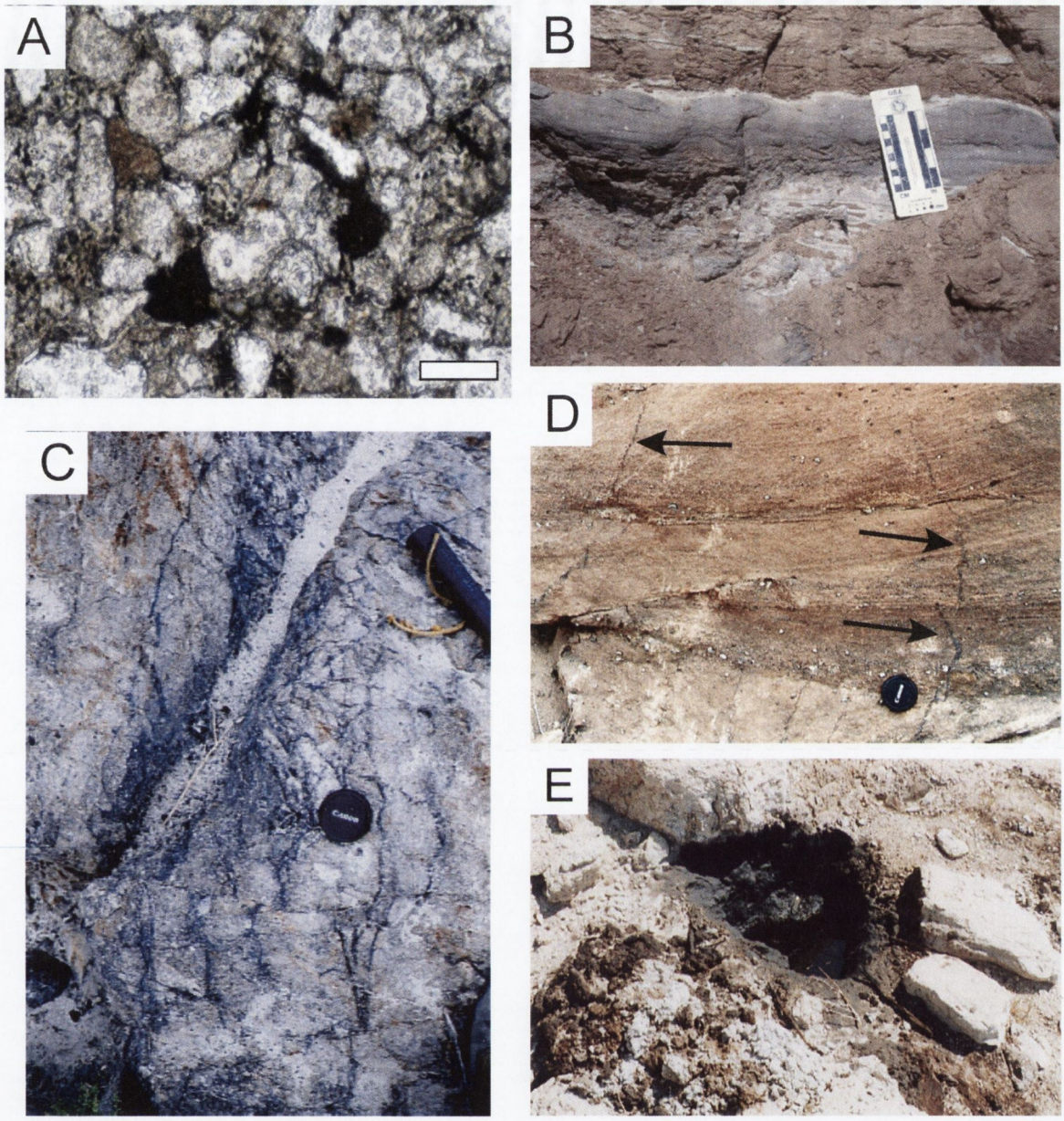


Figure 4.9: Aspects of hydrocarbon staining along the Little Grand Wash fault. (a) Photomicrograph of spherical oil globules interspersed around grains and within the matrix of the Curtis sandstone. Scale bar is 1mm. (b) Hydrocarbon-stained Curtis sandstone with a thin white reduction halo (scale card is 16cm long). (c) Hydrocarbon-stained Salt Wash sandstone with bitumen veining (black arrows). Distinct petroleum odor when rocks freshly broken (lens cap is 8cm in diameter). (d) Numerous fractures with a distinct hydrocarbon stain (lens cap is 8cm in diameter). (e) Fresh oil seep at the base of the hydrocarbon-saturated Salt Wash sandstones. The width of the shallow pit is approximately 20cm.

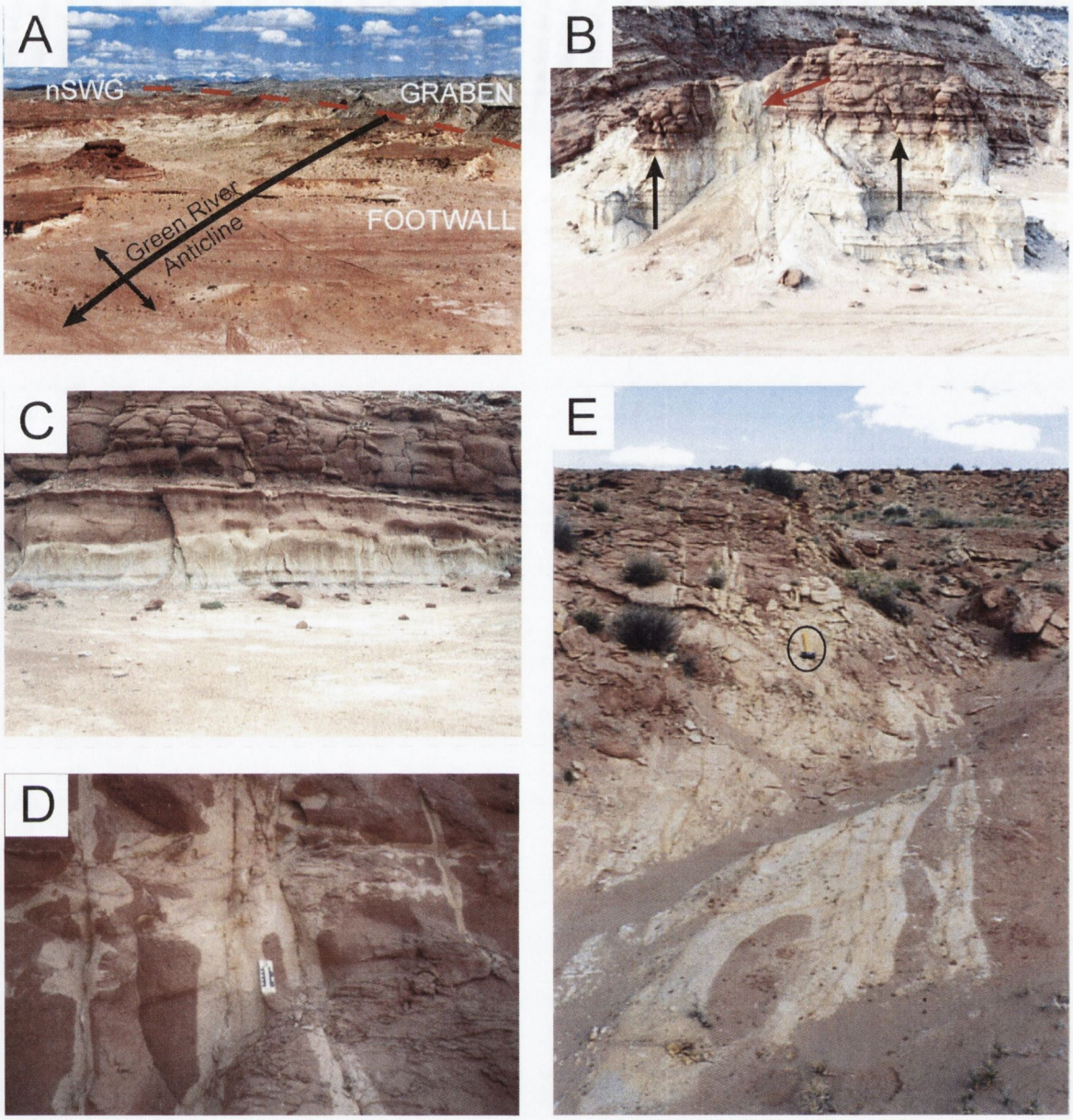


Figure 4.10: Field photographs of iron-oxide reduction within the footwall of the northern fault of the Salt Wash graben. (a) View of the reduced, yellow Entrada sandstones in the core of the Green River anticline facing east. Away from the anticline, sandstones revert back to a red colour. Trace of the fault (nSWG) marked with a dashed line. (b) Entrada sandstone butte with lower half completely reduced and upper half only reduced around a fracture cluster (red arrow). Note reduction is not bed confined with a varying upper contact (cf. black arrows). Height of butte approximately 18m. (c) Undulating reduction front in Entrada sandstone. (d) Reduction haloes surrounding fractures in Entrada sandstone at the base of a travertine deposit (scale card is 16cm long). (e) Reduction haloes surrounding fractures further away from the fault in Curtis sandstone (hammer circled for scale).

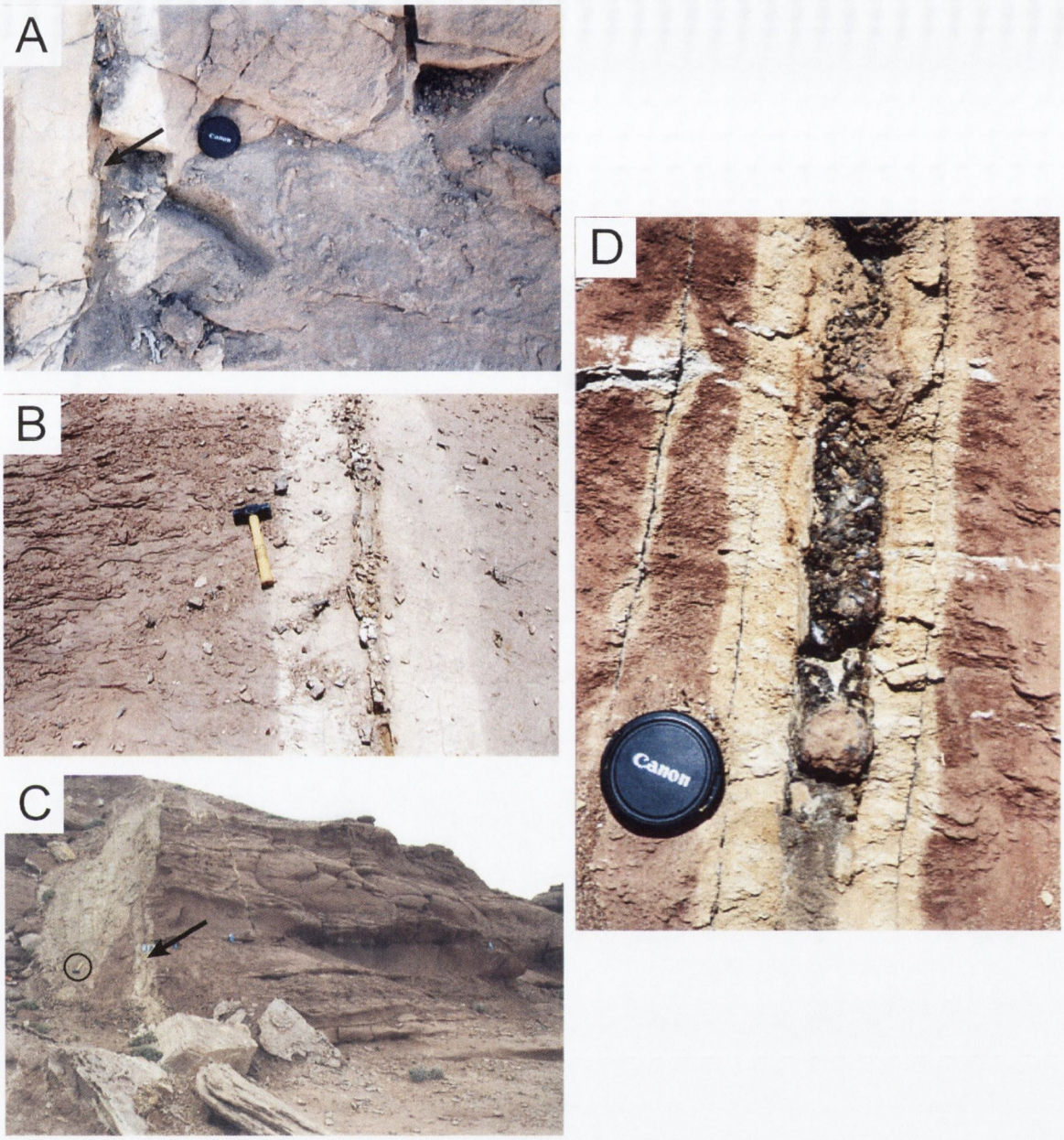


Figure 4.11: Field photographs of fractures surrounded by reduction haloes and infilled with either aragonite (a; lens cap is 8cm in diameter), gypsum (b-c; hammer is 45cm long) or celestine (d; lens cap is 8cm in diameter). Black arrows show location of fracture infill. Samples were collected from a, b and c for petrographical and geochemical analysis and correspond with transects 1, 2 and 3. See figure 4.1 for location of transects and celestine veins.

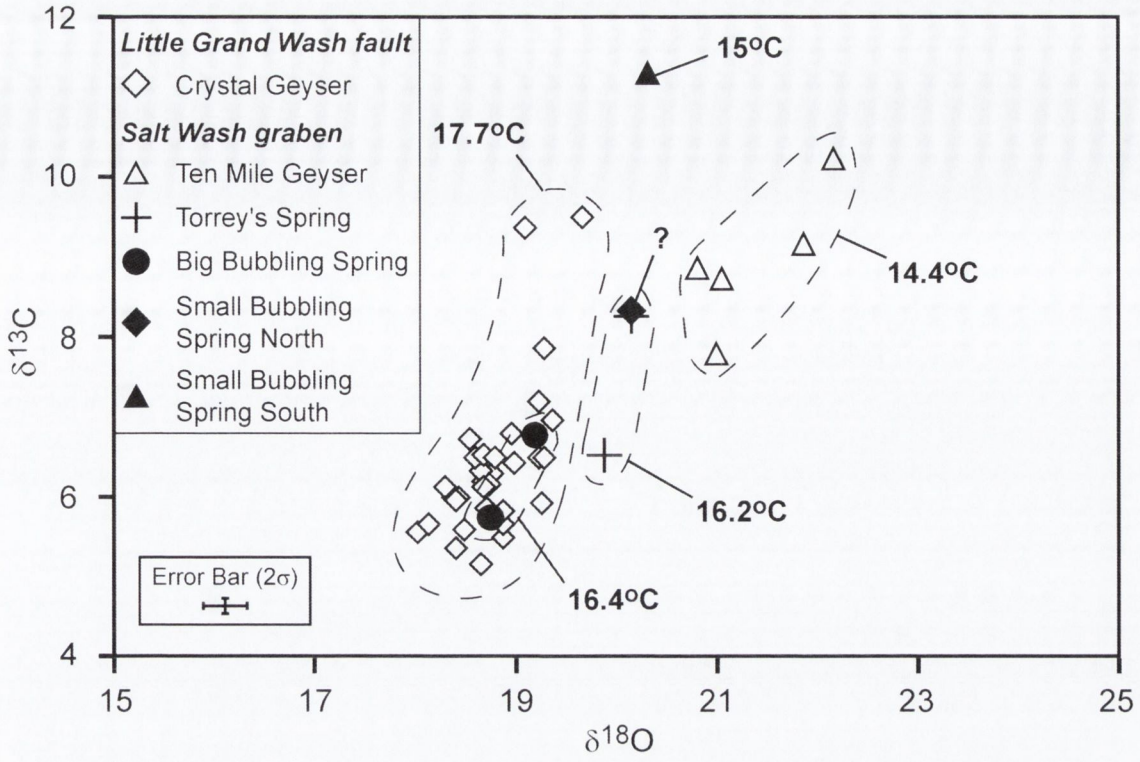


Figure 4.12: Isotopic composition of active travertines from the Little Grand Wash Fault and northern fault of the Salt Wash Graben. Dashed lines define the active deposits. Emergence temperatures of the carbonate-rich waters at each active effusion (except Small Bubbling Spring South) are from Heath (2004).

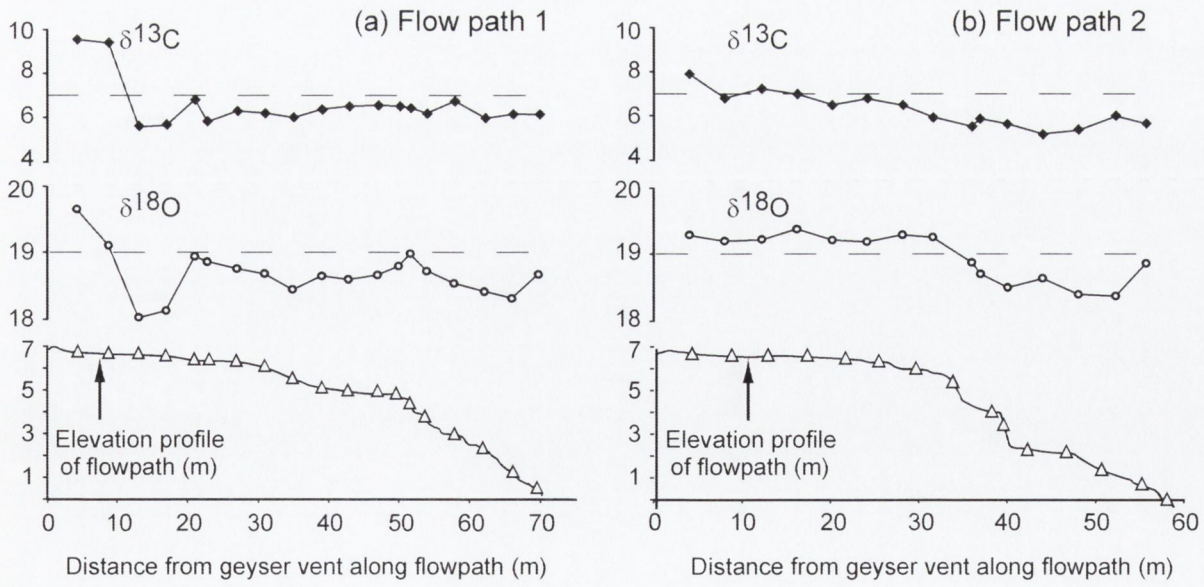


Figure 4.13: Variation in carbon and oxygen isotopes relative to topography and distance from Crystal Geyser vent along two separate flow paths.

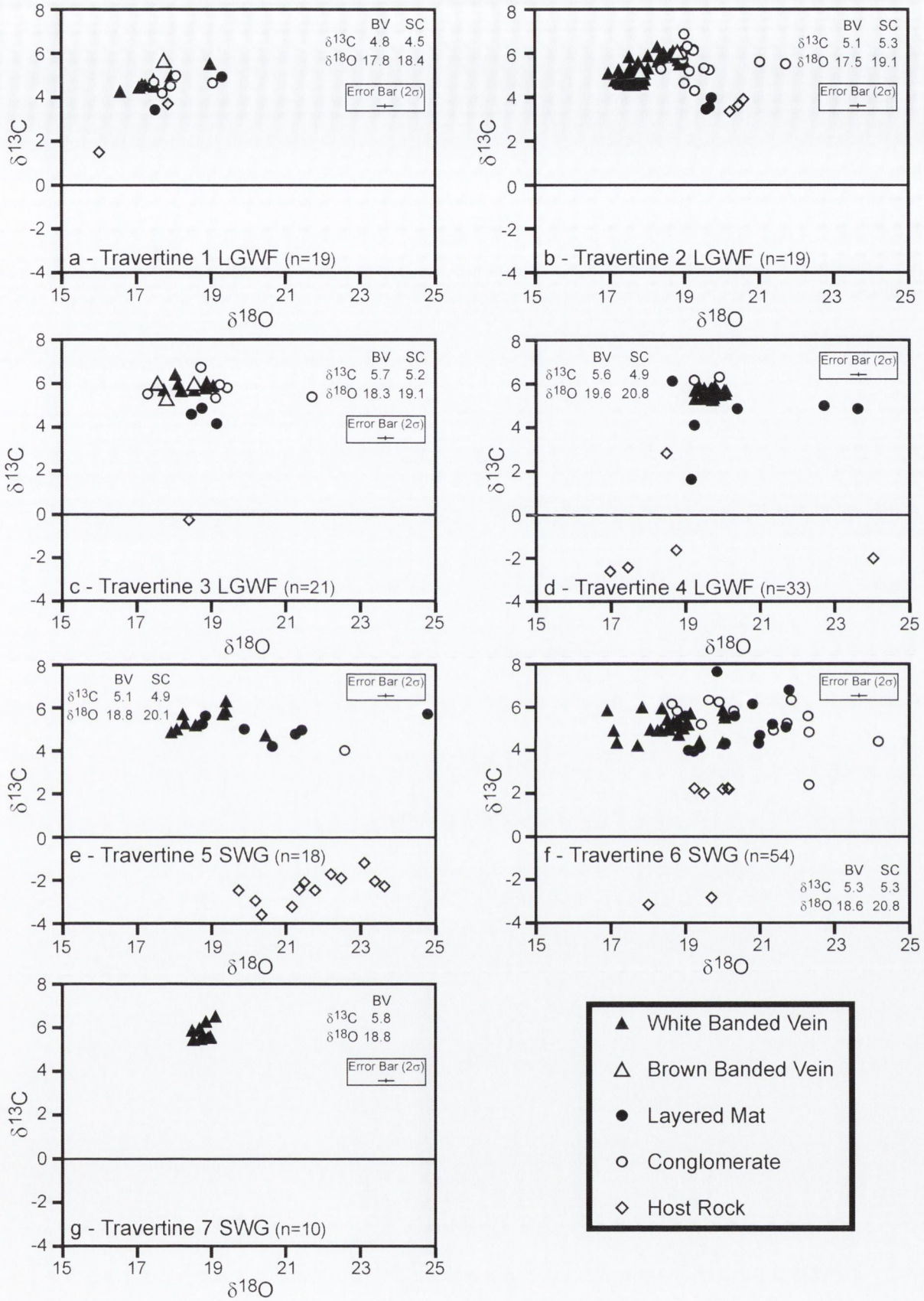


Figure 4.14: Isotopic composition of the differing lithofacies within each ancient travertine deposit. The average $\delta^{13}C$ and $\delta^{18}O$ values of the subsurface banded veins (BV) and surface layered mats and conglomerate cements (SC) are indicated for each deposit. n is the number of samples per deposit. See figure 4.1 for locations of the deposits.

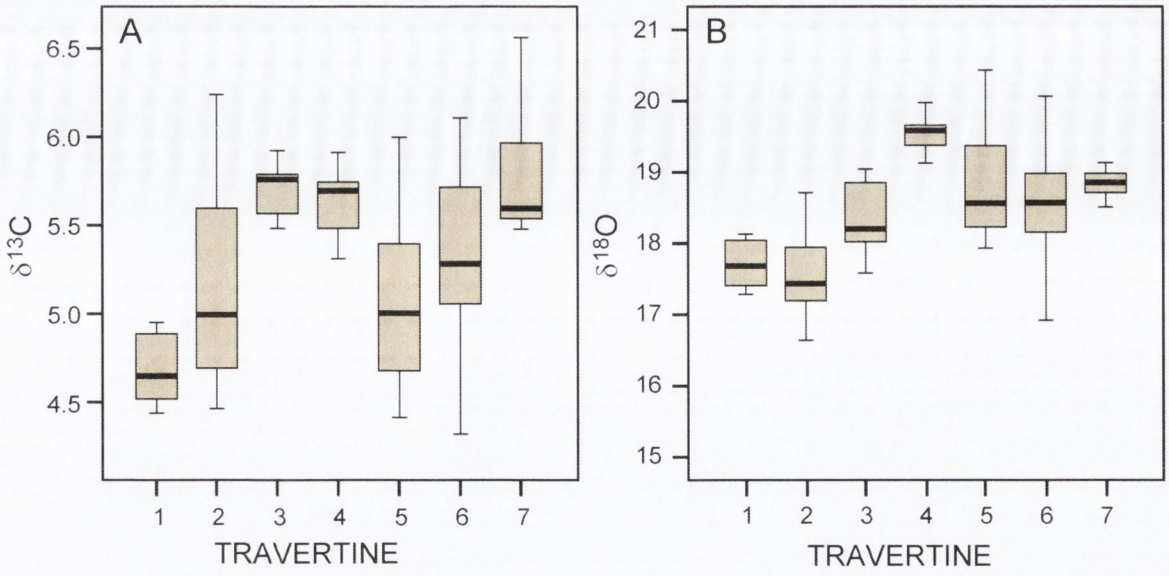


Figure 4.15: Box plots of carbon (a) and oxygen (b) isotopes showing the median, quartiles and extreme values of banded veins for each travertine deposit. See figure 4.1 for locations of travertines.

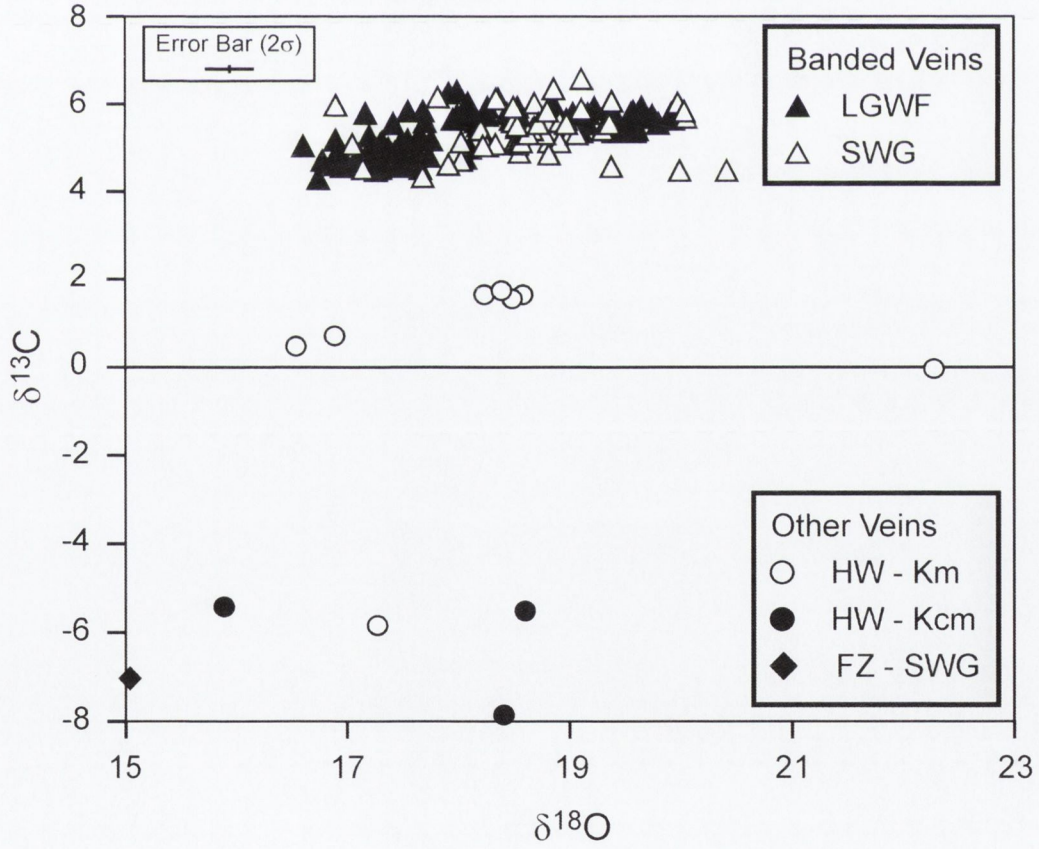


Figure 4.16: Isotopic comparison of banded veins from ancient travertines with carbonate veins from within the northern fault of the Salt Wash Graben (FZ-SWG), and south of the Little Grand Wash Fault (HW-Km) and northern fault of the Salt Wash Graben (HW-Kcm).

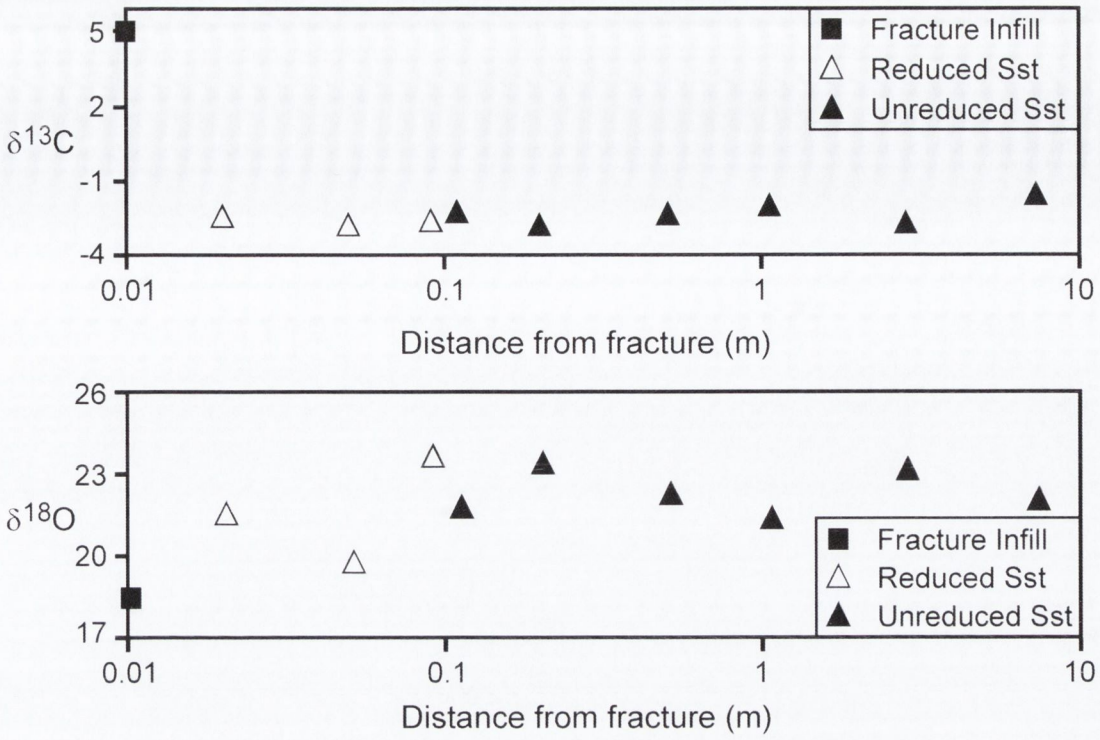


Figure 4.17: Variation in carbon and oxygen isotopes between an aragonite vein infilling a fracture and carbonate cements from reduced and unreduced Entrada sandstones surrounding the fracture. Samples taken from transect 1. See Fig. 4.1 for location of transect.

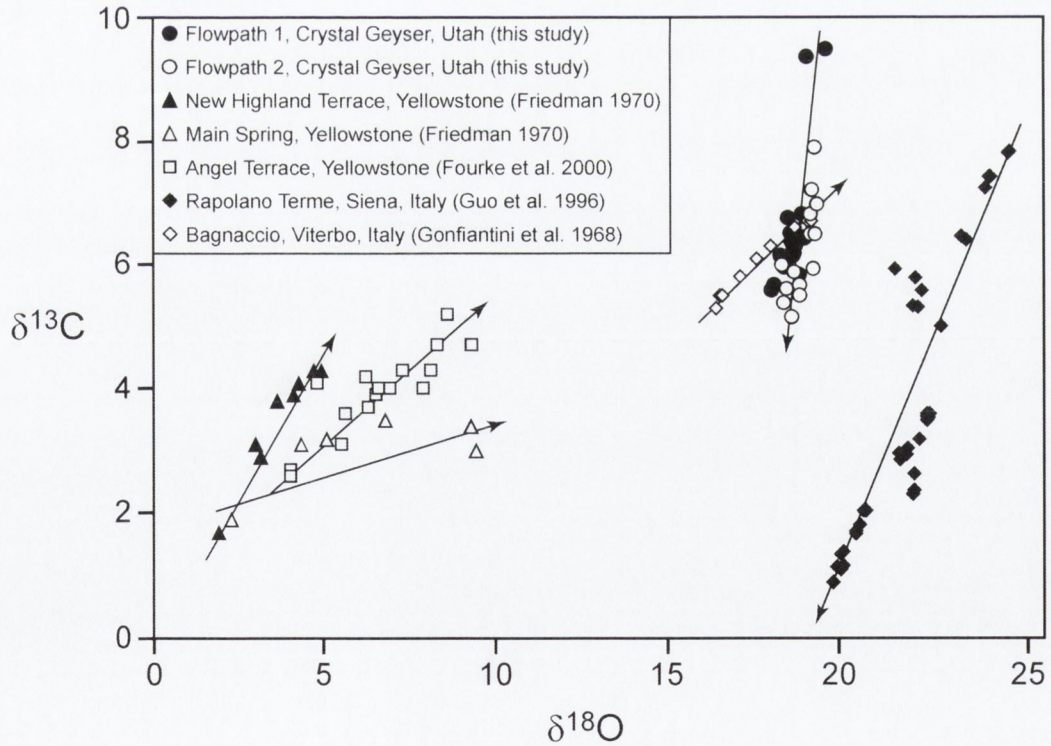


Figure 4.18: Isotopic comparison of spring-fed travertine deposits from several localities around the world. Lines with arrows indicate isotopic trends of travertine progressively downstream from spring vent. The positive trends are attributed to CO_2 degassing, evaporation, and decrease in temperature, while negative trends are attributed to fractionation dominated by microbial activity.

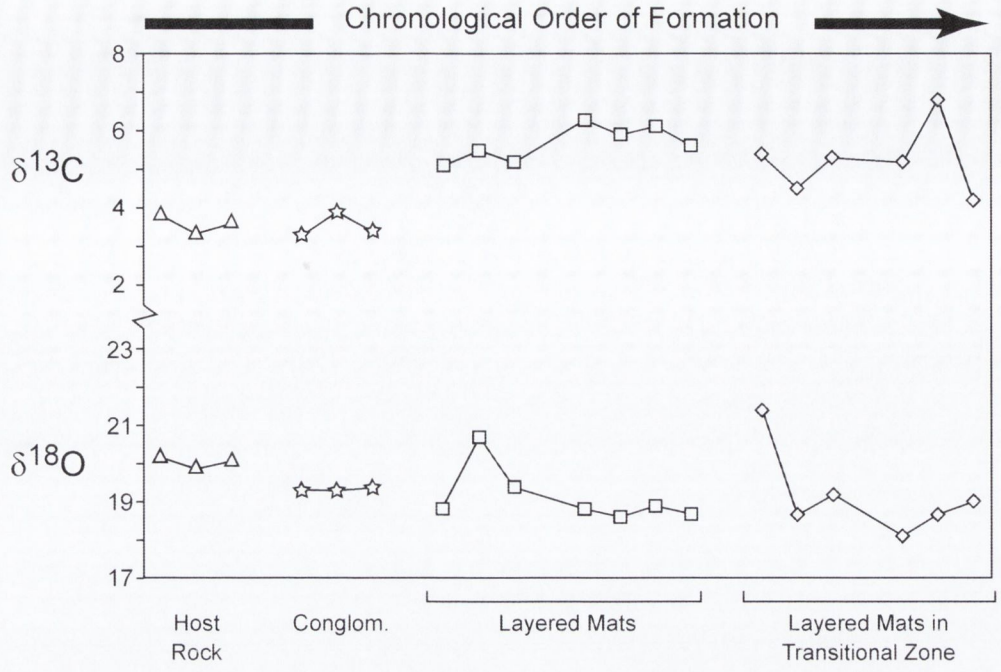


Figure 4.19: Isotopic variability of ancient travertine surface lithofacies and altered host rock relative to order of deposition. Surface lithofacies display variability in $\delta^{13}C$ and stability in $\delta^{18}O$. Refer to figure 4.4 for sample locations.

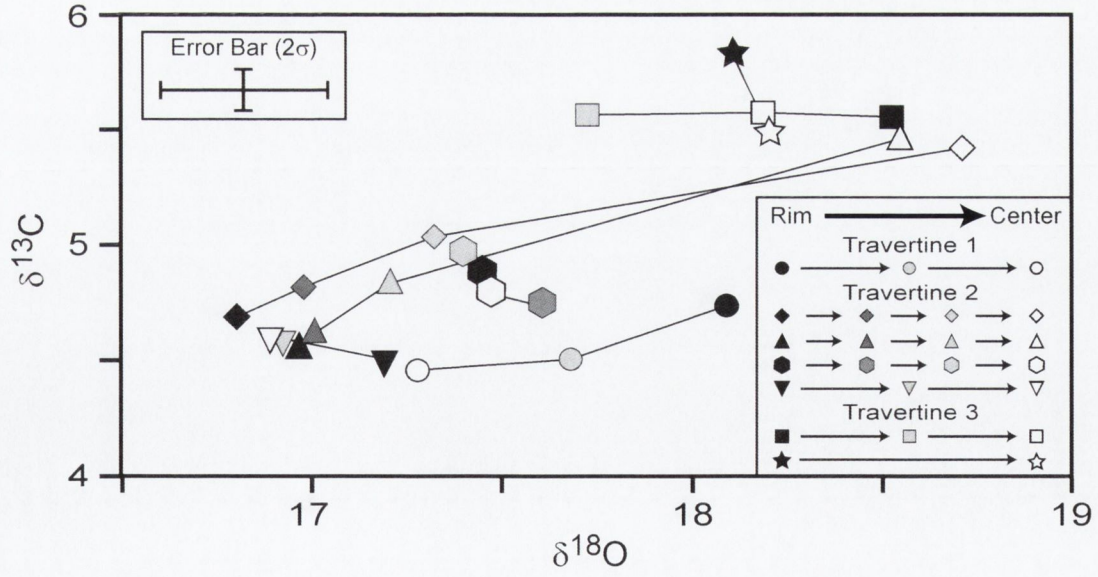


Figure 4.20: Variations in isotopic trends of white-banded veins from vein rim to centre. Positive (travertine 2), negative (travertine 1) and relatively constant (travertines 2 and 3) covariant trends are observed between ancient travertines. See figure 4.1 for locations of travertines.

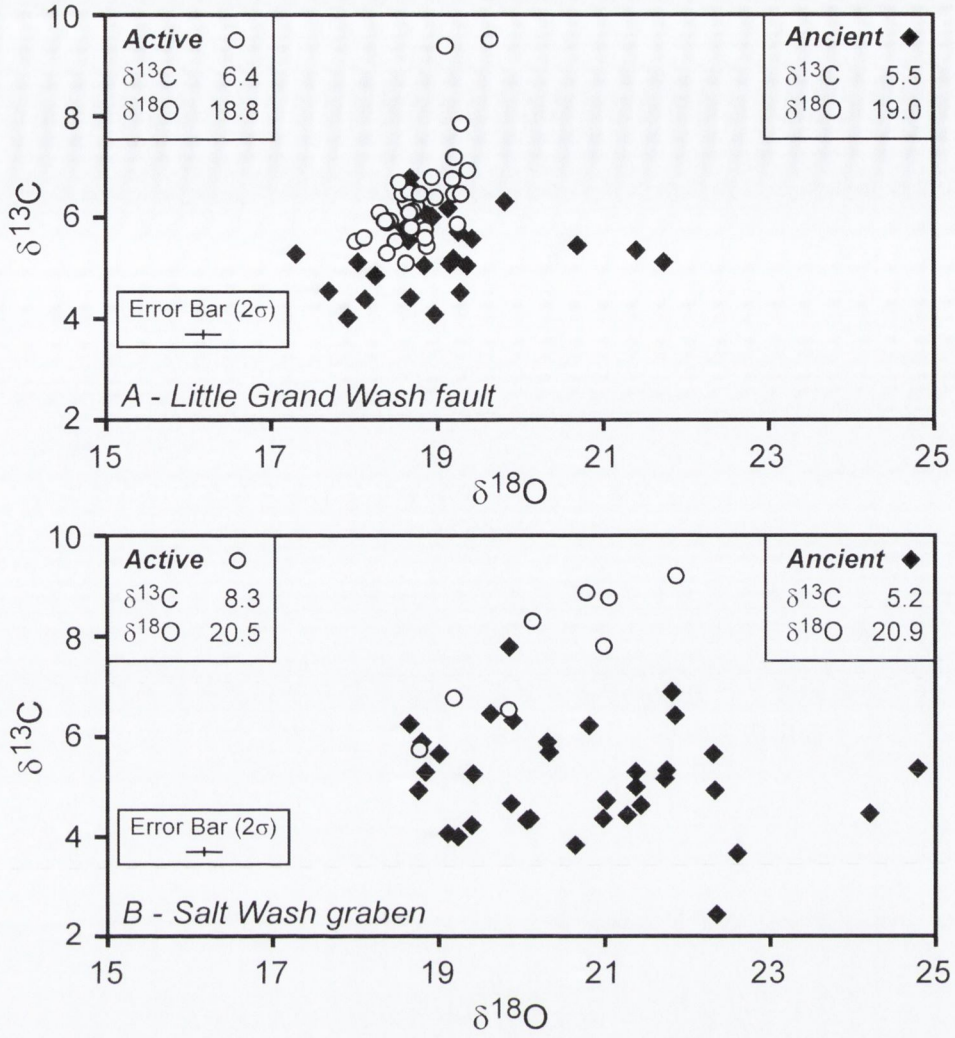


Figure 4.21: $\delta^{13}C$ and $\delta^{18}O$ comparisons between layered mats from ancient deposits and active travertine along the (a) Little Grand Wash fault and (b) northern fault of the Salt Wash graben. Mean $\delta^{13}C$ and $\delta^{18}O$ values for the ancient and active surface precipitates are shown in charts.

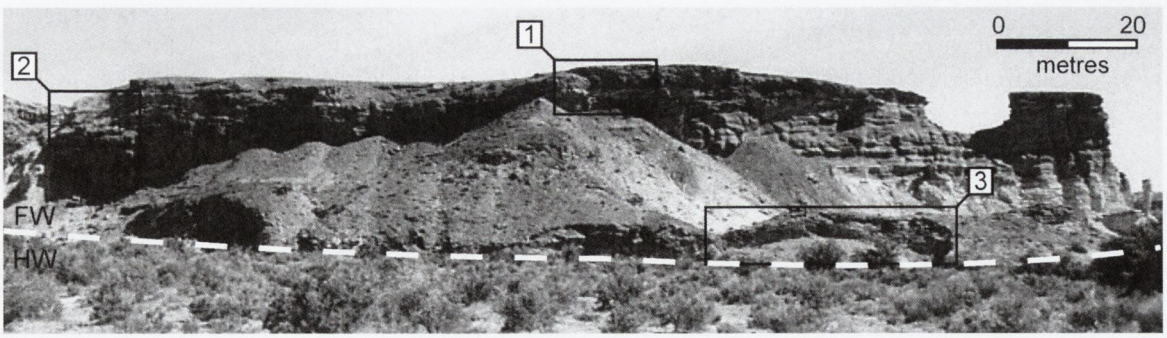


Figure 4.22: Sampling areas of ancient travertine on Ten Mile butte (Travertine 6) looking north across the northern fault of the Salt Wash graben. Dashed line indicates position of fault with an Entrada footwall (FW) and a Cedar Mountain hanging wall (HW). See figure 4.1 for location of Travertine 6.

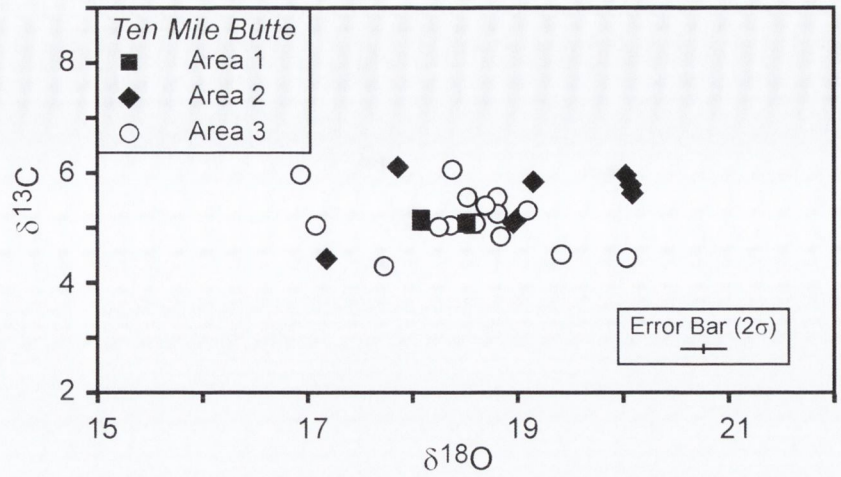


Figure 4.23: Isotopic comparison of white-banded veins from three separate travertine deposits at Ten Mile butte (Travertine 6). See figure 4.22 for position of deposits.

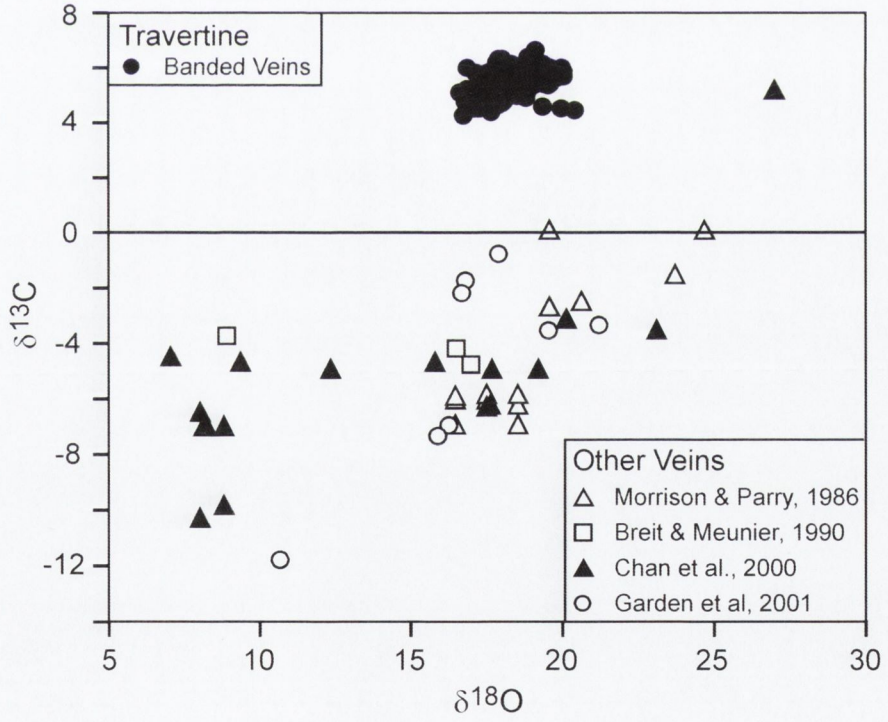


Figure 4.24: Isotopic comparison of banded veins from ancient travertines with carbonate veins from several localities in the northern half of the Paradox basin. The banded veins are isotopically distinct from all other veins in the region.

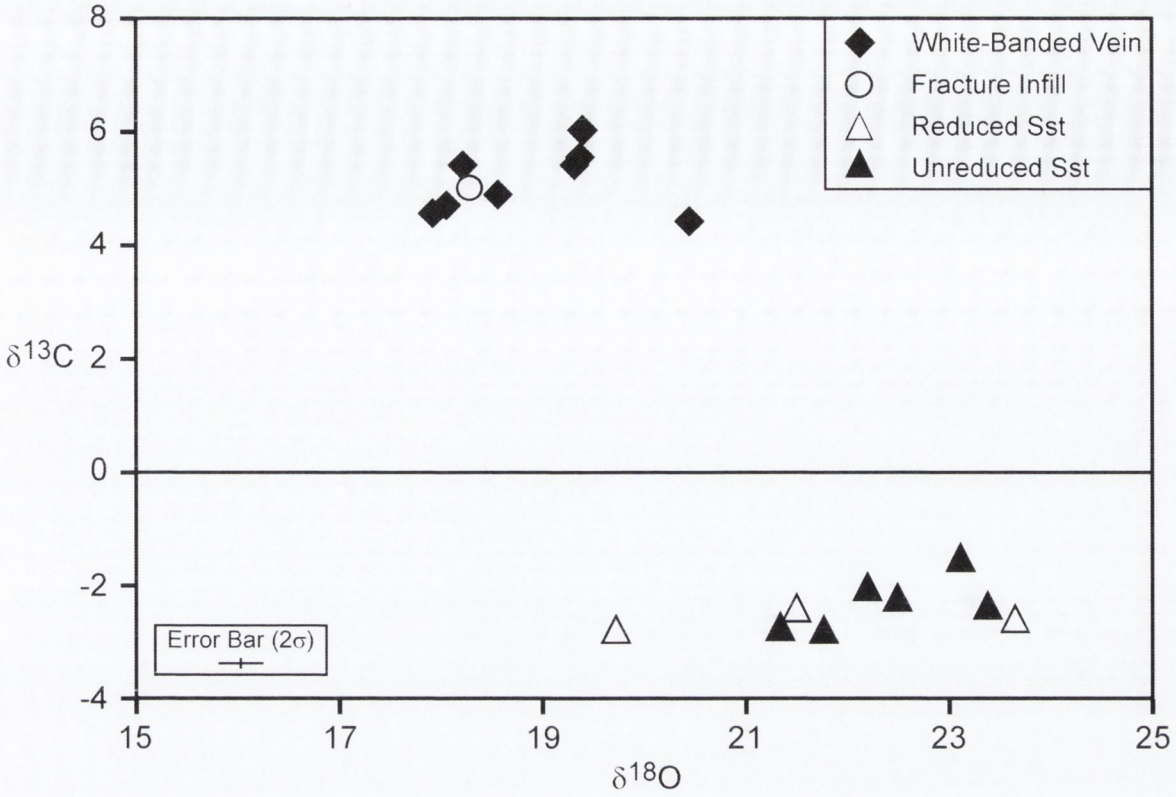


Figure 4.25: Isotopic comparison of the aragonite vein infilling the fracture and carbonate cements from the surrounding Entrada sandstone with white banded veins from the overlying travertine deposit (Travertine 5 in Fig. 4.1). The travertine carbonates are isotopically similar to the fracture infill but distinct from the Entrada sandstone.

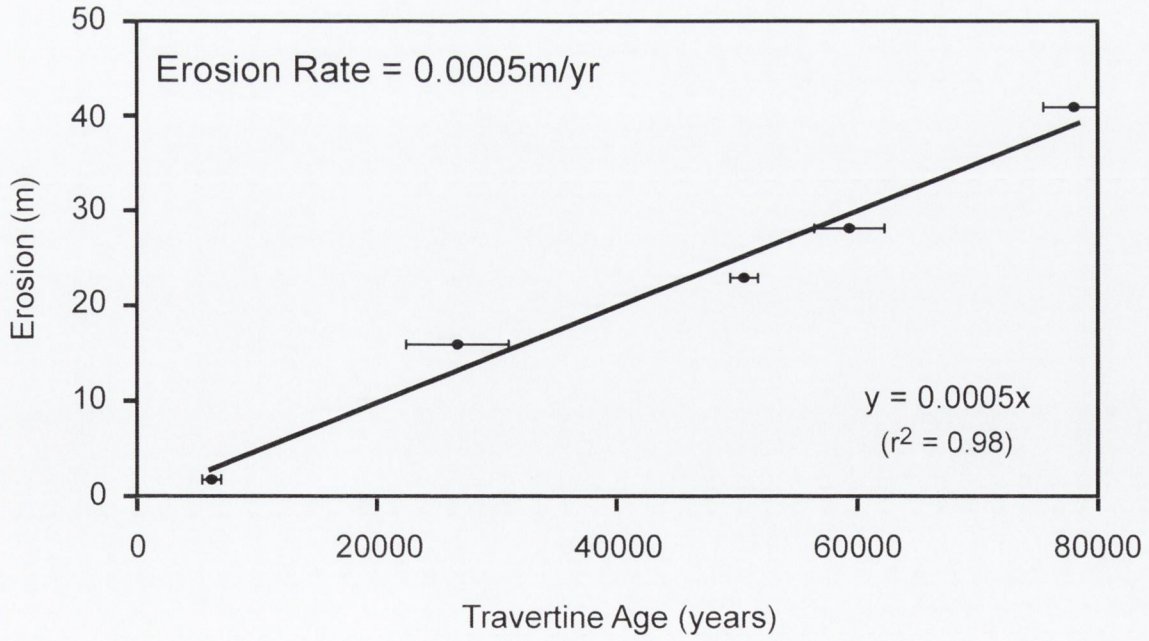


Figure 4.26: Linear relationship between travertine age and erosion (vertical separation) in the study area. The slope of the line of best fit indicates the local erosion rate of the area. Error bars are 2σ . See Table 4.7 for plotted data.

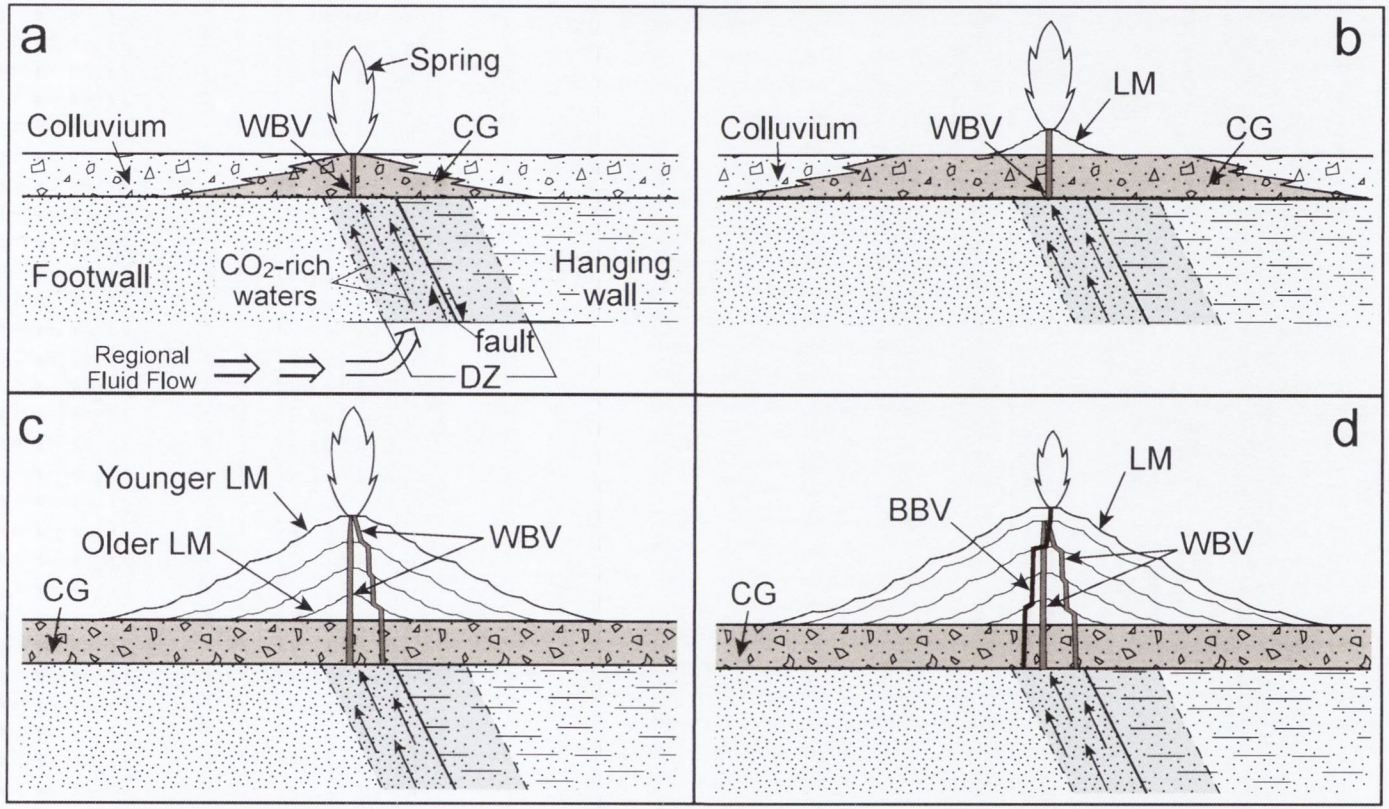


Figure 4.27: Schematic diagram showing different stages in the development of fault-associated travertine deposits of this study. (a) Waters enriched with CO_2 migrate up through a fault-related fracture network (DZ = damage zone) and initiate a spring. Erupting spring waters percolate through the surrounding colluvium and precipitate carbonate cement to produce a conglomerate (CG). (b) Lateral expansion of the conglomerate results in an impermeable surface and precipitation of the layered mats (LM) with a terrace morphology. Contemporaneously, white-banded veins (WBV) grow in conduits transporting water to the spring vent. (c) Layered mats continue to prograde and thicken resulting in further development of the white-banded veins. (d) Towards the later stages of growth of the travertine deposit, supply of CO_2-rich water to the spring vent becomes episodic resulting in the precipitation brown-banded veins (BBV) that crosscut the earlier white-banded veins. Eventually, the spring becomes inactive and the travertine deposit begins to erode.

Chapter 5: Modelling

5.1 Introduction

Surface mapping coupled with geochemical analyses have isolated the CO_2 surface leak points and flux around the Little Grand Wash Fault and Salt Wash Graben (see Chapter 4). Geochemical investigations of active geysers and springs along both structures by Heath (2004) have identified CO_2 source rocks at depth. This chapter attempts to link CO_2 from the source to the surface through the generation of a three-dimensional model to predict subsurface migration pathways, trapping structures and storage capacities of CO_2. As such, this chapter has been divided into three sections, which consist of:

1. **Model Construction and Validation:** data sources and workflow devised to construct the model are described along with the structural validation techniques.

2. **Fault Seal Analysis:** current techniques employed in the hydrocarbon industry are used to investigate the sealing potential of the Little Grand Wash Fault and northern fault of the Salt Wash Graben in relation to CO_2 flow and provide an insight into potential migration pathways through the faulted stratigraphy.

3. **Volumetrics:** CO_2 storage capacities of aquifers sealed by the Little Grand Wash Fault are calculated and compared with surface leak estimates to provide a conservative estimate on the integrity of the faulted system for CO_2 storage over geologic time scales.

The findings of the chapter indicate that CO_2 migration is confined to fault-parallel flow in the footwall of both faults with leakage rates being relatively low over a CO_2 storage period (e.g. 10^3 - 10^4 years). Although more research is needed, this chapter provides a preliminary assessment of the risks associated with storing CO_2 in fault-sealed aquifers.

5.2 Model Construction and Validation

5.2.1 Introduction

The construction and validation of a three-dimensional model requires a specific workflow tailored to the problem that considers the data involved and software available. For this study, a three-dimensional model was constructed to investigate how and in what proportions CO_2 is leaking to the surface. As field studies indicate leakage is controlled by structure, the primary focus of the model was to generate geologically feasible interpretations of the Little Grand Wash Fault, Salt Wash Graben and Ten Mile Graben based on field and well data. Secondary to this, the fold geometries responsible for focussing fluids towards these fault systems are incorporated as well.

A concern in the construction of this three-dimensional model is the paucity of subsurface data, with well density not being sufficient to control fault and strata geometry at depth. This is resolved by introducing published structure maps and projecting surface dip data. However, subsurface fault interpretations remain problematic. As such, general assumptions were made when projecting the faults into the subsurface. These were:

- All fault movement postdates deposition of the modelled stratigraphic sequence (Permian Organ Rock Formation to early Cretaceous Cedar Mountain Formation) with no thickness changes of strata across any of the faults (see section 3.5).
- Due to the scale of the model and lack of subsurface detail, all faults are modelled as isolated, planar, single strand features with constant dips derived from outcrop and limited wells that penetrate the faults at depth (see section 3.2.2).
- The vertical throw profiles for all the faults are constant, though the respective horizontal throw profiles are well constrained (see section 3.2.2). It is acknowledged that throw should change with depth (Childs et al., 1996; Mansfield and Cartwright, 1996) but a lack of subsurface data prevents identification of this change. This vertical preservation of throw down

sequence may introduce errors of up to 6% at the base of the modelled strata (see section 5.3.5.1).

The workflow devised to utilise the varying data sources is reliant on three software packages to construct and validate the model. Initially, a geospatial program (ArcView) was used to compile and manipulate the data into a series of structure and isopach maps. The maps were subsequently imported with additional data into a two-dimensional modelling program (2DMove) to generate a series of balanced cross sections. Finally, the sections were imported into a three-dimensional modelling program (3DMove) that converts the two-dimensional lines into surfaces to create the three-dimensional model. This workflow is elaborated below with each step described in further detail.

5.2.2 Model Construction

5.2.2.1 Data Sources

A variety of data sources have been employed to aid in the construction of the three-dimensional model. The main source of data is from a well summary database compiled by PI/Dwights and supplied by the Utah Geological Survey. The database contains summaries of about 200 exploration wells (oil, gas or water) drilled in the northwestern section of the Paradox basin and surrounding area in the last 100 years (Fig. 5.1). Each well summary lists the name, date, location, surface elevation and depth of the well. In addition, most list the stratigraphy and corresponding depth penetrated by each well, though this is generally restricted to sections of the stratigraphic sequence deemed economically important (i.e. potential reservoirs, seals and source rocks). These reported stratigraphic picks provide data to show regional variations in elevation and thickness of modelled stratigraphy throughout the study area.

Supplementing the database are 22 wire-line logs (gamma, neutron, sonic and resistivity) donated by Rileys Electric Logs Inc (Fig. 5.1). The logs provide an alternative data source to document well stratigraphy close to the faults. This proved important in assessing the reliability of stratigraphic picks in the database and resulted in minor alterations to stratigraphic elevations in some wells considered incorrectly picked in the database. This inconsistent picking of stratigraphy in some wells is attributed to the evolving interpretations of regional stratigraphy over a 100 year span

by numerous geologists and drillers. Gamma logs were also used to construct a V-shale curve (see section 5.3.3) for fault seal analysis conducted later in this chapter.

The density and distribution of the wells were insufficient to capture the main regional structure features within the stratigraphy throughout the modelled area. As such, published structure and isopach maps were integrated to fill data gaps. Using the published maps as a template, the well data was superimposed and maps amended to honour all data. This produced a series of structure and isopach maps, which were subsequently utilised in cross section building.

Finally, outcrop data gathered over two field seasons aided in the construction of faults and constrained bed dips within the three-dimensional model. The data are listed in Chapter 3. Additional dip data from McKnight (1940) and Doelling (2001) were used to constrain bed dips further away from the faults.

5.2.2.2 Map Generation

Isopach and structure maps for model construction were generated in ArcView. This program can combine various forms of spatial data to build maps with contour lines indicating changes in elevation (structure) or thickness (isopach). Six isopach and three structure maps were generated, though only one structure map combined with the isopach maps was eventually used to build the model.

The structure map used was for the top of the lower Jurassic Navajo Sandstone (Fig. 5.2). This formation was selected as it is in the middle of the modelled stratigraphic sequence, has good well data density and earlier detailed structure maps have been produced (Baker, 1933; McKnight, 1944). Other structure maps for the tops of the Pennsylvanian Honaker Trail Formation (Fig. 5.3) and Cretaceous Dakota Formation (Fig. 5.4) were also constructed but not subsequently used as they occur outside the modelled stratigraphy. All structure maps were constructed via the same three stage process. Published maps were scanned and contours digitised in ArcView (Fig. 5.5a). Formation tops from well data were compiled and imported into the program (Fig. 5.5b). Finally, digitised contours were realigned when comparing with well data (Fig. 5.5c).

The isopach maps are composed of one or more formations grouped together from the Pennsylvanian Elephant Canyon Formation to the Jurassic Morrison Formation (Fig. 3.6 to 3.11). The variations in grouping of formations between isopach maps is related to data quality with further division of the groups not

undertaken due to the data being too erratic or absent in the well database. All isopach maps, except for the Cutler Group (Fig. 3.6), are generated exclusively from well data. This process involves thickness data from the well database being compiled and imported into ArcView. Subsequent isopach contours are generated by using the contour tool in the program. The Cutler Group isopach map was generated using the same process that created the structure maps.

5.2.2.3 Cross Sections

Based on the generated maps and available data, the most efficient workflow devised for model construction consists of generating a series of balanced cross sections and connecting them in three-dimensional space. The benefits of using this approach is that the fault geometry and throw are well constrained and each interpreted section is structurally realistic through balancing.

The distribution and orientation of these sections were critical in building the model. The boundaries of the sections and resultant model are defined by major structural features that probably act as natural flow barriers to the east (Moab Fault and Salt Valley Anticline) and west (San Rafael Swell) and outlying CO_2 effusions to the north (Woodside Geyser) and south (Chaffin Ranch Geyser; Fig. 5.6). The distribution of sections within this area was dictated by the location and geometry of the studied faults. Each section is normal to fault strike and combined define the orientation of the fault. As strike varies along and between faults, the sections were divided into three areas encapsulating the Little Grand Wash Fault, Salt Wash and Ten Mile Grabens and an outer area with no faulting (Fig. 5.6). The spacing and orientation of sections within these areas was dependant on changes in fault orientation and throw, structural complexities (i.e. relay ramps) and fold geometry.

The cross sections were generated using the modelling program 2DMove. The Navajo structure map (Fig. 5.2) along with surface data for faults and strata as well as dip data were imported into the program and are presented in map view (Fig. 5.7a). Sections were then generated by using the steps detailed below.

1. Section positions were projected onto the map as lines and geologic data intersecting the section lines was collected (Fig. 5.7b). The section lines with accompanying geologic data points were then displayed in cross sectional view for section construction (Fig. 5.8a).

2. Faults were generated by extrapolating a straight line from the surface fault position at predetermined dips (Fig. 5.8b). Based on field and well data, the dips were 56° for the Little Grand Wash Fault, 75° for the Salt Wash Graben faults and 73° for the Ten Mile Graben faults.

3. The horizon for the top of the Navajo sandstone was generated by connecting all the data points and extending the two-dimensional lines to the section boundaries and fault/s (Fig. 5.8c). Footwall and hanging wall cutoffs were adjusted to correspond with throw determined directly from the horizontal throw profiles illustrated in section 3.2.2.

4. Subsequent stratigraphic horizons were added above and below the Navajo footwall (Fig. 5.8d) using thickness data from isopach maps (Fig. 3.6 to 3.11) and wire-line logs and extended to the section and fault boundaries (Fig. 5.8e). The Navajo hanging wall was then restored to zero throw (Fig. 5.8f) and horizons added above and below the existing hanging wall horizon (Fig. 5.8g). Each horizon was checked and readjusted to zero throw if necessary.

5. The hanging wall was replaced to the original throw and horizons were clipped or extended to the section boundary (Fig. 5.8h). Horizons were then adjusted to conform to surface dip data and outcropping positions of stratigraphy.

6. Finally, sections were again restored to zero throw and horizons unfolded for line length balancing to test the validity of the section interpretation (Fig. 5.8i). If there were any discrepancies, the sections were readjusted and continually balanced until structurally reasonable.

This procedure was repeated to create 115 balanced sections that were then exported into 3DMove for the final part of the workflow involving three-dimensional conversion. Representative cross sections for the Little Grand Wash Fault, Salt Wash Graben, Ten Mile Graben and the peripheral San Rafael Swell are shown in Fig. 5.9.

5.2.2.4 Surface Construction

Conversion of two-dimensional lines into three-dimensional surfaces and creation of a three-dimensional model was conducted in the modelling program 3DMove. The main priorities throughout this three-dimensional conversion were the preservation of fault geometries and throw generated in section construction and the development of surrounding fold geometries. Many workflows were tested before a successful workflow maintaining the aforementioned priorities was achieved. Documented below is this workflow that constitutes the final steps involved in the creation of the three-dimensional model.

1. Sections from the three areas were imported separately into 3DMove to form three sub-models (Fig. 5.10a).

2. Within each sub-model, individual stratigraphic horizons were selected (Fig. 5.10b) and two-dimensional lines were linked to form three-dimensional surfaces composed of data points bound by a triangular mesh. Surfaces were divided into footwall, hanging wall and non-faulted blocks to preserve the stratigraphic horizon cutoffs (Fig. 5.10c). All two-dimensional fault lines and non-faulted stratigraphic surfaces were converted directly to one complete surface.

3. To aide in the correct juxtaposition of stratigraphic horizons against faults, data point density was locally increased for surfaces surrounding faults and Allan lines were generated for every footwall and hanging wall cutoff (Fig. 5.10d). An Allan line is a line of intersection between a fault and stratigraphic surface (Allan, 1989) that provides a crisp, clean edge for each horizon cutoff. The addition of Allan lines and local increase in data points ensured triangular mesh forming the juxtaposed surfaces was correctly gridded to preserve the stratigraphic cutoffs. At low throw values around fault tips, data points forming the Allan lines were also increased to guarantee the correct gridding of juxtaposed horizons. This process was repeated for every stratigraphic surface in contact with a fault in the sub-models.

4. Once all the surfaces and Allan lines for every stratigraphic horizon had been generated in each sub-model, all data was imported into a single model (Fig. 5.10e). A single, coherent surface for each horizon was then produced by combining all the surfaces and Allan lines together. Excess triangular mesh at horizon boundaries and connecting footwall and hanging wall cutoffs was deleted to form an intact surface with local gaps representing fault rupture (Fig. 5.10f). Finally, each surface was re-gridded to reduce the number of data points and smooth areas between the combined sub-models.

5.2.3 Model Components

The three-dimensional geologic model covers 3920km^2 of the northern Paradox basin and surrounding area extending from the San Rafael Swell in the west to the Salt Valley anticline and Moab fault in the east and the Woodside geyser in the north to the Chaffin Ranch geyser in the south (Fig. 5.11). The model contains 11 stratigraphic horizons representing the tops of 11 units from the Organ Rock Formation to the Cedar Mountain Formation with subdivision based on major lithological changes and local formation divisions (Fig. 5.11a). The horizons are juxtaposed by 5 fault surfaces representing the Little Grand Wash Fault and bounding faults of the Salt Wash and Ten Mile Grabens. Oblique to the faults, the open, gently north-plunging Green River Anticline is cut by both the Little Grand Wash Fault and northern fault of the Salt Wash Graben (Fig. 5.11b). This juxtaposition results in fault-sealed anticlinal traps in the footwalls of both faults with three-way dip closure and a lateral southern fault closure. Potential reservoirs for these structural traps include the White Rim Sandstone, Wingate and Navajo Sandstones and Entrada Sandstone with corresponding top seals provided by the Moenkopi, Carmel and Morrison Formations, respectively. Source rocks supplying CO_2 to this system include the Sinbad Limestone from the Moenkopi Formation and older stratigraphy below the vertical limits of the model (see section 4.5.3.2).

5.2.4 Model Validation

With the creation of the three-dimensional model, uncertainty will arise regarding the validity of the structural interpretation. To assess this interpretation, multiple tests were performed during two-dimensional section and three-dimensional

surface construction. Initially, all available geological data was imported in 2DMove and utilised during section construction. This ensured bed geometries were well constrained by a combination of surface and well data. However, minimal subsurface fault data limited knowledge of down-dip fault geometries and resulted in all modelled faults being projected as single, planar features. Additional to honouring geological data, the cross sections must balance to be structurally correct. Section balancing is based on the concept that the length and/or area of a given bed will remain constant pre- and post deformation due to the law of conversation of volume (Goguel, 1952; Dahlstrom, 1969), which states that material can not be created nor destroyed during structural deformation. There are two main types of balancing performed in two-dimensional and three-dimensional structural restorations, which are (Midland Valley, 2004):

1. Unfolding restoration: where fault geometries are planar or ignored
2. Move on fault restoration: where the effects of non-planar fault geometry on hanging wall deformation are considered.

As all faults are planar, the unfolding restoration technique of line-length balancing, first described by Dahlstrom (1969) was used to balance the sections. This technique involves straightening the beds and translating fault blocks so horizon cutoffs are aligned (Fig. 5.8i). Errors in the section are highlighted if there are overlaps or gaps between horizon cutoffs or one or more beds show an abrupt change in thickness (Midland Valley, 2004). The benefit of using line-length balancing is it is a rapid and efficient process in identifying structurally incorrect interpretations; a technique needed when 115 sections are constructed. As previously detailed (section 5.2.4), balancing was the final step in section construction. Therefore, each completed cross section represents a structurally realistic interpretation of the study area that incorporates all available geological data.

This two-dimensional balancing technique can extend to the third dimension, as conservation of bed length in cross section is analogous to conservation of surface area in three dimensions (Williams et al, 1997). Thus balancing is expected to be conserved from a two-dimensional line to a three-dimensional surface. Yet, surface geometry may vary from the original balanced cross sections due to certain steps (i.e. Allan line development, re-gridding surfaces) in the three-dimensional conversion. To quantify any possible variations, cross sections were generated from the completed three-dimensional model and compared with original cross sections from the Little

Grand Wash Fault, Salt Wash Graben, Ten Mile Graben and San Rafael Swell. The Cedar Mountain (top), Navajo (middle) and Organ Rock (base) horizons for each original and generated section was compared, and variations in elevation (i.e. geometry) calculated.

The results of this comparison are displayed in Fig. 5.12. Horizon cutoffs do not alter between the original and generated sections, though differences along horizon strike were evident but small for the faulted sections and locally large for the San Rafael Swell section. These variations are focussed at areas of increased fold curvature and at section boundaries. The difference in elevations between sections at these sites indicates that the final stage of re-gridding surfaces to reduce the number of data points must have altered surface geometries to varying extents due to the smoothing accompanying data reduction. Re-gridding is a necessary step due to computational limits and the associated smoothing decreases fold curvatures and realigns section boundaries as a consequence. However, these differences are only appreciable distal from the faulted areas of the model (i.e. San Rafael Swell), minimal in folding adjacent to the faults (i.e. Green River Anticline) and non-existent for horizon cutoffs in contact with the faults. In addition, the geometry of the surfaces is maintained though smoothed in the re-gridding process. As such, the valid structural interpretation of the modelled area, defined in section construction, is predominantly maintained during three-dimensional conversion, especially proximal to the faults. Therefore, this three-dimensional model represents a structurally-valid interpretation of the region that can be utilised for fault seal and volumetric analyses later in this chapter.

5.3 Fault Seal Analysis

5.3.1 Introduction

Faults play an important role in the migration and entrapment of fluids in the subsurface. Barriers and restrictions to fluid flow can form if faults juxtapose reservoir rocks against nonreservoir rocks, or faulting processes generate membrane seals formed by argillaceous smearing, cataclasis or cementation. It is not necessary for both juxtaposition and membrane seals to develop to form an effective fault seal. If reservoir rock is juxtaposed against nonreservoir rock, a membrane seal is not

needed. Conversely, faults can seal at reservoir-reservoir juxtapositions where an adequate membrane seal forms.

Fault seal analysis is a technique that assesses these processes to indicate whether a fault will seal or leak. The technique was developed and is extensively used by the hydrocarbon industry to indicate whether faults will trap hydrocarbons over geological and production time scales. This section presents a new approach to fault seal analysis of the Little Grand Wash Fault and northern fault of the Salt Wash Graben that assesses the sealing potential of these faults in relation to trapping CO_2. This analysis combined with diagenetic outcrop relationships (see Chapter 4) are used to define the subsurface migration pathways of CO_2 through this faulted system.

5.3.2 Fault Seal Review

A fault can act as a barrier or conduit to fluid flow based on the juxtaposition of stratigraphy and material incorporated into or around the fault zone. Numerous studies on faulting in siliclastic sequences have identified four mechanisms that result in faults acting as seals (Watts, 1987; Allan, 1989; Yielding et al., 1997; Knipe et al., 1998).

1. Juxtaposition – the positioning of reservoir rocks (i.e. sandstone) against nonreservoir rocks (i.e. shale) across a fault will generate a hydraulically passive seal.
2. Argillaceous smear – the entrainment of clay or shale from wall rock into the fault zone will produce fault rocks with a lower permeability and higher capillary entry pressure.
3. Cataclasis – the crushing of sand grains in faulted sandstones produces a fine-grained, highly compacted fault gouge.
4. Cementation – the precipitation of minerals in or adjacent to the fault may partially to completely reduce the porosity of the fault rock.

The interaction of one or more of these processes will control the sealing behaviour of a fault. Further details of each process are listed below along with the techniques used to quantify each sealing process.

5.3.2.1 Juxtaposition

Movement of a fault will displace stratigraphic units of a hanging wall relative to the footwall. Favourable juxtaposition of reservoir rocks against nonreservoir rocks with low permeabilities will generate hydraulically passive seals regardless of fault zone processes (Fig. 5.13a; Watts, 1987; Allan, 1989). Mapping of juxtapositions across a fault can give a preliminary assessment of sealing potential provided throw and stratigraphy are known. Subsequent investigation of membrane seals formed by faulting can further constrain potential areas of leakage at reservoir-reservoir juxtapositions across a fault.

There are two general techniques used to assess sealing caused by stratigraphic juxtaposition, which are Allan diagrams (Fig. 5.13; Allan, 1989) and Juxtaposition diagrams (Fig. 5.14; Knipe, 1992; 1997). Allan diagrams are a graphical mapping technique that overlays footwall and hanging wall stratigraphic cutoffs onto a fault surface to illustrate geometric relationships between stratigraphy across a fault (Fig. 5.13b). Seals are identified at reservoir-nonreservoir juxtapositions, while potential leak points will be at reservoir-reservoir juxtapositions. Generally, these diagrams are orientated vertically or laterally straight (Fig. 5.13c), which can create geometric problems if the analysed fault is curved (Harper and Lundin, 1997; Badley et al., 1997; Clarke et al., 2005). This is overcome by creating Allan diagrams in three-dimensions (Fig. 5.13b), which alleviates the two-dimensional issues. However, a three-dimensional model is needed for this approach, which is a time consuming process that requires a detailed appreciation of structure and stratigraphy in the modelled area.

A Juxtaposition diagram provides an alternative approach to investigating fault seal related to stratigraphic juxtapositions (Fig. 5.14). The diagram is constructed as a triangle chart with footwall stratigraphy on the vertical axis, varying throw on the horizon axis and hanging wall stratigraphy overlaying footwall stratigraphy at increasing juxtapositions from left to right (Fig. 5.14b). Maximum throw on the horizontal axis is equivalent to footwall thickness on the vertical axis to ensure all stratigraphic units are juxtaposed against each other. The juxtaposition of stratigraphic units for a given throw is calculated by extending a vertical line from the throw value (Fig. 5.14b). Straight vertical lines represent constant throw of the fault down dip with a curved line representing variable throw with depth. The benefit of a juxtaposition diagram is it provides a quick and easy analysis of juxtaposition without the

construction of a model. However, the diagrams are limited by only representing a one-dimensional analysis of the fault if throw varies along strike as well as assuming constant cross-fault stratigraphic thicknesses, preventing analysis in certain structural settings (i.e. growth faults). Therefore, with the development of a three-dimensional model, Juxtaposition diagrams become redundant as three-dimensional Allan diagrams provide a more comprehensive and detailed insight into fault sealing caused by juxtaposition.

5.3.2.2 Argillaceous Smears

Pioneering studies on faulted, semi-lithified (Weber et al., 1978) and lithified (Lindsay et al., 1993) sand-shale sequences recognised the development of a continuous, multi-layered argillaceous gouge along the fault surface. The gouge is a product of shale and clay-rich beds in adjacent wall rocks being incorporated and smeared along the fault surface. Based on the incorporation mechanisms, smears have been subdivided into three categories, which are (Lindsay et al., 1993; Yielding et al., 1997):

1. Shear smears – This smear develops as a wedge that tapers away from the source bed (Fig. 5.15a; Weber et al., 1978). It is formed by a shearing motion of the fault and indicates faulting in partially lithified sediments.
2. Abrasion smears – This smear extends from the cutoffs of the faulted source beds to form a sliver of constant thickness along the fault surface (Fig. 5.15b). These smears are the most common type in lithified sediments and develop by clay- and shale-rich rocks being abraded and incorporated into the fault by sand-rich beds as they slip past. The thickness of an abrasion smear is dependant on source bed thickness and fault throw.
3. Injection smears – Volumetric changes during faulting can result in the injection of argillaceous material into the fault. This injection is highly dependant on local fault geometry and stratigraphy resulting in this smear being a localised and unpredictable phenomenon.

The dependence of shear and abrasion smear formation on fault throw and lithological properties of wall rocks led to the development of various algorithms that quantitatively predict the prevalence of argillaceous smear along a fault surface

(Webber et al., 1978; Bouvier et al., 1989; Lindsay et al., 1993; Yielding et al., 1997). All the algorithms are based on simple geometric relationships that consider fault throw, source bed thickness and the quantity and distribution of source beds in the faulted sequence. The localisation and unpredictability of injection smears preclude them from being reliably quantified. Documented below are the main algorithms used to quantify smears in the fault rocks.

5.3.2.2.1 Generalised Smear Potential

Argillaceous smears formed by shear-type faulting processes can be quantified by the *generalised smear potential* (GSP) algorithm (Fig. 5.15a; Yielding et al., 1997) expressed as:

$$GSP = \sum (\text{source bed thickness})^n / (\text{distance from source bed})^m$$

The exponents, m and n, are variables derived from experimental or field observations. Variations in m and n reflect the degree of lithification and plasticity of the source beds deformed. Faulted lithological sequences involving pure clay can use a derivative of the GSP called the *clay smear potential* (CSP) algorithm (Fig. 5.15a; Bouvier et al., 1989), which is expressed as:

$$CSP = \sum (\text{source bed thickness})^2 / (\text{distance from source bed})$$

The use of 2 and 1 for n and m respectively, is based on the concept that the integration of pure clay smears into faults from source beds is a ductile process that obeys the laws of Newtonian fluid dynamics (Lehner and Pilaar, 1996). Both algorithms assume the stratigraphy is semi-lithified at the time of faulting with the CSP being the purely ductile end member. High values for both algorithms indicate the fault is likely to seal while low values indicate leakage. Calibration of the algorithms is required to define the threshold value between sealing and non-sealing faults (see section 5.3.2.2.4).

5.3.2.2.2 Shale Smear Factor

In lithified stratigraphic sequences, abrasion-type faulting leads to the development of argillaceous smears of constant thickness. As such, quantifying

abrasion smears is dependant on fault throw as opposed to distance from source beds. Lindsay et al. (1993) developed the *shale smear factor* (SSF) algorithm (Fig. 5.15b) to constrain the likelihood of abrasion smear continuity along a fault. The algorithm is defined as:

$$SSF = \text{fault throw} / \text{source bed thickness}$$

Abrasion smears were estimated to be incomplete at SSF values greater than seven (Yielding et al., 1997), while values smaller than four (Gibson, 1994) were most likely to have a continuous smear to form a membrane seal. Unlike the GSP and CSP algorithms, in abrasion faults with more than one smear (i.e. compound smears) the SSF values for each smear are not added. Instead, the minimum value calculated from the relevant shale beds represents the SSF value for the compound smear (Lindsay et al., 1993; Yielding et al., 1997).

5.3.2.2.3 Shale Gouge Ratio

The GSP, CSP and SSF algorithms all depend on the thickness of argillaceous source beds in the faulted sequence. This can prove difficult to establish, and beyond the resolution of the data in thick heterogeneous sequences, where every argillaceous bed needs to be considered. As source data often only presents the bulk properties of units within a stratigraphic sequence, the *shale gouge ratio* (SGR) algorithm (Fig. 5.15b) developed by Yielding et al. (1997; 2002) is an attempt to quantify the proportion of shale or clay entrained into the fault by all smearing processes. In contrast to the other smear algorithms that predict the presence or absence of an argillaceous smear, the SGR predicts the proportion of argillaceous material along a fault. For a series of delimited source beds (Fig. 5.15b), the SGR is defined as:

$$SGR = \sum (\text{source bed thickness}) / \text{fault throw}$$

Alternatively, if the stratigraphic sequence has been subdivided into lithological or reservoir zones (Fig. 5.15b), the net argillaceous content of each zone can be calculated by:

$$SGR = \sum (\text{zone thickness} \times \text{argillaceous content of zone}) / \text{fault throw}$$

This modification of the SGR to calculate the argillaceous content of zones can be extended to additional lithologies (i.e. coal) that may enhance sealing capacity through integration into the fault gouge. In these cases, the additional lithologies are down-weighted in sealing potential relative to shale (Yielding et al., 1997). As with other algorithms, the SGR is not a measure of fault sealing capacity but rather an estimate of the argillaceous content along a fault. To use any of these algorithms for sealing capacity, they must be calibrated.

5.3.2.2.4 Argillaceous Smear Calibration

Argillaceous smear algorithms that predict membrane seal capacity of a fault must be calibrated to determine the effectiveness of the predicted seal. This process involves comparing algorithm results with similar faults where the sealing behaviour is established from pore pressure or fluid contact data (Bretan et al., 2003). In cases where there is no available data, published calibrations (Jev et al., 1993; Yielding., et al., 1997) can be used as a guide. However, caution is needed to ensure the published calibrations used have been calculated over similar time scales (i.e. production versus geological).

Multiple studies have reported values for the differing algorithms that indicate the threshold between a fault sealing and not sealing. In shear smear settings, research by Jev et al. (1993) using the CSP algorithm indicated a fault will leak at values less than fifteen and seal at values greater than thirty. No standardised threshold value for GSP is available as the algorithm is dependant on the local faulting conditions. In abrasion smear settings, the SSF predicts leakage at values greater than seven (Yielding et al., 1997) and sealing at values less than four (Gibson, 1994). Considering all smearing mechanisms, the SGR represents the most robust and calibrated algorithm used, with values less than fifteen percent likely to leak and values greater than twenty percent likely to seal (Fristad et al., 1997; Yielding et al., 1997; Manzocchi et al., 1999; Yielding et al., 2002; Bretan et al., 2003; Gibson, 2003). In addition, experimental and outcrop studies indicate that a continuous argillaceous smear will develop at SGR values greater than ca.20% (Foxford et al., 1998; Sperrevik et al., 2000; Yielding et al., 2002). Values between the stated end members represent a grey area dependant on local conditions. Ideally, pore pressure data would be used in each reservoir to determine the definitive threshold value for the sealing capacity of each fault.

5.3.2.3 Cataclasis

Cataclasis is the abrasive rubbing of hard surfaces (i.e. sandstone) against each other leading to grain breakage and comminution (Engelder, 1974). It is the dominant process responsible for reduction in porosity and permeability in sandstones via grain size reduction and increased grain packing (Fisher and Knipe, 1998). Cataclastic fault rocks are also commonly affected by cementation and quartz overgrowths that further decrease porosity and permeability (Hesthammer and Fossen, 2000; Ngwenya et al., 2000). Consequently, pore-throat radii are constricted and permeabilities decreased in cataclastic rocks leading to the potential development of a membrane seal (Yielding et al., 1997).

The formation of cataclastic fault rocks is controlled by the degree of lithification of the host rock (i.e. depth of burial) and the magnitude of stress on the fault plane during movement (Engelder, 1974; Watts, 1987). As such, these fault rocks generally develop in high-porosity sandstones at depths greater than one kilometre. However, experimental (Mandl et al., 1977) and field (Lucas and Moore, 1986) studies indicate that cataclasite structures can form at burial depths as low as one hundred metres.

The potential for cataclastic fault rocks to form significant fault seals remains speculative (Smith, 1980; Yoshioka, 1986; Scholz, 1987; Fristad et al., 1997). Field (Antonellini and Aydin, 1994; Fowles and Burley, 1994) and experimental (Fulljames et al., 1997; Crawford, 1998) studies into the hydraulic properties of cataclastic rocks show they can form membrane seals with permeability reductions up to three to four orders of magnitude. However, there is no consensus on their importance in trapping large fluid reservoirs (Gibson, 1994; Gibson, 1998; Yielding et al., 2002). In addition, quantitative predictions related to cataclastic rocks have been limited to estimating fault rock thickness (Yoshika, 1986; Scholz, 1987; Robertson, 1993), a variable not indicative of fault seal potential. As such, the current understanding of cataclasis membrane seals remains incomplete, with no quantitative algorithms available to predict the effects of cataclasis on fluid flow.

5.3.2.4 Cementation

Cementation produces a decrease in the porosity of fault rocks caused by the precipitation of minerals from local or external sources. There are two main processes

that promote cementation along a fault or associated structures, which are cataclasis or precipitation from migration fluids.

Fault rocks that develop by cataclasis in high-porosity sandstones are commonly accompanied by quartz cementation (Fisher and Knipe, 1998). The quartz cements form by Ostwald ripening and pressure solution during cataclasis (Ngwenya et al., 2000 and references within). Experimental studies by Ngwenya et al (2000) indicated that the quartz cementation reduces fault permeabilities by a further two orders of magnitude in addition to grain crushing and packing. However, as no algorithm exists for predicting the sealing potential of cataclasis membrane seals, cementation associated with the cataclasis also remains unquantifiable in fault seal analysis.

Dilation during faulting can generate open fractures, which increase permeability relative to the host rock and preferentially channel fluids along or within the fault or associated structures (Sibson, 1994; Sibson, 1996; Curewitz and Karson, 1997). Decreases in pore pressures and temperatures or mixing with other fluids can precipitate out mineral cements that can choke the fluid pathways by decreasing the permeability and increasing the capillary entry pressure of the cemented fault rock. Cements are usually concentrated along the fault in zones of enhanced fluid flow (i.e. branch lines and relay ramps) and continuous cemented faults have been shown to have very low permeabilities (<0.1μD) and high capillary entry pressures (>1500psi; Fisher and Knipe, 1998). However, microstructural and field evidence indicate cementation is rarely continuous with the sealing potential of cemented faults generally determined by the petrophysical properties of other material in the fault zone (Fisher and Knipe, 1998). In addition, cementation is dependant on an array of local and temporal factors (i.e. structural complexities, fluid flow rates, fluid interactions) that are difficult to quantify and complex to model. Therefore, the sealing potential related to cementation is less amenable to prediction by simple algorithms and as such, is generally not considered in fault seal analyses.

5.3.3 Model Appendages

Assessment of sealing potential for the Little Grand Wash Fault and northern fault of the Salt Wash Graben required the transfer of the three-dimensional model to the fault seal modelling program, Traptester. Stratigraphic horizons, faults and Allan

lines were exported from 3DMove and separately imported into Traptester to re-create the three-dimensional model. Additional data was also required before undertaking fault seal analysis, with the V_{shale} content needed to quantify the argillaceous content of beds in the modelled stratigraphy. V_{shale} is a curve that describes the mineralogical content of a stratigraphic sequence in terms of sand and shale. It is typically derived from gamma, resistivity or neutron logs that are corrected to true sand-shale contents by detailed analyses of thin sections through point counting or X-ray diffraction (Bretan et al., 2003). In the absence of a petrological investigation, the sand (0%) and shale (100%) end-members for the V_{shale} curve can be approximated by normalising the 100% shale value to the base shale measurement (Davies et al., 2003).

For this study, the V_{shale} curve was derived from a series of gamma logs situated around the modelled faults (Fig. 5.16a). Due to the thickness (~1200m) and large quantity of numerous shale units within the modelled stratigraphic sequence, combined with time constraints, a detailed petrographic investigation was beyond the scope of this research and the shale baseline was used to define the V_{shale} curve (Fig. 5.16b). Based on published petrographic investigations of the modelled stratigraphy (Trimble and Doelling, 1978; Peterson and Turner-Peterson, 1987; Chan, 1989; Garden et al., 2000), a V_{shale} cutoff of 0.5 was applied to discriminate between sand-rich and shale-rich beds (Fig. 5.16c). With the integration of the V_{shale} curve to define the mineralogical content of the stratigraphic sequence, Traptester was then used to predict the sealing potential of both faults.

5.3.4 Fault Seal Assessment

Juxtaposition and argillaceous smear analyses were conducted for the Little Grand Wash Fault and northern fault of the Salt Wash Graben in Traptester to assess the sealing potential of each fault. Cataclasis and cementation were not considered, as quantifying these sealing mechanisms is currently complex and controversial (see sections 5.3.2.3 and 5.3.2.4). Juxtaposition of footwall and hanging wall cutoffs against each fault were analysed in three-dimensions to identify regions of cross-fault reservoir-reservoir contact (Fig. 5.17). SGR calculations were then applied to these reservoir-reservoir contacts to indicate the likelihood of a continuous argillaceous smear forming. The SGR was used in preference to other smear algorithms as: (1) it considers all smearing processes; (2) is the most commonly used with the best defined

threshold values; and (3) the modelled stratigraphic sequence is thick (~1200m) and heterogeneous, limiting the effectiveness of other smear algorithms due to data resolution.

Figures 5.18a and 5.19a show reservoir against reservoir juxtapositions across the Little Grand Wash Fault and northern fault of the Salt Wash Graben, respectively. The favourable juxtapositions are more prevalent towards fault tips, where the same reservoirs maintain cross fault contacts. At higher displacements, favourable juxtapositions are limited, with some footwall reservoirs in periodic contact with stratigraphically higher hanging wall reservoirs. This is seen along the Little Grand Wash Fault with the lower section of the Navajo sandstone juxtaposed against the Entrada sandstone and the upper and lower sections of the Wingate sandstone juxtaposed against the Entrada and Navajo sandstones, respectively. Additionally, the northern fault of the Salt Wash Graben has the Wingate sandstone juxtaposed against the Entrada sandstone and the upper section of the White Rim sandstone juxtaposed against the Wingate sandstone. All these areas represent sites of potential leakage across the fault. The rest of the fault surface is assumed a seal due to reservoir-nonreservoir juxtapositions or nonreservoir-nonreservoir juxtapositions.

Figures 5.18b and 5.19b show the calculated SGR values for both faults at sites of reservoir-reservoir juxtaposition. SGR values in areas of reservoir self-juxtaposition towards fault tips are low (<15%). In contrast, portions of both faults where two different reservoirs are juxtaposed show SGR values in excess of 24%, except for one site on the Little Grand Wash Fault where the lower section of the Wingate sandstone is juxtaposed against the Navajo sandstone (SGR = 18%). Of importance to this study is the likelihood of trap integrity related to CO_2. A SGR of ca.20% is a threshold above which a continuous argillaceous smear will develop to form an effective membrane seal (section 5.3.2.2.4; Foxford et al., 1998; Sperrevik et al., 2000; Yielding et al., 2002). Thus, areas of reservoir self-juxtaposition at low throws (<100m) are predicted to leak while areas of differing reservoir juxtaposition at higher throws (>100m) are predicted to seal due to the development of a continuous argillaceous smear. One uncertainty is the sealing potential of the Little Grand Wash Fault at the Wingate-Navajo contact, where the SGR is close to the threshold for the development of a continuous smear. As no additional data is available, a definitive prediction on fault seal can not be made. However, indirect evidence based on the

confinement of travertines to the footwalls of both faults (Fig. 4.1) suggests the Little Grand Wash Fault does form an effective seal to cross-fault flow.

5.3.5 Uncertainty

The prediction of faults acting as barriers or conduits to cross-fault fluid flow is not an exact science. An awareness of uncertainties related to fault seal prediction is needed to assess the reliability of the results. Documented below are the main areas of uncertainty that may influence the fault seal assessment of the Little Grand Wash Fault and northern fault of the Salt Wash Graben. The uncertainty related to some parameters is difficult to quantify, though the confinement of travertines to the footwalls of both faults (Fig. 4.1) suggests both are preventing cross-fault CO_2 flow.

5.3.5.1 Geological Model

A fundamental factor influencing the reliability of the fault seal analysis is the precision of mapped horizon and fault surfaces incorporated into the three-dimensional model. Inaccurate horizon placements or fault geometries will lead to incorrect horizon juxtapositions and argillaceous smear calculations. To limit inaccuracies in horizon surfaces, constructed cross sections utilised all available outcrop, well and published data and were subsequently balanced to ensure geological correctness (see section 5.2.4). The accuracy of the fault surfaces was more problematic, with a lack of subsurface data forcing faults to be modelled as planar surfaces with constant dip and down-fault throw. Section balancing indicated the interpretations were structurally reasonable, though vertical variations in throw are expected and well documented in the literature (Peacock, 2002 and references within).

To assess the effect of vertical throw changes on juxtaposition and argillaceous smear, a Juxtaposition diagram was constructed with SGR values at reservoir-reservoir contacts (Fig. 5.20). Vertical blue lines indicate the current maximum throws for the two modelled faults. Using an aspect ratio (fault strike length/ fault dip length) of 2.15 (Nicol et al., 1996), the maximum change in throw within the modelled stratigraphic sequence will be ±15m for the Little Grand Wash Fault and ±20m for the northern fault of the Salt Wash Graben. These changes in throw (shaded area in Fig. 5.20) show no significant variation in juxtapositional

relationships or SGR values. As such, the simplification to a constant vertical throw does not appear to have a significant influence on the sealing potential of either fault.

5.3.5.2 Subsurface Structural Complexities

The presence of multiple fault strands (Childs et al., 1996) or intact relay zones (Imber et al., 2004) can increase the risk of fluid flow across a fault zone. However, assessing this risk has been difficult as these features are commonly below the resolution mapped in the subsurface (Childs et al., 1996; Yielding et al., 2002). Multiple fault strands and relay zones are evident along both the Little Grand Wash Fault and northern fault of the Salt Wash Graben (Fig. 3.3) but have not been incorporated into the model due to the lack of subsurface fault data. The potential influence of these structural complexities on leakage can be significant and as such will be considered separately.

Multiple fault strands can alter the sealing potential of a fault zone by partitioning the total throw between two or more fault strands to create favourable juxtapositions and/or decrease the likelihood of membrane seals forming (Childs et al., 1996). The effect of partitioning is evident at the centre of the Little Grand Wash Fault, where the total throw (260m) is partitioned between the northern (150m) and southern (110m) fault strands. If these fault strands and throw were maintained with depth, there would be several leak points for fluids to migrate across the fault zone (Fig. 5.21a). However, this is unquantifiable as no subsurface data exists to indicate the behaviour of both faults at depth, though the confinement of travertines at the surface (Fig. 4.1) does suggest both faults are sealed and prevent cross-fault fluid flow.

Relay zones are areas of high fault-parallel shear strain that provide soft (intact) or hard (breached) linkage between two interacting fault segments (Walsh and Watterson, 1991). If the relay zone is intact, a through-going ramp connects the footwall and hanging wall between fault segments to provide a fluid pathway through the fault zone. The possibility of breaching and hence ramp destruction can be estimated by calculating the separation/throw ratio (i.e. distance between interacting faults divided by total throw) and comparing it with the probability plot of Imber et al (2004; Fig. 5.21b). This technique was applied to the Little Grand Wash Fault to determine to probability of intact relay zone development at depth along the fault. The greatest distance between fault strands (194m) at the surface was divided by the total

throw (251m) at that location to give a separation/throw ratio of 0.77 (Fig. 5.21b). This corresponds to a less than 10% chance of intact relay zone development along the Little Grand Wash Fault, while the probability would be even less for the northern fault of the Salt Wash Graben due to smaller fault separations combined with greater throws. As such, the risk of cross-fault fluid flow from the presence of intact relay zones is quite small.

5.3.5.3 V_{shale}

V_{shale} is a critical parameter in calculating SGR values and inaccurate curves can lead to unreliable argillaceous smear predictions. Of key importance to V_{shale} is the methodology utilised to determine the curve. Ideally, wire-line logs should be calibrated with core data to determine the mineralogical content of the stratigraphic sequence. However, this is not always done due to budgetary, time or data constraints and commonly wire-line logs are solely used to determine V_{shale}. A potential problem of only using wire-line logs is the misinterpretation of mineralogical content, with gamma logs, in particular, poor detectors of certain clay minerals (i.e. kaolin and mica; Bretan et al., 2003). X-ray diffraction analyses of fault gouge from both modelled faults (see section 3.3) indicate illite and illite-smectite assemblages are the dominant clay minerals with minor amounts of kaolinite and no mica. This suggests the error related to using only gamma logs to determine mineralogical content and hence V_{shale} is probably small. However, without direct calibration with core data uncertainty remains, and as such SGR values that are close to the threshold value for a continuous argillaceous smear (i.e. 18%) are treated with caution while more higher values (>25%) are considered more robust.

5.3.5.4 Other Sealing Mechanisms

Fault seal analysis in this study was limited to assessing sealing caused by stratigraphic juxtaposition and argillaceous smear development. Cataclasis and cementation were not considered due to no suitable algorithms available to assess the sealing potential of these processes. However, field and experimental studies have demonstrated that both can form effective membrane seals (Antonellini and Aydin, 1994; Fowles and Burley, 1994; Fulljames et al., 1997; Crawford, 1998; Ngwenya et al., 2000). As such, the sealing capacity of Little Grand Wash Fault and northern fault

of the Salt Wash Graben can only be enhanced by these processes, though there effects remain unknown.

5.3.5.5 Fluid Properties

Fault seal analysis has been developed to predict the trapping capabilities of faults primarily in relation to hydrocarbons (i.e. Gibson, 1994; Leveille et al., 1997; Davies et al., 2003). This study differs in considering the trapping of CO_2 as opposed to hydrocarbons. Carbon dioxide is a more complex compound in relation to subsurface migration with contrasting properties dependent on phase (i.e. gas, liquid or supercritical). Considering local temperature and pressure conditions derived from the geothermal gradient (Nuccio and Condon, 1996) and depth of aquifers, CO_2 will be in the gas phase (Wingate, Navajo and Entrada Sandstones) or liquid phase (White Rim Sandstone) for all stratigraphy around the modelled faults (see section 5.4.3). In these phases, CO_2 is miscible with water, contrary to hydrocarbons, but varied in density. This results in migration being limited to one-phase flow that is only retarded by low-permeability barriers. Mechanisms that reduce permeability along a fault and cause sealing have been identified primarily as juxtaposition of reservoir-nonreservoir lithologies (Watts, 1987; Allen, 1989; Knipe, 1997) and presence of continuous argillaceous smears that develop at SGR values in excess of 20% (Foxford et al., 1998; Sperrevik et al., 2000; Yielding et al., 2002). These low-permeability mechanisms are prevalent in the central zones of the Little Grand Wash Fault and northern fault of the Salt Wash Graben, where cross-fault sealing is expected due to the confinement of CO_2 surface leak products (i.e. travertines) in the footwalls of both faults. Therefore, the fault seal techniques developed for hydrocarbons appear to be applicable for predicting the sealing behaviour of faults in relation to CO_2. However, further case studies of fault sealing potential related to CO_2 flow are needed to substantiate these findings and accurately calibrate threshold values for sealing mechanisms in relation to CO_2. In addition, care is needed in elucidating the CO_2 phase as thermodynamic and miscibility properties vary between phases.

5.3.6 Fault-Associated Migration of Carbon Dioxide

Natural focussed leakage of CO_2 in the Paradox Basin is evident along the Little Grand Wash Fault and northern fault of the Salt Wash Graben. To identify the

migration pathways of CO_2 in relation to both faults, fault seal potential and surrounding stratigraphic geometries need to be considered. Assessment of juxtaposition and argillaceous smear along both faults indicate leakage at lower throws (<100m) towards and at the fault tips due to reservoir self-juxtaposition and sealing at higher throws (>100m) due to reservoir-nonreservoir juxtapositions and development of continuous argillaceous smears. Considering surrounding stratigraphy, faulting of the shallowly north-plunging Green River Anticline has created structural highs in the footwalls of both faults. Assuming buoyancy drives CO_2 migration, flow would be channelled away from the fault tips and focussed along the hinge line into the central zone of both faults, where structural elements would combine to form an anticlinal trap with a lateral southern fault closure. The sealing nature of both faults would restrict cross-fault leakage; while confinement of CO_2 surface leak points to the immediate footwall (Fig. 4.1) suggests migration of CO_2 through this faulted system is restricted to fault-parallel flow in both footwalls.

A concern with this flow pathway is the upward migration of CO_2 through shale-rich cap rocks, which are lithologically similar to cap rocks that have retained their integrity in other natural CO_2 reservoirs elsewhere in the Paradox basin (i.e. Lisbon and McElmo Domes; Fig. 2.1). A potential mechanism to enable migration of CO_2 through these shale-rich units is by the development of open fracture networks that can be a feature of damage zones. Damage zones can contain an array of deformation features that can enhance or reduced the relative permeability of the host rock (Caine et al., 1996; Sibson et al., 1996; Gudmundsson et al., 2001). In this study, damage zones are characterised by a marked increase in fracture density close to the faults with intense fracture networks developing around structural complexities (see section 3.3.3). The localisation of CO_2 surface leak points around many of these structural complexities (i.e. fault bends and relay ramps; Fig. 4.1) in the immediate footwalls of both faults, provides direct evidence that CO_2 is upwardly migrating along these fracture networks in the footwall damage zone. Further work is needed to characterise the features (i.e. fracture networks) and relative permeabilities of damage zones in various lithologies at differing throws. This will provide a better understanding of cap rock integrity and migration pathways in reservoir setting cut by fault systems.

In summary, based on the fault seal analysis and outcrop mapping, the migration pathways of CO_2 through the faulted stratigraphy from depth to the surface

is predominantly influenced by the main structural features of the local area. Work by Heath (2004) has indicated that CO_2 is expelled from Triassic and sub-Permian source rocks to charge the Wingate and White Rim Sandstones, respectively. The folded nature of the stratigraphy (i.e. Green River Anticline) focuses CO_2 towards the central, sealing sections of the Little Grand Wash Fault and northern fault of the Salt Wash Graben to form anticlinal traps with lateral southern fault closures. Enhanced permeability in the footwall damage zone enables the CO_2 to migrate vertically through overlying shale-rich cap rocks to charge successively shallower fault-sealed aquifers (i.e. Navajo and Entrada Sandstones). This fault-parallel migration pathway is continued until the CO_2 escapes to the surface to precipitate as travertine or vent into the atmosphere.

5.3.7 Fault Seal Summary

Fault seal techniques developed in the hydrocarbon industry have been used to investigate the sealing potential of the Little Grand Wash Fault and northern fault of the Salt Wash Graben in relation to CO_2 migration. Within the studied traps, CO_2 is in the miscible gas or liquid phases resulting in migration being governed by one-phase flow and retarded only by low permeability barriers caused by favourable juxtapositions (reservoir against nonreservoir) and continuous argillaceous smears along faults and overlying shale-rich, cap rocks. Assessment of fault sealing mechanisms for both faults indicate leakage at low throws (<100m) due to reservoir self-juxtaposition and sealing at higher throws (>100m) due to reservoir-nonreservoir juxtaposition and development of continuous argillaceous smear. Folded geometries of the surrounding stratigraphy indicate CO_2 migration in the reservoir units is being channelled towards the central, sealing sections of both faults to form fault-sealed anticlinal traps. Leakage from these traps is most likely through the overlying shale-rich, cap rocks via fracture networks developed in the footwall damage zones of both faults.

The results of this analysis have highlighted two important points: (1) fault seal techniques can be adapted to investigate the sealing behaviour of faulted traps identified for potential CO_2 geologic storage; and (2) the damage zone can potentially play a fundamental role in providing vertical conduits for fluids to escape through overlying shale-rich cap rocks. Further case studies of fault-sealed CO_2 reservoirs are

now required to corroborate these findings and better calibrate fault sealing techniques to CO_2. Additional work is also needed in understanding of the role damage zones can play in compromising the sealing capacity of overlying cap rock units.

5.4 Volumetrics

5.4.1 Introduction

Assessing the storage capacity of CO_2 in subsurface reservoirs is a central theme of geological sequestration (Hendrick and Blok, 1993; Bachu et al., 1994; van der Meer, 1995; Brennan and Burruss, 2003). Ideal reservoir conditions for sequestration will have CO_2 in the supercritical phase ($T \geq 31.04^{o}C$; $P \geq 73.82$bars), saline pore-waters and relatively high porosities to ensure volumetrically-efficient and environmentally-friendly storage (Holloway and Savage, 1993; Bachu et al., 1994). At these conditions, one tonne of CO_2 will be immiscible with water and occupy less than $6m^3$ of rock, assuming 30% porosity and 80% displacement of in-situ pore waters (Chadwick et al., 2004). In this study area, all potential shallow traps (White Rim, Wingate, Navajo and Entrada Sandstones) identified by Heath (2004) are saline but have CO_2 in subcritical (gas or liquid) phases.

The aim of this section is to calculate the properties and storage capacity of CO_2 in saline aquifers that form anticlinal traps laterally sealed by the Little Grand Wash Fault. This will provide insight into the efficiency of storing CO_2 in subcritical phases. More importantly, comparison of the total storage capacity of the traps with the amount of CO_2 calculated to have leaked to the surface (see section 4.3.2.3) will demonstrate the effectiveness of the faulted stratigraphy in trapping migrating CO_2. Volumetric analysis of traps associated with the northern fault of the Salt Wash Graben were not performed due to gaps in the travertine data (see section 4.3.2.3) and the surface breaching of a main aquifer (Entrada Sandstone) diffusing regions of CO_2 leakage.

5.4.2 Method

CO_2 is a buoyant, reactive compound that will not remain static in the subsurface. At subcritical reservoir conditions ($T<31.04^{o}C$ or $P<73.82$bars; Fig. 5.22), CO_2 will coexist as a free bulk phase (gas or liquid) and as a CO_2-rich aqueous phase

dissolved in the local pore waters (Pruess and Garcia, 2002). With time, a third phase of CO_2 chemically bound in solid minerals will develop, though this has not been considered as numerical modelling is needed to adequately quantify this phase (Pruess et al., 2001; Johnson et al., 2004). Therefore, to calculate the storage capacity of the aquifers (White Rim, Wingate, Navajo and Entrada Sandstones) sealed by the Little Grand Wash Fault, mass estimates for the CO_2 in the free$_{(f)}$ and aqueous$_{(aq)}$ phases were solved by (Pruess et al., 2001):

$$M_{CO_2} = \phi_v (X_f \rho_f S_f + X_{aq} \rho_{aq} S_{aq})$$

where M_{CO2} is the mass of CO_2 (kg), ϕ_V is the available pore volume of each trap (m^3), X is mass fraction, ρ is density (kg/m^3) and S is saturation of the free$_{(f)}$ and aqueous$_{(aq)}$ phases in each aquifer. Available pore volume is defined as the trap volume multiplied by porosity. Volumetric calculations of trap size were performed in 3DMove, based on the assumptions of: (1) the lateral extent of travertine distribution at the surface defines the minimum lateral extent of the trap at depth; and (2) the CO_2 accumulation in each trap has a horizontal base. Using these assumptions, two fault-dip parallel wells were inserted into the three-dimensional model at the eastern and western boundaries of travertine precipitation along the Little Grand Wash Fault (Fig. 5.23a). The well that intersected each trapping horizon at the greatest depth was taken to be the base of the CO_2 accumulation. A horizontal surface was inserted at this depth (Fig. 5.23b) and the space between the overlying trapping horizon and the horizontal surface was calculated as the trap volume (Fig. 5.23c). This was repeated to get the trap volumes for all four aquifers (Fig. 5.23d). Porosities were assumed to not be affected by CO_2-induced mineral dissolution or precipitation and average values were taken from the literature (i.e. Hood and Patterson, 1984; Antonellini and Aydin, 1995; Hansley, 1995) to determine the available pore volume of each trap.

To assess the properties of CO_2 within each aquifer, the temperature and pressure conditions must be known. Temperature was calculated by:

$$T = T_0 + G\,Z$$

where T_0 is annual surface temperature (10°C; Utah Climate Centre), G is geothermal gradient (21.1°C/km; Smouse, 1993) and Z is depth to base of trap. Pressure was assumed hydrostatic and calculated by:

$$P = \rho_w g Z$$

where ρ_w is density of water (1000kg/m^3), g is gravity (9.8m/s^2) and Z is depth to base of trap. Based on the calculated pressures and temperatures, the density of the free phase is taken directly from Lemmon et al. (2005). The corresponding mass fraction is assumed 1, even though the phase will have a minor component of water vapour (Pruess et al., 2001). The mass fraction of the aqueous phase is calculated using the geofluids solubility model of Duan et al. (1995) and corrected for salinity conditions in the local pore waters using the equation (Seibt et al., 1999):

$$X^{CO2} = \frac{X_0^{CO2}}{10^{(0.085C)}}$$

where X^{CO2} is the mass fraction of CO_2 in saline pore waters at aquifer conditions, X_0^{CO2} is the mass fraction of CO_2 in pure water calculated from Duan et al. (1995) model and C is NaCl concentration of pore waters (~17000TDS ≈ 0.36 mol/L; Heath, 2004). The density of the aqueous phase was calculated using total solution densities also calculated by the Duan et al. (1995) model and conversion spreadsheets supplied and based on Brennan and Burruss (2003). The relative saturations of the free (S_f) and aqueous (1-S_f) phases are more difficult to quantify. Depending on the CO_2 discharge-recharge rates, individual aquifers could be free phase dominated (S_f=1), aqueous phase dominated (S_f =0) or mixed (0> S_f <1). The only method to limit this range of saturations would be through dynamic modelling of flow in the CO_2 system (K. Pruess per comm). This represents a significant portion of research that is beyond the scope of this study. Therefore, end-member saturation values were used to predict the maximum and minimum storage capacities of each aquifer. These values were subsequently compared with estimates of CO_2 surface leakage to assess the integrity of the faulted system in storing CO_2.

5.4.3 Results

The characteristics and storage capacities of CO_2 in the aquifers sealed by the Little Grand Wash Fault are listed in Table 5.1. Variations in temperature and pressure conditions result in CO_2 being in either the subcritical gas (Wingate, Navajo and Entrada Sandstones) or liquid (White Rim Sandstone) phases for the studied aquifers. This change in phase is accompanied by a significant shift in CO_2 density with shallow, gas-phase aquifers having low densities (36-100kg/m^3) compared to the deeper, liquid-phase White Rim sandstone (753kg/m^3). Proportional to density, storage efficiency in shallow aquifers requires between 10 to 27m^3 of pore volume to accommodate one tonne of CO_2, while the White Rim Sandstone only needs 1.3m^3. Efficiency is diminished for all aquifers if CO_2 is present in the aqueous phase with between 28 and 76m^3 of pore volume needed to store one tonne of CO_2 in the same aquifers at identical conditions.

The storage capacity of CO_2 in individual aquifers is dependant on available pore volume, aquifer conditions and CO_2 saturation. The Entrada Sandstone has the largest available pore volume ($7.9x10^6m^3$) but smallest CO_2 capacity ($1x10^5_{(aq)}$ - $2.8x10^5_{(f)}$ tonnes) due to the shallowness of the trap. Alternatively, the White Rim Sandstone has the smallest pore volume ($6.5x10^6m^3$) but largest capacity ($2.4x10^5_{(aq)}$ - $4.9x10^6_{(f)}$ tonnes) due to its depth causing CO_2 to be present in the liquid phase. The total CO_2 capacity for all four aquifers is between $6.4x10^5_{(aq)}$ and $6.3x10^6_{(f)}$ tonnes. Volumetric calculations of travertines along the Little Grand Wash Fault (see section 4.5) indicate approximately $1.9x10^6$ tonnes of CO_2 have leaked to the surface in the last 78,000 years. Comparison of the aquifer capacities and leak estimates reveal the combined aquifers discharged between 30% (free phase) and 300% (aqueous phase) of their total capacity. The actual proportion of CO_2 that has discharged from this system could not be determined from this investigation but would be between these two end member estimates.

Table 5.1: Properties and storage capacities of CO_2 in aquifers sealed by the Little Grand Wash Fault

Aquifer	Temperature[1] (K)	Pressure[1] (bars)	Phase	CO_2 Density		CO_2 Efficiency		Total Reservoir Volume (m^3)	Porosity[2] (%)	Available Pore Volume (m^3)	CO_2 Capacity	
				Free Phase (kg/m^3)	Aqueous (kg/m^3)	Free Phase (m^3/tonne)	Aqueous (m^3/tonne)				Free Phase (tonnes)	Aqueous (tonnes)
Entrada	286.8	17.6	Gas	36	13	27	76	$4.4x10^7$	0.18[a]	$7.9x10^6$	$2.9x10^5$	$1.0x10^5$
Navajo	288.0	22.9	Gas	49	16	20	61	$3.9x10^7$	0.18[b]	$7.0x10^6$	$3.5x10^5$	$1.2x10^5$
Wingate	291.7	40.4	Gas	100	26	10	39	$3.5x10^7$	0.20[b]	$7.1x10^6$	$7.1x10^5$	$1.8x10^5$
White Rim	300.3	80.1	Liquid	753	36	1.3	28	$2.6x10^7$	0.25[c]	$6.5x10^6$	$4.9x10^6$	$2.4x10^5$
										Total	$6.3x10^6$	$6.4x10^5$

1 Temperature and pressure values calculated at base of predicted CO_2 accumulations in each trap.
2 Average porosity data from Antonellini and Aydin (1995)[a], Hood and Patterson (1984)[b] and Hansley (1995)[c].

5.4.4 Discussion

For the range of temperature and pressure conditions found in sedimentary basins, CO_2 can be a gas, liquid or supercritical fluid (Fig. 5.22). The change in phase from gas to liquid or supercritical fluid with increasing depth is accompanied with a sharp increase in density (Chadwick et al., 2004). This is observed in this study with the gas-phase aquifers (27-100kg/m^3) having significantly lower densities than the liquid-phase White Rim aquifer (753kg/m^3). Densities required for effective storage of CO_2 range between 600-800kg/m^3 (Gunter et al., 2004). Therefore, the White Rim Sandstone is the only aquifer with reservoir conditions suitable for CO_2 storage.

Utilising the calculated densities, preliminary evaluations of storage capacities were derived from volumetric estimates. Minimum and maximum capacities were calculated based on the assumptions of no mineral precipitation associated with CO_2 storage and each faulted-sealed aquifer being aqueous ($S_f = 0$) or free phase ($S_f = 1$) filled. Depending on reservoir mineralogy, CO_2 can be precipitated out as carbonate minerals within the aquifers leading to small decreases in porosity, larger decreases in permeability and possible long term reductions in storage capacity (Pruess et al., 2001; Gunter et al., 2004; Johnson et al., 2004). In addition, variations in CO_2 influx and leakage rates in each aquifer control saturations and subsequent capacities of CO_2. To consider both factors in the storage capacity calculations would require a dynamic modelling approach using numerical simulators such as TOUGH2 (see Pruess, 2004). This modelling approach represents a significant amount of work that

is beyond the scope of this research, though this is the next logical step in better defining the leakage rates from this faulted system.

The total storage capacities for all four aquifers ranges from $0.6_{(aq)}$ to $6.3_{(f)}$ million tonnes of CO_2 with the White Rim Sandstone contributing between $37\%_{(aq)}$ and $78\%_{(f)}$ of the total capacity, respectively. These storage capacities indicate that the saturation state and density of CO_2 are the main factors influencing the storage capacity of a reservoir. Current industrial-scale projects (Sleipner, Weyburn, In Salah and Gorgon) are injecting CO_2 into the subsurface at rates of 1 to 4 million tonnes per year (Zweigel et al., 2004; Benson, 2005). Future sequestration projects are expected to be scaled up to a rate of 8-10 million tonnes per year to cover the annual amount of CO_2 expelled from a typical 1000MW coal-fired power plant (Benson, 2005). Even the maximum capacity of the studied aquifers would be small and uneconomic when compared with the current and planned storage projects. However, the benefit of the volumetric analysis is to quantify the leak rates of CO_2 from a natural reservoir in a structural setting that may be considered in future storage projects.

Estimating leak rates from this natural system is important in quantifying the risk associated with seal failure. All seals will leak through time with integrity dependant on the time scale considered. Geologic storage of CO_2 must be secure for hundreds to several thousands of years (Wildenborg et al., 2005). Depending on CO_2 saturations, volumetric calculations of modelled aquifers and mapped travertines indicate the combined, fault-sealed aquifers have leaked between 30% (free phase) and 300% (aqueous) of their total capacity over a 78,000 year period. This converts to a leak rate of 0.2% (free phase) to 1.9% (aqueous) every 500 years or 3.9% (free phase) to 37.9% (aqueous) every 10,000 years. Whether these rates are tolerable is unclear as no guidelines could be located to indicate the maximum leak rates acceptable for CO_2 storage. A possible concern would be any adverse effects to the surrounding environment from leakage. Carbon dioxide flux calculations in section 4.4.4 suggest this is not an issue for this system and is supported by personal observations and anecdotal evidence that indicate little or no adverse effects to the local ecosystem or humans from CO_2 leakage. Therefore, while CO_2 storage in fault-sealed reservoirs increases the risk of leakage, the rate of leakage may not be significant for the duration of time needed for storage. Further work is needed to better define the leak rates of this system through the implementation of dynamic

models as well as investigating additional fault-sealed CO_2 reservoirs to ascertain the frequency and rates of leakage in these structural settings.

5.4.5 Volumetric Summary

Volumetric investigations of modelled aquifers sealed by the Little Grand Wash Fault were conducted to estimate the storage capacity of CO_2 in the faulted system. Varying aquifer conditions result in CO_2 being in the gas (Wingate, Navajo and Entrada Sandstones) or liquid (White Rim Sandstone) phases, with each aquifer containing CO_2 in a free bulk phase (gas or liquid), dissolved in water and possibly precipitated out as a mineral phase. To quantify all three states in each aquifer would require modelling beyond the scope of this research and simplified maximum (free-phase filled) and minimum (aqueous-filled) storage capacities were calculated instead. The White Rim Sandstone stores the most CO_2, due to its dense, liquid-phase conditions, though the total storage capacity of the system is significantly smaller than current or planned industrial-scale geologic storage projects. Comparison of the total subsurface capacity with surface estimates of CO_2 leakage indicates the combined aquifers have leaked at a rate of 3.9 to 37.9% of their total capacity every 10,000 years. Whether these rates are acceptable for geologic storage projects is uncertain, though the leakage does not appear to have a significant adverse effect on the surrounding environment.

5.5 Conclusions

A three-dimensional model was created from a variety of exploration well, wire-line log, published and field data. Isopach and structure maps generated from this available data were used as templates to create cross sections. The sections were subsequently connected in three-dimensional space to create surfaces representing faults or stratigraphic tops for units from the Permian Organ Rock to the Cretaceous Cedar Mountain Formations. Validation of the three-dimensional model was primarily through structural balancing and surface geologic data. The resultant model was used to investigate subsurface CO_2 migration pathways and trap integrity through fault seal and volumetric analyses. Fault seal analysis of the Little Grand Wash Fault and northern fault of the Salt Wash Graben indicated both faults leak at low throws (<100m) due to reservoir self-juxtaposition and seal at higher throws (>100m) due to reservoir-nonreservoir juxtapositions and development of continuous argillaceous

smears. The folded geometry of the surrounding stratigraphy channels CO_2 to these central, sealing sections of both faults to form anticlinal traps with lateral southern fault closures. Subsequent leakage of CO_2 from each trap is up through overlying cap rocks via fracture networks developed in the footwall damage zones of both faults. Quantifying the proportion of CO_2 that has leaked via this migration pathway was estimated by calculating the CO_2 storage capacities of the aquifers sealed by the Little Grand Wash Fault and comparing these capacities with CO_2 surface leak estimates derived from travertines. Volumetric calculations indicate the combined aquifers leak between 3.9 (free phase) and 37.9% (aqueous) of their total CO_2 capacity every 10,000 years, which may or may not be low enough for CO_2 geologic storage projects that require subsurface residence times of hundreds to thousands of years. Future work as outlined in this chapter could include additional case studies of fault-sealed CO_2 reservoirs to further test and calibrate fault seal techniques in relation to CO_2, dynamic modelling to better define storage capacities and associated leak rates, and investigation of damage zones in different lithological and displacement settings to characterise the flow conductivity along these structures.

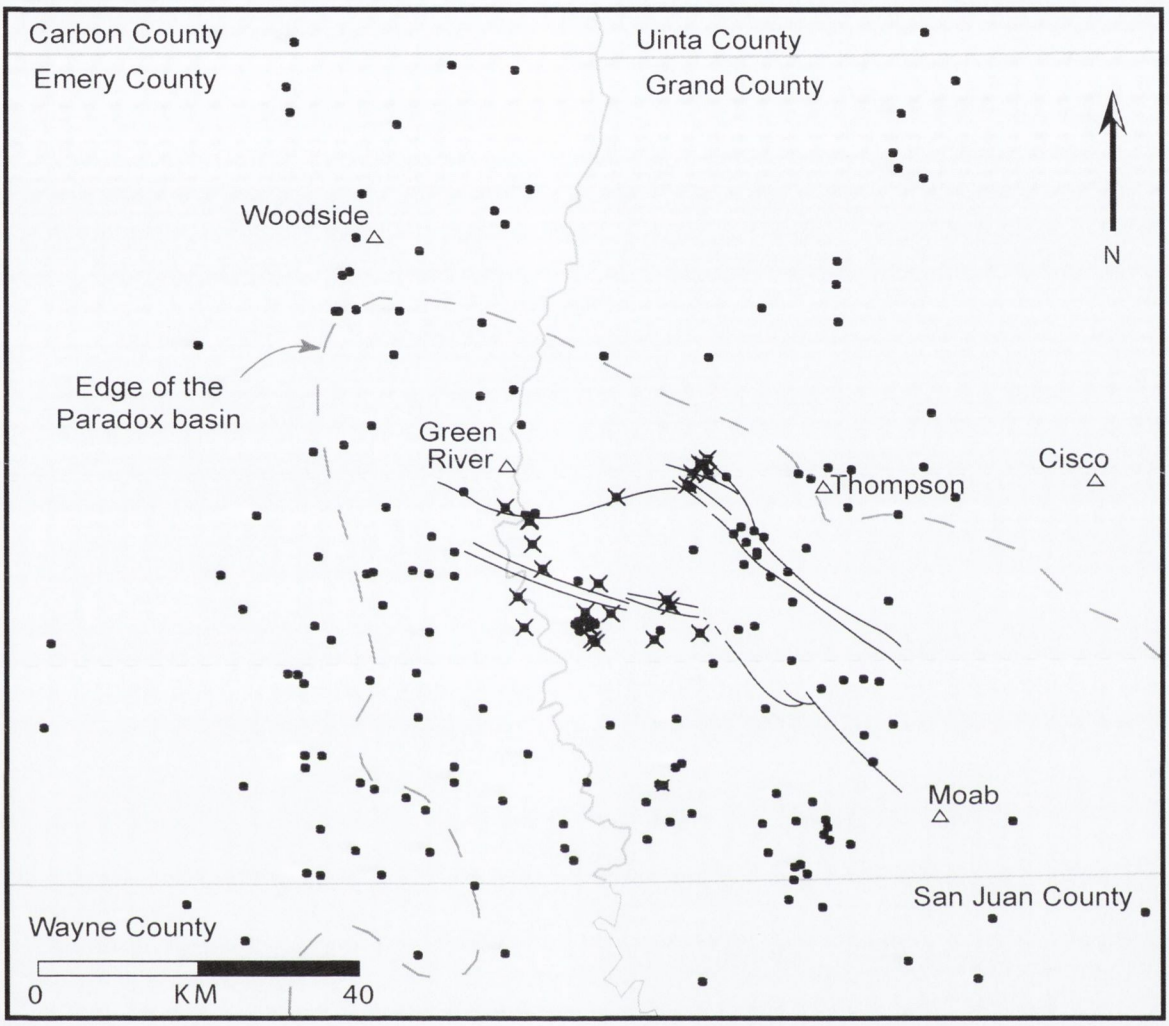


Figure 5.1: Distribution of boreholes used for modelling at the northern end of the Paradox basin and surrounding area. Circles indicate location of boreholes from the well summary database, while crosses indicate boreholes with geophysical logs. Black lines indicate position of faults.

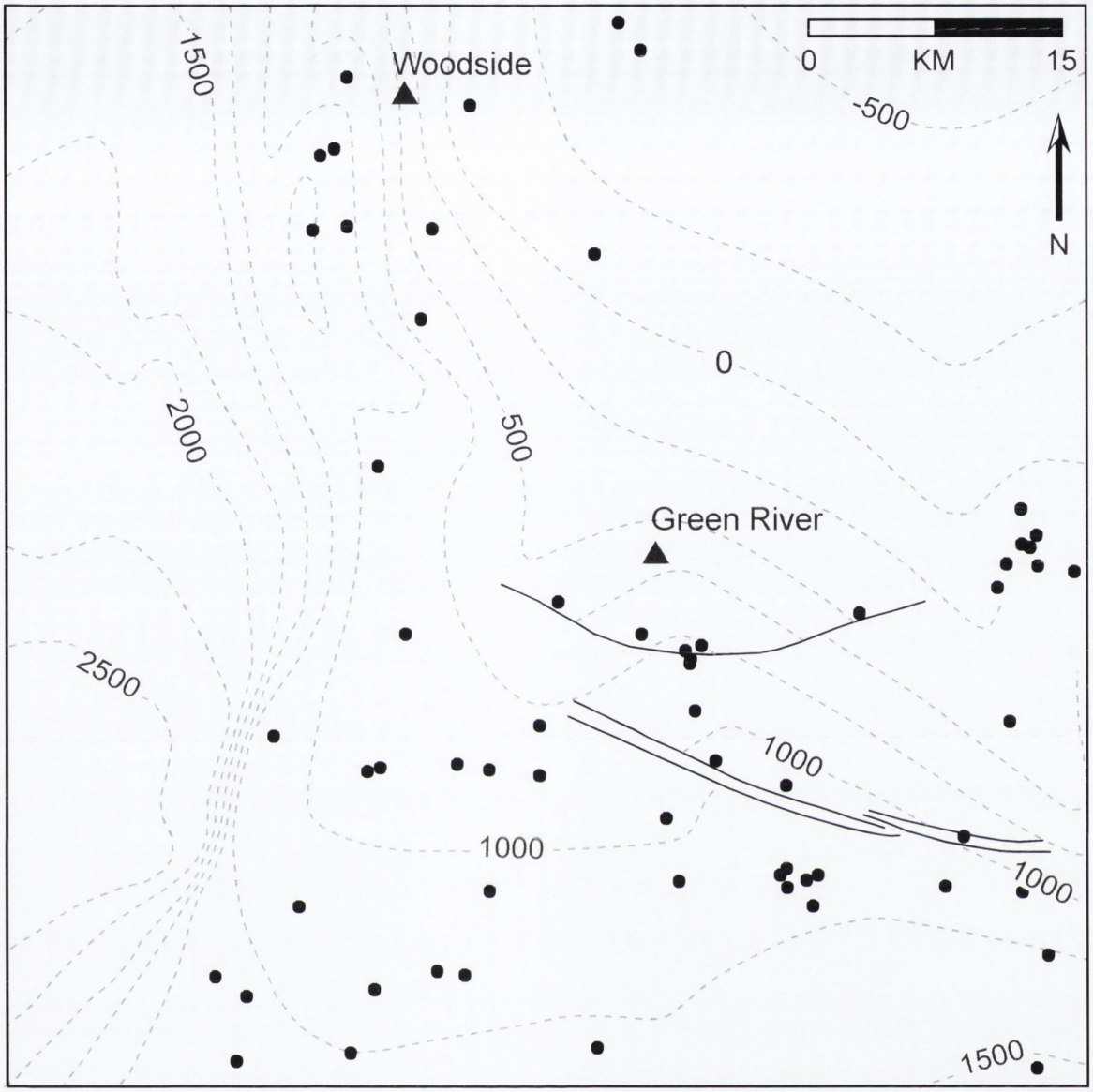


Figure 5.2: Structure contours for the top of the lower Jurassic Navajo Sandstone (after Baker, 1935; McKnight, 1944). Black circles indicate the position of boreholes from the well summary database. Contours are relative to sea level and increase in 250m increments.

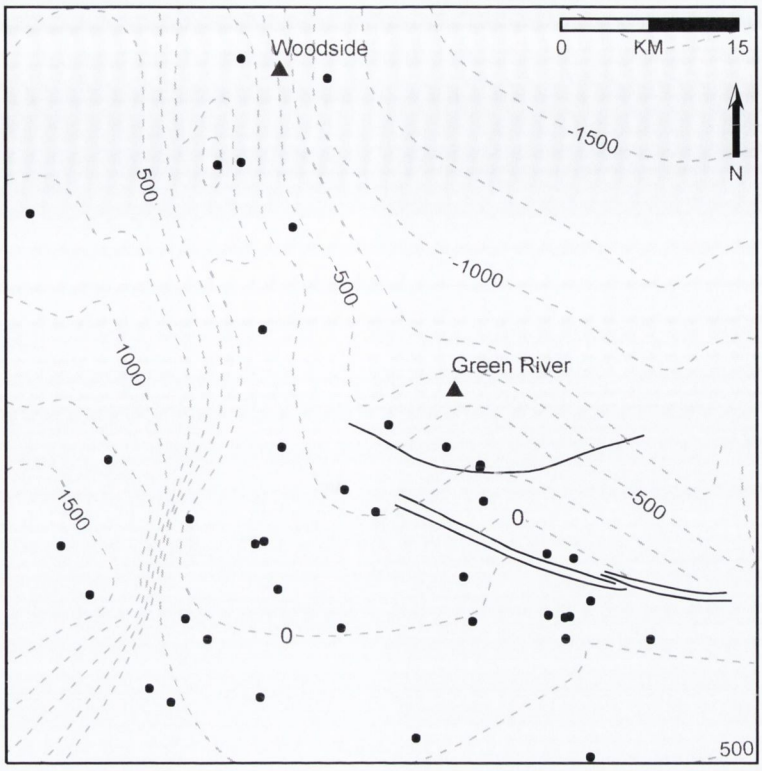


Figure 5.3: Structure contours for the top of the Pennsylvanian Honaker Trail Formation (after Condon, 1997). Black circles indicate the position of boreholes from the well summary database. Contours are relative to sea level and increase in 250m increments.

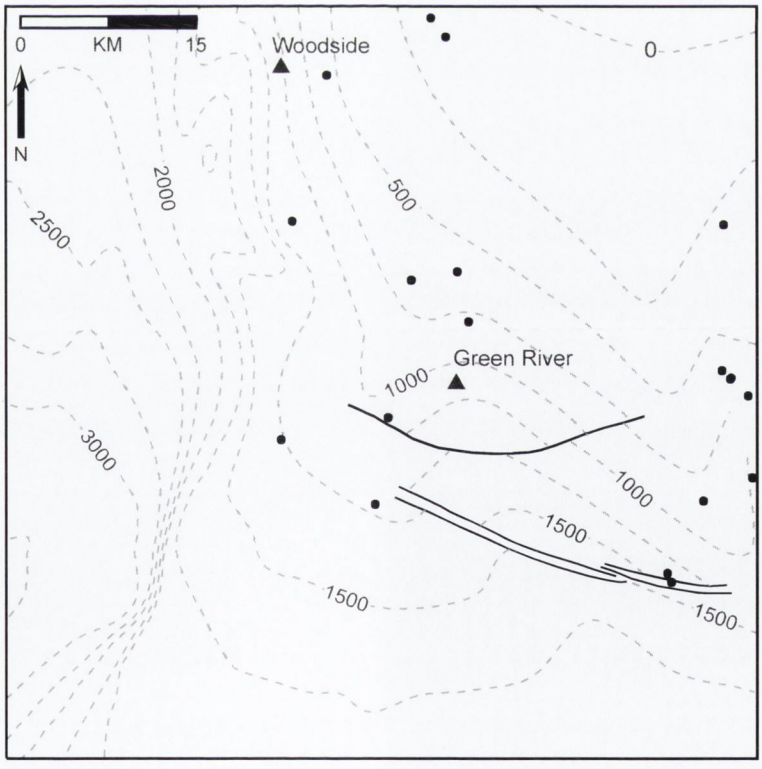


Figure 5.4: Structure contours for the top of the lower Cretaceous Dakota Formation (after Williams, 1964; Williams and Hackman, 1971). Black circles indicate the position of boreholes from the well summary database. Contours are relative to sea level and increase in 250m increments.

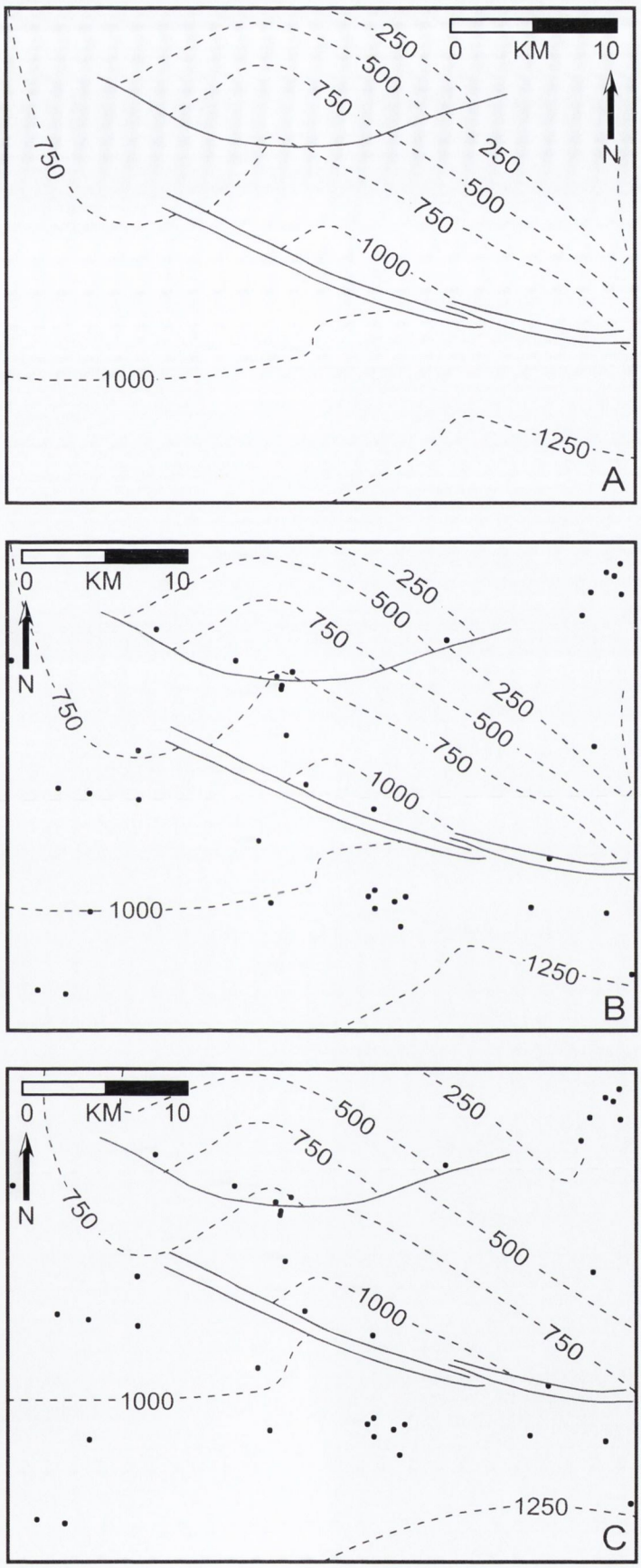


Figure 5.5: Development of the Navajo Sandstone structure map. (a) Structure contours are digitised in ArcView from the McKnight (1944) map. (b) Borehole data from the well database and wire-line logs are added. (c) Contours are adjusted and extended to conform with borehole data, where necessary.

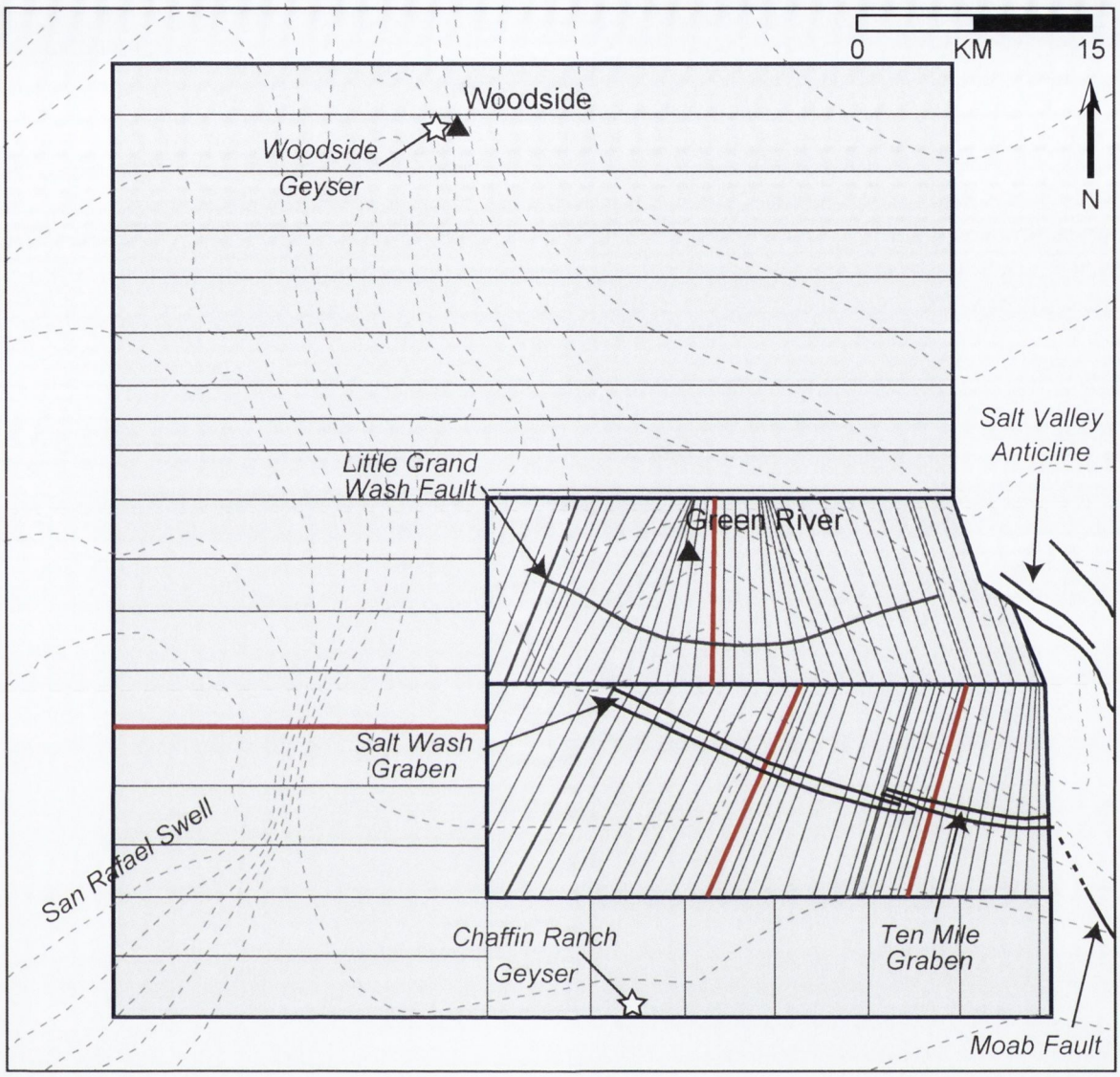


Figure 5.6: Distribution of cross sections generated in 2DMove. The shaded area indicates the limits of the model with thin black lines representing cross section positions. Thick black lines define submodels, while dashed lines represent structure contours for the top of the Navajo Sandstone (Fig. 5.2). Red lines indicate cross sections displayed in Figure 5.9.

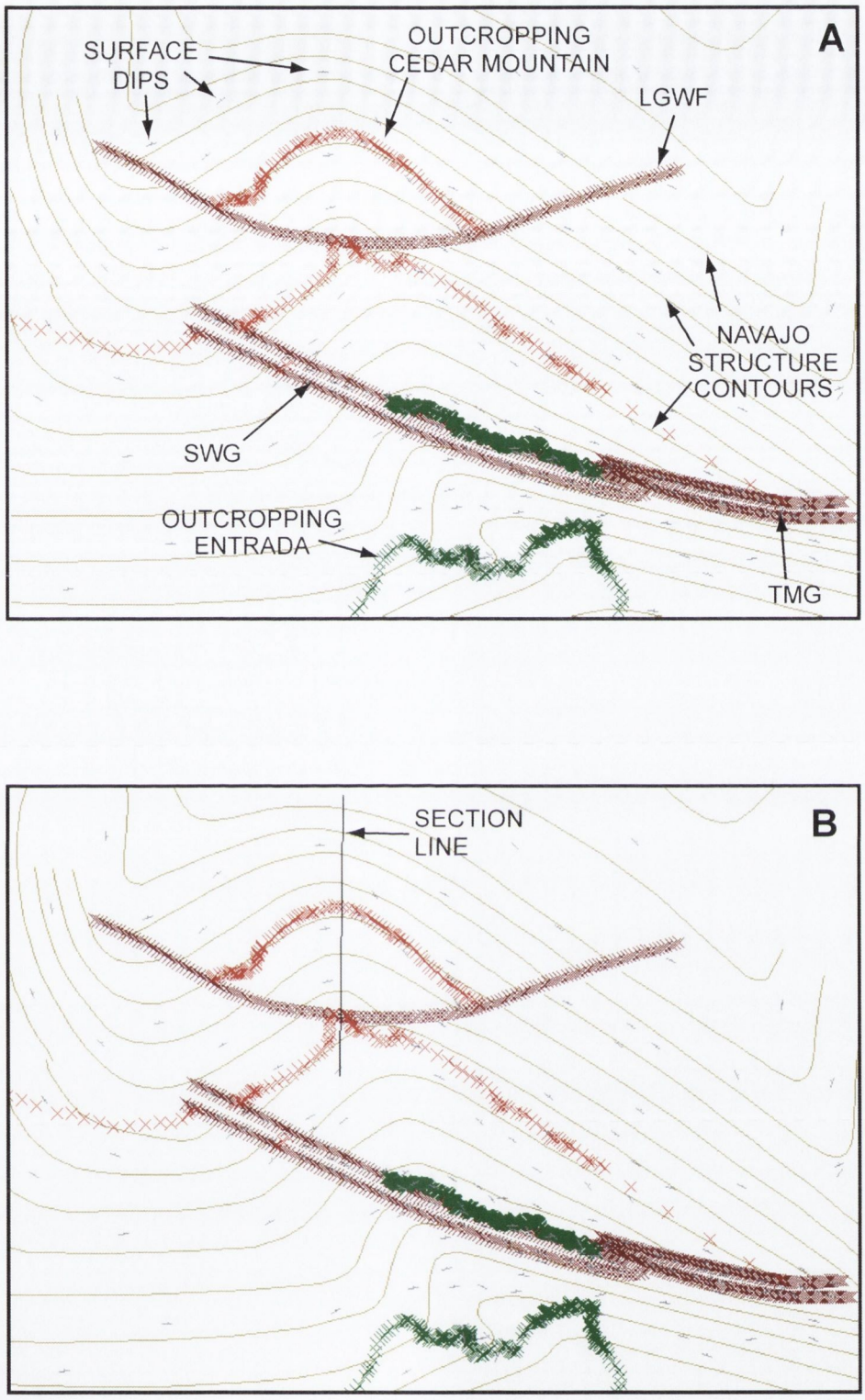


Figure 5.7: 2DMove section construction in map view. (a) Various geologic data used to create sections into the program. Surface position and elevation of faults and outcropping strata represent by crosses. (b) Section is projected and geologic data collected in map view.

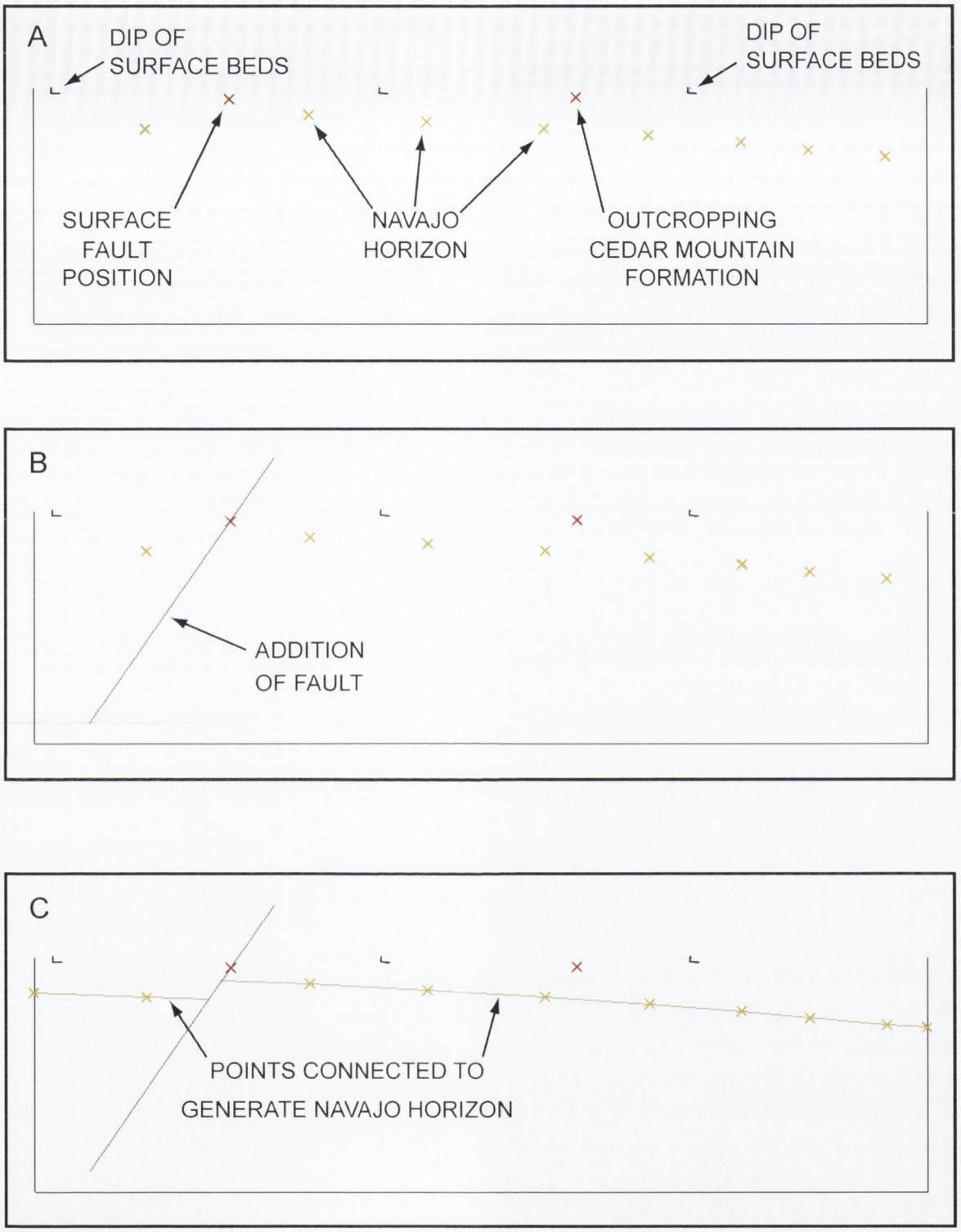


Figure 5.8: 2DMove section construction in section view. (a) Geologic data collected in map view, is displayed as a series of points in section view. (b) The fault is added as a straight line to the section. (c) All points for the Navajo are connected and extended to the fault and section boundaries to create a horizon.

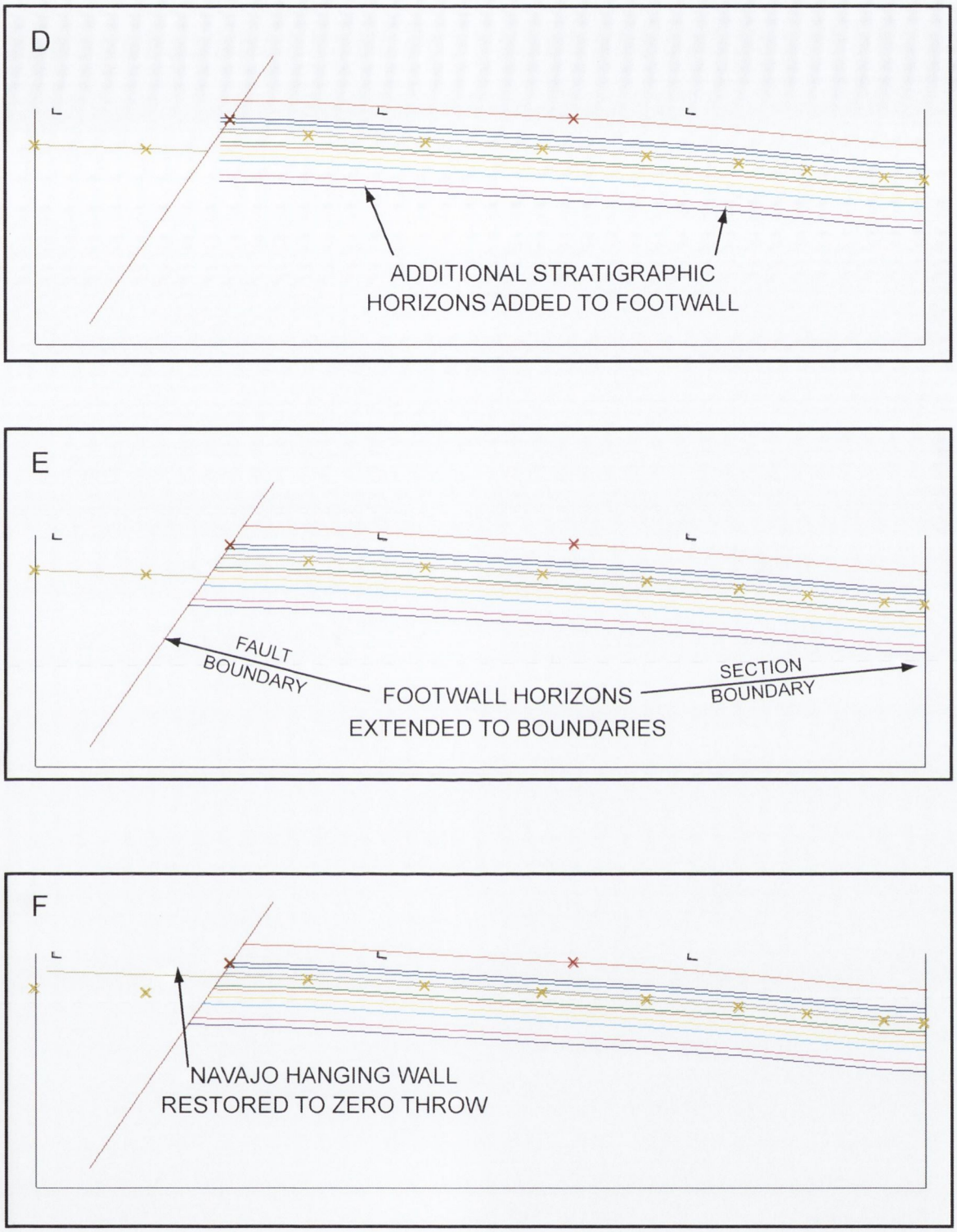


Figure 5.8: 2DMove section construction in section view (continued). (d) Additional stratigraphic horizons are added above and below the Navajo horizon in the footwall. (e) The horizons are tied to fault and section boundaries. (f) The Navajo hanging wall is restored to zero throw, joining the footwall.

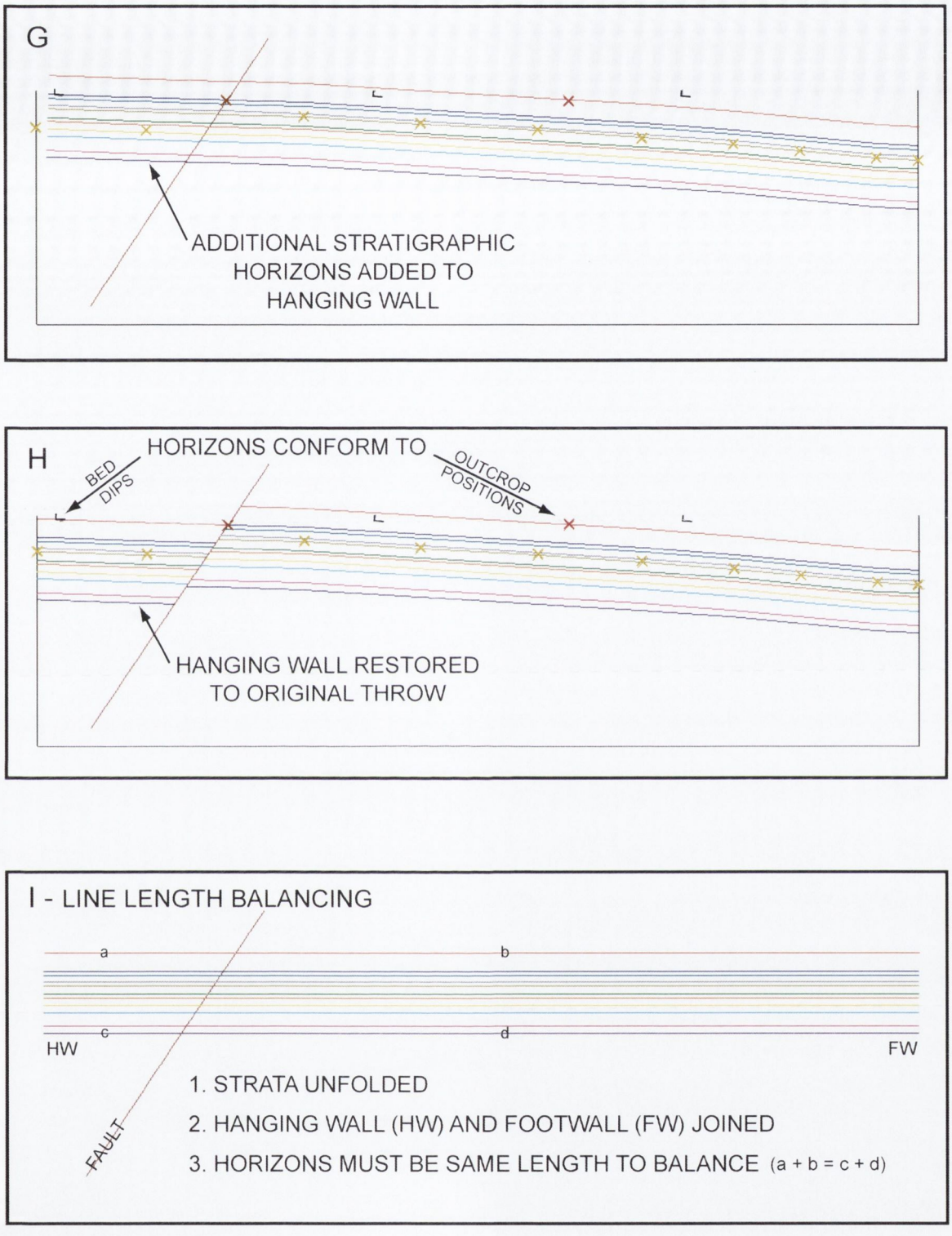


Figure 5.8: 2DMove section construction in section view (continued). (g) Additional stratigraphic horizons are added above and below the Navajo horizon in the footwall. (h) The hanging wall is re-faulted to original throw. Horizons are adjusted to correspond to bed dips and outcrop positions. (i) The section is balance by unfolding the horizons, aligning the footwall and hanging walls and ensuring all horizons are the same length.

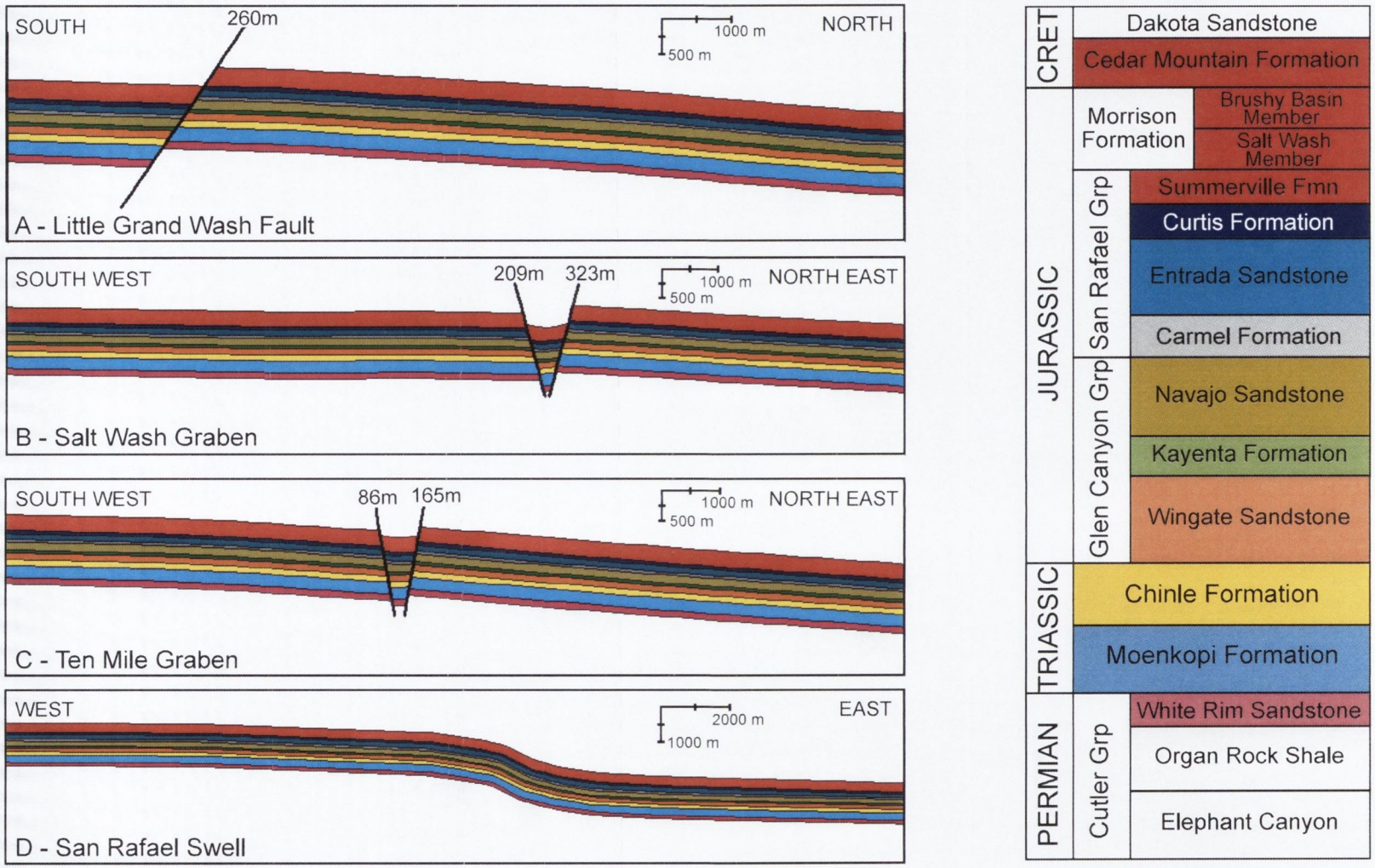


Figure 5.9: Balanced cross sections of the Little Grand Wash fault (a), Salt Wash graben (b), Ten Mile graben (c) and San Rafael Swell (d). Differing colours in the stratigraphic column correspond with stratigraphic horizons in the sections. The amount of throw is specified at the top of each fault. Position of each section indicated in Figure 5.6.

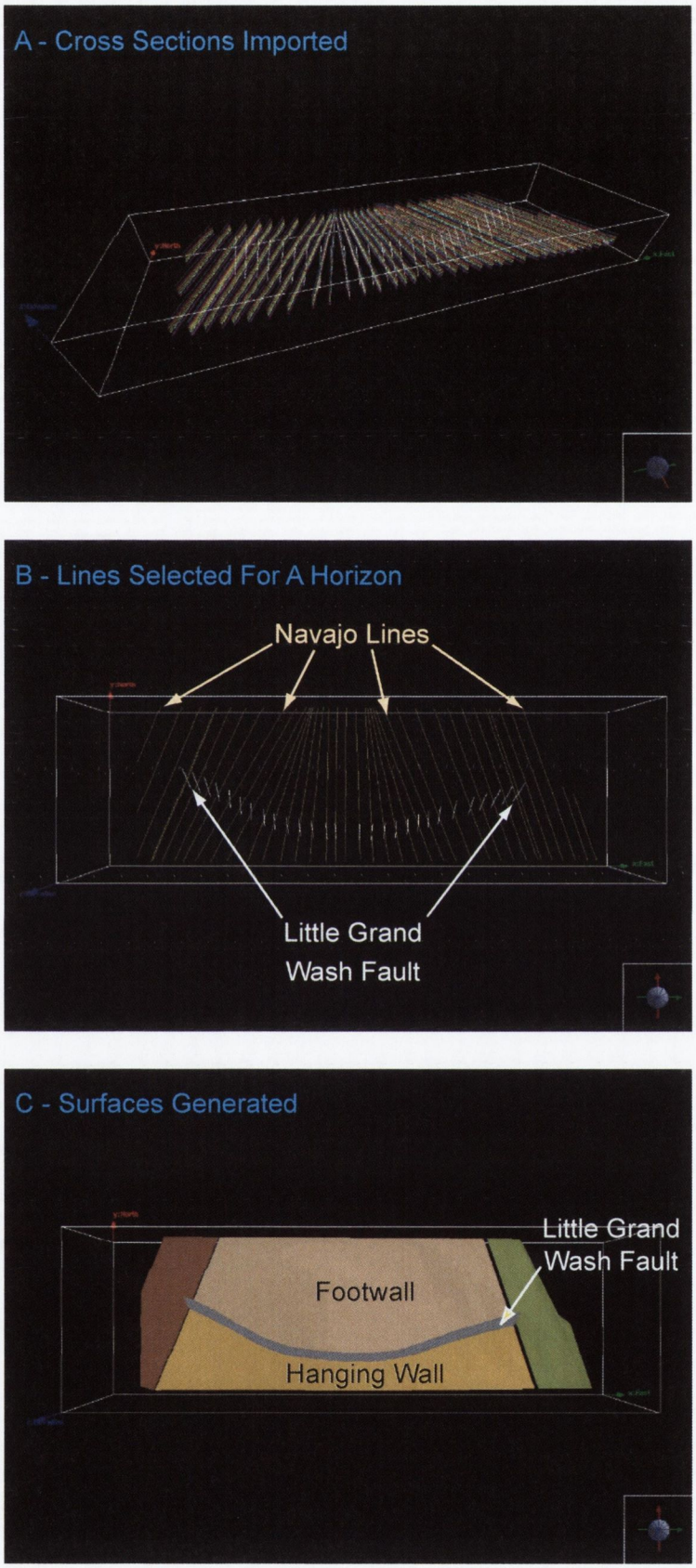


Figure 5.10: 3DMove surface construction. (a) All cross sections for a submodel are imported. (b) All two-dimensional lines for a horizon are selected. (c) The lines are connected to form three-dimensional surfaces. Separate surfaces are generated for the footwall, hanging wall and non-faulted blocks to maintain stratigraphic cutoffs. Fault lines are also joined to make a coherent, planar surface.

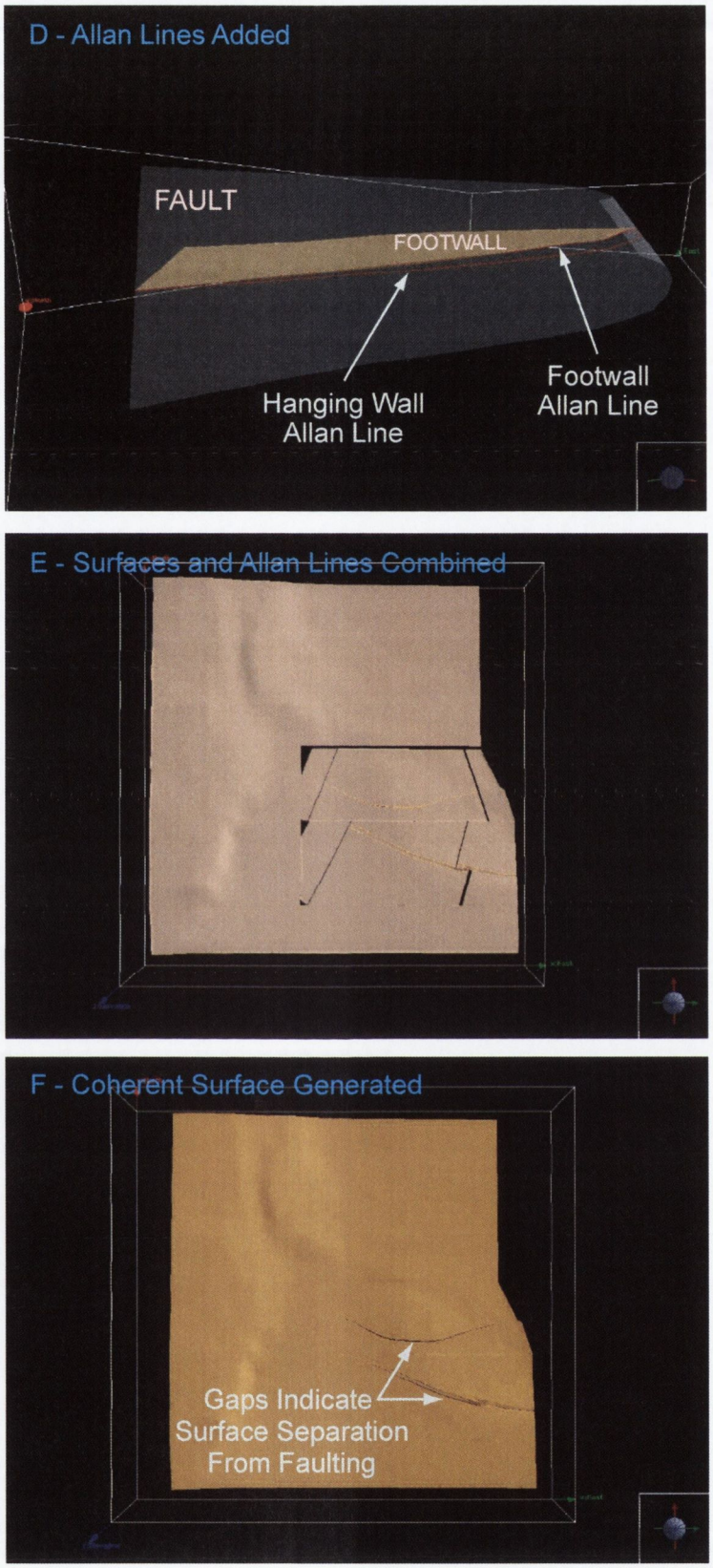


Figure 5.10: 3DMove surface construction (continued). (d) Allan lines are generated at each footwall and hanging wall cutoff to define the intersection between fault and stratigraphy. (e) All surfaces and Allan lines generated for each horizon are then imported into a single model. (f) These components are joined, regridded and excess surface mesh is deleted to make a coherent surface representing the top of a stratigraphic unit. Gaps indicate the separation between the footwall and hanging wall cutoffs along a fault.

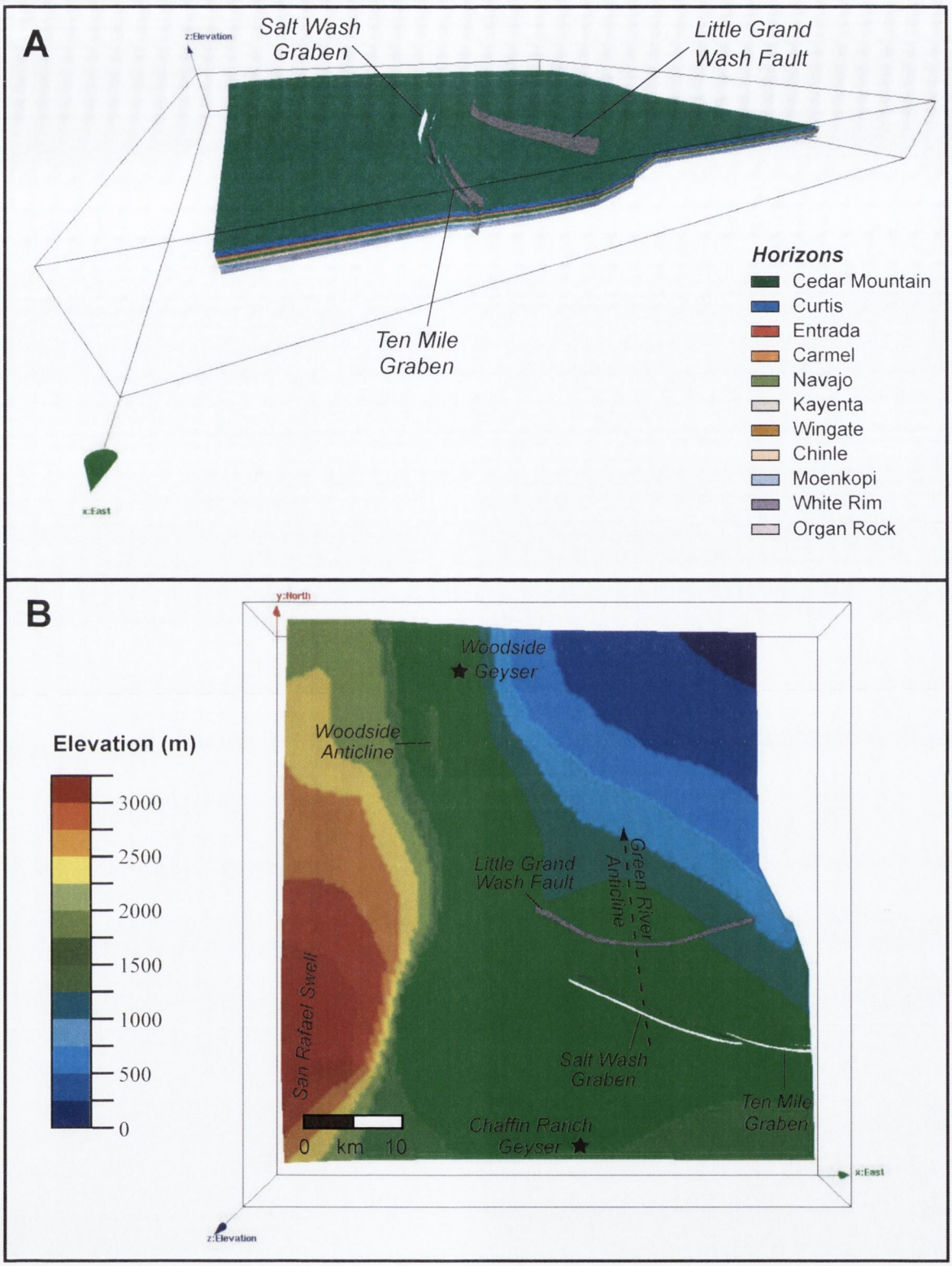


Figure 5.11: Completed three-dimensional model of the Green River area. (a) The model contains five fault surfaces that cut eleven stratigraphic horizons. (b) Variation in elevation (metres), relative to sea level, for the top of the Cedar Mountain Formation. Distinct structural elements influencing horizon elevation include the San Rafael Swell, Woodside anticline and Green River anticline.

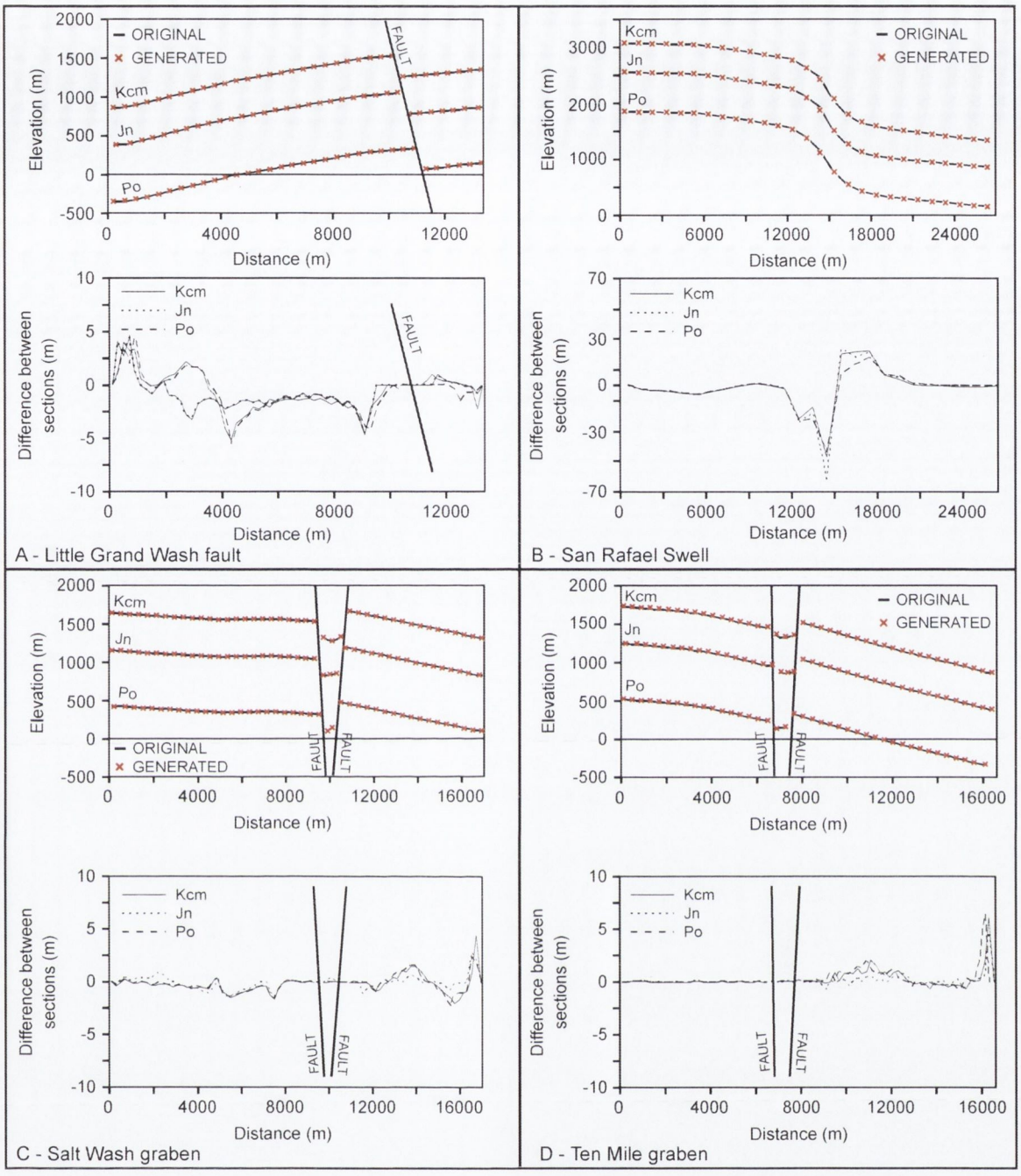


Figure 5.12: Comparison of original cross sections constructed and balanced in 2DMove with cross sections generated from the completed three-dimensional model in 3DMove. The Cedar Mountain (Kcm), Navajo (Jn) and Organ Rock (Po) horizon tops for each section were compared. The top plot for each area displays the cross sectional profile of point data for the original and generated sections. The bottom plot indicates the difference in elevation between sections at each data point. Note differences occur at increased fold curvatures and are absent at horizon cut-offs at the faults. The cross sections are the same as shown in Figure 5.9. Note the larger variation in scale in Figure 5.12b.

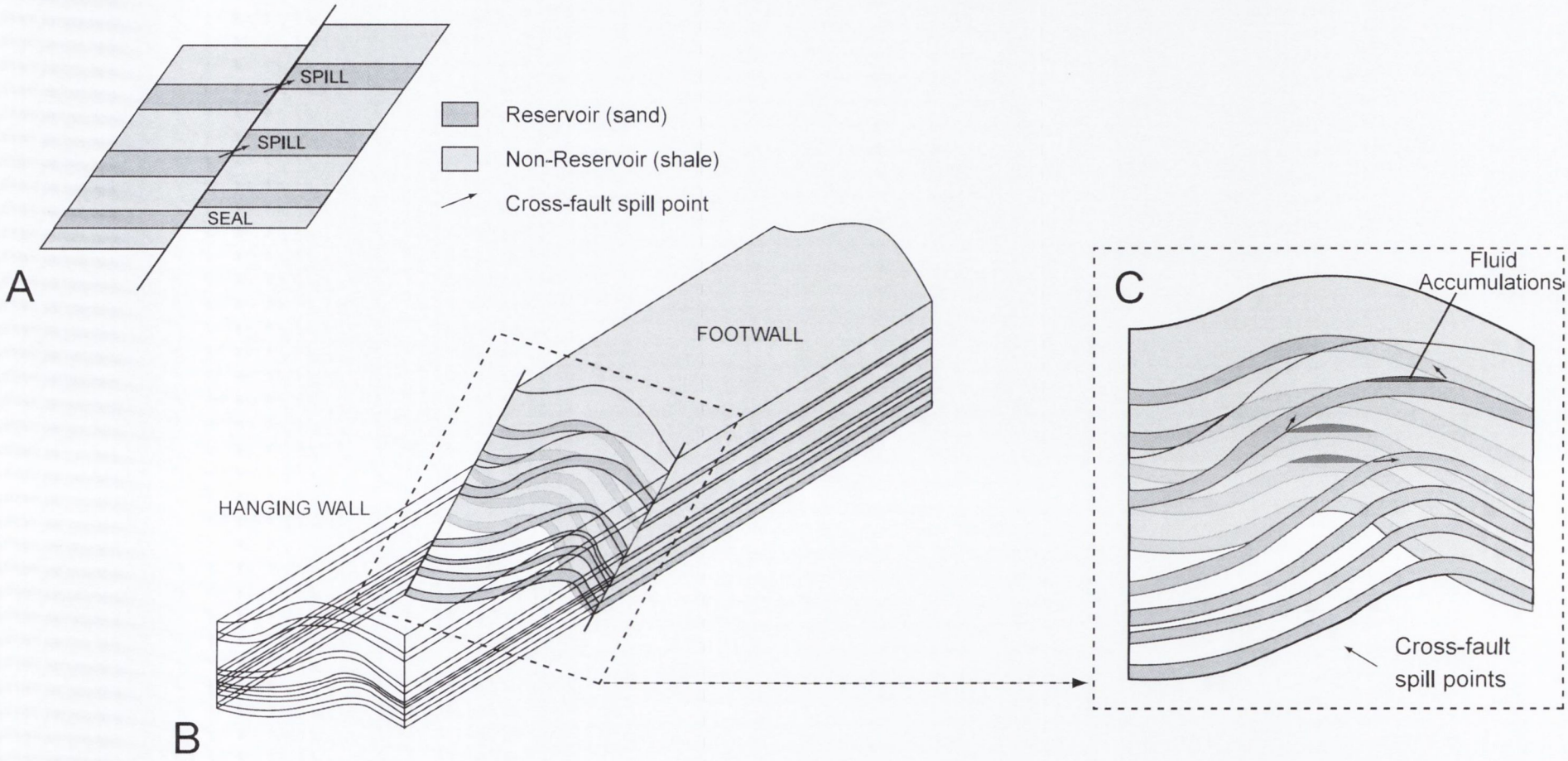


Figure 5.13: Principles of Allan diagrams (after Allan, 1989; Clarke et al., 2005). (a) In cross sectional view, a fault can either form a passive seal or leak point through the juxtaposition of stratigraphic units. (b) The interaction of juxtaposed stratigraphy can be complex in three dimensions, though analysis in this form provides the best prediction of juxtaposition. (c) The most common form of the Allan diagram projects the fault surface onto a flat plane, which creates geometric issues if the fault surface is curved.

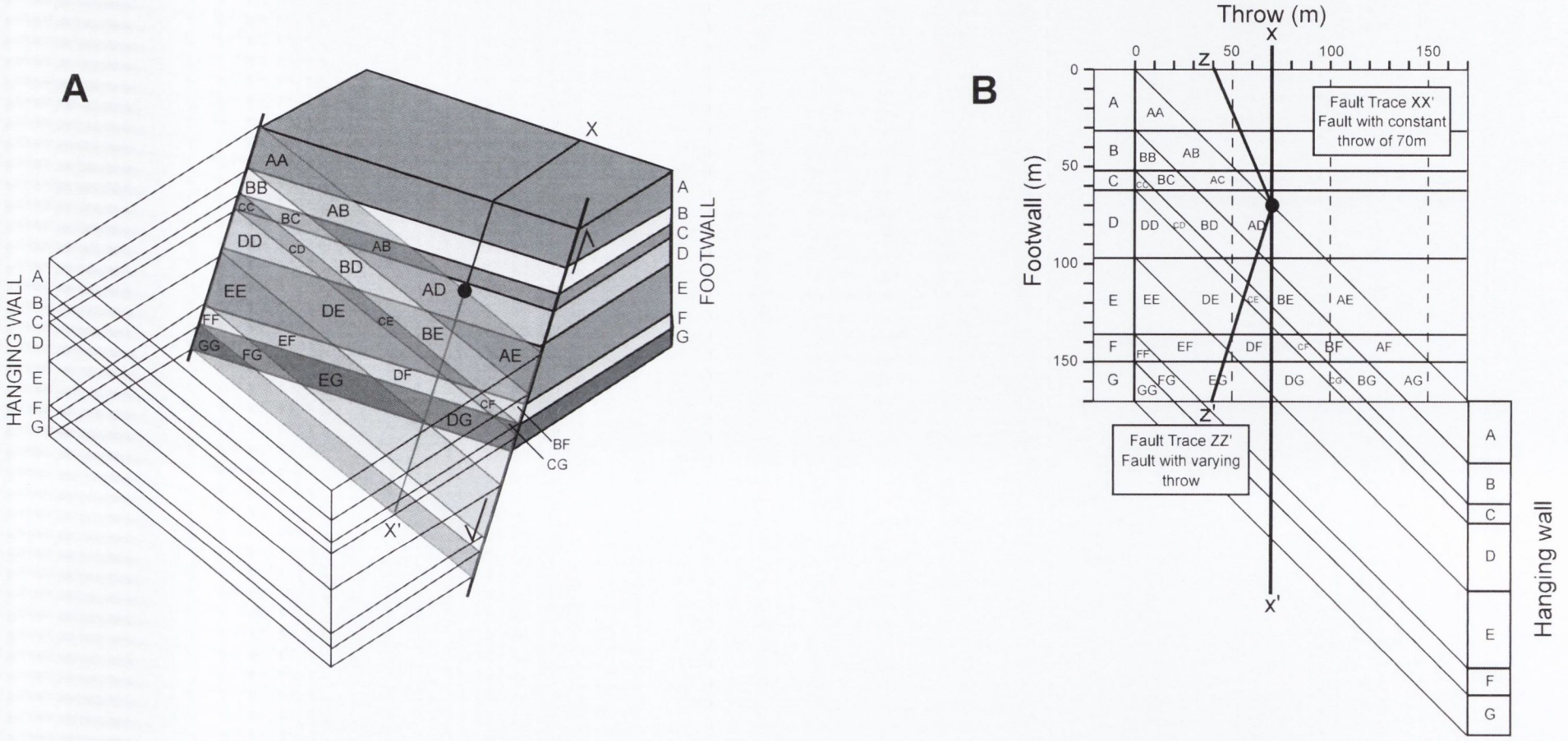


Figure 5.14: Principles of Juxtaposition diagrams (Knipe, 1992; 1997). (a) A three-dimensional normal fault block model with throw increasing from left to right. With the increase in throw, hanging wall units are juxtaposed against increasingly older footwall units. (b) A generic juxtaposition diagram extrapolated from the simple fault block model with the entire footwall sequence on the vertical axis and the overlying hanging wall sequence at increasing throws from left to right. Vertical lines (XX') represent constant throw with depth, while curved lines (ZZ') represent vertical variation in throw.

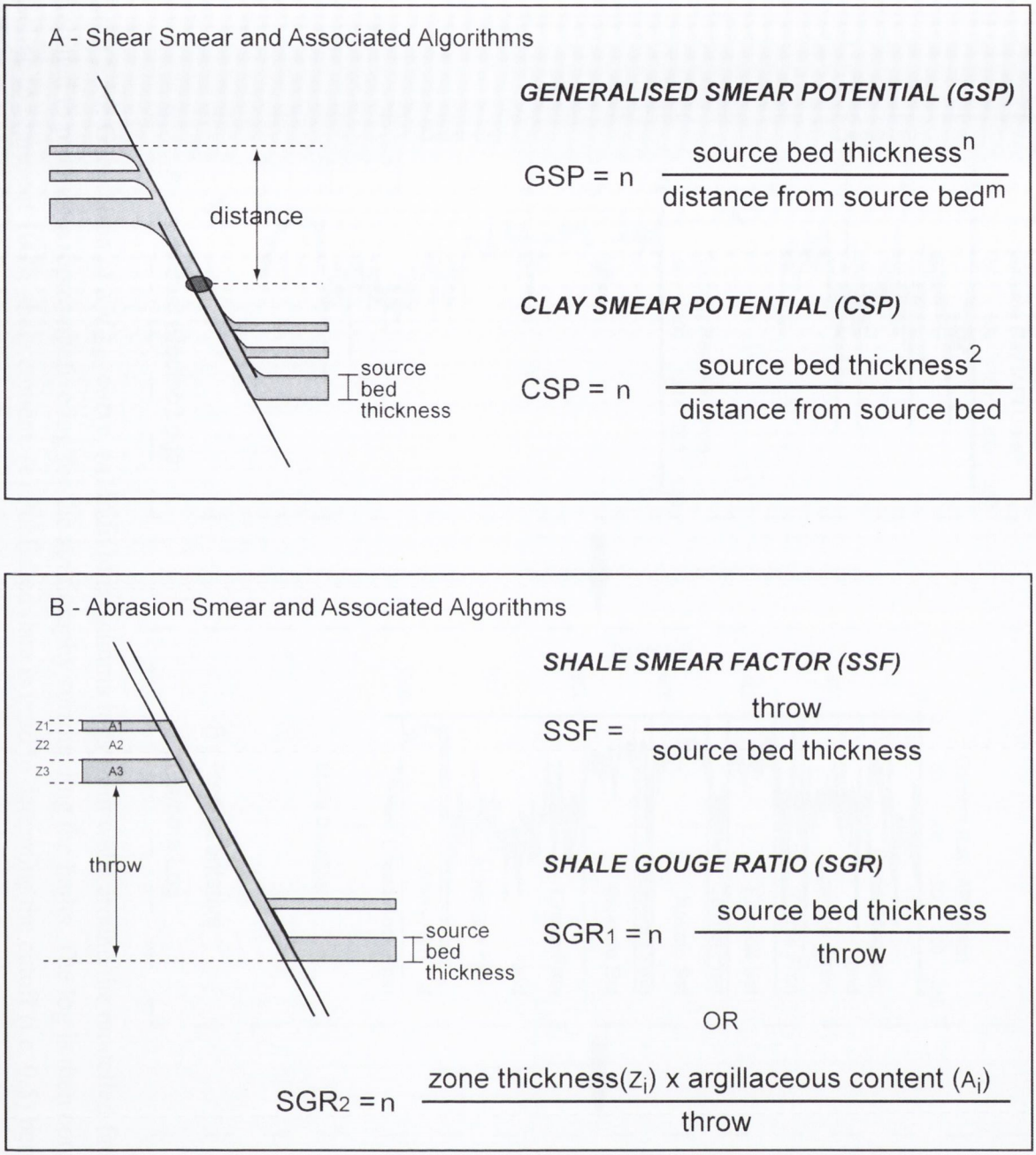


Figure 5.15: Published algorithms used to predict the likelihood of argillaceous smear developing along a fault surface. (a) Smears that form by shear-type faulting can be estimated by the Generalised Smear Potential (Yielding et al., 1997) or the Clay Smear Potential (Bouvier et al., 1989) in pure clay lithological sequences. (b) Smears that form by abrasion-type faulting can be estimated by the Shale Smear Factor (Lindsay et al., 1993). The quantity of argillaceous material entrained along the fault surface by any smearing mechanism can be estimated using the Shale Gouge Ratio (Yielding et al., 1997; 2002). The amount of argillaceous material can be calculated for delimited shale beds (SGR_1) or net content for a series of zones (SGR_2).

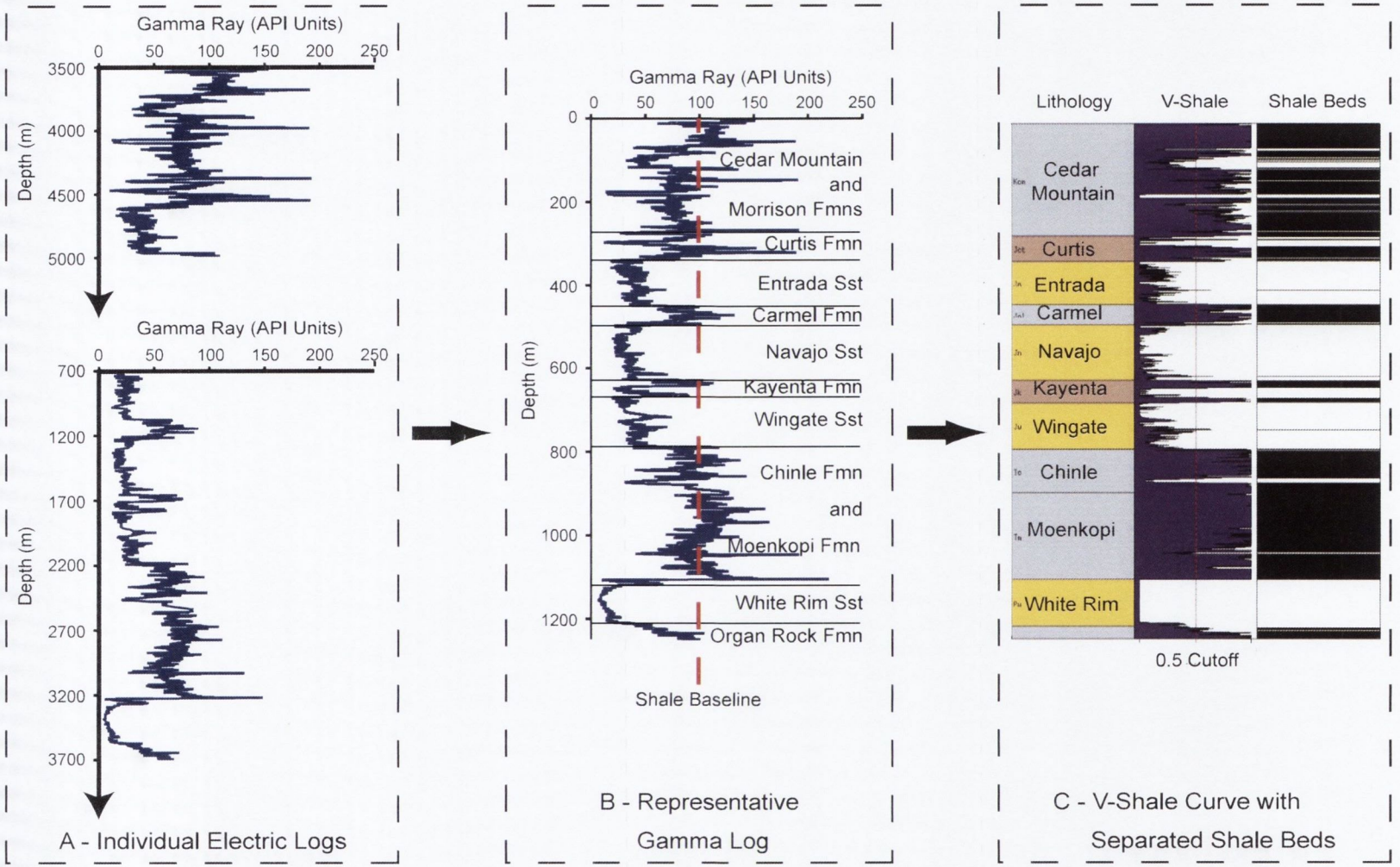


Figure 5.16: Generation of a V_{shale} curve. (a) Individual gamma logs from wells around the modelled faults are digitised. (b) The gamma logs are combined to produce a representative log for the stratigraphy surrounding the faults. The log is then converted to a V_{shale} curve by adjusting the shale baseline to represent 100% shale content. (c) Published data is used to determine the cutoff (i.e. 0.5) between shale- and sand-rich beds.

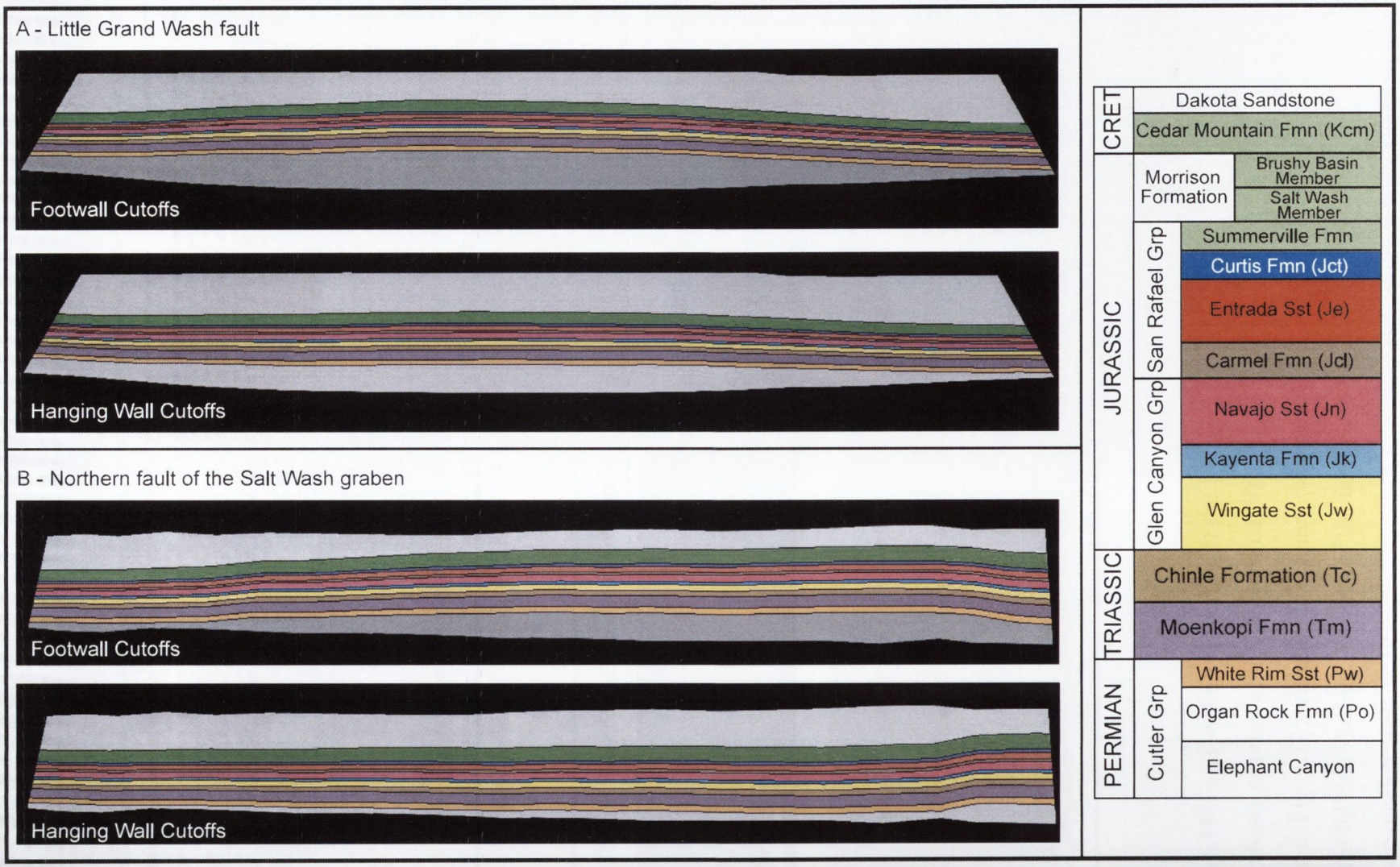
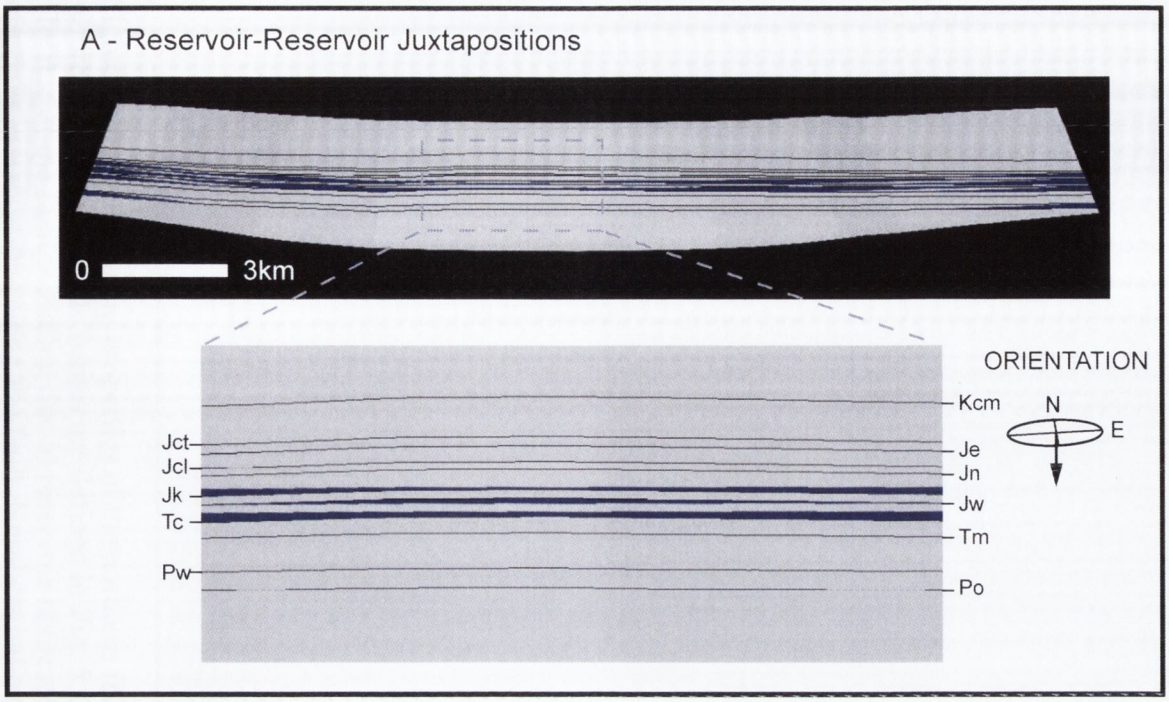


Figure 5.17: Footwall and hanging wall cutoffs for the Little Grand Wash fault (a) and northern fault of the Salt Wash graben (b) in Traptester. Colour coded stratigraphic column indicates grouping of units in the model. Fmn = formation; sst = sandstone.



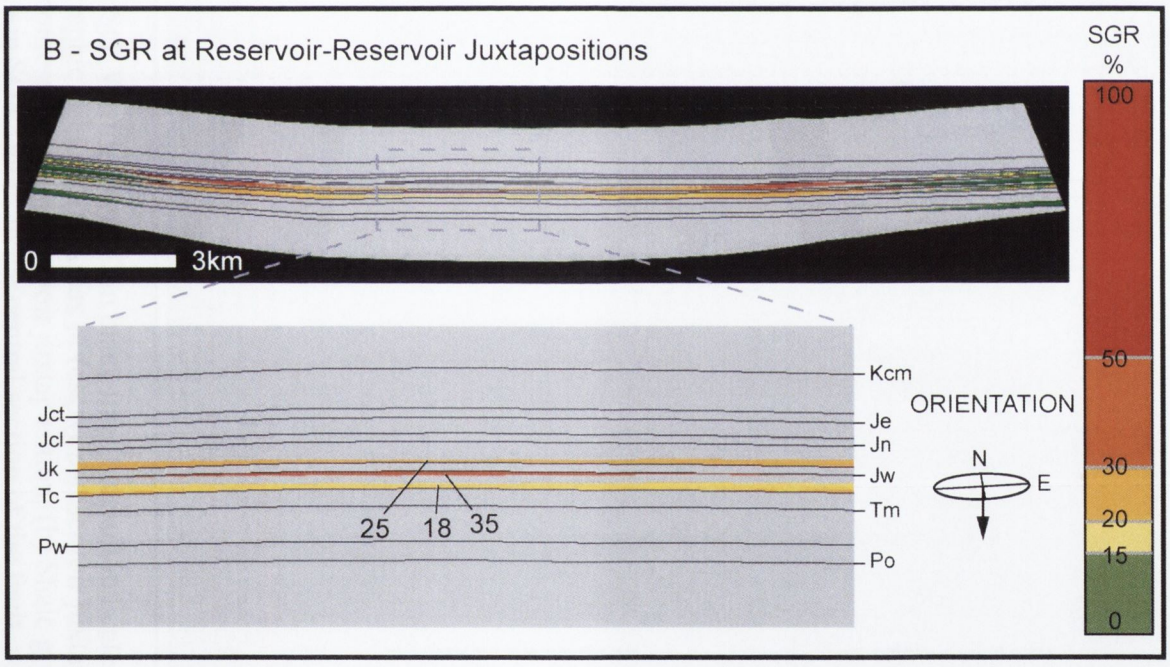


Figure 5.18: Fault sealing properties of the Little Grand Wash fault. Thin black lines on fault indicate position of the footwall cutoffs. Abbreviated stratigraphic names are defined in Fig. 5.17 stratigraphic column. (a) Areas of reservoir-reservoir juxtaposition indicated by blue shading. The rest of the fault is sealing due to reservoir-nonreservoir or nonreservoir-nonreservoir juxtaposition. (b) Shale gouge ratio (SGR) values at reservoir-reservoir juxtapositions along the fault. Numbers indicate minimum SGR values in the central section of the fault.

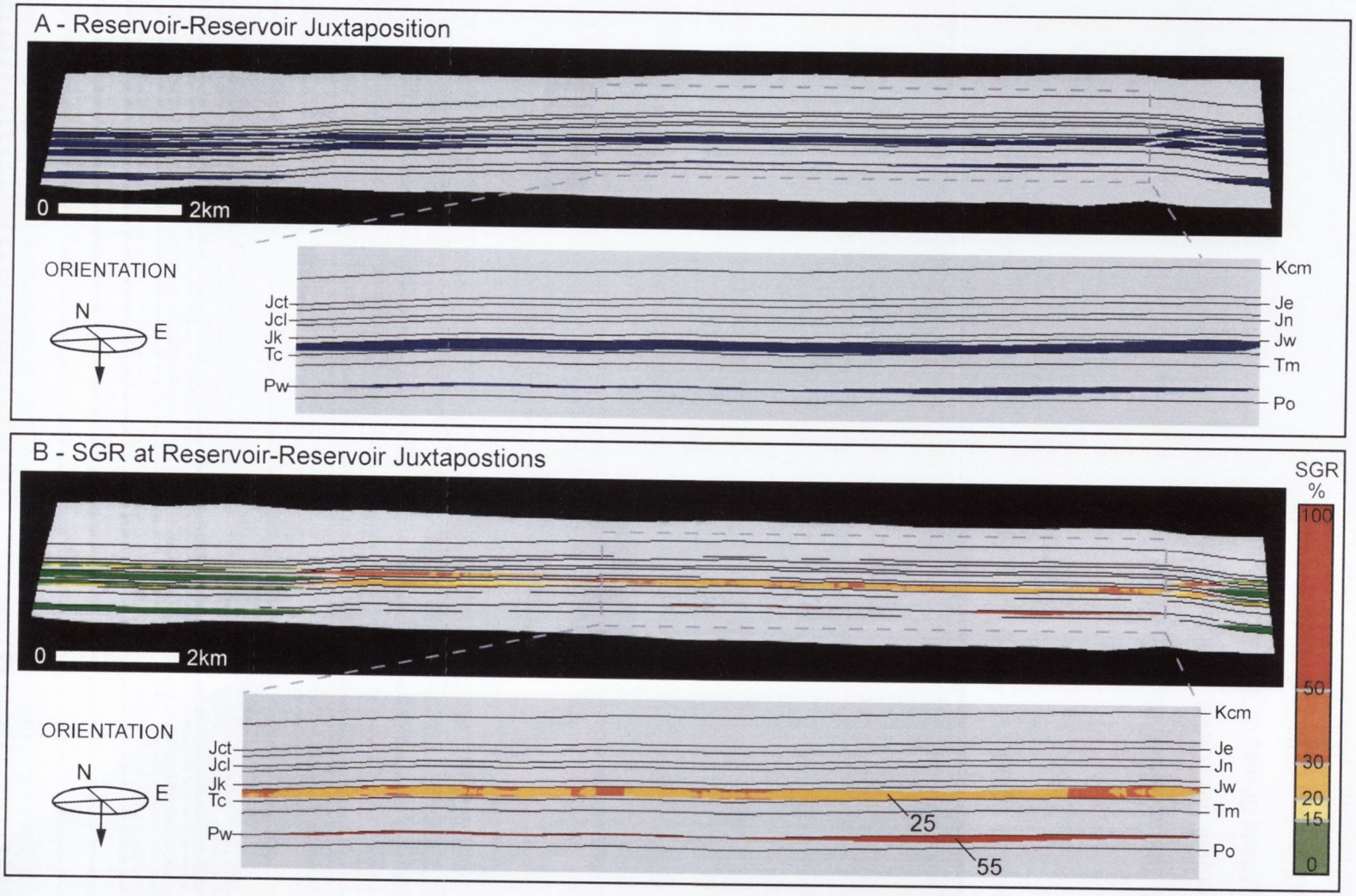


Figure 5.19: Fault sealing properties of the northern fault of the Salt Wash graben. Thin black lines on fault indicate position of the footwall cutoffs. Abbreviated stratigraphic names are defined in Fig. 5.17 stratigraphic column. (a) Areas of reservoir-reservoir juxtaposition indicated by blue shading. The rest of the fault is sealing due to reservoir-nonreservoir or nonreservoir-nonreservoir juxtaposition. (b) Shale gouge ratio (SGR) values at reservoir-reservoir juxtapostions along the fault. Numbers indicate minimum SGR values in the central section of the fault.

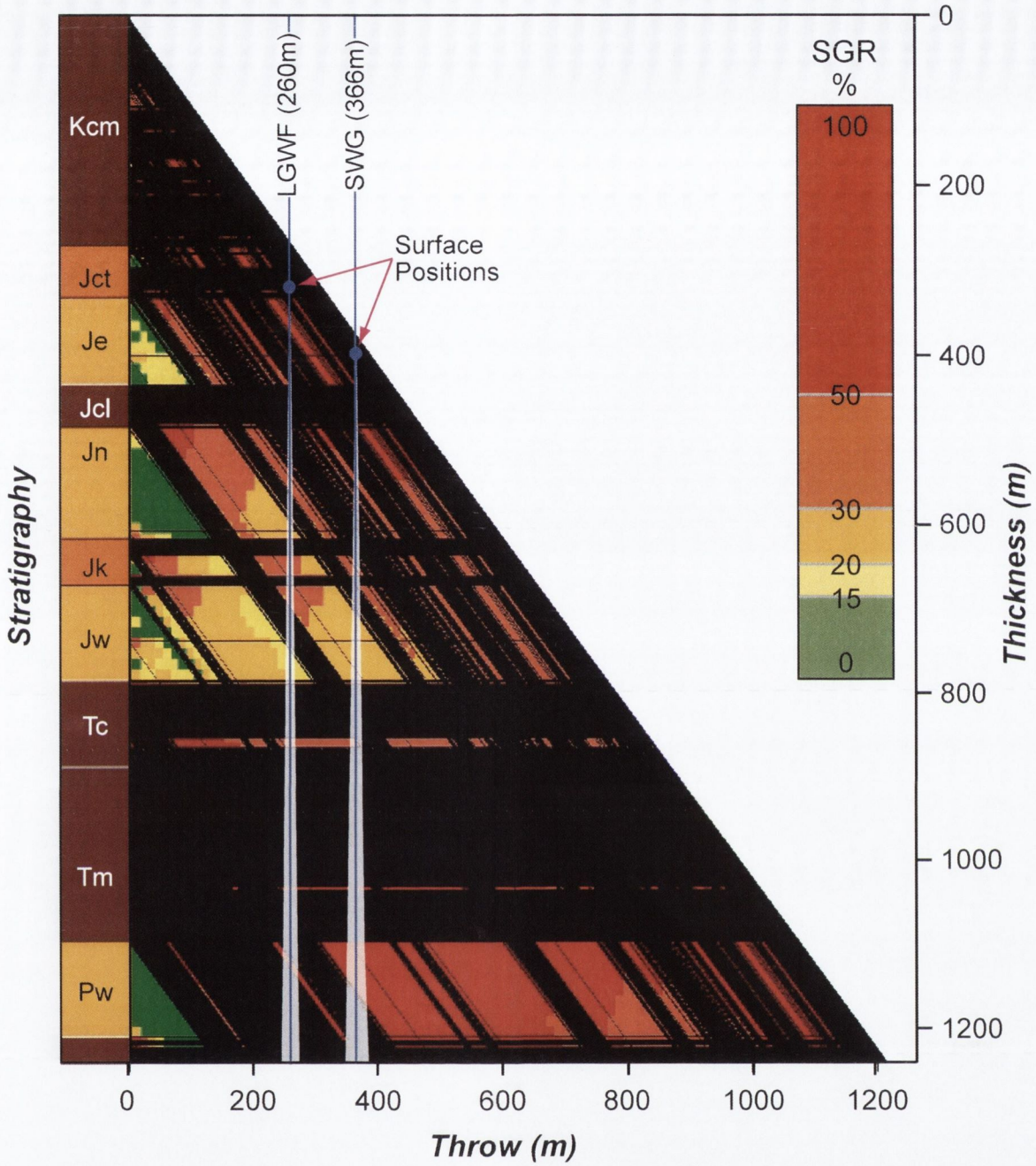
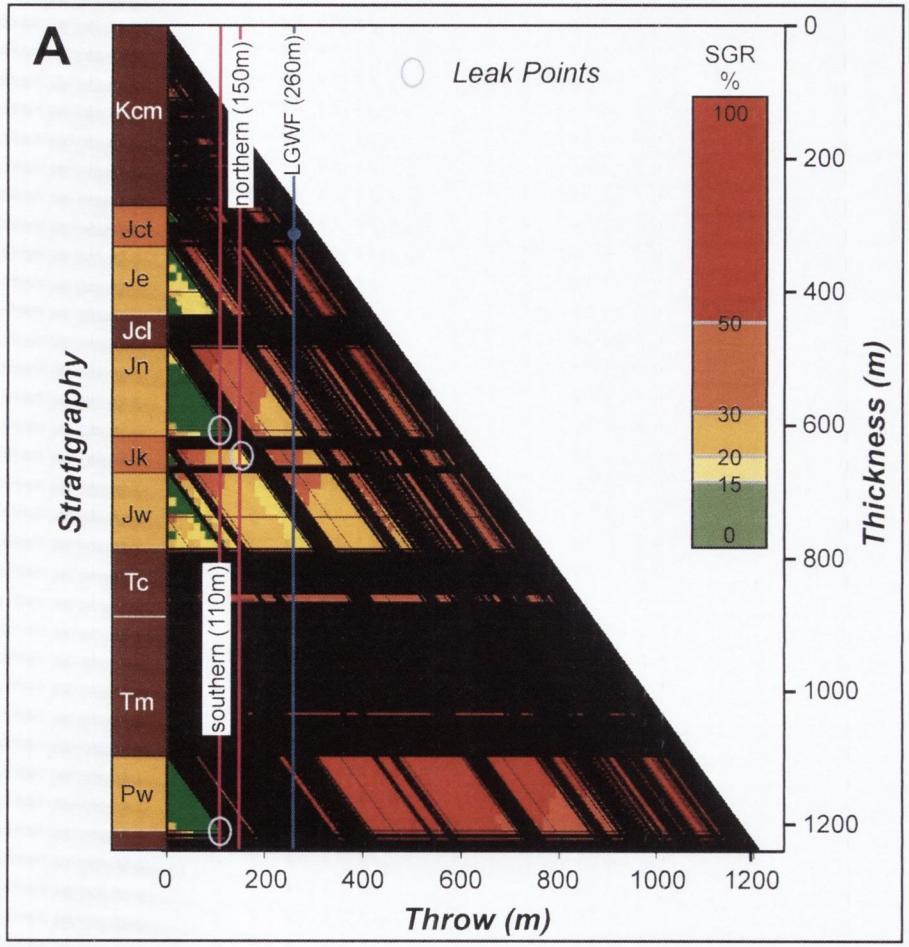


Figure 5.20: Juxtaposition diagram of the modelled stratigraphy showing the minimal effects of vertical fault throw changes on fault seal behaviour. Blue lines represent the maximum surface throws of the Little Grand Wash fault (LGWF) and northern fault of the Salt Wash graben (SWG) that are vertically constant in the model . White shaded areas indicate maximum changes in down-dip throw along both faults. Black areas on the juxtaposition diagram represent juxtaposition sealing and coloured areas indicate Shale Gouge Ratio (SGR) values at reservoir-reservoir juxtapositions. Abbreviated stratigraphic names are defined in the stratigraphic column of Fig. 5.17.



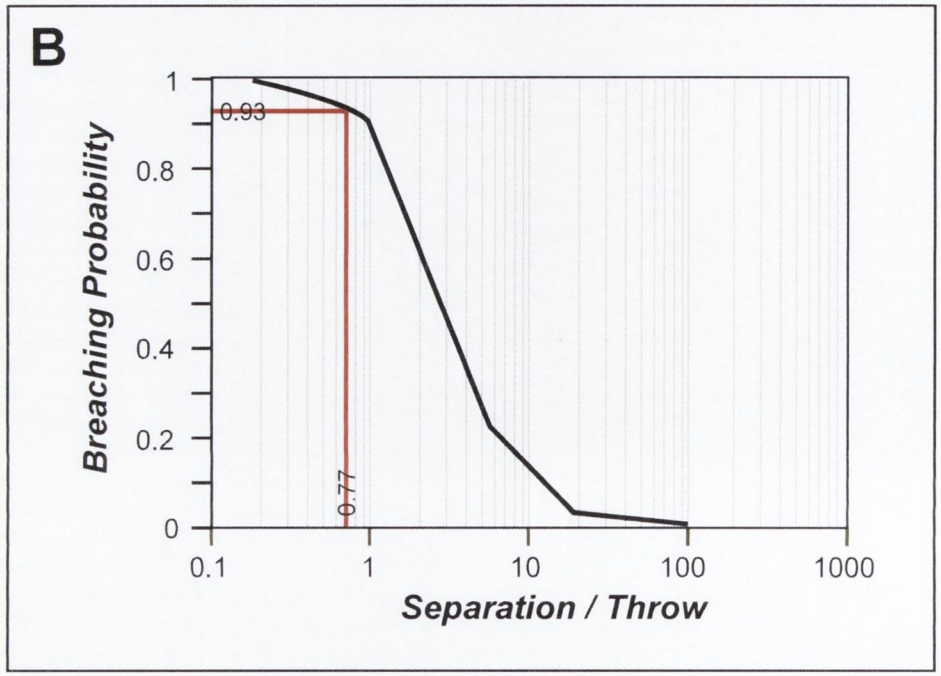


Figure 5.21: Potential leakage caused by structural complexities. (a) Juxtaposition diagram showing the effects of multiple fault strands in altering fault seal behaviour. The maximum throw for the Little Grand Wash fault (260m) is modelled as a single fault strand in the model, though field mapping indicates throw is partitioned between a northern (150m) and southern (110m) fault strand (see Fig. 3.2). This partitioning reduces throw and provides cross-fault flow pathways (i.e. leak points). See Fig. 5.20 for explanation of Juxtaposition diagram. (b) Probability plot of relay breaching relative to fault strand separation and total fault throw (after Imber et al., 2004). A separation/throw ratio of 0.77 for the greatest distance between fault strands on the Little Grand Wash fault indicates there is a 93% chance that all relay ramps along the fault will be breached.

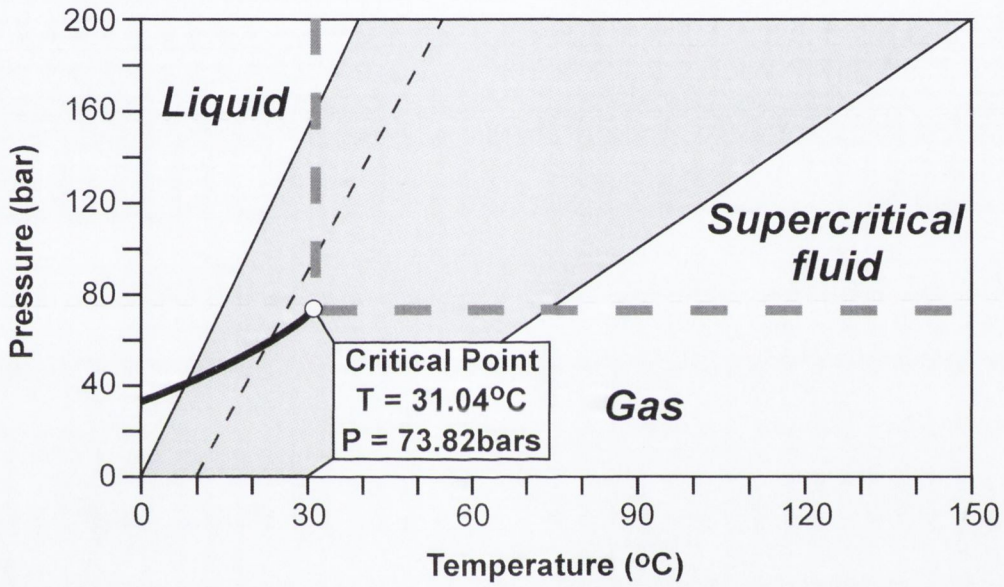


Figure 5.22: Influence of temperature and pressure on CO_2 phase. Thin dashed line indicates average subsurface conditions of field area. Shaded area indicates range of conditions found in sedimentary basins worldwide (after Gunter et al., 2004).

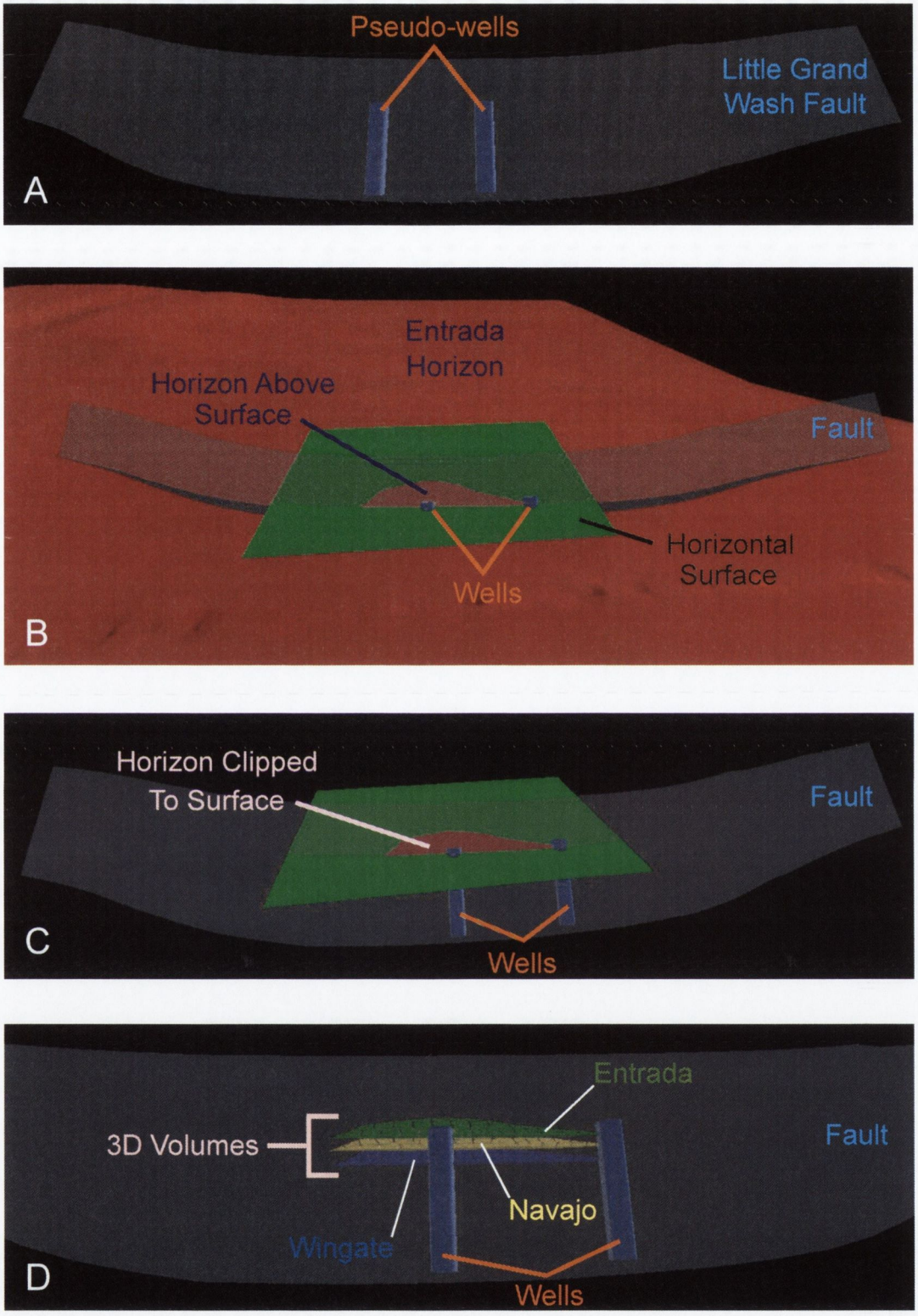


Figure 5.23: Workflow to calculate volume of a trap filled with CO_2 in 3DMove. (a) Fault-parallel, pseudo-wells are inserted at the surface boundaries for travertine deposition along the Little Grand Wash fault. (b) A horizontal surface is inserted at the greatest depth either well penetrates the trapping horizon. (c) Excess horizon below this surface is deleted and the space between the horizon and horizontal surfaces is calculated to represent trap volume. (d) This workflow is repeated to get trap volumes for the Entrada, Navajo, Wingate and White Rim Sandstones.

Chapter 6: Discussion, Conclusions and Future Work

6.1 Discussion

6.1.1 CO_2 Flow Pathways

Outcrop and geochemical investigations of the products of CO_2 surface leakage (i.e. travertines) combined with the generation and utilisation of a three-dimensional geological model have constrained the migration pathways of CO_2 through the faulted stratigraphy in the study area. The migration of CO_2 from source to surface based on these results is detailed in chapters 3, 4 and 5 is described in the following section and illustrated in Fig. 6.1.

Research by Heath (2004) has indicated that CO_2 was most likely generated by clay-carbonate reactions during the burial of the Colorado Plateau in the Cretaceous (Fig. 6.2). Potential CO_2 source rocks include any Jurassic or older stratigraphy with significant carbonate and clay contents, though the Sinbad Limestone of the Moenkopi Formation, Elephant Canyon Formation and Honaker Trail Formation are considered the primary sources due to their lithological composition and presence above the thick (>350m), relatively impermeable Paradox evaporites (Fig. 2.3; Heath, 2004). Travertine geochemistry (section 4.5.3.3) indicates that the CO_2 source has remained consistent throughout their precipitation history with small shifts in $\delta^{13}C$ likely reflecting the influence of the multiple source rocks supplying CO_2.

Upon generation, the CO_2 rises to charge overlying aquifers (White Rim and Wingate Sandstones) and mix with saline meteoric waters. Potentiometric surface data from groundwater wells show the meteoric waters flow from the northwest to the southeast in the study area (Fig. 6.2; Hood and Patterson, 1984). The folded stratigraphy focuses the southeast flow of the CO_2-rich meteoric fluids up-dip along the open, north-plunging Green River Anticline towards the central sections of the Little Grand Wash Fault and northern fault of the Salt Wash Graben. Both of these faults provide effective seals through lithological juxtaposition and clay smear development (section 5.3.4). This restricts flow across the faults and results in CO_2-rich waters pooling in the footwall highs created by the faulting of the anticline. Fracture networks developed in the footwall damage zone of both faults enhance permeability (section 3.3.3); especially around structural complexities and enable CO_2 to migrate vertically through overlying clay-rich cap rocks to charge successively shallower fault-sealed aquifers (i.e. Navajo and Entrada Sandstones).

This up-sequence charging of fault-sealed aquifers and subsequent leakage through fault-associated fracture networks in the clay-rich cap rocks is repeated until all the aquifers are inundated with CO_2. Continued supply of CO_2 to the system eventually results in the CO_2-rich waters escaping to the surface to either precipitate as travertine or to vent into the atmosphere. This surface leakage has been prevalent for at least 78,000 years (±4300) and has resulted in an average expulsion of an estimated 24.1 tonnes of CO_2 per year along the Little Grand Wash Fault (section 4.4.5). Comparisons with subsurface storage capacities along the fault indicate that this leakage depletes the aquifers of between 3.9 and 37.9% of the total CO_2 content every 10,000 years (section 5.4.3) to suggest the system is constantly being recharged at depth.

6.1.2 Factors Affecting Seal Integrity

The faulting of the Green River Anticline has created a series of stacked three-way anticlinal traps in the footwalls of the Little Grand Wash Fault and northern fault of the Salt Wash Graben. Top seals for the traps are provided by the multiple clay-rich beds in the stratigraphic sequence (Fig. 2.3), while lateral seals are provided by the faults. Field and geochemical investigations (chapter 4) combined with fault seal assessments (section 5.3) indicate that both faults form effective barriers to prevent lateral fluid flow due to lithological juxtaposition and/or development of continuous clay smear. Conversely, the presence of fluids and fluid-related products in the footwalls of both faults indicate that the top seals are failing to trap the fluids. In particular, the concentration of fluids and their associated products in the footwall damage zone of both faults suggests that interaction between the faults and top seals are instigating fault-parallel leakage of fluids through the clay-rich beds.

Large-scale faults are commonly surrounded by a zone of damage that can consist of minor faults, fractures, joints and/or deformation bands (Chester and Logan, 1986; Fowles and Burley, 1994; Antonellini and Aydin, 1994, 1995; Caine et al., 1996; Knipe et al., 1997). Depending on the subsidiary structures present, the damage zone can be a barrier or conduit to fluid flow (Caine et al., 1996). For example, damage zones dominated by deformation bands reduce the permeability of the host rock and commonly form partial barriers to across-fault fluid flow (Antonellini and Aydin, 1994, 1995; Hesthammer et al., 2000b; Shipton and Cowie, 2001, Jourde et

al., 2002; Shipton et al., 2002; Odling et al., 2004). In contrast, open fractures and joints enhance permeability and promote fault-parallel fluid flow (Sibson, 1996; Curewitz and Karson, 1997; Gudmundsson et al., 2001; Jourde et al., 2002). The presence of mineralization and diagenesis within and bordering fractures in the footwall damage zones of both faults suggest that the latter scenario is prevalent in the study area.

Fluid flow within damage zones is generally localised to discrete areas of the fault where there is an increase in fracture aperture, density and connectivity (Gudmundsson et al., 2001; Leckenby et al., In Press). These sites of increased fracturing provide pathways by enhancing the permeability of the host rock and are concentrated around structural complex sections of a fault that include fault intersections, fault bends, fault jogs, fault tips and relay zones (Curewitz and Karson, 1996, Sibson, 1996, Gartell et al., 2004). Fracture analyses conducted along the Little Grand Wash Fault highlight this relationship with marked increases in fracture intensity locally observed around relay zones as opposed to structurally simpler sections of the fault (see section 3.4). Furthermore, travertine deposits within clay-rich units (i.e. Summerville and Morrison Formations) are restricted to fault bends and relay zones along this fault (Fig. 4.1). These field relationships suggest that the damage zone is creating structural permeability within the clay-rich beds, preferentially around structural complexities that enables fluids to escape from the fault-sealed traps through the top seal.

Several other factors must be considered to assess the hydrologic behaviour of the subsidiary structures present within the damage zone. The effective stress history (consolidation state) of a rock and timing of faulting are also important in determining the permeability of faulted strata. Faulting at increasing to maximum effective stresses experienced in an area will cause the rock to compact and decrease permeability (Bolton et al., 1998; Zhang and Cox, 2000). Alternatively, faulting at effective stresses lower than previously experienced by an area will cause the rock to dilate and enhance permeability (Bolton et al., 1998; Zhang and Cox, 2000). In soil mechanics terminology, overconsolidation of the rock before faulting (Atkinson and Bransby, 1978; Lamb and Whitman, 1979) can result in permeability enhancement in clay-rich rocks of up to two orders of magnitude (Zhang and Cox, 2000). In addition, permeability parallel to the fault plane is one order of magnitude higher than across the fault plane (Zhang and Cox, 2000). Thus, faulting of overconsolidated rocks

during basin uplift can result in permeability enhancement, which will be most pronounced parallel to the fault plane.

The timing of movement for the Little Grand Wash Fault and northern fault of the Salt Wash Graben is poorly constrained. $^{40}Ar/^{39}Ar$ dating (Exxon, unpublished data) and indirect evidence suggest that both faults were active in the early Tertiary and possibly earlier (section 3.5). This corresponds to the period of maximum burial and subsequent uplift of the area (Fig. 6.2). Any faulting during this uplift period would generate dilational structures that would enhance the permeability of clay-rich beds adjacent to the faults. Unfortunately, the removal of post-Cretaceous sediments prevents better constraints on Tertiary fault movement, though local seismic activity around the study area in the Quaternary (Hecker, 1993) suggests there may have been fault reactivation during this current period of uplift. Therefore, the development of fracture networks in the damage zones of both faults provided potential pathways for fluid migration through clay-rich cap rocks that would be generally considered as vertical barriers to flow. Whether these pathways are open or closed for fluid flow is dependant on the effective stress history of the area and timing of fault activity.

These results have implications for a wide range of hydrogeological applications, where faults interact with clay-rich lithologies to provide lateral seals and/or breach vertical seals. In particular, clay-rich lithologies are generally assumed to be low-porosity, homogenous units that will form effective barriers to limit fluid migration. If the strata are overconsolidated, interaction with faults may lead to enhanced permeability of clay-rich lithologies resulting in the reduction of column heights in hydrocarbon reservoirs or leakage of injected CO_2 or radioactive waste from geologic storage sites. Indeed, overconsolidated clay-rich lithologies without deformation show significant anisotropic permeability to indicate the importance of burial history for a region (i.e. Bolton et al., 2000). Therefore, risk assessment of potential reservoirs for varying fluid regimes should consider burial history and fault activity to assess the likelihood of leakage through clay-rich lithologies.

6.1.3 Applications to CO_2 Storage

This study investigated a natural CO_2 reservoir that has leaked over a prolonged period via seismic-scale normal faults. Field, geochemical and modelling investigations have identified the subsurface migration pathways of the CO_2 from

source to surface and quantified the rates at which CO_2 leaks from the system. Using this natural CO_2 reservoir as a direct analogue for potential storage sites for CO_2 disposal, significant contributions towards risk assessment for this emerging technology can be suggested. Specifically, this section is subdivided to discuss: (1) where CO_2 may leak from a geologic reservoir; (2) potential rates of CO_2 leakage; (3) possible consequences of leakage; (4) remediation techniques available to retard leakage; and (5) factors influencing the suitability of geological reservoirs for CO_2 storage.

6.1.3.1 Where Could CO_2 Leak?

One of the fundamental aspects of CO_2 storage is that the injected CO_2 will be isolated from the atmosphere and near-surface environment by its emplacement within deep, sealed geological reservoirs over an extended period (Oldenburg, 2005). This research has identified multiple factors that can compromise the integrity of these reservoirs. Faults play a dominant role both in trapping and in transmitting of CO_2 in the study area. Sporadically distributed boreholes throughout the study area also provide pathways for CO_2 to escape to the surface. Documented below are the main factors influencing the sealing capabilities of these structures and possible methodologies to identify the hydraulic behaviour of these structures in relation to CO_2.

6.1.3.1.1 Across-Fault Leakage

The hydraulic nature of a fault is dependant on the CO_2 phase. Subcritical phases of CO_2 (gas or liquid) are miscible with water and governed by single-phase flow. Conversely, supercritical CO_2 is immiscible with water and therefore governed by two-phase flow similar to hydrocarbons.

Retardation of single-phase flow can only be achieved by low permeability barriers. For faults these low permeability barriers can be generated by a number of mechanisms. Juxtaposition of reservoir rock against low-permeability clay-rich nonreservoir rock can create a juxtaposition seal (Allen, 1989; Knipe, 1992; 1997). In mixed clastic sequences, clay-rich rock can be incorporated into the fault to form a clay smear membrane seal (Yielding et al., 1997). At reservoir-reservoir juxtapositions, low permeability cataclasites or deformation bands may develop, though their reduction on bulk permeability is questionable (Gibson 1994; 1998;

Yielding et al, 2002; Shipton et al., 2005). Therefore, fault seal assessments considering juxtaposition and entrainment of clay into the fault should incorporate a method applicable to assessing the risk of across fault leakage (see section 5.3). Specifically, faults should provide barriers to lateral flow of subcritical CO_2 when there is reservoir-nonreservoir juxtaposition and/or development of continuous clay smears at shale gouge rations in excess of 20% (Fristad et al., 1997; Yielding et al., 1997; Yielding et al, 2002). In section 4.3.2 the distribution of travertine deposits agrees well with the leak points predicted by these methods.

In two-phase flow, faults act as absolute barriers to CO_2 lateral migration until the buoyancy force in the CO_2 column is sufficient to overcome the capillary entry pressure of the fault rock. As capillary entry pressure is inherently related to pore throat dimensions (Schowalter, 1979), clay-rich fault rocks also provided by juxtaposition and clay smears represent effective seals. The absence of supercritical CO_2 in the studied traps prevents identification of the thresholds for fault sealing, though values calibrated from hydrocarbon investigations (Fristad et al., 1997; Yielding et al., 1997; Manzocchi et al., 1999; Yielding et al., 2002; Bretan et al., 2003; Gibson, 2003) should provide initial values that can be refined with further research. Thus, further case studies are required to substantiate or refute this study's findings and refine the threshold values for fault sealing in relation to subcritical and more importantly supercritical CO_2.

6.1.3.1.2 Cap Rock (Fault Parallel) Leakage

Integrity of clay-rich cap rocks can be undermined by the presence of faults. Structures within the damage zone surrounding a fault can create pathways through the adjacent host rock. In the study area these pathways are best developed around structural complexities that include fault bends and relay ramps. Fault intersections, jogs and tips could also act as high structural density pathways (Curewitz and Karson, 1997; Hancock et al., 1999). In clay-rich rocks, whether these pathways are open or closed to fluid flow is dependant on the consolidation state of the rock when faulted. Faulting at increasing to maximum effective stresses experienced by a host rock (i.e. during basin burial) will cause the damage zone pathways to deform in a ductile fashion and may form consistent clay-rich barriers. In contrast, faulting at lower effective stresses experienced by a host rock (i.e. during basin uplift) can cause the damage zone pathways to dilate and form conduits. Even clay-rich rocks without

deformation will generally exhibit increases in permeability during uplift but to what extent remains undefined (see Bolton et al., 2000). Therefore, any area identified for potential CO_2 storage should consider the burial history and timing of fault activity to assess the risk of CO_2 leakage from cap rocks forming imperfect seals. Structural complexities proximal to top seals should also be avoided as they are commonly conduits for significant phases of fluid flow (Sibson, 1996; Curewitz and Karson, 1997; Gartell et al, 2004). These features are difficult to resolve with subsurface mapping techniques and rarely detected. However, the likelihood of fractures in cap rock should be included in risk analysis of any potential reservoir.

6.1.3.1.3 Boreholes

Possible leakage of CO_2 from existing boreholes that penetrate geological storage sites is a major concern of future storage projects. Research by Scherer et al. (2005) has indicated that the acidic properties of CO_2-saturated waters can attack well cements leading to corrosion and possible leakage. Oil and gas wells drilled close to the Little Grand Wash Fault and northern fault of the Salt Wash Graben penetrate CO_2-filled traps and provide pathways for rapid transport of CO_2 to the surface (i.e. Crystal and Ten Mile Geysers). However, not all wells in the study area leak. Two that penetrate footwall reservoirs along the Little Grand Wash Fault have remained intact (i.e. Amerada Hess 1 and 2; Fig. 3.1). Reasons for this disparity are unclear due to the lack of records documenting post-drilling treatment of the wells. However, the absence or degradation of artificial cement infilling the wells is a probable cause. Alternatively, this could be a function of the highly heterogenous distribution of the CO_2 accumulations in the subsurface. If the wells could be re-occupied, testing of the pH of the fluids in the wells would help confirm this.

Remediation of leaking wells is possible, though in regions of extensive hydrocarbon exploration and production the number of leaking wells could be high and remediation costs expensive. Therefore, site selection for CO_2 geological storage should consider the number and integrity of wells an injected CO_2 plume may encounter throughout the period of desired storage. In addition, the composition and pH of the CO_2-rich waters within the geologic storage site must be monitored to prevent prolonged periods of acidic conditions, which can lead to corrosion of well cements and possible leakage. Failure to do these tasks can result in significant leakage and high remediation costs throughout the duration of the storage project.

6.1.3.2 How Much Could Leak?

Leakage rates from a storage site are a case specific measurement that is dependant on the mass of CO_2 stored in the reservoir, quality of the seal/s and effectiveness of leakage pathways (i.e. faults and boreholes). Nevertheless, quantification of this leakage rate can provide insight into the magnitude of leakage associated with fault-sealed reservoirs over CO_2 storage time-scales. Volumetric estimates indicate that a minimum of 1.9 million tonnes of CO_2 leaked to the surface over a 78,000 year (±4300) period from a series of fault-sealed traps with a combined CO_2 storage capacity of between 0.6 and 6.3 million tonnes (section 5.4.3). This represents a leak rate of greater than 0.2% to 1.9% every 500 years or 3.9% to 37.9% every 10,000 years. Whether this leak rate is acceptable for CO_2 storage projects is dependant on policy guidelines and emissions trading targets that are yet to be developed. However, any storage site with sustained, focussed leakage of CO_2 would probably be viewed as undesirable by the public. Additionally, if CO_2 concentrations are suspected to be a threat, then CO_2 flux and not leakage rate is a better measure to quantify potential adverse conditions to the environment (see below).

6.1.3.3 What Are The Consequences of Leakage?

Potential consequences of CO_2 leakage from geological storage sites can be divided into subsurface and near surface effects. In the subsurface, leaked CO_2 may contaminate existing energy, mineral and/or groundwater resources. In this study, the leaking CO_2 invades multiple aquifers, mixing with the groundwater and probably increases salinity by mobilising ions from CO_2 reactions with host rock (see Rochelle et al., 2004; Schutt et al., 2005). As the local groundwaters are already saline (Hood and Patterson, 1984) this does no pose a significant environmental threat in the study area. However, subsurface resource contamination from CO_2 leakage in other geologic settings could be a significant issue and must be considered when planning a CO_2 storage project.

The near surface environment is defined as the area roughly 10m above and below the ground surface (Oldenburg and Unger, 2005). Potential adverse effects of CO_2 leakage to this environment can be gauged by determining the leakage flux and considering the nature of leakage. Flux is a measure of the rate at which CO_2 passes out of the ground per unit area. In this study, conservative estimates of flux ($0.6\mu mol/m^2/s$) are significantly below typical ecosystem fluxes ($2\text{-}20\mu mol/m^2/s$;

Janssens et al., 2001; Drewitt et al., 2002) and fluxes that cause tree mortality (400μmol/m^2/s; Benson and Hepple, 2005). This suggests that CO_2 emissions in the near surface environment along the studied faults are benign. This is supported by anecdotal and personal observations indicating CO_2 leakage from geysers and springs has not been detrimental to plant, human or animal life.

However, the nature and location of CO_2 leakage must also be considered with hazardous situations arising in low-lying, confined or poorly-ventilated spaces due to CO_2 being denser than air (Hepple, 2005). Thus, sustained CO_2 leakage into the shallow subsurface and poorly-ventilated subsurface structures such as basements and burrows can lead to harmful effects for plants and humans or other animals respectively (Oldenburg and Unger, 2005). These harmful effects are numerous and varied and are explained in detail by Hepple (2005). Conversely, direct CO_2 leakage into the atmosphere (i.e. geysers and volcanoes) generally poses no threat to the surrounding environment (Oldenburg and Unger, 2005). This is seen in the study area with anecdotal and personal observations indicating CO_2 leakage from geysers and springs has not been detrimental to plant, human or animal life. However, leakage in a different setting to the sparsely populated, high altitude desert setting of the study area may result in more harmful consequences. Thus, selection of geological formations for CO_2 storage should consider the potential consequences of CO_2 leakage into subsurface reservoirs or inhabited areas.

6.1.3.4 Remediation of Leaks

As a response to the potential harmful effects of CO_2 leakage from geological storage sites, a range of remediation techniques have been devised or adapted predominantly from natural gas storage projects to limit the effects of leakage (for review see Benson and Hepple, 2005). Remediation can aim to either stop the leak or capture the products of leakage. As previously stated (see section 6.1.3.1), leakage from a geological storage site is through seals (cap rock or faults) or via inadequately sealed wells. Techniques to stop leakage through seals include decreasing the pressure of the leaking geological formation, increasing the pressure of overlying formations or extraction and reinjection of CO_2 into a suitable storage site. Wells can be individually repaired or plugged to stop leakage or blowouts.

Upon leakage, CO_2 can invade aquifers and the shallow subsurface or vent into the atmosphere. Generally, CO_2 will be intercepted and extracted from areas of

subsurface contamination and either reinjected into a suitable storage site or vented into the atmosphere. Once the CO_2 leaks to the surface, wind or large fans at point sources can be used to dilute CO_2 to safe levels. It should be noted that remediation of subsurface systems is expensive, difficult to perform and not always successful (Benson and Hepple, 2005). Thus, the integrity of the seal/s in trapping the injected CO_2 will determine the success and cost of a CO_2 storage project.

6.1.3.5 Factors Influencing Reservoir Storage Suitability

Selecting geological storage sites suitable for the injection and retention of CO_2 over extended time-scales (10^2-10^4 years) is a complicated process that requires consideration of numerous geologic and logistic factors. The main geologic reservoir options for CO_2 storage based on availability and storage capacities are depleted oil and gas fields, saline aquifers and unmineable coal seams (Lewis and Shinn, 2001; Gale, 2004; Benson, 2005). This study has investigated fault-sealed saline aquifers that temporarily store CO_2. Based on this research, the dominant geologic factors influencing the efficiency and integrity of CO_2 storage were highlighted. These geologic factors are documented below, along with a brief summary on the logistic factors that ultimately determine the viability of storing CO_2 in a geological reservoir.

6.1.3.5.1 CO_2 Phase

The in-situ temperature and pressure conditions of a reservoir will control the phase of CO_2, which in turn defines its thermophysical and flow properties. The most important thermophysical property relevant to CO_2 storage is density, which determines how efficiently CO_2 is stored in a reservoir. Reservoirs with CO_2 in the liquid or supercritical phases will have sufficiently large densities (600-800kg/m^3) to make geological storage volumetrically efficient. In contrast, CO_2 in the gas phase will be too diffuse (<300kg/m^3) for economic storage in a reservoir.

Variation in phase also determines whether CO_2 will be governed by single- or two-phase flow. This flow property is important for CO_2 storage as it determines the effectiveness of a seal in trapping CO_2. Two-phase flow of CO_2 in the supercritical phase will result in a seal being absolute until the capillary entry pressure of the sealing unit (i.e. cap rock or fault) is exceeded. Once exceeded, the rate of CO_2 leakage will be controlled by the permeability of the sealing unit. In contrast, single-phase flow of CO_2 in the subcritical phases (gas or liquid) is solely reliant on the

permeability of the sealing unit. Thus, a seal will be more effective in trapping supercritical CO_2 as opposed to subcritical CO_2 provided the capillary entry pressures of the sealing unit have not been exceeded. Therefore, supercritical CO_2 is considered the best phase suitable for storage in geological reservoirs due to its efficient densities and two-phase flow properties.

6.1.3.5.2 Leakage

The integrity of a geological reservoir is a major concern for potential CO_2 storage sites. This study has identified multiple ways CO_2 may leak from a reservoir via cap rock, faults or boreholes. The cap rock represents the most important component in trapping CO_2 within a reservoir for storage time-scales (10^2-10^4 years). Two factors that may compromise the sealing potential of a lithologically-good cap rock are its effective stress history and the presence of faults. A clay-rich cap rock will consolidate and compact at increasing to maximum effective stresses experienced by the strata (i.e. during basin burial) and will be overconsolidated and dilate at subsequently lower effective stresses (i.e. during basin uplift; Bolton et al., 2000). This study combined with other research (Bolton et al., 1998; Zhang and Cox, 2000) suggests that faulting of clay-rich cap rocks at these lower effective stresses will localise dilation, enhance permeability and create flow pathways through the sealing unit, preferentially at structural complexities along a fault.

Conversely, faults can also form effective barriers to trap migrating CO_2. Using techniques adapted from the hydrocarbon industry, this study demonstrates that faults can form lateral seals to trap CO_2 provided there are favourable reservoir-nonreservoir juxtapositions and development of continuous clay smears. Therefore, the presence of faults may enhance or decrease the sealing potential of a reservoir depending on the consolidation state of the cap rock and sealing attributes of the fault.

Abandoned and active boreholes that penetrate a reservoir are the other main structure that may compromise the integrity of a potential storage site. Leakage via a borehole can occur if it was inadequately sealed with cement or acidic CO_2-rich waters attack and corrode borehole cements. Remediation is possible but expensive, so geological reservoirs with a minimal amount of boreholes would be preferred. Therefore, the most secure reservoirs for CO_2 storage should consist of a consolidated cap rock without boreholes or faults. However, in most situations this can not be avoided, and as such boreholes should be kept to a minimum and rigorously inspected

for sealing integrity (see Benson and Hepple, 2005), faults should be assessed for their sealing potential (see section 5.3) and faulted, overconsolidated strata should be avoided.

6.1.3.5.3 Storage Capacity

Potential storage sites are only viable if they can accommodate significant quantities of CO_2. Current, industrial-scale projects are injecting CO_2 into the subsurface at rates of 1 to 4 million tonnes per year for 20 to 30 years, while future projects are expected to be scaled up to 8 to 10 million tonnes per year (Benson, 2005). Factors effecting the storage capacity of a reservoir vary depending on the reservoir type (i.e. saline aquifer, oil and gas fields, coal seams) and its characteristics (i.e. solubility, pore volume, adsorption). For this study, the critical parameters influencing the storage capacity of saline aquifers were reservoir pore volume, CO_2 solubility in the brine and proportion of free phase to dissolved CO_2. Similarly, oil and gas field storage capacities are predominantly determined by reservoir pore volume, CO_2 solubility in the hydrocarbons and degree of water invasion (Bachu, 2002). Conversely, storage capacities for coal seams are predominantly determined by bed thickness and adsorption capacity of the coal (Gale and Fruend, 2001). As demonstrated from this study, it is not always possible to quantify all parameters affecting storage capacity (i.e. free phase to dissolved CO_2). However, reservoir pore volume for saline aquifers and oil and gas fields and bed thickness for coal seams can provide first-order approximations on the storage capacities of a potential reservoir.

6.1.3.5.4 Logistics

The ultimate factor determining the feasibility of a geological reservoir for CO_2 storage is based on the logistics of the project. Logistics covers all non-geological aspects of CO_2 storage from identifying CO_2 point sources to assessing infrastructural needs and calculating the economic viability of a project. Major point sources that could supply CO_2 to a geologic storage site consist of power plants, refineries and other industrial plants. Key factors to consider when assessing the suitability of a geologic reservoir include the proximity of the sources to the reservoir and mass of CO_2 available for storage. Intertwined with point sources are the infrastructural requirements needed to capture, transport and inject CO_2 from the source to storage site. In many cases, this infrastructure is already available from the

extraction and transport of hydrocarbons (i.e. Sleipner and Weyburn storage projects). However, significant infrastructure requirements may be needed in regions with little or no hydrocarbon potential. Finally, the total cost of a project from the capture of the CO_2 to its injection and monitoring in a geologic reservoir must be economically viable for the project to be sustainable. These costs can be minimised by selecting storage sites with pre-existing infrastructure and offset by economic benefits from increased resource recovery (i.e. hydrocarbons or methane from coal seams) and/or financial incentives provided by the public sector. To date, industrial-scale CO_2 projects (i.e. Sleipner, Weyburn, In Salah, Gorgon and Snohvit) have been associated with hydrocarbon fields due to the infrastructure and economic benefits. However, large-scale deployment of this technology in the near-future will require a diversification of geologic reservoir types used (i.e. saline aquifers and coal seams) and further consideration of logistical requirements in non-hydrocarbon settings.

6.2 Conclusions

The following general conclusions have resulted from this study:

- The Little Grand Wash Fault is a steeply dipping, arcuate normal fault with a maximum throw of 260m. The central section of the fault splits into two main fault strands, introducing a series of structural complexities (i.e. fault bends, fault intersections and relay zones). A single $^{40}Ar/^{39}Ar$ date indicates fault movement in the early Tertiary, though movement before and/or after this period is probable.

- The Salt Wash and Ten Mile Grabens are linked by a left-stepping relay ramp and bound by steep, inward-dipping normal faults. The grabens are kinematically linked with maximum throws of 366m and 210m for the northern and southern faults, respectively. There are no dates for movement on any of the faults, though indirect evidence suggests movement in the early Tertiary and possibly earlier in the Triassic.

- All the studied faults are composed of a fault core surrounded by a zone of damage in the adjacent host rock. The fault core consists of argillaceous-

rich gouge and entrained pods or slabs of host rock that are bound and internally separated by two or more slip zones. This is surrounded by a damage zone consisting of minor faults, fractures, veins and deformation bands that extends up to 150m from the fault and is most extensively developed around structural complexities.

- The Green River Anticline is an open, shallowly north-plunging fold that was generated from salt tectonism in the Triassic to mid Jurassic. The anticline is cut by both northwest-striking fault systems to create structural highs in the footwalls of the Little Grand Wash Fault and northern fault of the Salt Wash Graben. Abundant fault-related mineralization (travertines) and diagenesis (iron-oxide reduction, hydrocarbon staining and sulphate veins) are situated in the immediate footwalls of both structural highs, proximal to the anticlinal fold axis.

- The travertines are terrestrial carbonate deposits that precipitate directly from CO_2-rich waters erupting from geysers and springs along both faults. Each deposit is composed of four distinct lithofacies that define surface growth (carbonate cemented conglomerates and layered carbonate mats) and subsurface migration pathways of CO_2-rich waters through the deposit to the geyser or spring vent (white- and brown-banded veins).

- The CO_2-rich waters supplying the travertines are a product of CO_2 generated from clay-carbonate reactions rising and mixing with shallow meteoric waters (Heath, 2004). Comparison of active and ancient travertine deposits indicate this hydrologic system has been operating for the last 78,000 years (±4300). Minor isotopic variations in the travertine record indicate the likely influence of multiple source rocks supplying the CO_2 and fluctuations in the emergence temperatures of the erupting waters.

- A conservative 1.9 million tonnes of CO_2 are estimated to have leaked to the surface along the Little Grand Wash Fault over the last 78,000 years (±4300) to give a leakage rate of 24.1tonnes/year or a flux of 0.6μmol/m^2/s. The total CO_2 storage capacity of aquifers (White Rim Sandstone $2.4x10^5$-$4.9x10^6$ tonnes; Wingate Sandstone $1.8x10^5$-$7.1x10^5$ tonnes; Navajo Sandstone $1.2x10^5$-$3.5x10^5$ tonnes; Entrada Sandstone $1.0x10^5$-$2.9x10^5$ tonnes) sealed by the Little Grand Wash Fault is between 0.6 and 6.3 million tonnes. This indicates that the fault-sealed aquifers have leaked between 30 and 300% of their total capacity over a 78,000 year period. In CO_2 storage time-scales, this converts to a leak rate of 0.2% to 1.9% every 500 years or 4% to 38% every 10,000 years.

- Assessment of fault sealing mechanisms for the Little Grand Wash Fault and northern fault of the Salt Wash Graben indicate leak points at low throws (<100m) due to reservoir (i.e. aquifer) self-juxtaposition and sealing at higher throws (>100m) due to reservoir-nonreservoir juxtaposition and development of continuous clay smear. The structural highs created by the faulting of the Green River Anticline channel the CO_2 in the reservoir units to the central, high throw sections of both faults to form fault-sealed anticlinal traps.

- Leakage of CO_2 from each trap is vertically through the overlying, clay-rich cap rock via fracture networks developed in the damage zone of both faults. Flow is localised around structural complexities, where the fracture network is best developed. This charging and subsequent leakage of CO_2 from the fault-sealed traps is repeated until the CO_2-rich waters erupt at the surface to precipitate as travertine or vent into the atmosphere.

- The presence of iron-oxide reduction, hydrocarbon staining and sulphate veins in footwall sandstones along both faults indicate additional fluids have migrated through the area. Furthermore, the close spatial association of these fluid flow features in relation to the travertines suggest multiple

fluids have used similar pathways to migrate through the faulted stratigraphy.

6.3 Future Work

The broad range of topics investigated in this study has led to multiple lines of inquiry that could be further pursued to better characterise the field area or elaborate understanding on CO_2 leakage from geological reservoirs. Detailed below are potential future research themes that could be initiated or continued based on results from this study.

- A detailed paradiagenetic study of the sandstones in the footwalls of the Little Grand Wash Fault and northern fault of the Salt Wash Graben is needed to clarify the source and timing of fluids responsible for iron-oxide reduction. Other studies in the region have indicated that hydrocarbons are responsible for iron-oxide reduction (Hansley, 1995; Chan et al., 2000; Garden et al., 2001; Parry et al., 2003), though preliminary investigations in the study area suggest a possibly different source. Therefore, clarification of the nature of the fluid responsible for iron-oxide reduction in the study area may lead to a re-evaluation of the reducing fluid responsible for reduction in other parts of the Paradox Basin and surrounding areas.

- The role damage zones can play in providing a conduit or barrier to fluid flow has been well documented in this and other studies (Fowles and Burley, 1994; Antonellini and Aydin, 1994, 1995; Caine et al., 1996; Knipe et al., 1997; Jourde et al., 2002; Odling et al., 2004).The challenge now is to characterise the structures present in a variety of lithologies at differing throws and fault settings. Furthermore, the relative permeabilites of these structures should be established to determine their influence on the hydraulic behaviour of the fault zone as a whole. While extensive, the results of such an analysis would have major applications in the hydrocarbon, hydrology and geologic storage (CO_2 or radioactive waste) sectors.

- Current dates for ancient travertine deposits in the study area provide an indication on the spatial and temporal variability of CO_2 leakage along the Little Grand Wash Fault and northern fault of the Salt Wash Graben. Further high resolution dating of these ancient deposits would constrain the duration and rate of leakage at each travertine site. This would further constrain the spatial and temporal changes in CO_2 leakage along both faults, allowing better definition of CO_2 leak rates and flux through time. Travertines from other springs in the Paradox Basin (i.e. Springerville; Allis et al., 2001; Moore et al., 2005) should also be sampled to see if leakage has been occuring for the same amount of time at the same rate across the basin.

- Current estimates of storage capacities for aquifers sealed by the Little Grand Wash Fault are limited by the inability to define the proportion of CO_2 dissolved in solution within each trap (see section 5.4.2). Numerical modelling of CO_2 flow through this system would provide better estimates on the saturation states of CO_2 within each trap and improve the understanding of CO_2-meteoric water interaction within this system. This would refine the storage capacity estimates and combined with surface leak estimates would provide a more definitive answer as to the integrity of the fault-sealed traps in storing CO_2.

- Fault seal techniques developed for the hydrocarbon industry were employed to predict the sealing behaviour of faults in relation to subcritical CO_2. Further case studies of fault-sealed CO_2 reservoirs should now be undertaken to corroborate these findings and better calibrate fault seal techniques to subcritical and more importantly supercritical CO_2 in potential storage sites. Confidence in defining the sealing behaviour of faults in relation to CO_2 would increase the range of geological reservoirs that could be considered for future CO_2 storage projects.

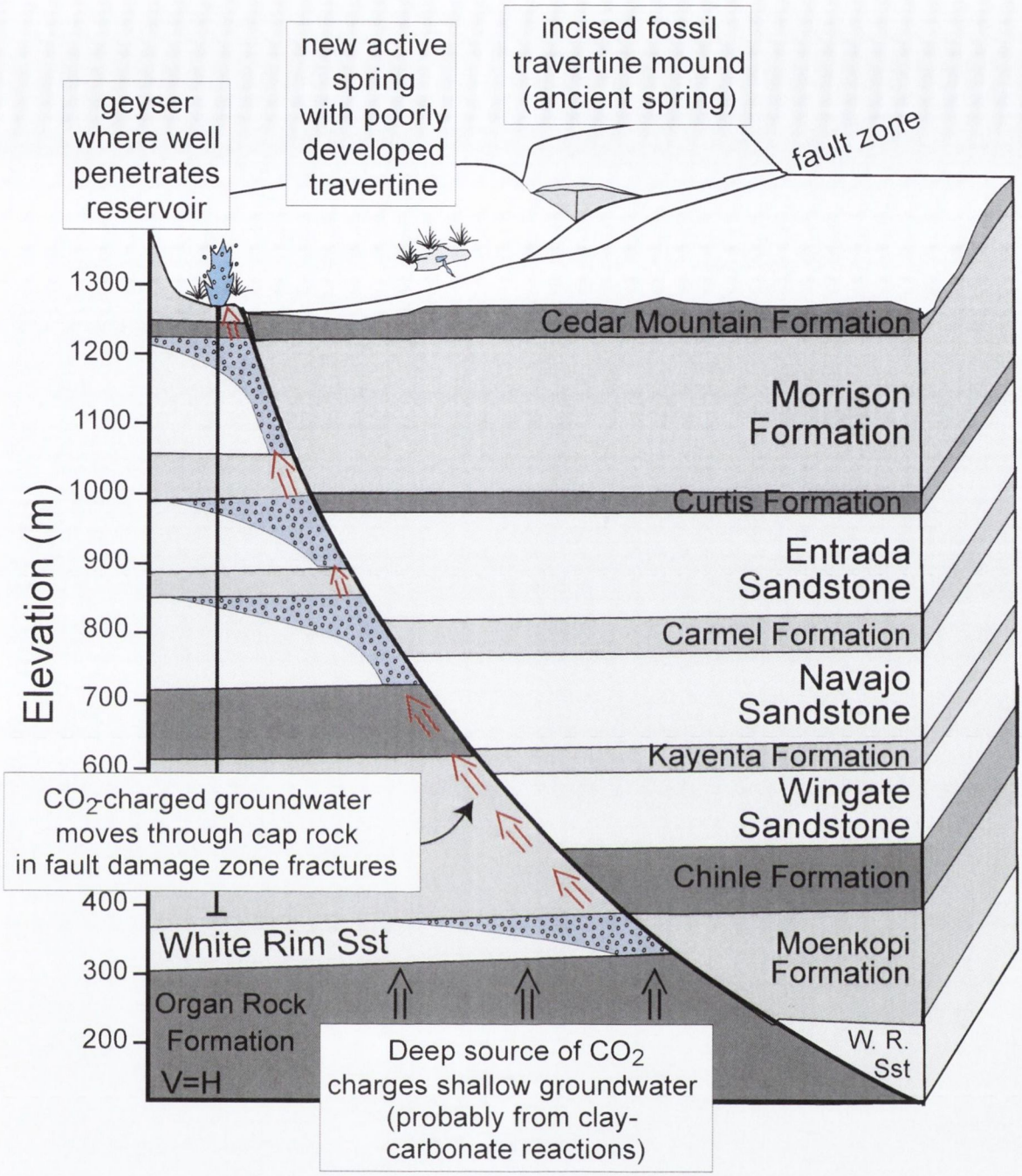


Figure 6.1: Schematic north-south cross-section through the Little Grand Wash Fault (after Williams, 2004; Shipton et al., 2005), used to illustrate the conceptual model of CO_2 migration developed from this study. Carbon dioxide rises from depth to charge shallow aquifers. Structural elements combine to pool the CO2-rich waters in three-way anticlinal traps with lateral seals provided by the Little Grand Wash Fault and northern fault of the Salt Wash Graben.

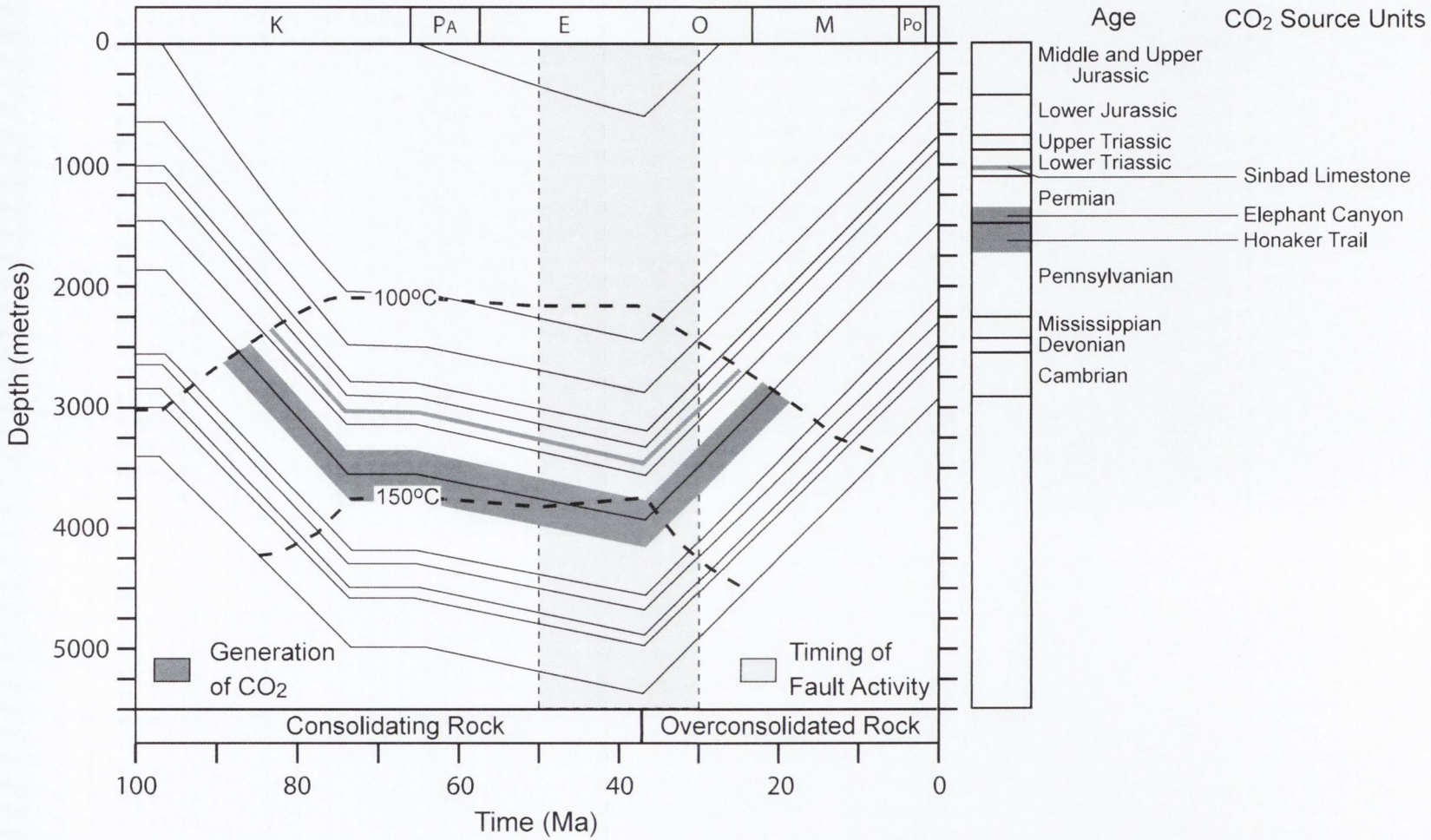


Figure 6.2: Burial and thermal history of the Green River area (from Nuccio and Condon, 1996) accompanied with the timing of CO_2 generation and fault activity from the Cretaceous (100 Ma) to present. Carbon dioxide was generated by clay-carbonate reactions involving a series of source rocks from the mid Cretaceous to early Miocene. Fault activity based on K-Ar dating of clay gouge (unpublished Exxon data) was limited to the Little Grand Wash Fault.

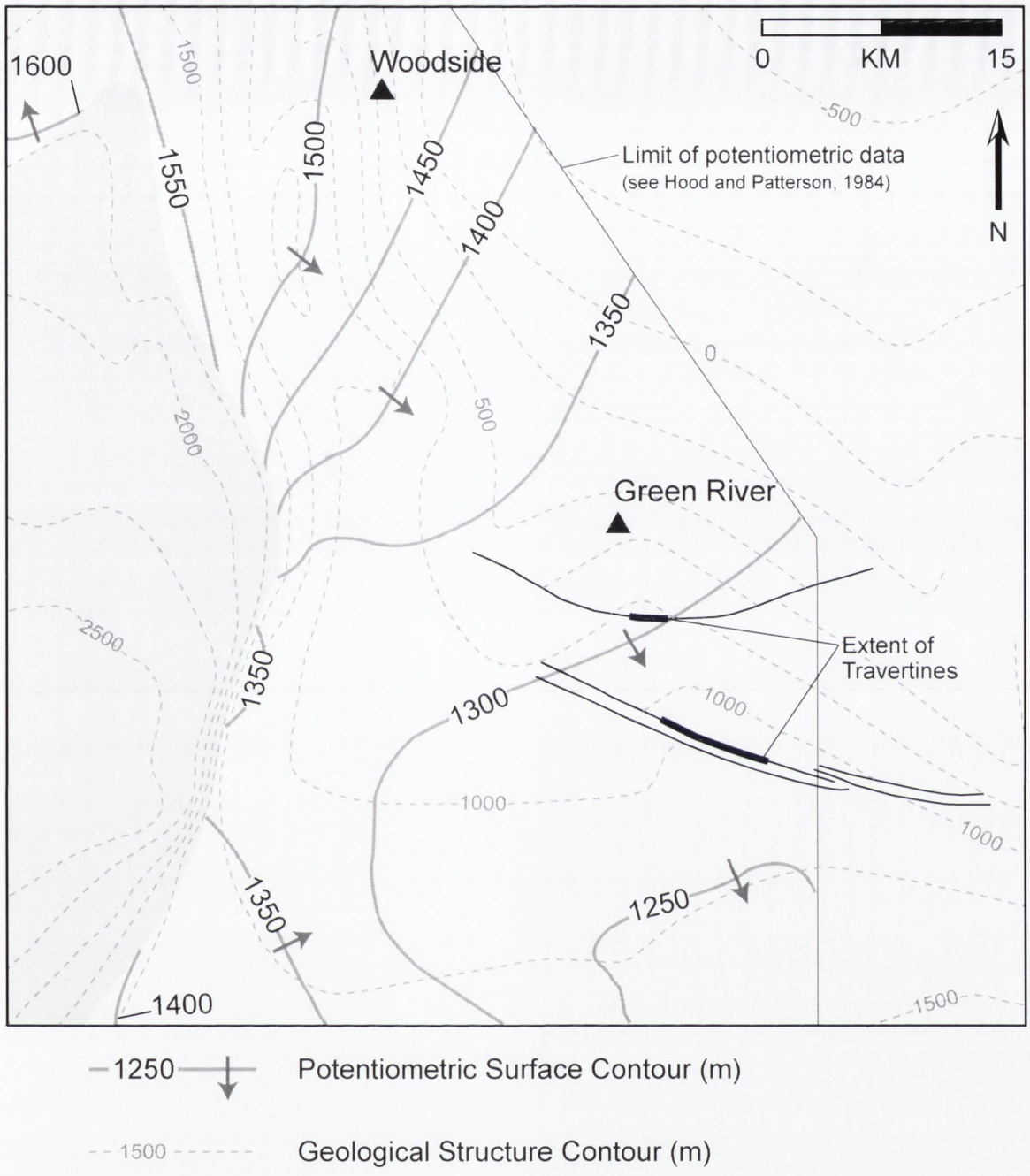


Figure 6.3: Map of the study area showing the direction of groundwater flow based on potentiometric data for the Navajo Sandstone aquifer (from Hood and Patterson, 1984). Each potentiometric surface contour shows the approximate elevation, relative to sea level, at which water levels would stand in a tightly cased well. Shaded area indicates region where aquifer is partially to completely missing. Structure contours for the top of the Navajo Sandstone (Fig. 5.2) and extent of travertines in the footwalls of the Little Grand Wash Fault and northern fault of the Salt Wash Graben are displayed to show the relationship between structure and fluid flow.

References

Allan, U.S., 1989. Model for hydrocarbon migration and entrapment within faulted structures. *AAPG Bulletin*, 73, 803-811.

Allis, R., White, S., Chidsey, T., Gwynn, W., Morgan, C., Adams, M., Moore, J., 2001. Natural CO_2 Reservoirs on the Colorado Plateau and Southern Rocky Mountains: Candidates for CO_2 Sequestration. *Proceedings of the First National Conference on Carbon Sequestration*, Washington DC, May 2001.

Allis, R., Bergfeld, D., Moore, J., McClure, K., Morgan, C., Chidsey, T., Heath, J. and McPherson, B., 2005. Implications of results from CO_2 flux surveys over known CO_2 systems for long-term monitoring. *Proceedings of the Fourth Annual Conference on Carbon Sequestration and Sequestration*, Virginia, May 2005.

Amundson R. and Kelly E., 1987. The chemistry and mineralogy of a CO_2-rich travertine depositing spring in the California Coast Range. *Geochimica et Cosmochimica Acta*, 51, 2883-2890.

Antonellini, M. and Aydin, A., 1994. Effect of faulting on fluid flow in porous sandstones; petrophysical properties. *AAPG Bulletin*, 78, 355-377.

Antonellini, M. and Aydin, A., 1995. Effect of faulting on fluid flow in porous sandstones; geometry and spatial distribution. *AAPG Bulletin*, 79, 642-671.

Arts, R., Eiken, O., Chadwick, A., Zweigel, P., van der Meer, B. and Kirby, G., 2004. Seismic monitoring at the Sleipner underground CO_2 storage site (North Sea). In: Baines, S.J. and Worden, R.H. (eds). *Geological Storage of Carbon Dioxide*. Geological Society, London, Special Publications, 233, 181-192.

Atkinson, J.H. and Bransby, P.L., 1978. *The mechanics of soils: An introduction to critical state soil mechanics*. McGraw-London.

Auler, A. and Smart, P.L., 2001. Late Quaternary paleoclimate in semiarid northeastern Brazil from U-series dating of travertine and water-table speleothems. *Quaternary Research*, 55, 159-167.

Baars, D.L. and Stevenson, G.M., 1981. Tectonic evolution of the Paradox Basin, Utah and Colorado. In: Wiegand, D.L. (ed) 1981. *Geology of the Paradox Basin.* Field Conference - Rocky Mountain Association of Geologists, 23-31.

Bachu, S., Gunter, W.D. and Perkins, E.H., 1994. Aquifer disposal of CO_2: hydrodynamic and mineral trapping. *Energy Conversion and Management*, 35, 269-279.

Bachu, S., 2002. Sequestration of CO_2 in geological media in response to climate change: road map for site selection using the transform of the geological space into the CO_2 phase space. *Energy Conversion and Management*, 43, 87-102.

Badley, M., Freeman, B., Needham, T., Yielding, G., Driggs, A., Hairr, R. and Lindsay, D., 1997. Fault seal analysis: methodologies and case studies. *In: Proceedings of conference on hydrocarbon seals relating to deformation zones and caprocks*. Trondheim, Norway.

Baer, J. L., and Rigby, J.K., 1978. Geology of the Crystal Geyser and the environmental implications of its effluent, Grand County, Utah. *Utah Geology*, 5, 125-130.

Baines, S.J. and Worden, R.H., 2004a. The long-term fate of CO_2 in the subsurface: natural analogues for CO2 storage. In: Baines, S.J. and Worden, R.H. (eds). *Geological Storage of Carbon Dioxide*. Geological Society, London, Special Publications, 233, 59-86.

Baines, S.J. and Worden, R.H., 2004b. Geologic storage of carbon dioxide. In: Baines, S.J. and Worden, R.H. (eds). *Geological Storage of Carbon Dioxide*. Geological Society, London, Special Publications, 233, 1-6.

Baker, A.A., 1933. Geology and oil possibilities of the Moab District, Grand and San Juan counties, Utah. *U. S. Geological Survey Bulletin*, B 0841.

Barnes I., 1965. Geochemistry of Birch Creek, Inyo County, California: A travertine depositing creek in an arid climate. *Geochimica et Cosmochimica Acta*, 29, 85-112.

Barnes I., Irwin W.P. and White D.E., 1978. Global distribution of carbon-dioxide discharges and major zones of seismicity. United States Geological Survey, *Water Resources Investigations* 78-39, Open File report.

Barbeau, D.L., 2003. A flexural model for the Paradox Basin: implications for the tectonics of the Ancestral Rocky Mountains. *Basin Research*, 15, 97-115.

Beach, A., Welbon, A.I., Brockbank, P.J., McCallum, J.E., 1999. Reservoir damage around faults; outcrop examples from the Suez Rift. *Petroleum Geoscience*, 5, 109-116.

Beitler, B., Chan, M.A., and Parry, W.T., 2003. Bleaching of Jurassic Navajo Sandstone on Colorado Plateau Laramide highs; evidence of exhumed hydrocarbon supergiants? *Geology*, 31, 1041-1044.

Benson, S.M., 2005. Overview of geologic storage of CO_2. In: Benson, S.M., Oldenburg, C., Hoversten, M. and Imbus, S. (eds). *Carbon dioxide capture for storage in deep geological formations- results from the CO_2 capture project, Volume Two: Geological storage of carbon dioxide with monitoring and verification*, 665-672. CO_2 Capture Project, Elsevier.

Benson, S.M. and Hepple, R.P., 2005. Prospects for early detection and options for remediation of leakage from CO_2 storage projects. In: Benson, S.M., Oldenburg, C., Hoversten, M. and Imbus, S. (eds). *Carbon dioxide capture for storage in deep geological formations- results from the CO_2 capture project, Volume Two: Geological storage of carbon dioxide with monitoring and verification*, 1189-1204. CO_2 Capture Project, Elsevier.

Blakey, R.C., 1974. Stratigraphic depositional analysis of the Moenkopi Formation, southeastern Utah. *Utah Geological and Mineral Survey Bulletin*, 104.

Blakey, R.C., Peterson, F. and Kocurek, G., 1988. Synthesis of late Paleozoic and Mesozoic eolian deposits of the Western Interior of the United States. *Sedimentary Geology*, 56, 3-125.

Bolton, A. J., Maltman, A. J. and Clennell, M. B., 1998. The importance of overpressure timing and permeability evolution in fine-grained sediments undergoing shear. *Journal of Structural Geology*, 20, 1013-1022.

Bouvier, J. D., Kaars-Sijpesteijn, C. H., Kluesner, D. F., Onyejekwe, C. C. and van der Pal, R. C., 1989. Three-dimensional seismic interpretation and fault sealing investigations, Nun River Field, Nigeria. *AAPG Bulletin*, 73, 1397-1414.

Brennan, S.T. and Burruss, R.C., 2003. Specific sequestration volumes; a useful tool for CO_2 storage capacity assessment. *U. S. Geological Survey Open File Report*, OF 03-0452.

Breit, G.N. and Meunier, J., 1990. Fluid inclusion, $\delta^{18}O$, and $^{87}Sr/^{86}Sr$ evidence for the origin of fault-controlled copper mineralization, Lisbon Valley, Utah, and Slick Rock District, Colorado. *Economic Geology*, 85, 884-891.

Bretan, P., Yielding, G. and Jones, H., 2003. Using calibrated shale gouge ratio to estimate hydrocarbon column heights. AAPG Bulletin, 87, 397-413.

Bromley, M.H., 1991. Architectural features of the Kayenta Formation (Lower Jurassic), Colorado Plateau, USA; relationship to salt tectonics in the Paradox Basin. *Sedimentary Geology*, 73, 77-99.

Brook, E.J., 2005. Tiny bubbles tell all. *Science*, 310, 1285 – 1287.

Bryant, C., 1987. The oil and gas potential of the Escalante known geological structure. *Utah Geological and mineral Survey Open-File Report*, 102.

Burton E.A. and Walter L.M., 1987. Relative precipitation rates of aragonite and Mg calcite from seawater: Temperature or carbonate ion control? *Geology*, 15, 111-114.

Caine, J.S., Evans, J.P. and Forster, C.B., 1996. Fault zone architecture and permeability structure. *Geology*, 24, 1025-1028.

Cappa, J.A. and Rice, D.D., 1995. Carbon dioxide in Mississippian rocks of the Paradox Basin and adjacent areas, Colorado, Utah, New Mexico, and Arizona. *U. S. Geological Survey Bulletin*, 2000-H.

Casanova, J., 1986. East African rift stomatolites. In: L.E., Frostick, R.W., Renaut, I., Reid and J.J., Tiercelin (eds) 1986. *Sedimentation in the African Rifts*. Geological Society of London Special Publication, 25, 201-210.

Cater, F.W., 1970. Geology of the salt anticline region in southwestern Colorado. *U. S. Geological Survey Professional Paper* 637.

Case, J. E., Joesting, H. R. and Byerly, P. E., 1963. Regional geophysical investigations in the La Sal Mountains area, Utah and Colorado. *U. S. Geological Survey Professional Paper* 316-F, p. 91-116.

Chadwick, R.A., Holloway, S., Brook, M.S. and Kirby, G.A., 2004. The case for underground CO_2 sequestration in northern Europe. In: Baines, S.J. and Worden, R.H. (eds). *Geological Storage of Carbon Dioxide*. Geological Society, London, Special Publications, 233, 17-28.

Chafetz H.S. and Folk R.L., 1984. Travertines: Depositional morphology and bacterially constructed constituents. *Journal of Sedimentary Petrology*, 54, 289-316.

Chan, M.A., 1989. Erg margin of the Permian White Rim Sandstone, SE Utah. *Sedimentology*, 36, 235-251.

Chan, M. A., Parry, W.T. and Bowman, J.R., 2000. Diagenetic hematite and manganese oxides and fault-related fluid flow in Jurassic sandstones, Southeastern Utah. *AAPG Bulletin*, 84, 1281-1310.

Chen, J., Zhang, D.D., Wang, S., Xiao, T. and Huang, R., 2004. Factors controlling tufa deposition in natural waters at waterfall sites. *Sedimentary Geology*, 166, 353-366.

Chester, F. M. and Logan, J. M., 1986. Implications for mechanical properties of brittle faults from observations of the Punchbowl fault zone, California. Pure and Applied Geophysics, 124, 79-106.

Childs, C., Watterson, J. and Walsh, J. J., 1996. A model for the structure and development of fault zones. Journal of the Geological Society of London, 153, 337-340.

Clark, I. and Fritz, P., 1997. *Environmental Isotopes in Hydrogeology*. Lewis Publishers, Boca Raton, 328pp.

Clark, I.D. and Fontes, J., 1990. Paleoclimatic reconstruction in northern Oman based on carbonates from hyperalkaline groundwaters. *Quaternary Research*, 33, 320-336.

Clarke, S.M, Burley, S.D. and Williams, G.D., 2005. A three-dimensional approach to fault seal analysis: fault-block juxtaposition and argillaceous smear modeling. *Basin Research*, 17, 269-288.

Clemmensen, L.B., Olsen, H. and Blakey, R.C., 1989. Erg-margin deposits in the Lower Jurassic Moenave Formation and Wingate Sandstone, southern Utah. *Geological Society of America Bulletin*, 101, 759-773.

Condon, S.M., 1997. Geology of the Pennsylvanian and Permian Cutler Group and Permian Kaibab Limestone in the Paradox Basin, southeastern Utah and southwestern Colorado. *U. S. Geological Survey Bulletin*, 2000-P.

Cox, S.F., Knackstedt, M.A. and Braun, J., 2001. Principles of structural control on permeability and fluid flow in hydrothermal systems. *Society of Economic Geologists Reviews*, 14, 1-24.

Crawford, B. R., 1998. Experimental fault sealing; shear band permeability dependency on cataclastic fault gouge characteristics. In: Coward, M. P., Daltaban, T. S. and Johnson, H. (eds). *Structural geology in reservoir characterization*, Geological Society, London, Special Publications, 127, 27-47.

Curewitz, D. and Karson, J.A., 1997. Structural settings of hydrothermal outflow; fracture permeability maintained by fault propagation and interaction. *Journal of Volcanology and Geothermal Research*, 79, 149-168.

Czernichowski-Lauriol, I., Sanjuan, B., Rochelle, C., Bateman, K., Pearse, J., and Blackwell, P., 1996. Analysis of the geochemical aspects of the underground diposal of CO_2. In: Apps, J.A. and Tsang, C.F. (eds). *Deep injection disposal of hazardous and industrial waste*, 565-583. Academic Press.

Dahlstrom, C. D. A., 1969. Balanced cross sections. *Canadian Journal of Earth Sciences*, 6, 743-757.

Davidson, J., Freund, P. and Smith, A., 2001. *Putting carbon back in the ground.* IEA Greenhouse Gas R&D Programme, February.

Davies, R.K., An, L., Jones, P., Mathis, A. and Cornette, C., 2003. Fault-seal analysis South Marsh Island 36 Field, Gulf of Mexico. AAPG Bulletin, 87, 479-491.

Davis, G. H., 1978. Monocline fold pattern of the Colorado Plateau. In: Matthews, V., (ed) 1978. *Laramide folding associated with basement block faulting in the western United States, Memoir - Geological Society of America*, 151, 215-233.

Dawers, N.H. and Anders, M.H., 1995. Displacement-length scaling and fault linkage. *Journal of Structural Geology*, 17, 607-614.

Dethier, D.P., 2001. Pleistocene incision rates in the Western United States calibrated using Lava Creek B Tephra. *Geology*, 29, 783-786.

Demaison, G.J., 1977. Tar sands and supergiant oil fields. *American Association of Petroleum Geologists*, 61, 1950-1961.

Dockrill, B., Kirschner, D.L. and Shipton, Z.K., In Revision. Internal structure and evolution of fault-related active and ancient travertine deposits in east-central Utah, U.S.A.. *Sedimentary Geology*.

Doelling, H.H., 1994. Tufa deposits in western Grand County. *Survey Notes - Utah Geological Survey*, 26, 8-10.

Doelling, H.H., 2001. Geologic map of the Moab and eastern part of the San Rafael Desert 30' x 60' quadrangles, Grand and Emery Counties, Utah, and Mesa County, Colorado. Utah Geological Survey, Map 180.

Doelling, H.H., 2002. Interim geological map of the San Rafael Desert 30'x60' quadrangle, Grand and Emery County, Utah: Utah Geological Survey Map OFR-404.

Doelling, H.H., Huntoon, P.W. and Oviatt, C.G., 1988. Salt deformation in the Paradox region. *Utah Geological and Mineral Survey Bulletin*, 122.

Dong, H., Hall, C.M., Peacor, D.R. and Halliday, A.N., 1995. Mechanisms of argon retention in clays revealed by laser ^{40}Ar-^{39}Ar dating, *Science*, 267, 355-359.

Drewitt, G. B., Black, T. A., Nesic, Z., Humphreys, E. R., Jork, E. M., Swanson, R. V., Ethier, G. J., Griffis, T. J. and Morgenstern, K., 2002. Measuring forest floor CO_2 fluxes in a Douglas-fir forest. *Agricultural and Forest Meteorology*, 110, 229-317.

Dromgoole, E.L. and Walter, L.M., 1990. Iron and manganese incorporation into calcite: Effects of growth kinetics, temperature and solution chemistry. *Chemical Geology*, 81, 311-336.

Duan, Z., Moller, N. and Weare, J.H., 1995. Equation of state for $NaCl-H_2O-CO_2$ system-prediction of phase equilibria and volumetric properties. *Geochimica et Cosmochimica Acta*, 59, 2869-2882. (http://geotherm.ucsd.edu/)

Edmonds, J., Freund, P. and Dooley, J.J., 2000. The role of carbon management technologies in addressing atmospheric stabilization of greenhouse gases, In: Williams, D.J., Durie, B., McMullan, P., Paulson, C. and Smith, A., (eds). *Proceedings of the Fifth International Conference on Greenhouse Gas Control Technologies*, 46-51. CSRIO, Cairns, Australia.

Engelder, J.T., 1974. Cataclasis and the generation of fault gouge. *Geological Society of America Bulletin*, 85, 1515-1522.

Eschner, T.B. and Kocurek, G., 1986. Marine destruction of eolian sand seas; origin of mass flows. *Journal of Sedimentary Petrology*, 56, 401-411.

Fairchild, I.J., Marshall, J.D. and Bertrand-Sarafati, J., 1990. Stratigraphic shifts in carbon isotopes from Proterozoic stromatolitic carbonates (Mauritania): influences of primary mineralogy and diagenesis. *American Journal of Science*, 290A, 46-79.

Ferrill, D.A. and Morris, A.P., 2001. Displacement gradient and deformation in normal fault systems. Journal of Structural Geology, 23, 619-638.

Fisher, Q. J. and Knipe, R. J., 1998. Fault sealing processes in siliciclastic sediments. In: Jones, G., Fisher, Q. J. and Knipe, R. J. (eds). *Faulting, fault sealing and fluid flow in hydrocarbon reservoirs*. Geological Society, London, Special Publications, 147, p. 117-134

Foland, K.A., Hubacher, F.A. and Arehart, G.B., 1992. $^{40}Ar/^{39}Ar$ dating of very fine-grained samples: An encapsulated-vial procedure to overcome the problem of ^{39}Ar recoil loss. *Chemical Geology*, 102, 269-276.

Folk R.L., Chafetz H.S. and Tiezzi P.A., 1985. Bizarre forms of depositional and diagenetic calcite in hot-spring travertines, Central Italy. In: N. Schneidermann and

P.M. Harris (Eds.) *Carbonate Cements*. The Society of Economic Paleontologists and Mineralogists Special Publications, 36, 349-369.

Ford T.D. and Pedley H.M., 1996. A review of tufa and travertine deposits of the world. *Earth-Science Reviews*, 41, 117-175.

Fouke, B.W., Farmer, J.D. Des Marais, D.J., Pratt, L., Sturchio, N.C., Burns, P.C. and Discipulo, M.K., 2000. Depositional facies and aqueous-solid geochemistry of travertine-depositing hot springs (Angel Terrace, Mammoth Hot Springs, Yellowstone National Park, U.S.A.). *Journal of Sedimentary Research*, 70, 565-585.

Foxford, K. A., Garden, I.R., Guscott, S.C., Burley, S.D., Lewis, J.L.L., Walsh, J.J. and Watterson, J. 1996. The field geology of the Moab Fault. In: Huffman, A.C., Lund, W.R. and Godwin L.H., (Eds.) 1996. *Geology and resources of the Paradox Basin*. Utah Geological Association Guidebook 25, 265-283.

Foxford, K. A., Walsh, J. J., Watterson, J., Garden, I. R., Guscott, S. C. and Burley, S. D., 1998. Structure and content of the Moab fault zone, Utah, USA, and its implications for fault seal prediction. In: Jones, G., Fisher, Q. J. and Knipe, R. J. (eds). Faulting, fault sealing and fluid flow in hydrocarbon reservoirs. Geological Society, London, Special Publications, 147, p. 87-103.

Fowles, J. and Burley, S., 1994. Textural and permeability characteristics of faulted, high porosity sandstones. Marine and Petroleum Geology, 11, 608-623.

Friedman, I., 1970. Some investigations of the deposition of travertine from Hot Springs-I. The isotopic chemistry of a travertine-depositing spring. *Geochimica et Cosmochimica Acta*, 34, 1303-1315.

Friedman, I. and O'Neil, J.R., 1977. Compilation of stable isotope fractionation factors of geochemical interest. *US Geological Survey Professional Paper*, 440-KK.

Fristad, T., Goth, A., Yielding, G. and Freeman, B., 1997. Quantitative fault seal prediction: a case study from Oseberg Sud. In: Moller, P. and Koestler, A.G. (eds).

Hydrocarbon seals: Importance for exploration and production. NPF Special Publication, 7, 107-124.

Fulljames, R.J., Zijerverld, L.J. and Franssen, R.C.M.W., 1997. Fault seal processes: synthetic analysis of fault seals over geological and production time scales. In: Moller, P. and Koestler, A.G. (eds). *Hydrocarbon seals: Importance for exploration and production.* NPF Special Publication, 7, 51-59.

Gale, J., 2004. Why do we need to consider geological storage of CO_2? In: Baines, S.J. and Worden, R.H. (eds) 2004. *Geological Storage of Carbon Dioxide.* Geological Society, London, Special Publications, 233, 7-16.

Gale, J. and Freund, P., 2001. Coal-bed methane enhancement with CO_2 sequestration: worldwide potential. *Environmental Geosciences*, 8, 210-217.

Garden, I.R., Guscott, S. C., Burley, S. D., Foxford, K. A., Walsh, J. J. and Marshall, J., 2001. An exhumed palaeo-hydrocarbon migration fairway in a faulted carrier system, Entrada Sandstone of SE Utah, USA. *Geofluids*, 1, 195-213.

Gartrell, A., Zhang, Y., Lisk, M. and Dewhurs, D., 2004. Fault intersections as critical hydrocarbon leakage zones: integrated field study and numerical modelling of an example from the Timor Sea, Australia. *Marine and Petroleum Geology*, 21, 1165-1179.

Gibson, R.G., 1994. Fault-zone seals in siliciclastic strata of the Columbus Basin, offshore Trinidad. *AAPG Bulletin*, 78, 1372-1385.

Gibson, R.G., 1998. Physical character and fluid-flow properties of sandstone-derived fault zones. In: Coward, M. P., Daltaban, T. S. and Johnson, H. (eds). Structural geology in reservoir characterization. Geological Society, London, Special Publications, 127, 83-97.

Gibson, R.G. and Bentham, P.A., 2003. Use of fault-seal analysis in understanding petroleum migration in a complexly faulted anticlinal trap, Columbus Basin, offshore Trinidad. AAPG Bulletin, 87, 465-478.

Given, R.K. and Wilkinson, B.H., 1985. Kinetic control of morphology, composition and mineralogy of abiotic sedimentary carbonates. *Journal of Sedimentary Petrology*, 55, 109-119.

Goguel, J., 1952. *Tectonics* (1962 Translation). W.H. Freeman and Co, San Francisco.

Gonfiantini R., Panichi C., and Tongiorgi E., 1968. Isotopic disequilibrium in travertine deposition. *Earth and Planetary Science Letters*, 5, 55-58.

Gouveia, F.J., Johnson, M.R., Leif, R.N. and Friedmann, S.J., 2005. *Aerometric measurement and modeling of the mass of CO_2 emissions from Crystal Geyser, Utah.* Lawrence Livermore National Laboratory, Livermore, CA, UCRL-TR-211870.

Gudmundsson, A., Berg, S.S., Lyslo, K.B. and Skurtveit, E., 2001. Fracture networks and fluid transport in active fault zones. *Journal of Structural Geology*, 23, 343-353.

Gunter, W.D., Wiwchar, B. and Perkins, E.H., 1997. Aquifer disposal of CO_2-rich greenhouse gases: extension of the time scale of experiment fro CO_2-sequestering reactions by geochemical modeling. *Mineralogy and Petrology*, 59, 121-140.

Gunter, W.D., Bachu, S. and Benson, S., 2004. The role of hydrogeological and geochemical trapping in sedimentary basins for secure geological storage of carbon dioxide. In: Baines, S.J. and Worden, R.H. (eds). *Geological Storage of Carbon Dioxide*. Geological Society, London, Special Publications, 233, 129-146.

Guo, L, and Riding, R., 1994. Origin and diagenesis of Quaternary travertine shrub facies, Rapolano Terme, central Italy. *Sedimentology*, 41, 499-520.

Guo, L., Andrews, J., Riding, R., Dennis, P. and Dresser, Q., 1996. Possible microbial effects on stable carbon isotopes in hot-spring travertines. *Journal of Sedimentary Research*, 66, 468-473.

Hancock, P.L., Chalmers, R.M.L, Altunel, E. and Cakir, Z., 1999. Travitonics: using travertines in active fault studies. *Journal of Structural Geology*, 21, 903-916.

Hancock, P. L., Chalmers, R. M. L., Altunel, E., Cakir, Z. and Becher-Hancock, A., 2000. Creation and destruction of travertine monumental stone by earthquake faulting at Hierapolis, Turkey. In: McGuire, W. J., Griffiths, D. R., Hancock, P. L. and Stewart, I. S. (eds). *The archaeology of geological catastrophes*. Geological Society, London, Special Publications, 171, 1-14.

Hanks, C.L., Lorenz, J., Teufel, L.W. and Krumhardt, A.P., 1997. Lithologic and structural controls on natural fracture distribution and behavior within the Lisburne Group, northeastern Brooks Range and North Slope subsurface, Alaska. AAPG Bulletin, 81, 1700-1720.

Hanor, J.S., 2000. Barite-celestine geochemistry and environments of formation. In: Alpers, C.N., Jambor, J.L. and Nordstrom, D.K., (eds) 2000. *Sulphate minerals: crystallography, geochemistry and environmental significance*. Reviews in Mineralogy and Geochemistry, 40.

Hansley, P.L., 1995. Diagenetic and burial history of the Lower Permian White Rim Sandstone in the Tar Sand Triangle, Paradox Basin, southeastern Utah. *U. S. Geological Survey Bulletin*, 2000-I.

Harper, T.R. and Ludin, E.R., 1997. Fault seal analysis: reducing our dependence on empiricism. In: Moller, P. and Koestler, A.G. (eds). *Hydrocarbon seals: Importance for exploration and production*. NPF Special Publication, 7, 149-165.

Hazel, J.E., 1994. Sedimentary response to intrabasinal salt tectonism in the Upper Triassic Chinle Formation, Paradox Basin, Utah. *U. S. Geological Survey Bulletin*, 2000-F.

Heath, J.E., 2004. *Hydrogeochemical characterization of leaking carbon dioxide-charged fault zones in east-central Utah*. Masters Thesis, Utah State University.

Hecker, S., 1993. Quaternary tectonics of Utah with emphasis on earthquake-hazard characterization. *Utah Geological Survey Bulletin*, 127.

Hendriks, C.A. and Blok, K., 1993. Underground storage of carbon dioxide. *Energy Conversion and Management*, 34, 949-957.

Hepple, R.P., 2005. Human health and ecological effects of carbon dioxide exposure. In: Benson, S.M., Oldenburg, C., Hoversten, M. and Imbus, S. (eds). *Carbon dioxide capture for storage in deep geological formations- results from the CO_2 capture project, Volume Two: Geological storage of carbon dioxide with monitoring and verification*, 1143-1172. CO_2 Capture Project, Elsevier.

Hesthammer, J. and Fossen, H., 2000a. Uncertainties associated with fault sealing analysis, *Petroleum Geoscience*, 6, 37-45.

Hesthammer, J., Johansen, T. E. S. and Watts, L. 2000b. Spatial relationships within fault damage zones in sandstone, *Marine and Petroleum Geology*, 17, 873-893.

Heyman, O.G., Huntoon, P. W. and White-Heyman, M. A., 1986. Laramide deformation of the Uncompahgre Plateau; geometry and mechanisms. In: Stone, D.S. and Johnson, K.S., (eds) 1986. *New interpretations of Northwest Colorado geology*, Rocky Mountain Association of Geologists, 65-76.

Holloway, S. and Savage, D., 1993. The potential for aquifer disposal of carbon dioxide in the UK. *Energy Conversion and Management*, 34, 925-932.

Hood, J. W. and Patterson, D. J., 1984. Bedrock aquifers in the northern San Rafael Swell area, Utah, with special emphasis on the Navajo Sandstone. *Utah Department of Natural Resources*, Technical Publication 78.

Hintze, J.F. 1993. *Geological History of Utah.* Brigham Young University Geology Studies, Special Publication 7.

Huffman, A.C., Lund, W.R. and Godwin, L.H., 1996. Geology and resources of the Paradox basin. *Utah Geological Association Publication* 25.

Hunt, C.B., 1956. Cenozoic geology of the Colorado Plateau. *U. S. Geological Survey Professional Paper* 279.

Huntoon, J.E., Dubriel, R.F. and Stanesco, J.D., 1994. Tectonic influence on development of the Permian-Triassic unconformity and basal Triassic strata, Paradox Basin, southeastern Utah. In: Caputo, M.V., Peterson, J.A. and Franczyk, K.J., (eds) 1994. *Mesozoic Systems of the Rocky Mountain Region, USA.* Society of Economic Paleontologists and Mineralogists (Society for Sedimentary Geology), Rocky Mountain Section, 109-131.

Huntoon, J.E., Hansley, P.L. and Naeser, N.D., 1999. The search for a source rock for the giant Tar Sand Triangle accumulation, southeastern Utah. AAPG Bulletin, 83, 467-495.

Hutcheon, I. and Abercrombie, H.J., 1990. Carbon dioxide in clastic rocks and silicate hydrolysis. *Geology*, 18, 541-544.

Imber, J., Tuckwell, G.W., Childs, C., Walsh, J.J., Manzocchi, T., Heath, A.E., Bonson, C.G. and Strand, J., 2004. Three-dimensional distinct element modeling of relay frowth and breaching along normal faults. *Journal of Structural Geology*, 26, 1897-1911.

Intergovernmental Panel on Climate Change (IPCC), 2001. *The Scientific Basis. Summary for Policy Makers and Technical Summary of the Working Group I Report.* Cambridge University Press, Cambridge.

Irwin, C.D., 1971. Stratigraphic analysis of the Upper Permian and Lower Triassic strata in southern Utah. *American Association of Petroleum Geologists*, 55, 1976-2007.

Irwin, W. P. and Barnes, I., 1980. Tectonic relations of carbon dioxide discharges and earthquakes. *Journal of Geophysical Research*, 85, 3115-3121.

Janssen, A., Swennen, R., Podoor, N. and Keppens, E., 1999. Biological and diagenetic influence in Recent and fossil tufa deposits from Belgium. *Sedimentary Geology*, 126, 75-95.

Janssens, I.A., Kowalski, A.S. and Ceulemans, R., 2001. Forest floor CO_2 fluxes estimated by eddy covariance and chamber-based model. *Agricultural and Forest Meteorology*, 106, 61-69.

Jev, B. I., Kaars-Sijpesteijn, C. H., Peters, M. P. A. M., Watts, N. L. and Wilkie, J. T., 1993. Akaso Field, Nigeria; use of integrated 3-D seismic, fault slicing, clay smearing, and RFT pressure data on fault trapping and dynamic leakage. *AAPG Bulletin*, 77, 1389-1404.

Johnson, J.W., Nitao, J.J. and Knuass, K.G., 2004. Reactive transport modeling of CO_2 storage in saline aquifers to elucidate fundamental processes, trapping mechanisms and sequestration partitioning. In: Baines, S.J. and Worden, R.H. (eds) 2004. *Geological Storage of Carbon Dioxide*. Geological Society, London, Special Publications, 233, 107-128.

Johnson, J.W., Nitao, J.J. and Morris, J.P., 2005. Reactive transport modeling of cap-rock integrity during natural and engineered CO_2 storage. In: Benson, S.M., Oldenburg, C., Hoversten, M. and Imbus, S. (eds). *Carbon dioxide capture for storage in deep geological formations- results from the CO_2 capture project, Volume Two: Geological storage of carbon dioxide with monitoring and verification*, 787-814. CO_2 Capture Project, Elsevier.

Jourde, H., Flodin, E.A., Aydin, A., Durlofsky, L.J. and Wen, X., 2002. Computing permeability of fault zones in eolian sandstone from outcrop measurements. *AAPG Bulletin*, 86, 1187-1200.

Julia, R., 1983. Travertines. In: P.A., Scholle, D.G., Bebout, and C.H., Moore (eds) 1983. Carbonate Depositional *Environments*. AAPG Memoir 33, 64-72.

Kelley, V.C., 1958. Tectonics of the region of the Paradox Basin. In: Sanborn, A.F., (ed) 1958. *Guidebook to the Geology of the Paradox Basin*. Intermountain Association of Petroleum Geologists 9th Field Conference, 31-38.

Kerrich, R., 1986. Fluid infiltration into fault zones; chemical, isotopic, and mechanical effects. *Pure and Applied Geophysics*, 124, 225-268.

Kiser, L.C., 1976. Stratigraphic and petroleum potential of the Permian Kaibab Beta Member, east-central Utah. In J.G., Hill, (ed) 1976. *Symposium on the Geology of the Cordilleran Hingeline*. Rocky Mountain Association of Geologists Field Conference, 161-172.

Knipe, R. J., 1992. Faulting processes and fault seal. In: Larsen, R. M., (ed). *Structural and tectonic modelling and its application to petroleum geology*. Norwegian Petroleum Society (NPF) Special Publication, 1, 325-342.

Knipe, R. J., 1997. Juxtaposition and seal diagrams to help analyze fault seals in hydrocarbon reservoirs, *AAPG Bulletin*, 81, 187-195.

Knipe, R. J., Fisher, Q. J., Jones, G., Clennell, M.R., Farmer, A.B., Harrison, A., Kidd, B., McAllister, E., Porter, J.R. and White, E.A., 1997. Fault seal analysis: successful methodologies, application and future directions. In: Moller, P. and Koestler, A.G. (eds). *Hydrocarbon seals: Importance for exploration and production*. NPF Special Publication, 7, 15-40.

Knipe, R. J., Jones, G. and Fisher, Q. J., 1998. Faulting, fault sealing and fluid flow in hydrocarbon reservoirs; an introduction. In: Jones, G., Fisher, Q. J. and Knipe, R. J.

(eds). *Faulting, fault sealing and fluid flow in hydrocarbon reservoirs*. Geological Society, London, Special Publications, 147, vii-xxi.

Knott, S.D., Beach, A., Brockbank, P.J., Brown, J. L., McCallum, J.E. and Welbon, A.I., 1996. Spatial and mechanical controls on normal fault populations. Journal of Structural Geology, 18, 359-372.

Kocurek, G., 1981. Erg reconstruction: the Entrada Sandstone (Jurassic) of northern Utah and Colorado. *Palaeogeography, Palaeoclimatology, Palaeoecology*, 36, 125-153.

Kumar, A., Noh, M.H., Pope, G.A., Sepehrnoori, K., Bryant, S.L. and Lake, L.W., 2005. Simulating CO_2 storage in deep saline aquifers. In: Benson, S.M., Oldenburg, C., Hoversten, M. and Imbus, S. (eds). *Carbon dioxide capture for storage in deep geological formations- results from the CO_2 capture project, Volume Two: Geological storage of carbon dioxide with monitoring and verification*, 877-896. CO_2 Capture Project, Elsevier.

Labaume, P, Sheppard, S.M. F. and Moretti, I., 2001. Fluid flow in cataclastic thrust fault zones in sandstones, Sub-Andean Zone, southern Bolivia. *Tectonophysics*, 340 , 141-172.

Lamb, T.W. and Whitman, R.V., 1979. *Soil mechanics*. Wiley-New York.

Leckenby, R.J., Sanderson, D.J. and Lonergan, L., In Press. Estimating flow heterogeneity in natural fracture systems. *Journal of Volcanology and Geothermal Research.*

Lee, A., Christensen, Dag., Cappelen, F., Hartog, J., Thompson, A., Johns, G., Senior, B. and Akhurst, M., 2005. Policies and incentives developments in CO_2 capture and storage technology: a focused survey by the CO_2 capture project. In: Thomas, D.C. (eds). *Carbon dioxide capture for storage in deep geological formations- results from the CO_2 capture project, Volume One: Capture and separation of carbon dioxide from combustion sources*, 17-36. CO_2 Capture Project, Elsevier.

Lehner, F.K. and Pilaar, W.F., 1997. The emplacement of clay smears in synsedimentary normal faults: inferences from field observations near Frechen, Germany. In: Moller, P. and Koestler, A.G. (eds). *Hydrocarbon seals: Importance for exploration and production*. NPF Special Publication, 7, 39-50.

Lemmon, E.W., McLinden, M.O. and Friend, D.G., 2005. Thermophysical Properties of Fluid Systems. In: Linstrom P.J. and Mallard W.G. (eds). *NIST Chemistry WebBook, NIST Standard Reference Database Number 69*. National Institute of Standards and Technology, Gaithersburg MD, 20899 (http://webbook.nist.gov).

Leveille, G.P., Knipe, R., More, C., Ellis, D., Dudley, G., Jones, G., Fisher, Q.J. and Allinson, G.J., 1997. Compartmentalization of Rotliegendes gas reservoirs by sealing faults, Jupiter Fields area, southern North Sea. In: Ziegler, K., Turner, P. and Daines, S.R. (eds). *Petroleum geology of the southern North Sea: future potential*. Geological Society, London, Special Publications, 123, 87-104.

Lewis, C. and Shinn, J., 2001. Global warming – an oil and gas company perspective: prospects for geological sequestration? *Environmental Geosciences*, 8, 177-186.

Lindsay, N. G., Murphy, F. C., Walsh, J. J. and Watterson, J., 1993. Outcrop studies of shale smears on fault surfaces. In: Flint, S.S. and Bryant, I.D. (eds). *The geological modelling of hydrocarbon reservoirs and outcrop analogues*. Special Publication of the International Association of Sedimentologists, 15, 113-123.

Lorah, M. M., and Herman, J.S. 1988. The chemical evolution of a travertine-depositing stream: geochemical processes and mass transfer reactions. *Water Resources Research*, 24, 1541-1552.

Lucas, S.E. and Moore, J.C, 1986. Cataclastic deformation in accretionary wedges; Deep Sea Drilling Project Leg 66, southern Mexico, and on-land examples from Barbados and Kodiak Island. In: Moore, J.C. (ed). *Structural fabric in Deep Sea Drilling Project cores from forearcs*. Geological Society of America Memoir, 166, 89-103.

Lucchitta, I., 1979. Late Cenozoic uplift of the southwestern Colorado Plateau and adjacent lower Colorado River region. *Tectonophysics*, 61, 63-95.

Ludwig, K.R., 2001. Users manual for Isoplot/Ex rev. 2.49: A geochronological toolkit for Microsoft Excel. Berkeley Geochronology Center Special Publication No. 1a.

Lupton, C.T., 1914. Oil and gas near Green River, Grand County, Utah, *U. S. Geological Survey Bulletin*, 541-D, 115-133.

McKnight, E.T., 1940. Geology of the area between Green and Colorado rivers, Grand and San Juan counties, Utah. *U. S. Geological Survey Bulletin* 908.

Mandl, G.K., de Jong, L. N. J. and Maltha, A., 1977. Shear zones in granular material; an experimental study of their structure and mechanical genesis. *Rock Mechanics. Supplementum*, 9, 95-144.

Magnin, F., Guendon, J. L., Quinif, Y., Roiron, P.and Thinon, M., 1990. Travertine as evidence for environmental and climatic changes; a middle Pleistocene example in Mediterranean France. *Chemical Geology*, 84, 173-175.

Mansfield, C. S. and Cartwright, J. A., 1996. High resolution fault displacement mapping from three-dimensional seismic data; evidence for dip linkage during fault growth. *Journal of Structural Geology*, 18, 249-263.

Manzocchi, T., Walsh, J. J., Nell, P. and Yielding, G., 1999. Fault transmissibility multipliers for flow simulation models. *Petroleum Geoscience*, 5, 53-63.

Mayo, A.L. and Muller, A.B., 1997. Low temperature diagenetic-metamorphic and magmatic contributions of external CO_2 gas to a shallow ground water system. *Journal of Hydrology*, 194, 286-304.

Mayo, A.L., Shrum, D.B. and Chidsey, T.C., 1991. Factors contributing to exsolving carbon dioxide in ground water systems in the Colorado Plateau, Utah. *Utah Geological Association Publication*, 19, 335-341.

Meyer, H.J., 1984. The influence of impurities on the growth rate of calcite. *Journal of Crystal Growth*, 106, 639-646.

Micklethwaite, S. and Cox, S.F., 2004. Fault-segment rupture, aftershock-zone fluid flow, and mineralization. *Geology*, 32, 813-816.

Midland Valley, 2004. *3DMove User Guide*. Midland Valley, Glasgow, Scotland.

Minissale, A., Kerrick, D.M., Magro, G., Murrell, M.T., Paladini, M., Rihs, S., Sturchio, N.C., Tassi, F. and Vaselli, O., 2002. Geochemistry of Quaternary travertines in the region north of Rome (Italy): structural, hydrologic and paleoclimatic implications. *Earth and Planetary Science Letters*, 203, 709-728.

Molenaar, C. M., 1981. Mesozoic stratigraphy of the Paradox Basin; an overview. In: Wiegand, D.L., (ed) 1981. *Geology of the Paradox Basin*. Field Conference - Rocky Mountain Association of Geologists, 119-127.

Moore, J., Adams, M., Allis, R., Lutz, S. and Rauzi, S., 2005. Mineralogical and geochemical consequences of the long-term presence of CO_2 in natural reservoirs: An example from the Springerville–St. Johns Field, Arizona, and New Mexico, U.S.A. *Chemical Geology*, 217, 365-385.

Moratti, G., Piccardi, L., Vannucci, G., Belardinelli, M. E., Dahmani, M., Bendkik A. and Chenakeb, M., 2003. The 1755 "Meknes" earthquake (Morocco): field data and geodynamic implications. *Journal of Geodynamics*, 36, 305-322.

Morgan, C.D. and Chidsey, T.C., 1991. Gordon Creek, Farnham Dome and Woodside fields, Carbon and Emery Counties, Utah. In: Chidsey, T.C., (ed) 1991. *Geology of east-central Utah*. Utah Geological Association Publication, 19, 301-309.

Morrison, S. J. and Parry, W. T., 1986. Formation of carbonate-sulfate veins associated with copper ore deposits from saline basin brines, Lisbon Valley, Utah; fluid inclusion and isotopic evidence. *Economic Geology*, 81, 1853-1866.

Muir-Wood, R., 1993. Neohydrotectonics. *Zeitschrift Geomorphologie Supplementary*, 94, 275-284.

Muller, W., 2003. Strengthening the link between geochronology, textures and petrology. *Earth and Planetary Science Letters*, 206, 237-251.

Nelson, S.T., Davidson, J.P. and Sullivan, K.R., 1992. New age determinations of central Colorado Plateau laccoliths, Utah- Recognizing disturbed K-Ar systematics and re-evaluating tectonomagmatic relationships. *Geological Society of America Bulletin*, 104, 1547-1560.

Ngwenya, B. T., Elphick, S. C., Main, I. G. and Shimmield, G. B., 2000. Experimental constraints on the diagenetic self-sealing capacity of faults in high porosity rocks. *Earth and Planetary Science Letters*, 183,187-199.

Nicol, A., Watterson, J., Walsh, J. J., and Childs, C., 1996. The shapes, major axis orientations and displacement patterns of fault surfaces. Journal of Structural Geology, 18, 235-248.

Nuccio, V.F. and Condon, S.M., 1996. Burial and thermal history of the Paradox Basin, Utah and Colorado, and petroleum potential of the Middle Pennsylvanian Paradox Basin. *U. S. Geological Survey Bulletin*, 2000-O.

Odling, N. E., Harris, S. D. and Knipe R. J., 2004. Permeability scaling properties of fault damage zones in siliclastic rocks. *Journal of Structural Geology*, 26, 1727-1747.

Oldenburg, C.M., 2000. CO_2 injection for enhanced gas production and carbon sequestration. *SPE Paper 74367*, Lawrence Berkeley National Laboratory Report LBNL-49232.

Oldenburg, C.M., 2005. Storage Integrity Preface. In: Benson, S.M., Oldenburg, C., Hoversten, M. and Imbus, S. (eds). *Carbon dioxide capture for storage in deep geological formations- results from the CO_2 capture project, Volume Two: Geological storage of carbon dioxide with monitoring and verification*, 685-686. CO_2 Capture Project, Elsevier.

Oldenburg, C.M. and Unger, A.A.J., 2005. Modeling of near-surface leakage and seepage of CO2 for risk characterization. In: Benson, S.M., Oldenburg, C., Hoversten, M. and Imbus, S. (eds). *Carbon dioxide capture for storage in deep geological formations- results from the CO_2 capture project, Volume Two: Geological storage of carbon dioxide with monitoring and verification*, 1205-1216. CO_2 Capture Project, Elsevier.

Onstott, T.C., Mueller, C., Vrolijk, P.J. and Pevear, D.R., 1997. Laser $^{40}Ar/^{39}Ar$ microprobe analyses of fine-grained illite. *Geochimica et Cosmochimica Acta*, 61, 3851-3861.

Ormerod, W.G, Freund, P. and Smith, A., 1999. *Ocean storage of CO_2*. IEA Greenhouse Gas R&D Programme, February.

Orr, J.C., 2002. Global *ocean storage of anthropogenic carbon, final report.* EC Environmental and Climate Programme. At http://www.ipsl.jussieu.fr/OCMIP/reports/ GOSAC_finalreport_hires.pdf.

Park, H. J. and West, T. R., 2002. Sampling bias of discontinuity orientation caused by linear sampling technique. Engineering Geology, 66, 99-110.

Parker, J.M., 1981. Lisbon Field area, San Juan County, Utah. In: Wiegand, D.L., (ed) 1981. *Geology of the Paradox Basin*, Rocky Mountain Association of Geologists, 89-100.

Parry, W. T., Chan, M.A. and Beitler, B., 2004. Chemical bleaching indicates episodes of fluid flow in deformation bands in sandstone. *AAPG Bulletin*, 88, 175-191.

Peacock, D. C. P., 2002. Propagation, interaction and linkage in normal fault systems. *Earth-Science Reviews*, 58, 121-142.

Peacock, D. C. P. and Sanderson, D. J., 1991. Displacements, segment linkage and relay ramps in normal fault zones. *Journal of Structural Geology*, 13, 721-733.

Pearse, J.M., Holloway, S., Wacker, H., Nelis, M.K., Rochelle, C. and Bateman, K., 1996. Natural occurrences as analogues for carbon dioxide disposal. *Energy Conversion and Management*, 37, 1123-1128.

Pearse, J., Czernichowski-Laurioal, S., Lombardi, S., Brune, S., Nador, A., Baker, J., Pauwels, H., Hatziyannis, G., Beaubien, B. and Faber, E., 2004. A review of natural CO_2 accumulations in Europe as analogues for geological sequestration. In: Baines, S.J. and Worden, R.H. (eds) 2004. *Geological Storage of Carbon Dioxide*. Geological Society, London, Special Publications, 233, 43-59.

Pentecost, A., 1990. The formation of travertine shrubs: Mammoth Hot Springs, Wyoming. *Geological Magazine*, 127, 159-168.

Pentecost, A., 1993. British travertines: a review. *Proceedings of the Geologist Association*, 104, 23-39.

Pentecost, A., 1995. Geochemistry of carbon dioxide in six travertine-depositing waters of Italy. *Journal of Hydrology*, 167, 263-278.

Peterson, F. and Turner-Peterson, C.E., 1987. The Morrison Formation of the Colorado Plateau; recent advances in sedimentology, stratigraphy, and paleotectonics. *Hunteria*, 2.

Peterson, J.A., 1989. Geology and petroleum resources, Paradox Basin Province. *U. S. Geological Survey Open File Report*, OF 88-0450-U, p69.

Pittman, E.D., 1992. Relationship of porosity and permeability to various parameters derived from mercury injection-capillary pressure curves for sandstone. *AAPG Bulletin*, 76, 191-198.

Pipiringos, G.N. and O'Sullivan, R.B., 1978. Principal unconformities in Triassic and Jurassic rocks, Western Interior United States; a preliminary survey, *U.S. Geological Survey Professional Paper 1035–A*.

Pruess, K., 2004. The TOUGH Codes - A family of simulation tools for multiphase flow and transport processes in permeable media, *Vadose Zone Journal*, 3, 738-746.

Pruess, K. and Garcia, J., 2002. Multiphase flow dynamics during CO_2 disposal into saline aquifers. *Environmental Geology*, 42, 282-295.

Pruess, K., Xu, T., Apps, J. and Garcia, J., 2001. *Numerical modeling of aquifer disposal of CO_2*. Extended paper from presentation at the SPE/EPA/DOE Exploration and Production Environmental Conference held in San Antonio, Texas, 26-28 February 2001.

Reeves, S., 2003. Enhanced CBM recovery: Coal-bed CO_2 sequestration assessed. *Oil and Gas Journal*, July 14th.

Reeves, S., Pekot, L. and Clarkson, C., 2001. Geologic sequestration of CO_2 in deep, unmineable coal beds: An integrated research and commercial scale field demonstration project. SPE 71749. *Proceedings of the SOE Annual Technical Conference and Exhibition*, New Orleans, September, 2001.

Rihs, S., Condomines, M. and Poidevin, J., 2000. Long-term behaviour of continental hydrothermal systems; U-series study of hydrothermal carbonates from the French Massif Central (Allier Valley). *Geochimica et Cosmochimica Acta*, 64, 3189-3199.

Robertson, E.C., 1983. Relationship of fault displacement to gouge and breccia thickness. *American Institute of Mining Engineers Transactions*, 124, 1426-1432.

Rochelle, C.A., Czernichowski-Laurioal, I. and Milodowski, A.E., 2004. The impact of chemical reactions on CO_2 storage in geological formations: a brief review. In: Baines, S.J. and Worden, R.H. (eds) 2004. *Geological Storage of Carbon Dioxide*. Geological Society, London, Special Publications, 233, 87-106.

Rohrlach, B., Madera, A. and Watt, R., 1999. Geology, alteration and mineralisation of the Tampakan copper deposit. *Australasian Institute of Mining and Metallurgy*, 4, 517-525.

Ross, M.L., 1998. Geology of the Tertiary intrusive centers of the La Sal Mountains, Utah; influence of preexisting structural features on emplacement and morphology. *U. S. Geological Survey Bulletin* B-2158, 61-83.

Sant' Anna, L.G., Riccomini, C., Rodrigues-Francisco, B.H., Sial, A.N., Carvalho, M.D. and Moura, C.A.V., 2004. The Paleocene travertine system of the Itaborai basin, Southeastern Brazil. *Journal of South American Earth Sciences*, 18, 11-25.

Sanders, J.E. and Friedman, G.M., 1967. Origin and occurrence of limestones. *Carbonate rocks-origin, occurrence and classification*, 169-265.

Scherer, G.W., Celia, M.A., Prevost, J.H., Bachu, S., Bruant, R., Duguid, A., Fuller, R., Gasda, S.E., Radonjic, M. and Vichit-Vadakan, W., 2005. Leakage of CO_2 through abandoned wells: Roles of corrosion of cement. In: Benson, S.M., Oldenburg, C., Hoversten, M. and Imbus, S. (eds). *Carbon dioxide capture for storage in deep geological formations- results from the CO_2 capture project, Volume Two: Geological storage of carbon dioxide with monitoring and verification*, 827-850. CO_2 Capture Project, Elsevier.

Scholle, P.A., Stemmerik, L. and Harpoth, O., 1990. Origin of major karst-associated celestite mineralization in Karstryggen, central East Greenland. *Journal of Sedimentary Petrology*, 60, 397-410.

Scholz, C.H., 1987. Wear and gouge formation in brittle faulting. *Geology*, 15, 493-495.

Schowalter, T. T., 1979. Mechanics of secondary hydrocarbon migration and entrapment. *American Association of Petroleum Geologists Bulletin*, 63, 723-760.

Seibt, A., Naumann, D., Hoth, P. and Huenges, E., 1999. Gas-solubility in formation waters of the north German Basin: Implications for geothermal energy recovery CO_2 storage. *Scientific Technical Report 99/04*, GeoForschungsZentrum Potsdam, 63-86.

Shoemaker, E.M., Case, J.E. and Elston, D.P., 1958. Salt anticlines of the Paradox Basin. In: Sanborn, A.F., (ed) 1958. *Guidebook to the Geology of the Paradox Basin*, Intermountain Association of Petroleum Geologists, 9th Annual Field Conference, 39-59.

Shipton, Z. K. and Cowie, P.A., 2001. Damage zone and slip-surface evolution over μm to km scales in high-porosity Navajo Sandstone, Utah. *Journal of Structural Geology*, 23, 1825-1844.

Shipton, Z.K., Evans, J.P., Robeson, K.R., Forster, C.B. and Snelgrove, S., 2002. Structural heterogeneity and permeability in faulted eolian sandstone; implications for subsurface modeling of faults. *AAPG Bulletin*, 86, 863-883.

Shipton, Z.K, Evans, J.P., Kirschner, D., Kolesar, P.T., Williams, A.P. and Heath, J., 2004. Analysis of CO_2 leakage through "low-permeability" faults from natural reservoirs in the Colorado Plateau, east-Central Utah. In: Baines, S.J. and Worden, R.H. (eds) 2004. *Geological Storage of Carbon Dioxide*. Geological Society, London, Special Publications, 233, 43-59.

Shipton, Z.K, Evans, J.P., Dockrill, B., Heath, J., Williams, A.P., Kirschner, D. and Kolesar, P.T., 2005. Natural leaking CO_2-charged systems as analogues for failed geologic storage reservoirs. In: Benson, S.M., Oldenburg, C., Hoversten, M. and Imbus, S. (eds). *Carbon dioxide capture for storage in deep geological formations-results from the CO_2 capture project, Volume Two: Geological storage of carbon dioxide with monitoring and verification*, 699-712. CO_2 Capture Project, Elsevier.

Sibson, R.H., 1994. Crustal stress, faulting and fluid flow. In: Parnell, J. (ed). *Geofluids: Origin, Migration and Evolution of Fluids in Sedimentary Basins*. Geological Society, London, Special Publications, 78, 69-84.

Sibson, R.H., 1996. Structural permeability of fluid-driven fault-fracture meshes. *Journal of Structural Geology*, 18, 1031-1042.

Siegenthaler, U. and Joos, F., 1992. Use of a simple model for studying ocean tracer distributions and the global carbon cycle. *Tellus*, 44B, 186-207.

Smith, D. A., 1980. Sealing and nonsealing faults in Louisiana Gulf Coast salt basin. *AAPG Bulletin*, 64, 145-172.

Smouse, D., 1993. Salt Wash. In: Hill, B.G. and Bereskin, S.R. (eds). *Oil and gas fields of Utah*. Utah Geological Association Publication, 22.

Spangler, L.E., Naftz, D.L. and Peterman, Z.E., 1996. Hydrology, chemical quality and characterization of salinity in the Navajo aquifer in and near Greater Aneth oil field, San Juan County, Utah. *U.S. Geological Survey Water-Resources Investigations Report* 96-4155.

Sperrevik, S., Faerseth, R.B. and Gabrielsen, R.H., 2000. Experiments on clay smear formation along faults. *Petroleum Geoscience*, 6, 113-123.

Stanesco, J.D. and Dubriel, R.F., 1992. Fluvial and eolian facies of the Organ Rock Shale Member of the Permian Cutler Formation, southeastern Utah. *Geological Society of America, Abstracts with Programs*, 24, 64.

Steele, B.A., 1987. Depositional environments of the White Rim Sandstone member of the Permian Cutler Formation, Canyonlands National Park, Utah. *U.S. Geological Survey Bulletin*, 1592.

Stevens, S.H., Pearse, J.M. and Rigg, A.A., 2001. Natural analogues for geological storage of CO_2: an intergrated global research programme. *Proceedings of the First National Conference on Carbon Sequestration*, Washington DC, May 2001.

Stevens, S.H., 2005. Natural CO_2 fields as analogs for geologic CO_2 storage. In: Benson, S.M., Oldenburg, C., Hoversten, M. and Imbus, S. (eds). *Carbon dioxide capture for storage in deep geological formations- results from the CO_2 capture project, Volume Two: Geological storage of carbon dioxide with monitoring and verification*, 687-697. CO_2 Capture Project, Elsevier.

Stevenson, G.M. and Baars, D. L., 1986. The Paradox; a pull-apart basin of Pennsylvanian age. In: Peterson, J.A. (ed) 1986. Paleotectonics and sedimentation in the Rocky Mountain region, United States, *American Association of Petroleum Geologists Memoir*, 41, 513-539.

Stewart, J.H., Poole, F.G. and Wilson, R.F., 1972. Stratigraphy and origin of the Triassic Moenkopi Formation and related strata in the Colorado Plateau region. *U.S. Geological Survey Professional Paper*, 691.

Sturchio, N.C., Pierce, K.L., Murrell, M.T., Sorey, M.L., 1994. Uranium-series ages of travertines and timing of the last glaciation in the northern Yellowstone area, Wyoming-Montana. *Quaternary Research*, 41, 265-277.

Sumner, D.Y., and Grotzinger, J.P., 1996. Were kinetics of Archean calcium carbonate precipitation related to oxygen concentration? *Geology*, 24, 119-112.

Surdam, R.C., Jiao, Z.S. and MacGowan, D.B., 1993. Redox reactions involving hydrocarbons and mineral oxidants; a mechanism for significant porosity enhancement in sandstones. *AAPG Bulletin*, 77, 1509-1518.

Szabo, B.J. and Winograd, I.J., 1995. Paleoclimatic, paleohydrologic and tectonic applications of uranium-series dating of travertine and calcite vein samples from southern Great Basin and Grand Canyon areas. *U. S. Geological Survey Open File Report*, OF 95-0037.

Taberner, C., Marshall, J.D., Hendry, J.P., Pierre, C. and Thirlwall, M. F., 2002. Celestite formation, bacterial sulphate reduction and carbonate cementation of Eocene reefs and basinal sediments (Igualada, northeastern Spain). *Sedimentology*, 49, 171-190.

Tranos, M.D., Papadimitriou, E.E. and Kilias, A.A., 2003. Thessaloniki-Gerakarou Fault Zone (TGFZ): the western extension of the 1978 Thessaloniki earthquake fault (Northern Greece) and seismic hazard assessment. *Journal of Structural Geology*, 25, 2109-2123.

Trimble, L.M. and Doelling, H.H., 1978. Geology and uranium-vanadium deposits of the San Rafael River mining area. *Utah Geological and Mineral Survey Bulletin*, 113.

Trudgill, B. and Cartwright, J., 1994. Relay-ramp forms and normal-fault linkages, Canyonlands National Park, Utah. Geological Society of America Bulletin, 106, 1143-1157.

Tucker, M.E., and Wright, V.P., 1996. *Carbonate Sedimentology*, Blackwell Science.

Turi, B., 1986. Stable isotope geochemistry of travertines. In P. Fritz and J.C. Fontes (Eds), *Handbook of Environmental Isotope Geochemistry*, Vol. 2B, The Terrestrial Environment, Elsevier, 207-238.

Turner, C.E. and Fishman, N.S., 1991. Jurassic Lake T'oo'dichi'; a large alkaline, saline lake, Morrison Formation, eastern Colorado Plateau. *Geological Society of America Bulletin*, 103, 538-558.

Utah Climate Centre (http://climate.usu.edu/).

van der Meer, L.G.H., 1995. The CO_2 storage efficiency of aquifers. *Energy Conversion and Management*, 36, 513-518.

van der Pluijm, B.A., Hall, C.M., Vrolijk, P.J., Pevear, D.R. and Covey, M.C., 2001. The dating of shallow faults in the Earth's crust. *Nature*, 412, 172-175.

Vrolijk, P. and van der Pluijm, B.A., 1999. Clay gouge. Journal of Structural Geology, 21, 1039-1048.

Walker, T. R., Waugh, B. and Grone, A. J., 1978. Diagenesis in first-cycle desert alluvium of Cenozoic age, southwestern United States and northwestern Mexico. *Geological Society of America Bulletin*, 89, 19-32.

Walsh, J.J. and Watterson, J., 1989. Displacement gradients on fault surfaces. *Journal of Structural Geology*, 11, 307-316.

Walsh, J.J. and Watterson, J., 1991. Geometric and kinematic coherence and scale effects in normal fault systems. In: Roberts, A.M., Yielding, G. and Freeman, B. (eds). *The geometry of normal faults*. Geological Society, London, Special Publications, 56, 193-203.

Warren, J.K., 1999. *Evaporites: their evolution and economics*. Oxford, Blackwell Science, 438pp.

Watts, N. L., 1987. Theoretical aspects of cap-rock and fault seals for single- and two-phase hydrocarbon columns. *Marine and Petroleum Geology*, 4, 274-307.

Weber, C.J., Mandl, G., Pilaar, W.F., Lehnar, F. and Precious, R.G., 1978. The role of faults in hydrocarbon migration and trapping in Nigerian growth structures. 10th Annual Offshore Technology Conference, Houston, Texas.

Welsh, J.E., Stokes, W.L. and Wardlaw, B.R., 1979. Regional stratigraphic relationships of the Permian "Kaibab" or Black Box Dolomite of the Emery High, central Utah. In: Baars D.L. (ed) 1979. *Permianland*: Four Corners Geological Society 9th Field Conference,143-149.

White, S.P., Allis, R.G., Moore, J., Chidsey, T., Morgan, C., Gwynn, W. and Adams, M., 2005. Simulation of reactive transport of injected CO_2 on the Colorado Plateau, Utah, USA. *Chemical Geology*, 217, 387-405.

Wildenborg, A.F.B. and van der Meer, L.G.H., 2002. The use of oil, gas and coal fields as CO2 sinks. In: Davidson, O. and Metz, B. (eds). *Proceedings of the Intergovernmental Panel on Climate Change. Working Group III: Mitigation of Climate Change*, 61-68. Regina, Canada.
http://arch.rivm.nl/env/int/ipcc/docs/css2002/ccs02-04.pdf

Wildenborg, A.F.B., Leijnse, A.L., Kreft, E., Nepveu, M.N., Obdam, A.N.M, Orlic, B., Wipfler, E.L., van der Grift, B., van Kesteren, W., Gaus, I., Czernichowski-Lauriol, I., Torfs, P. and Wojcik, R., 2005. Risk assessment methodology for CO2 storage: the scenario approach. In: Benson, S.M., Oldenburg, C., Hoversten, M. and Imbus, S. (eds). *Carbon dioxide capture for storage in deep geological formations-results from the CO_2 capture project, Volume Two: Geological storage of carbon dioxide with monitoring and verification*, 1293-1316. CO_2 Capture Project, Elsevier.

Williams, A.P, 2004. *Structural analysis of carbon dioxide leakage through the Salt Wash and Little Grand Wash Faults from natural reservoirs in the Coorado Plateau, southeastern Utah*. Masters Thesis, Utah State University.

Williams, G. D., Kane, S. J., Buddin, T. S. and Richards, A. J., 1997. Restoration and balance of complex folded and faulted rock volumes; flexural flattening, jigsaw fitting and decompaction in three dimensions. *Tectonophysics*, 273, 203-218.

Williams, P.L., 1964. Geology, structure, and uranium deposits of the Moab Quadrangle, Colorado and Utah. *U.S. Geological Survey Miscellaneous Investigation Series*, Map I-360.

Williams, P.L. and Hackman, R.J., 1971. Structure, and uranium deposits of the Salina Quadrangle, Utah. *U.S. Geological Survey Miscellaneous Investigation Series*, Map I-591-B.

Wilson, M. and Monea, M., 2004. IEA GHG Weyburn CO_2 monitoring and storage project summary report 2000-2004, Volume III. *Proceedings of the Seventh International Conference on Greenhouse Gas Control Technologies*, Vancouver.

Wo, S. and Liang, J.T., 2005. CO_2 storage in coalbeds: CO_2/N_2 injection and outcrop seepage modeling. In: Baines, S.J. and Worden, R.H. (eds) 2004. *Geological Storage of Carbon Dioxide*. Geological Society, London, Special Publications, 233, 897-924.

Woodward-Clyde Consultants, 1983. *Overview of the regional geology of the Paradox Basin study area*. Columbus, Ohio, Battelle Memorial Institute, Office of Nuclear Waste Isolation, Report ONWI-92.

Worden, R.H. and Smith, L.K., 2004. Geological sequestration of CO_2 in the subsurface: lessons from CO_2 injection enhanced oil recovery projects in oil fields. In: Baines, S.J. and Worden, R.H. (eds) 2004. *Geological Storage of Carbon Dioxide*. Geological Society, London, Special Publications, 233, 211-224.

Wright, J.C., Shawe, D.R. and Lohman, S.W., 1962. Definition of members of Jurassic Entrada Sandstone in east-central Utah and west-central Colorado. *American Association of Petroleum Geologists Bulletin*, 46, 2057-2070.

Yielding, G., Freeman, B. and Needham, D.T, 1997. Quantitative fault seal prediction. *AAPG Bulletin*, 81, 897-917.

Yielding, G., 2002. Shale Gouge Ratio: calibration by geohistory. In: Koestler, A.G. and Hunsdale, R. (eds). *Hydrocarbon Seal Quantification*. NPF Special Publication, 11, 1-15.

Yokoyama, T., Makishima, A. and Nakamura, E., 1999. Separation of Thorium and Uranium from Silicate Rock Samples Using Two Commercial Extraction Chromatographic Resins. *Analytical Chemistry*, 71, 135-141.

Yoshioka, N., 1986. Fracture energy and the variation of gouge and surface roughness during frictional sliding of rocks. *Journal of Physics of the Earth*, 34, 335-355.

Zhang, S. and Cox, S.F., 2000. Enhancement of fluid permeability during shear deformation of a synthetic mud. *Journal of Structural Geology*, 22 , 1385-1393.

Zhou, G. and Zheng, Y., 2003. An experimental study of oxygen isotope fractionation between inorganically precipitated aragonite and water at low temperatures. *Geochimica et Cosmochimica Acta*, 67, 387-399.

Zweigel, P., Hamborg, M., Arts, R., Lothe, A.E. and Tommeras, A., 2000. Prediction of migration of CO2 injected into an underground depository: Reservoir geology and migration modeling in the Sleipner case (North Sea). In: Williams, D.J., Durie, B., McMullan, P., Paulson, C. and Smith, A., (eds). *Proceedings of the Fifth International Conference on Greenhouse Gas Control Technologies*, 360-365. CSRIO, Cairns, Australia.

Zweigel, P., Arts, R., Lothe, A.E. and Lindeberg, E.B.G., 2004. Reservoir geology of the Utsira Formation at the first industrial-scale underground CO_2 storage site (Sleipner area, North Sea). In: Baines, S.J. and Worden, R.H. (eds) 2004. *Geological Storage of Carbon Dioxide*. Geological Society, London, Special Publications, 233, 165-180.

APPENDICES

APPENDIX I

OUTCROP FAULT DATA

Strike	Dip	Dip Direction	Rake	Fault[1]	Comment
120	83	South		LGWF	Main fault
98	68	South		LGWF	Main fault
130	73	South	90	LGWF	Main fault
262	68	South		LGWF	Main fault
280	82	South	74 To The West	LGWF	Main fault
282	86	South	70 To The West	LGWF	Main fault
84	66	South		LGWF	Main fault
86	72	South		LGWF	Main fault
70	56	South		LGWF	Main fault
83	86	South		LGWF	Main fault
102	63	South	58 To The West	LGWF	Main fault
86	84	South		LGWF	Main fault
75	72	South	82 To The East	LGWF	Main fault
85	71	South	86 To The East	LGWF	Main fault
95	68	South	88 To The East	LGWF	Main fault
100	60	South	80 To The East	LGWF	Main fault
114	62	South		LGWF	Main fault
110	68	South		LGWF	Main fault
96	73	South		LGWF	Main fault
98	58	South		LGWF	Main fault
105	65	South		LGWF	Main fault
102	62	South		LGWF	Main fault
92	68	South		LGWF	Main fault
93	80	South		LGWF	Main fault
83	63	South		LGWF	Main fault
87	81	South		LGWF	Main fault
81	62	South		LGWF	Main fault
75	70	South		LGWF	Main fault
78	59	South		LGWF	Main fault
85	67	South		LGWF	Main fault
88	80	South		LGWF	Main fault
129	77	North	65 To The West	LGWF	Subsidiary fault
108	73	South	55 To The West	LGWF	Subsidiary fault
137	72	South		LGWF	Subsidiary fault
100	67	North		LGWF	Subsidiary fault
138	76	South	80 To The East	LGWF	Subsidiary fault
130	63	South		LGWF	Subsidiary fault
94	68	North	85 To The East	LGWF	Subsidiary fault
135	75	North		LGWF	Subsidiary fault
88	54	South		LGWF	Subsidiary fault
80	58	South		LGWF	Subsidiary fault
80	80	South		LGWF	Subsidiary fault
83	49	South		LGWF	Subsidiary fault

1 LGWF -Little Grand Wash Fault; nSWG -northern fault of the Salt Wash Graben; sSWG -southern fault of the Salt Wash Graben; nTMG -northern fault of the Ten Mile Graben; sTMG -southern fault of the Ten Mile Graben.

2 Unpublished borehole data from Exxon. Only fault dip data provided.

Strike	Dip	Dip Direction	Rake	Fault[1]	Comment
	56			LGWF	Well DS-1 (Exxon)[2]
	56			LGWF	Well DS-2 (Exxon)[2]
	63			LGWF	Well DS-3 (Exxon)[2]
	69			LGWF	Well DS-4 (Exxon)[2]
	48			LGWF	Well DS-5 (Exxon)[2]
	55			LGWF	Well DS-6 (Exxon)[2]
	65			LGWF	Well DS-7 (Exxon)[2]
114	78	South	68 To The East	nSWG	Main fault
108	73	South	55 To The West	nSWG	Main fault
282	86	South	77 To The West	nSWG	Main fault
274	52	South	83 To The West	nSWG	Main fault
284	82	South	87 To The West	nSWG	Main fault
278	80	South	88 To The East	nSWG	Main fault
288	68	South		nSWG	Main fault
90	58	South		nSWG	Main fault
280	74	South		nSWG	Main fault
294	89	South		nSWG	Main fault
104	84	South		nSWG	Main fault
305	57	South		nSWG	Main fault
266	64	South		nSWG	Main fault
271	56	South		nSWG	Main fault
277	70	South		nSWG	Main fault
288	72	South		nSWG	Main fault
277	80	South		nSWG	Main fault
280	80	South		nSWG	Main fault
90	83	South		nSWG	Main fault
238	48	South		nSWG	Main fault
112	76	South		nSWG	Main fault
142	82	South		nSWG	Main fault
134	85	South		nSWG	Main fault
110	70	South		nSWG	Main fault
106	79	North	86 To The West	sSWG	Main fault
129	77	North	65 To The West	sSWG	Main fault
114	71	North	89 To The West	sSWG	Main fault
117	84	North	83 To The East	sSWG	Main fault
321	71	East		sSWG	Main fault
291	77	East		sSWG	Main fault
296	82	East		sSWG	Main fault
99	80	North		sSWG	Main fault
112	68	East		sSWG	Main fault
115	78	East		sSWG	Main fault

1 LGWF -Little Grand Wash Fault; nSWG -northern fault of the Salt Wash Graben; sSWG -southern fault of the Salt Wash Graben; nTMG -northern fault of the Ten Mile Graben; sTMG -southern fault of the Ten Mile Graben.

2 Unpublished borehole data from Exxon. Only the fault dip data is provided.

Strike	Dip	Dip Direction	Rake	Fault[1]	Comment
107	66	North		sSWG	Main fault
116	79	East		sSWG	Main fault
108	75	North		sSWG	Main fault
100	70	North		sSWG	Main fault
120	80	East		sSWG	Main fault
114	72	North		sSWG	Main fault
109	74	North		sSWG	Main fault
100	69	North		sSWG	Main fault
110	67	East		sSWG	Main fault
98	81	North		sSWG	Main fault
285	87	South	62 To The West	nTMG	Main fault
287	69	South	81 To The West	nTMG	Main fault
278	72	South	74 To The West	nTMG	Main fault
274	52	South	83 To The West	nTMG	Main fault
284	82	South	87 To The West	nTMG	Main fault
98	80	South	88 To The East	nTMG	Main fault
290	80	South	89 To The West	nTMG	Main fault
262	68	South		nTMG	Main fault
290	65	South		nTMG	Main fault
285	80	South		nTMG	Main fault
280	75	South		nTMG	Main fault
282	67	South		nTMG	Main fault
278	74	South		nTMG	Main fault
283	68	South		nTMG	Main fault
288	70	South		nTMG	Main fault
286	72	South		nTMG	Main fault
300	76	South		nTMG	Main fault
80	89	North	85 To The East	sTMG	Main fault
120	82	North	84 To The East	sTMG	Main fault
123	73	North	76 To The East	sTMG	Main fault
298	74	North	88 To The West	sTMG	Main fault
290	66	North		sTMG	Main fault
288	73	North		sTMG	Main fault
292	64	North		sTMG	Main fault
285	59	North		sTMG	Main fault
288	75	North		sTMG	Main fault
280	77	North		sTMG	Main fault
283	64	North		sTMG	Main fault
273	76	North		sTMG	Main fault

1 LGWF -Little Grand Wash Fault; nSWG -northern fault of the Salt Wash Graben; sSWG -southern fault of the Salt Wash Graben; nTMG -northern fault of the Ten Mile Graben; sTMG -southern fault of the Ten Mile Graben.

2 Unpublished borehole data from Exxon. Only the fault dip data is provided.

APPENDIX II

SCANLINE FRACTURE DATA

Scanline 1 (Area 1)
Salt Wash Sandstone
95-145m from relay ramp

Position (m)	Fracture Strike
1	280
2.5	281
5.9	272
9.5	281
11	299
13	271
14.4	271
19.2	280
21.2	282
23	267
28.1	292
28.9	287
32.5	284
33.6	277
34.4	252
36.6	269
37.1	210
38.1	271
44.2	264

Scanline 2 (Area 1)
Salt Wash Sandstone
55-85m from relay ramp

Position (m)	Fracture Strike
3	320
4.6	262
4.7	282
6.3	296
7.2	262
7.8	282
10.1	305
10.6	285
10.9	271
11.7	268
11.9	300
12	288
12.3	278
12.9	256
13	268
13.1	266

Scanline 2 (continued)

Position (m)	Fracture Strike
13.2	266
13.7	296
13.8	278
13.9	271
14.3	288
14.4	266
14.5	270
14.6	274
14.7	265
14.8	262
14.9	270
15	285
15.1	268
15.2	274
16.2	270
16.8	242
17	258
17.1	261
17.2	277
17.5	270
17.7	272
17.8	289
17.9	273
18	275
18.2	265
19.7	276
19.9	271
20.7	286
22.3	263
23.2	263
23.3	309
23.6	265
24	275
24.6	272
25.1	266
25.4	309
25.2	275
27.1	265
28.3	256
29.3	302
31	298

Scanline 3 (Area 1)
Salt Wash Sandstone
Eastern edge of relay ramp

Position (m)	Fracture Strike
0	269
0.2	262
0.3	270
0.3	269
0.4	262
0.5	267
0.65	277
0.7	301
0.7	303
1.05	301
1.1	307
1.15	304
1.2	309
1.4	273
1.4	311
1.55	284
1.55	319
1.75	309
1.85	301
1.95	294
2	304
2.25	298
2.45	298
2.6	306
2.6	307
2.65	281
2.8	306
2.9	300
2.9	274
3	308
3.1	288
3.2	291
3.4	308
3.4	COVERED
3.8	COVERED
3.8	318
3.85	301
4	307
4.15	313
4.15	298

Scanline 3 (continued)

Position (m)	Fracture Strike
4.3	284
4.35	306
4.35	COVERED
7.3	COVERED
7.3	304
7.7	289
8	317
8.2	294
8.7	308
8.9	296
9	331
9.05	291
9.25	309
9.25	COVERED
9.8	COVERED
9.8	291
10.05	306
10.1	287
10.1	295
10.25	291
10.35	301
10.4	301
10.65	296
10.9	300
11.1	296
11.3	268
11.4	267
11.5	268
11.6	281
11.7	302
11.7	306
11.8	270
11.8	306
11.9	251
11.9	292
12.3	284
12.6	298
12.8	292
13	300
13.4	298
13.5	281
13.7	285

Scanline 3 (continued)

Position (m)	Fracture Strike
13.95	301
14.1	325
14.3	274
14.6	276
14.7	310

Scanline 4 (Area 1)
Salt Wash Sandstone
In relay ramp

Position (m)	Fracture Strike
0	269
0.3	4
0.8	20
1	39
1.4	204
1.6	210
1.65	210
1.75	208
1.85	250
1.9	196
2.3	205
2.41	185
2.48	195
2.52	200
2.61	220
2.61	250
2.61	255
2.61	245
2.64	215
2.65	185
2.67	335
2.73	180
3.1	185
4	268
4.2	260
4.4	265
4.46	351
4.56	315
4.58	120
4.62	304
4.64	262
4.8	180

Scanline 4 (continued)

Position (m)	Fracture Strike
4.9	231
5.25	259
5.75	240
5.85	232
5.9	308
6	310
6.1	225
6.55	311
6.65	275
6.75	305
6.9	211
7.3	225
7.35	186
7.75	190
8	256
8.1	280
8.2	270
8.25	200
8.3	105
8.5	124
8.8	200
8.85	266
8.95	240
9.05	270
9.2	250
9.3	355
9.35	337
9.4	235
9.43	182
9.5	269
9.6	322
9.7	270
9.8	190
9.9	285
9.92	185
9.95	175
10	155
10.6	355
10.7	265
10.73	225
10.8	280
10.9	290

Scanline 4 (continued)

Position (m)	Fracture Strike
11	260
11.29	292
11.35	288
11.4	74
11.5	256
11.7	271
11.75	37
11.88	78
11.93	78
12.05	252
12.15	274
12.2	276
12.3	28
12.62	285
12.72	118
12.85	150
12.9	88
12.95	136
13	340
13.1	310
13.2	112
13.3	118
13.33	115
13.45	127
13.6	102
13.65	87
13.7	2
13.75	108
13.78	131
13.8	114
13.82	80
13.85	77
13.86	75
14.2	106
14.28	89
14.35	121
14.5	93
14.7	108
14.75	66
14.8	89
14.9	84
14.95	117

Scanline 4 (continued)

Position (m)	Fracture Strike
15.05	90
15.1	72
15.15	70
15.18	80
15.3	60
15.35	68
15.5	74
15.75	72
15.9	76
16.05	102
16.45	140
16.6	122
16.75	82
16.9	160
17	82
17.8	27
17.9	26
18.1	146
18.6	338
18.65	327
18.7	331
18.9	336
20	262
20.3	14
20.6	28
20.9	15
21.2	2
21.6	15
21.7	70
22	72
22.6	76
22.7	240
23.1	91
23.15	60
23.3	75
23.5	58
23.55	86
23.6	76
23.65	58
23.7	58
23.9	253
23.85	80

Scanline 4 (continued)

Position (m)	Fracture Strike
24.4	81
24.8	48
24.9	46
25.5	89
26.25	88
26.35	50
26.4	69
26.55	82
26.65	93
27.1	82
27.2	62
27.32	56
27.6	78
28.05	102
28.5	70
28.7	32
28.8	88
29	37
29.2	92
29.4	80
29.5	54
29.9	79
30	36
30.3	122
30.5	22
30.6	70
30.8	92
31.2	282
31.5	152
31.8	138
32	114
32.2	82
32.4	260
32.8	75
33	45
34	260
35	126

Scanline 5 (Area 1)
Salt Wash Sandstone
In relay ramp

Position (m)	Fracture Strike
1.5	336
2.3	315
2.35	321
2.6	270
3.12	350
3.6	181
4.6	190
4.65	292
4.7	310
5.45	200
5.93	316
6.85	300
7.35	295
7.5	295
8.15	282
8.25	265
8.55	210
9	325
9.9	210
9.95	333
10	332
10.29	325
10.35	345
11.07	215
11.3	280
11.5	174
11.7	145
12.4	125
12.55	334
12.65	285
12.7	329
12.75	359
12.85	325
13	333
13.1	340
13.18	325
13.25	332
13.37	334

Scanline 6 (Area 2)
Curtis Formation
Immediate Footwall

Position (m)	Fracture Strike
1.15	120
1.16	86
1.2	102
1.35	120
1.55	125
1.7	122
1.9	114
2.85	183
3	172
3.5	131
3.65	139
3.7	126
3.8	119
4.45	150
4.9	145
5.1	254
5.2	147
5.8	175
6.1	275
7	275
7.3	295
7.4	295
7.5	138
8.6	281
9.1	212
9.35	212
9.6	290
10.1	208
10.2	204
10.6	214
10.9	131
11.1	143
11.7	258
12	280
12.3	320
12.6	258
12.7	124
13.6	141
14	143
14.4	135

Scanline 6 (continued)

Position (m)	Fracture Strike
14.5	150
14.52	150
14.55	150
14.65	295
15.5	270
15.9	135
15.95	105
16.1	122
16.15	322
16.2	300
16.35	101
16.4	137
16.5	132
16.55	128
16.57	134
16.58	134
16.7	128
16.8	132
17.1	123
17.15	110
17.25	109
17.5	122
17.6	102
17.65	150
17.7	112
17.85	121
17.9	115
18.05	106
18.3	116
18.4	117
18.65	120
18.75	98
18.9	110
19.1	105
19.45	100
19.9	163
20.2	92
20.25	92
20.7	181
21.1	112
21.55	176
21.8	167

Scanline 6 (continued)

Position (m)	Fracture Strike
22.3	127
22.5	127
22.6	124
22.8	113
23	100
23.8	245
24.8	113
25.05	122
25.2	100
25.35	102
25.55	113
25.7	88
26	114
26.2	122
26.3	103
26.55	76
26.65	110
26.75	105
27	128
27.3	116
27.45	120
27.55	130
27.65	117
27.8	132
28.5	90
28.65	165
29.05	128
29.1	130
29.12	142
29.2	85
29.25	110
29.3	100
29.4	120
29.55	115
29.6	135
29.7	117
29.75	140
29.8	117
30	110
30.2	100
30.4	95
30.55	103

Scanline 6 (continued)

Position (m)	Fracture Strike
30.85	105
30.95	180
31.2	190
31.35	125
31.8	163
31.9	110
32	128
32.3	83
32.4	85
32.65	151
33.37	195
33.7	180
34.13	156
34.6	110
35.25	115
35.5	166
35.7	137
36.15	125
36.3	125
37	115

Scanline 7 (Area 2)
Mancos Formation
Immediate Hanging Wall

Position (m)	Fracture Strike
0	329
0.2	343
0.5	357
0.9	278
1	89
1	341
1.2	108
1.5	39
1.6	93
1.8	83
2.2	123
2.3	39
2.4	98
2.8	75
3	77
3	274
3.3	300
3.8	296
4	281
4.5	187
5.1	47
5.1	260
5.4	93
6.2	210
6.5	250
6.8	223
7	156
7.2	211
7.2	203
7.4	207
7.7	257
7.8	233
7.9	203
8.3	68
8.3	304
8.8	123
9.1	201

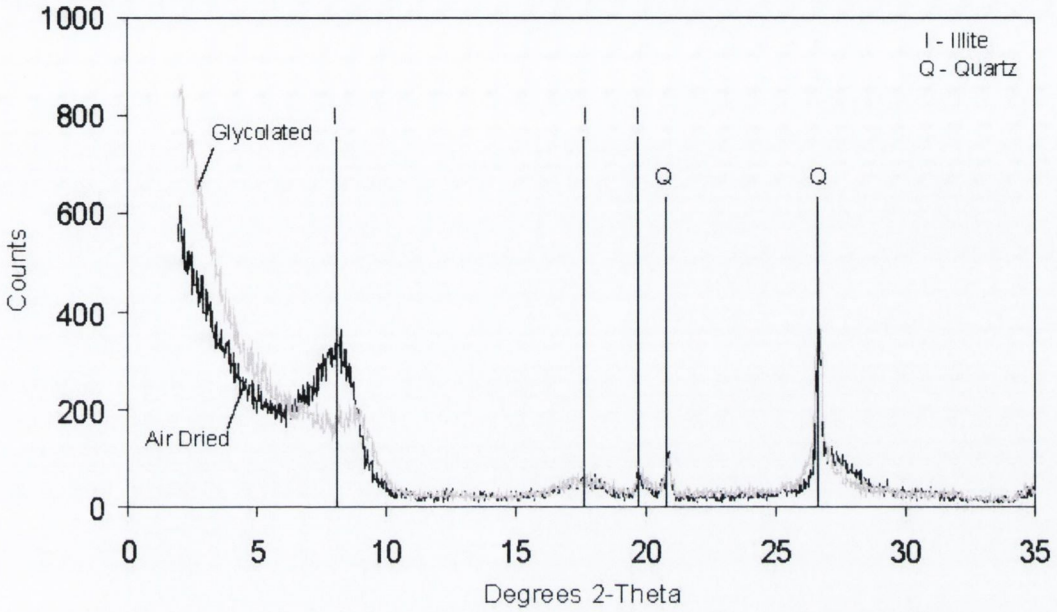
Scanline 7 (continued)

Position (m)	Fracture Strike
9.7	38
10.1	89
10.3	79
10.3	341
10.9	257
11	345
11.3	62
11.4	129
11.7	122
11.7	134
11.8	149
12	311
12.1	44
12.1	182
12.6	235
13	344
13.2	259
13.9	263
14.4	209
14.7	269
14.9	323
15.5	259
15.9	262
15.9	277
16.5	224
16.7	212
16.8	256
17.2	359
17.9	276
18.4	120
18.4	262
18.7	341
19.3	106
19.6	230
19.8	285

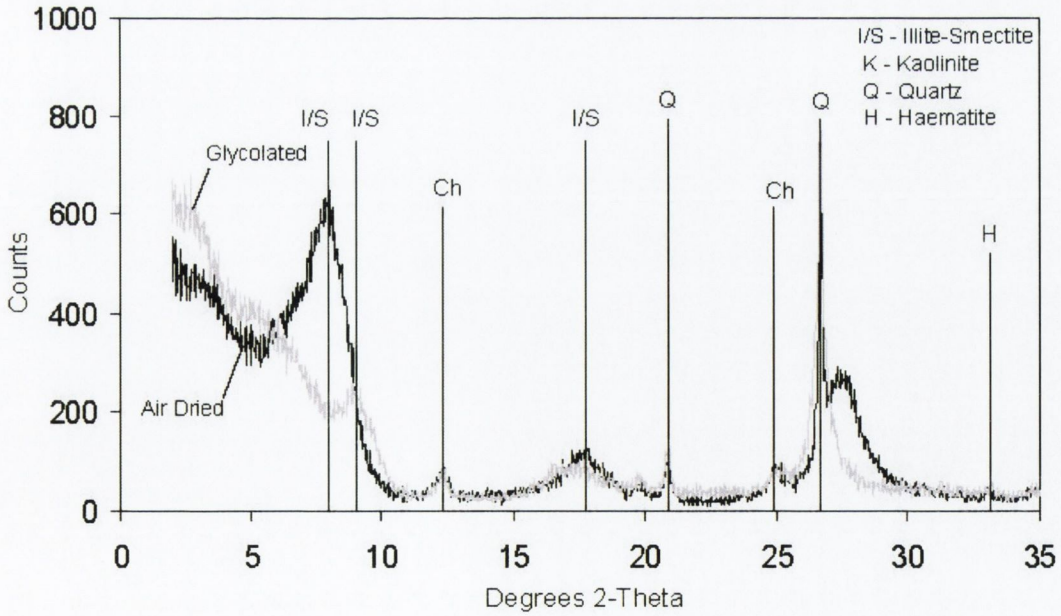
APPENDIX III

X-RAY DIFFRACTION TRACES

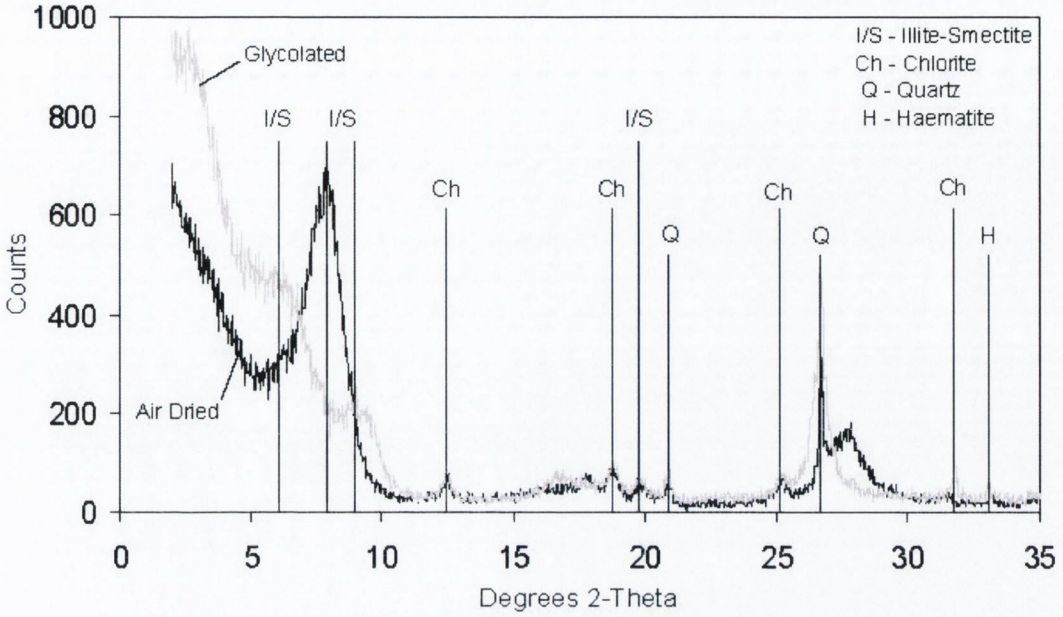
1. Clay Fraction in the Little Grand Wash Fault Footwall (Morrison Formation)



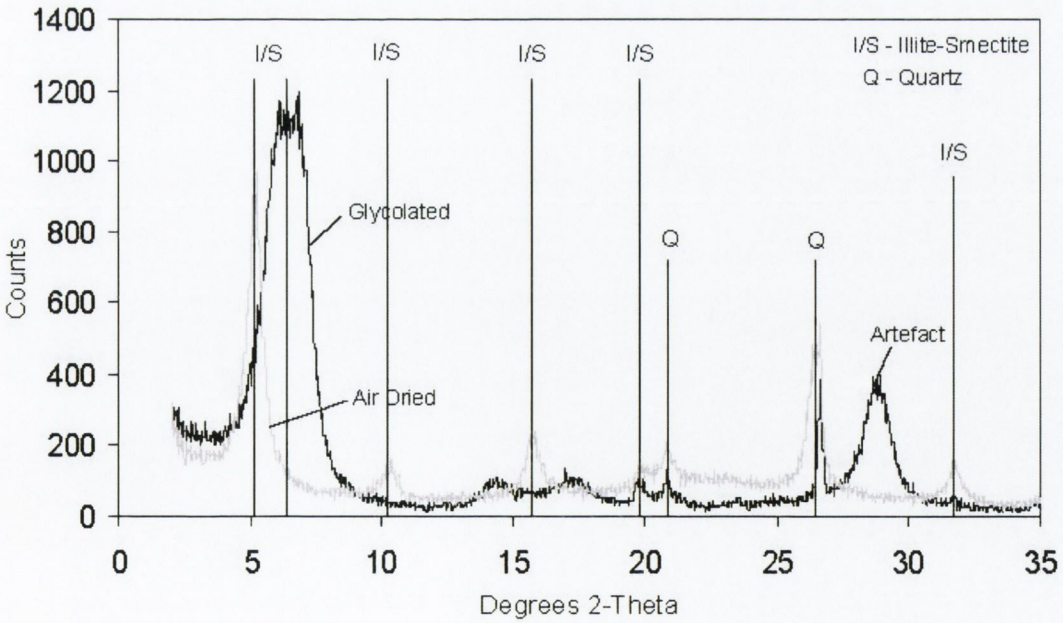
2. Fault Gouge of the Little Grand Wash Fault



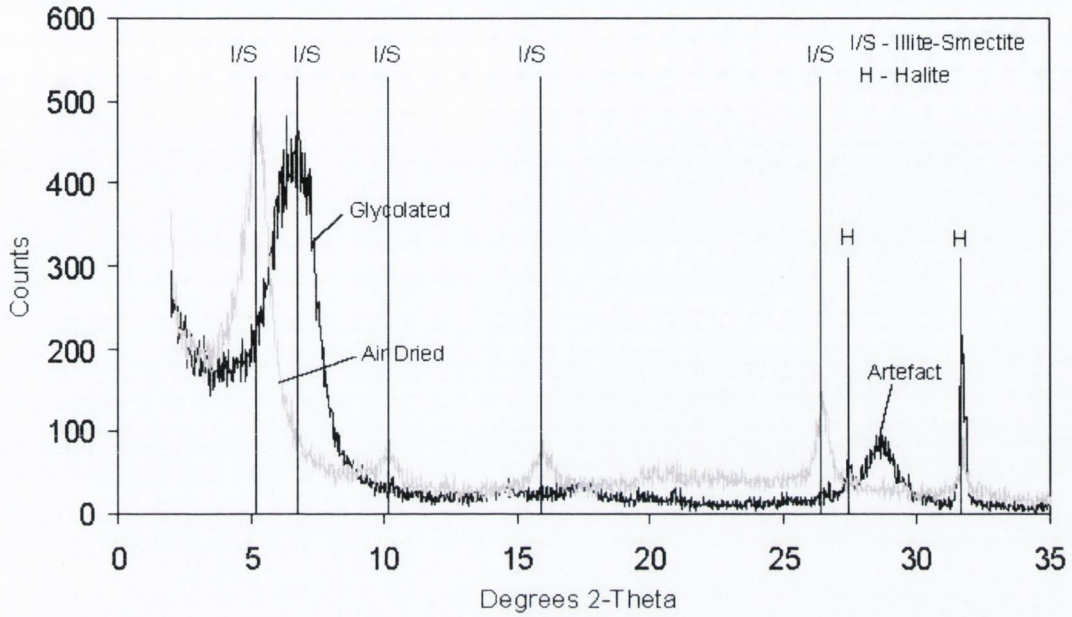
3. Clay Fraction in the Little Grand Wash Fault Hanging Wall (Mancos Formation)



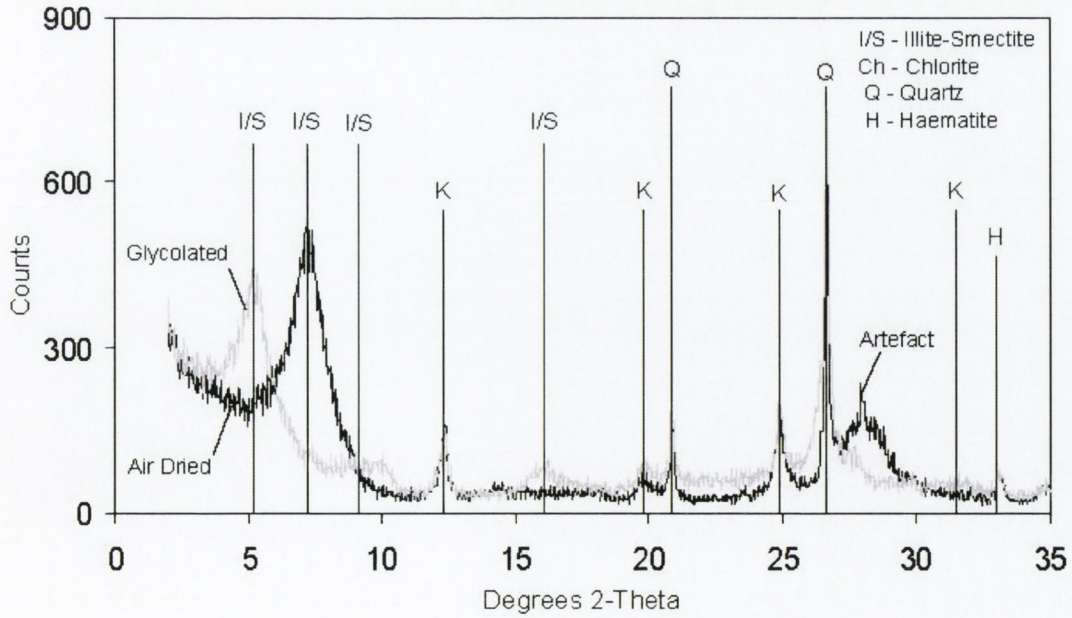
4. Clay Fraction in the Northern Salt Wash Graben Footwall (Entrada Sandstone)



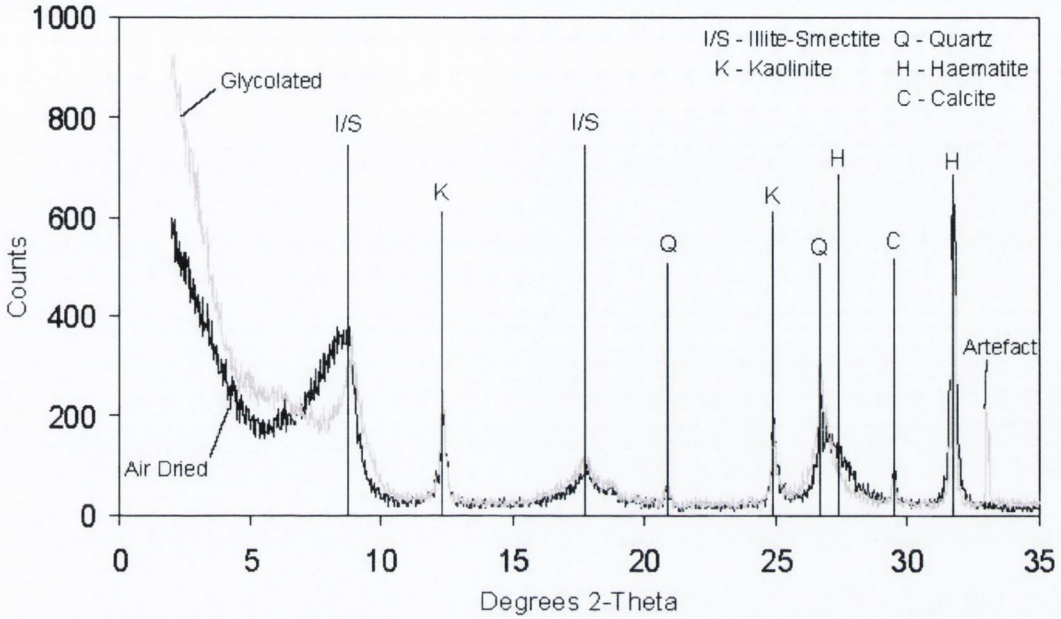
5. Clay Fraction in the Northern Salt Wash Graben Footwall (Entrada Sandstone)



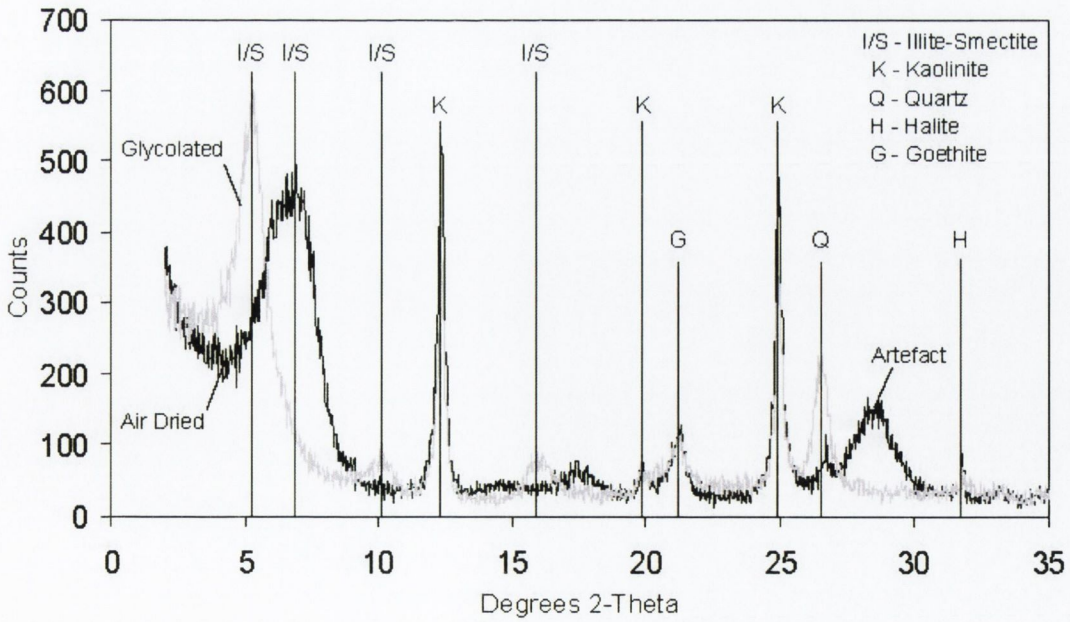
6. Fault gouge in the northern fault of the Salt Wash Graben



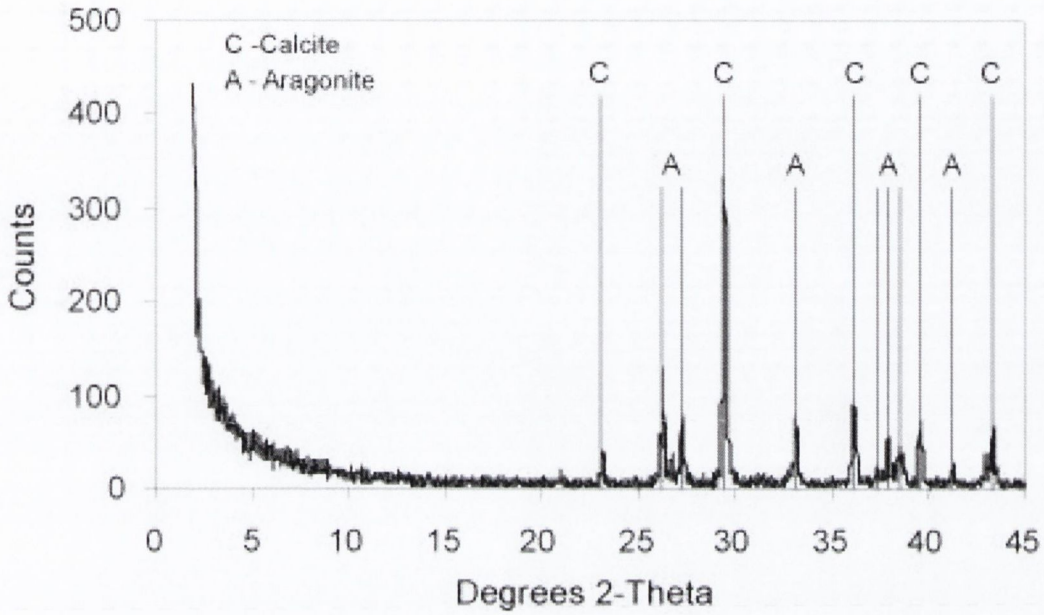
7. Fault Gouge in the Northern Fault of the Salt Wash Graben



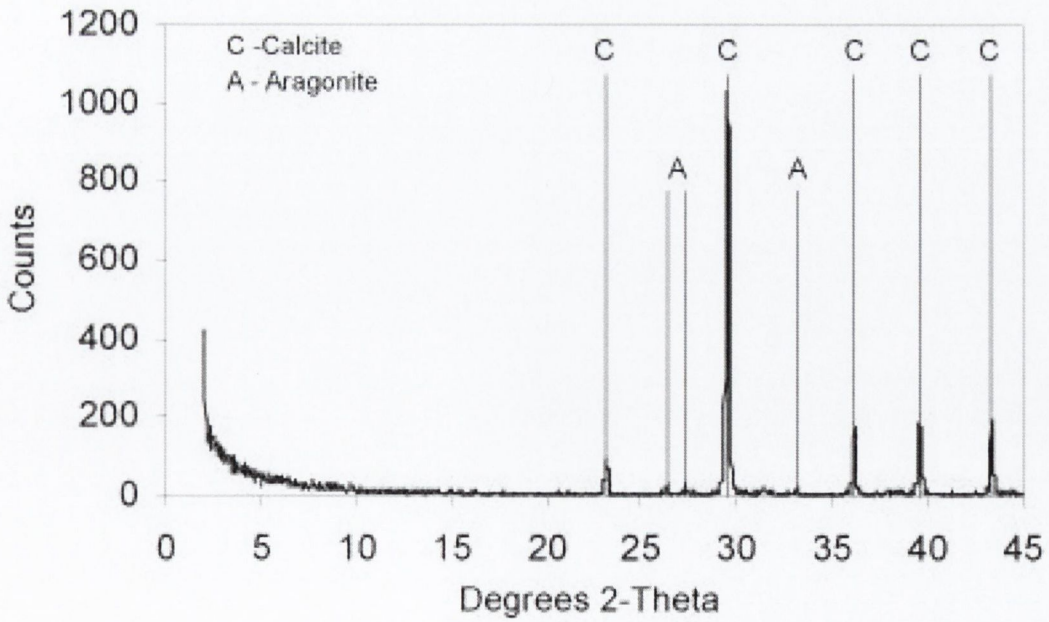
8. Clay Fraction in the Salt Wash Graben (Cedar Mountain Formation)



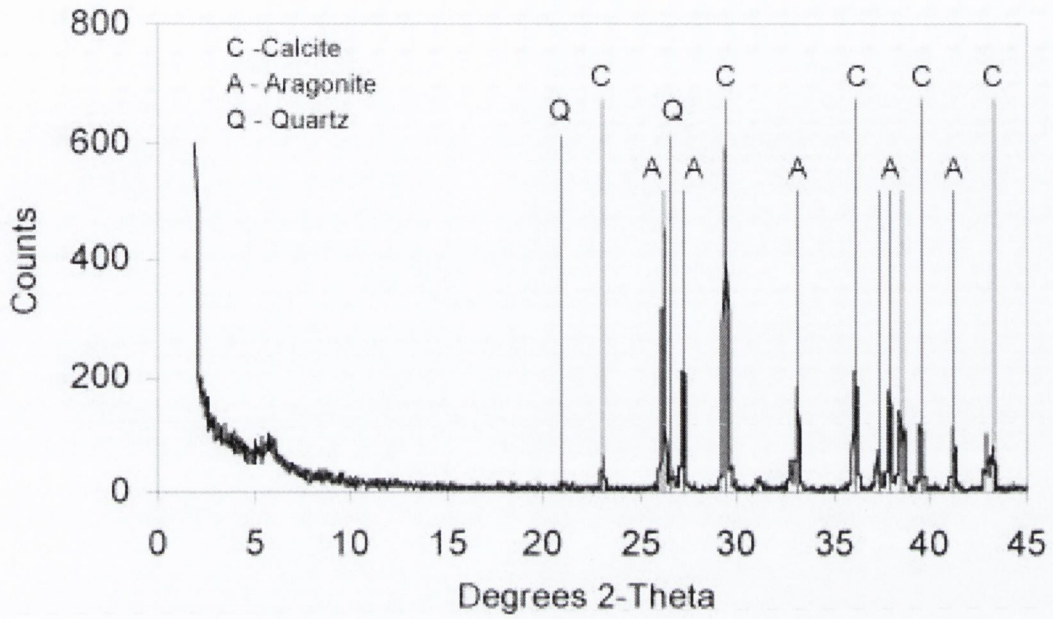
9. Carbonate from Active Crystal Geyser Travertine (8m from vent)



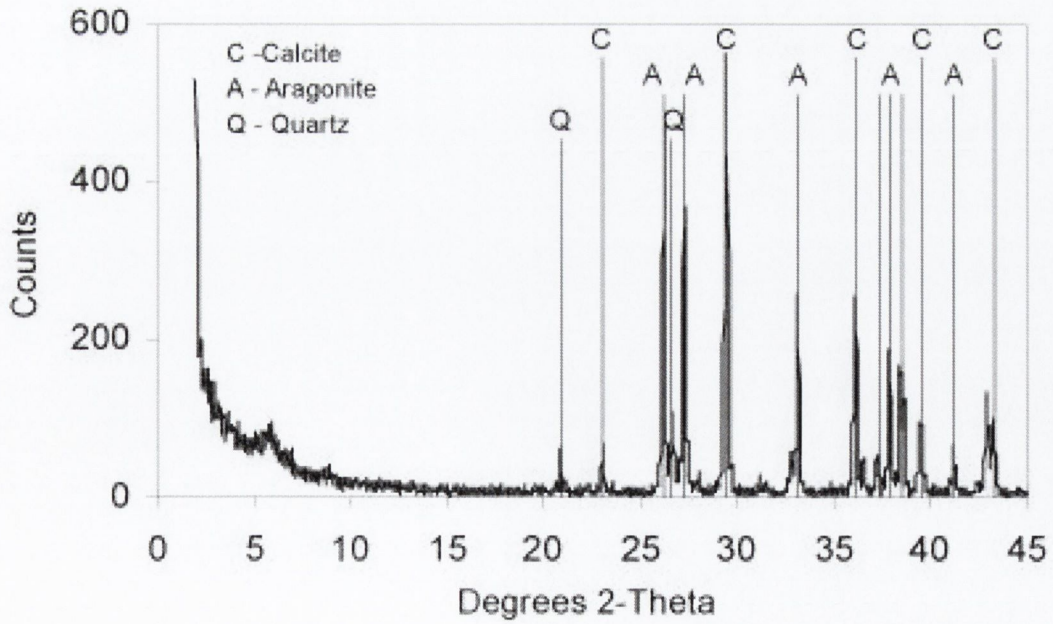
10. Carbonate from Active Crystal Geyser Travertine (55.7m from vent)



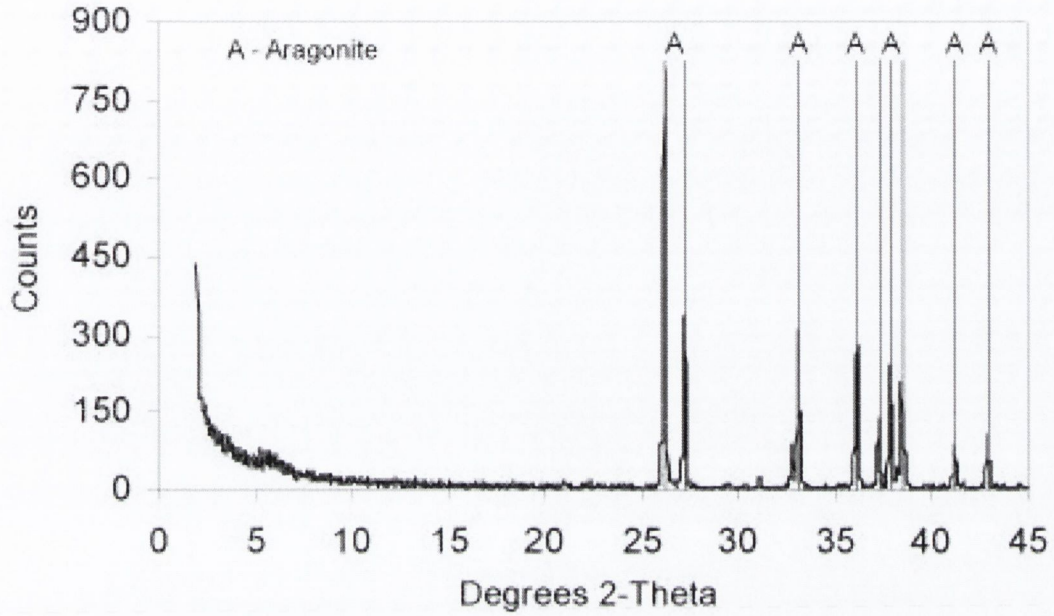
11. Layered Carbonate Mat from Travertine 2



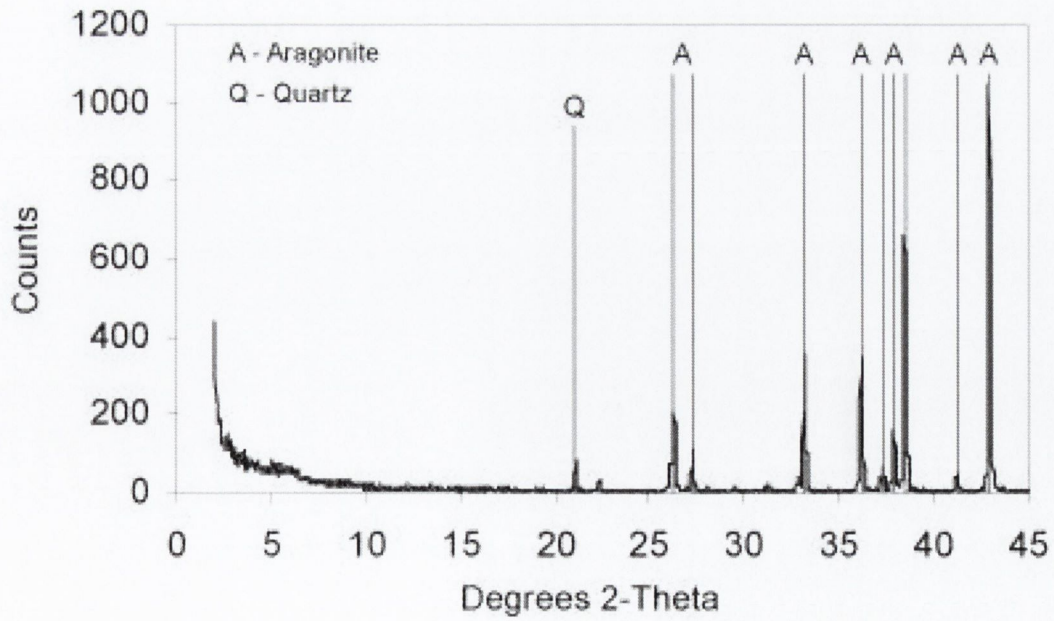
12. Layered Carbonate Mat from Travertine 2



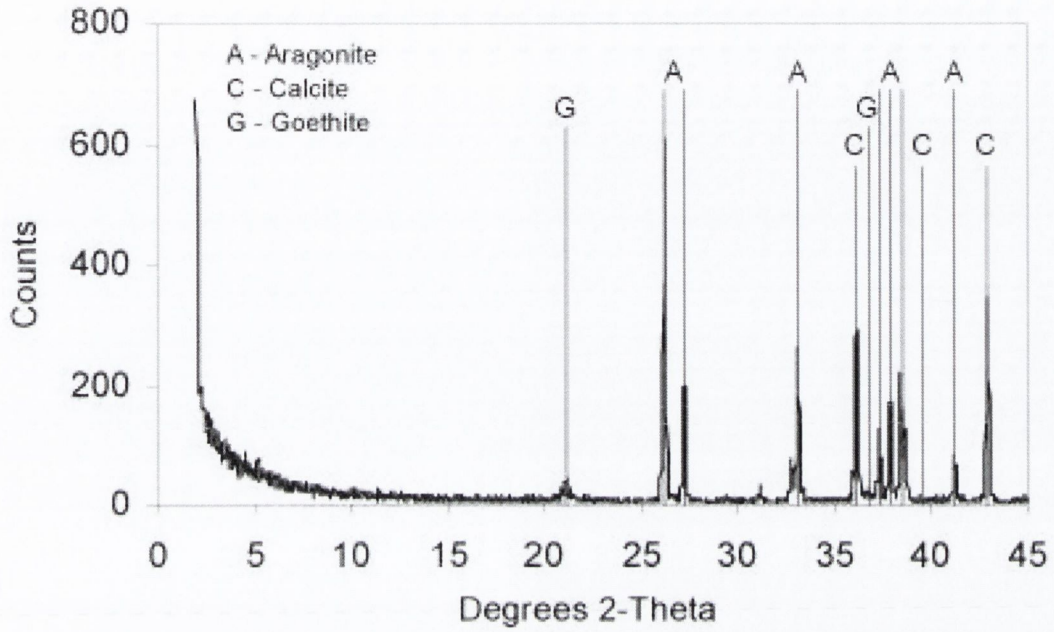
13. White-Banded Vein from Travertine 2



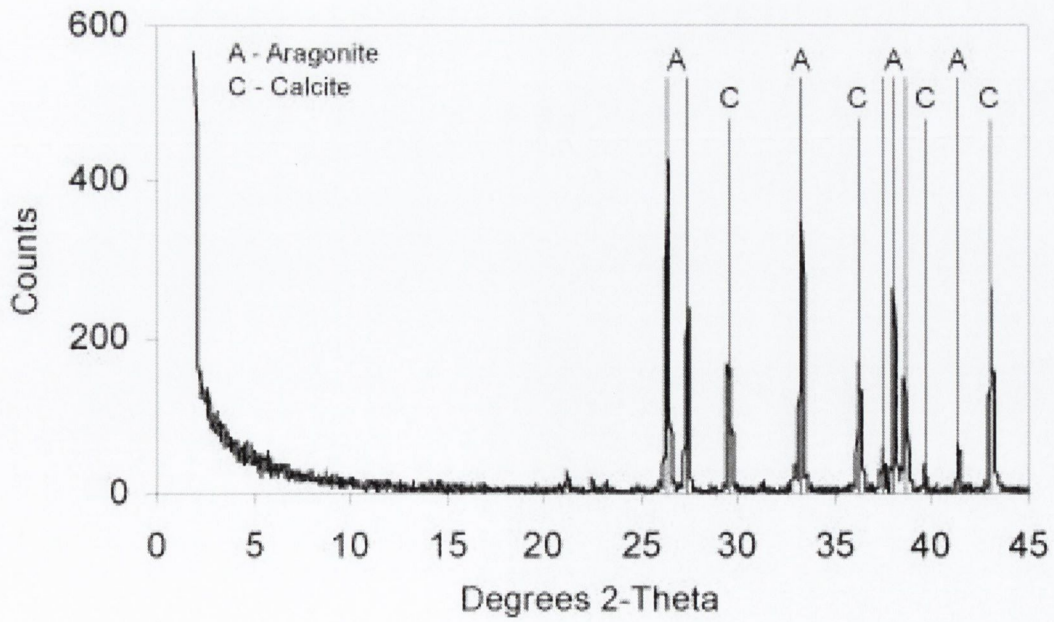
14. White-Banded Vein from Travertine 2



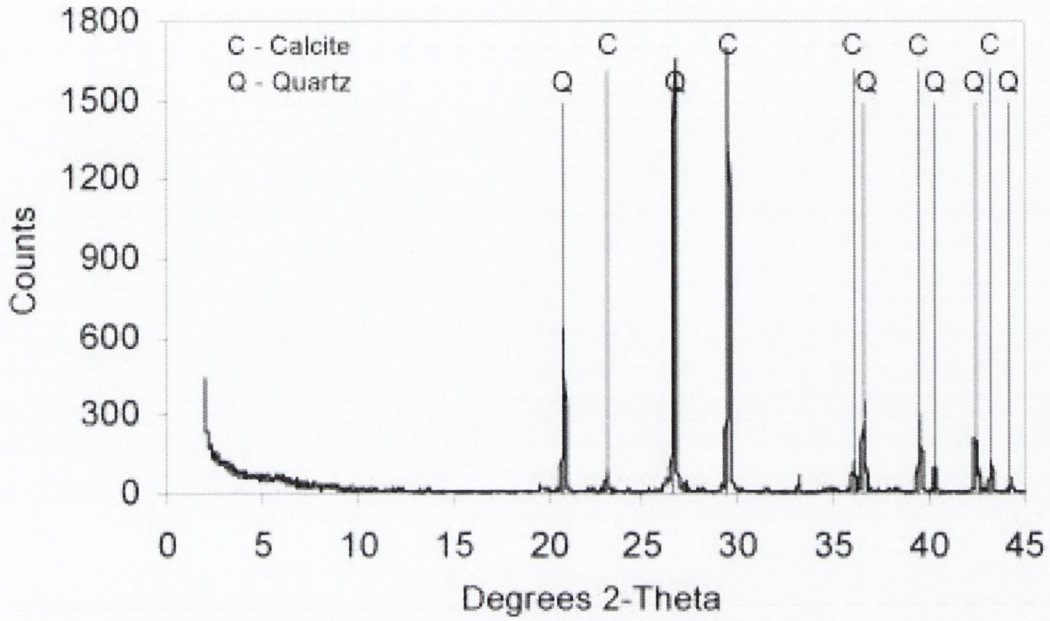
15. Brown-Banded Vein from Travertine 2



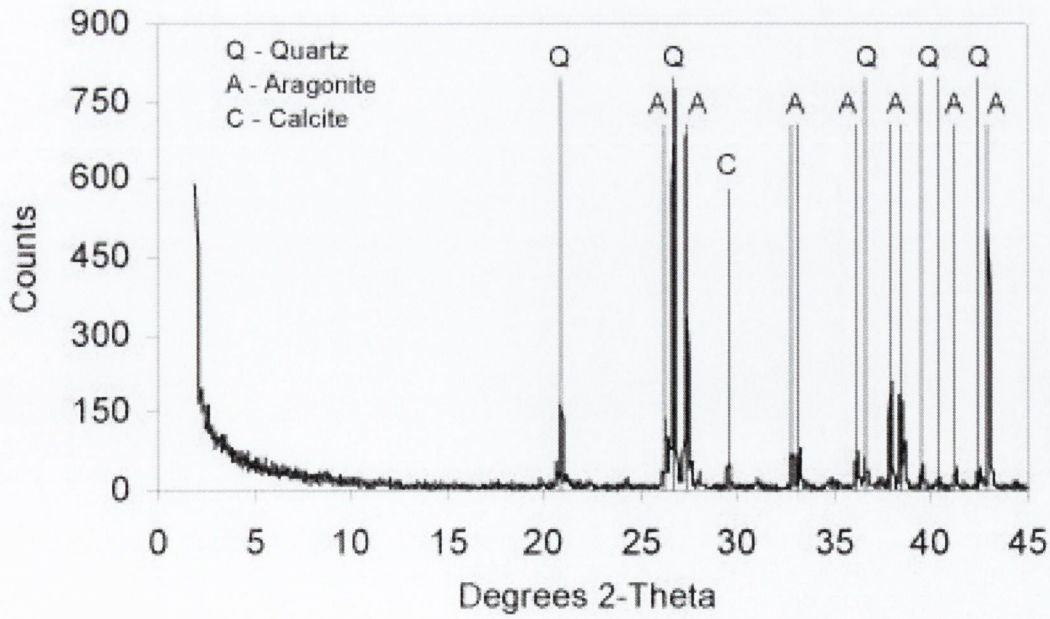
16. Brown-Banded Vein from Travertine 2



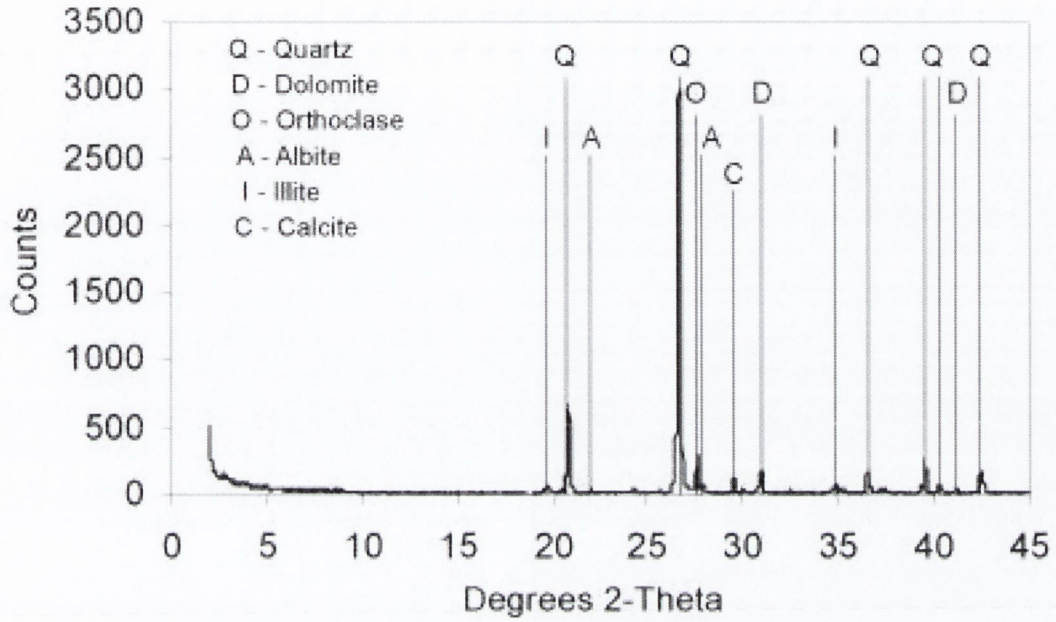
17. Conglomerate Cement from Travertine 2



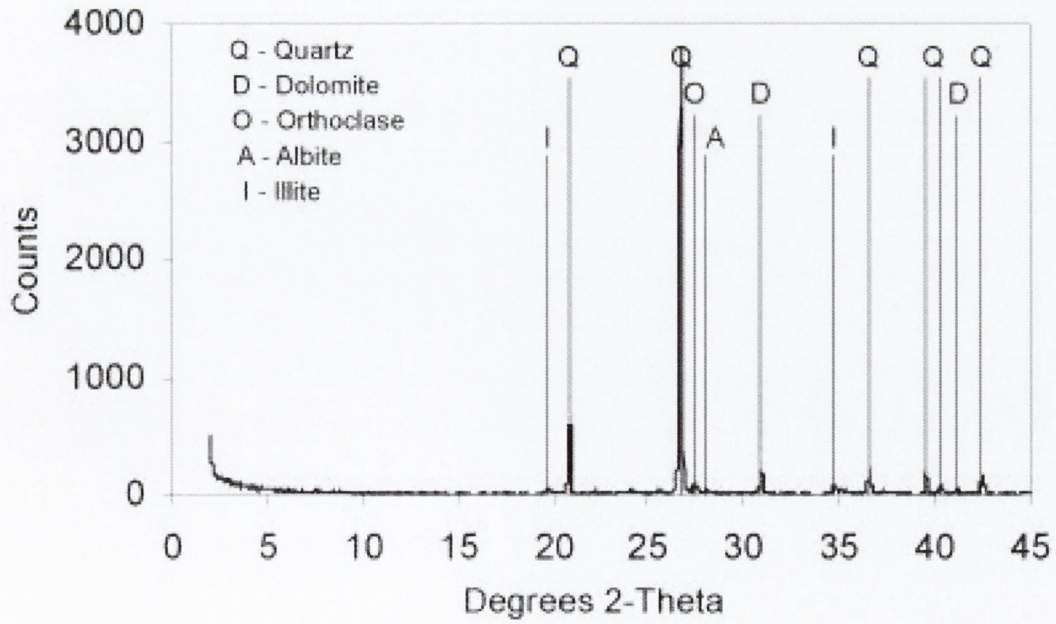
18. Fracture Infill for Transect 1



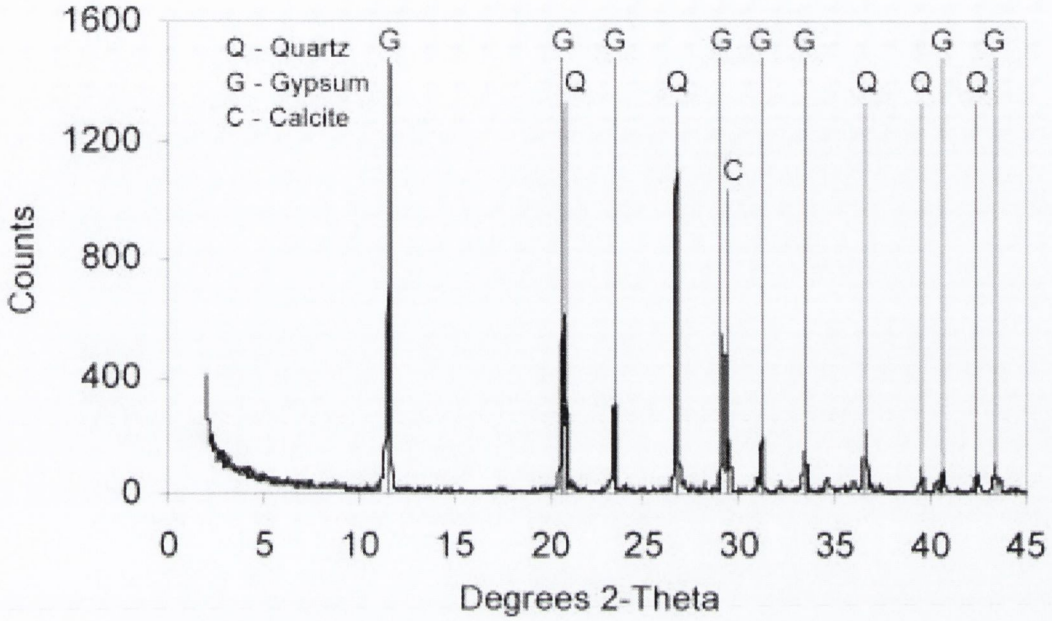
19. Reduced Sandstone for Transect 1



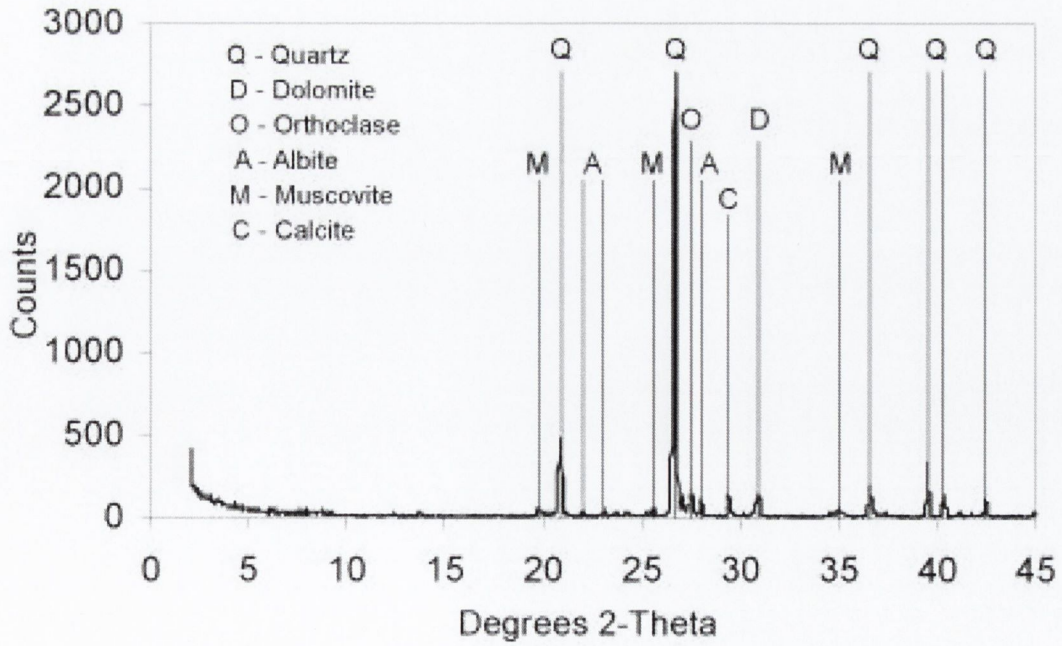
20. Unreduced Sandstone for Transect 1



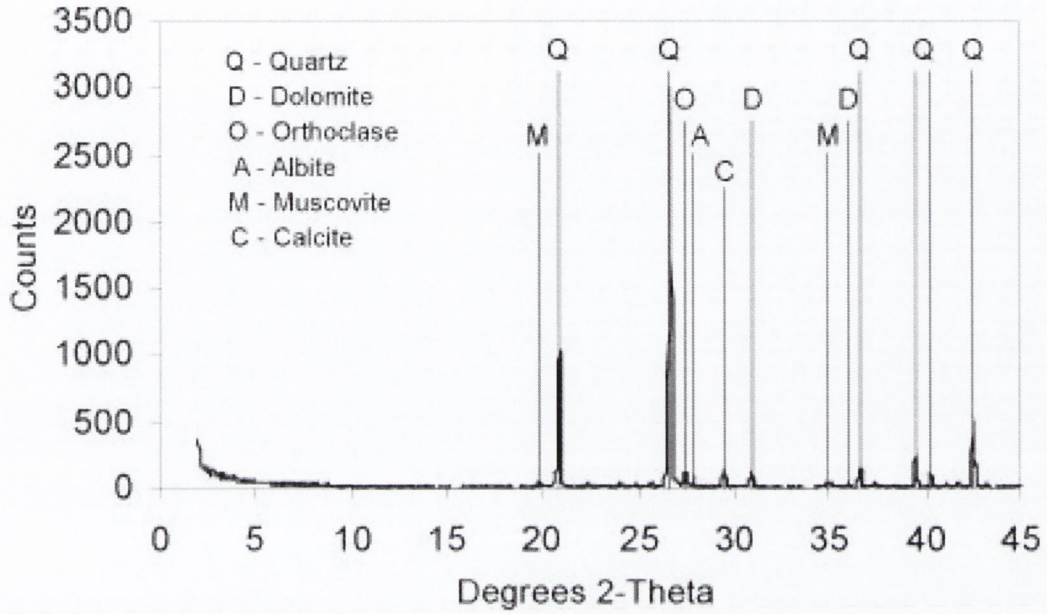
21. Fracture Infill for Transect 2



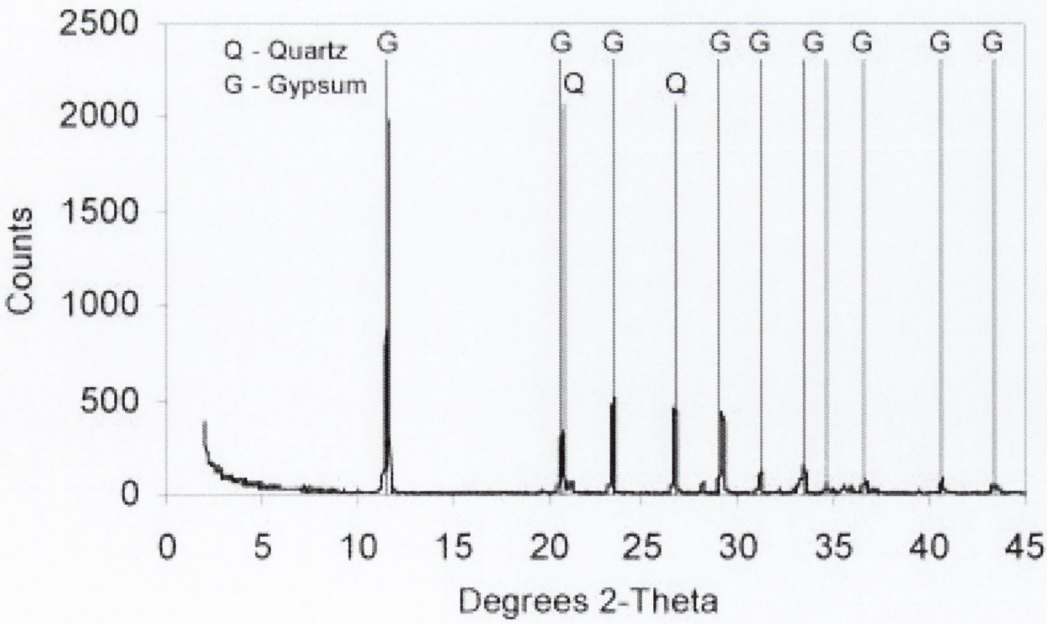
22. Reduced Sandstone for Transect 2



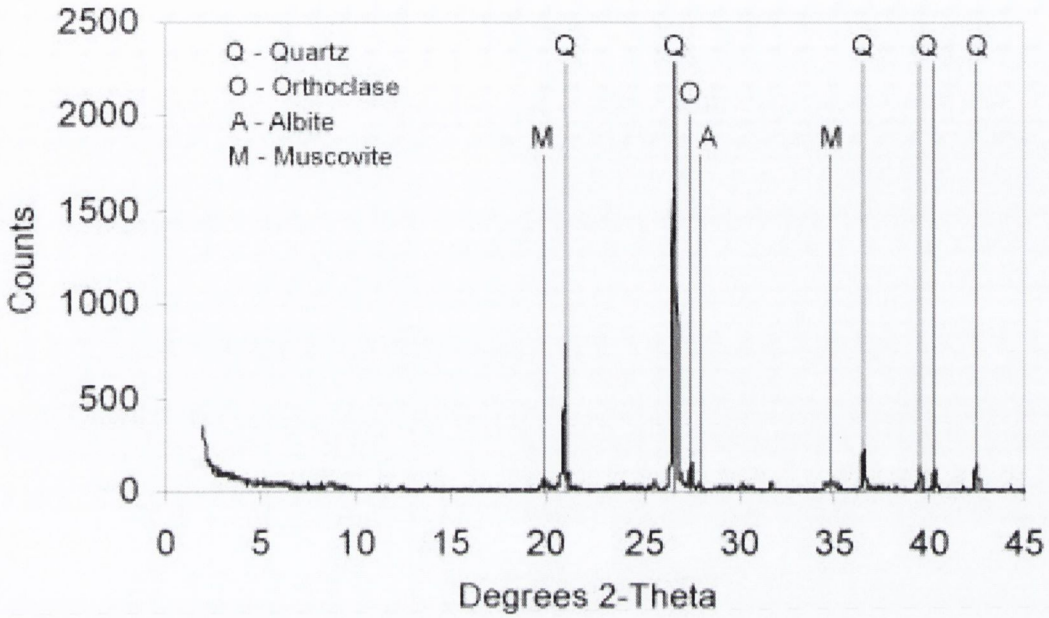
23. Unreduced Sandstone for Transect 2



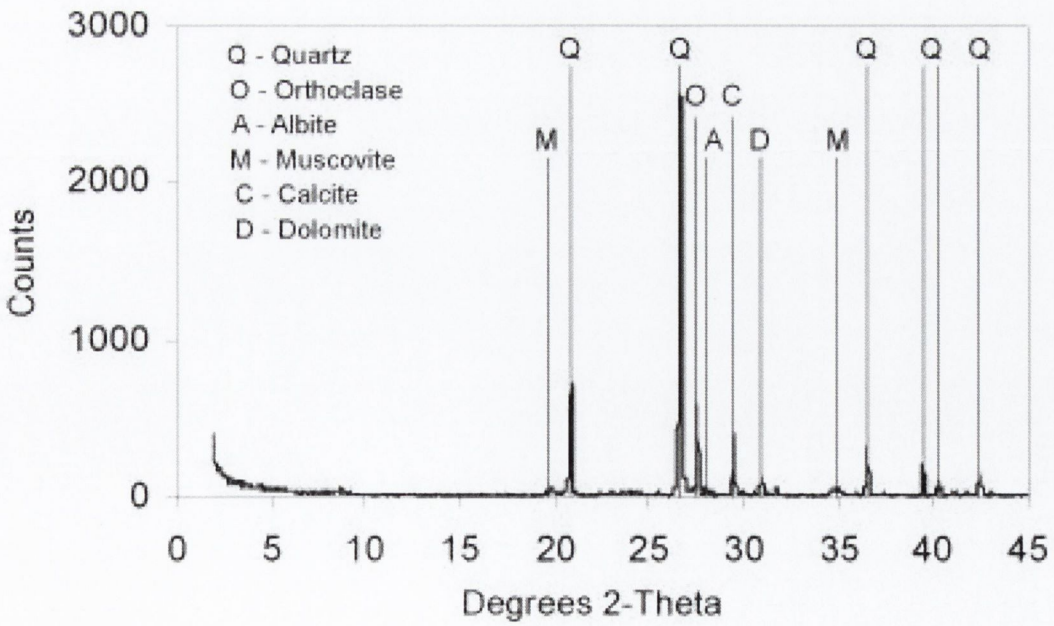
24. Fracture Infill for Transect 3



25. Reduced Sandstone for Transect 3



26. Unreduced Sandstone for Transect 3



APPENDIX IV

STABLE ISOTOPE DATA

Ancient Travertine 1

$\delta^{18}O$	$\delta^{13}C$	Lithofacies
16.8	4.2	White-Banded Vein
17.7	4.5	White-Banded Vein
18.1	4.7	White-Banded Vein
18.1	5.0	White-Banded Vein
17.4	4.6	White-Banded Vein
17.4	4.5	White-Banded Vein
17.3	4.4	White-Banded Vein
17.7	4.8	White-Banded Vein
19.2	5.5	White-Banded Vein
18.0	5.6	White-Banded Vein
19.3	4.6	Layered Carbonate Mat
18.1	4.5	Layered Carbonate Mat
17.9	4.2	Layered Carbonate Mat
18.3	4.9	Layered Carbonate Mat
17.7	4.7	Layered Carbonate Mat
17.7	3.4	Conglomerate
19.5	4.9	Conglomerate
16.2	1.5	Host Rock (Curtis)
18.0	3.7	Host Rock (Curtis)

Ancient Travertine 2

$\delta^{18}O$	$\delta^{13}C$	Lithofacies
16.8	4.7	White-Banded Vein
17.0	4.8	White-Banded Vein
17.3	5.1	White-Banded Vein
18.7	5.4	White-Banded Vein
17.2	4.6	White-Banded Vein
16.6	5.0	White-Banded Vein
17.3	4.5	White-Banded Vein
18.6	5.5	White-Banded Vein
17.2	4.8	White-Banded Vein
17.0	4.6	White-Banded Vein
17.1	4.8	White-Banded Vein
17.1	4.6	White-Banded Vein
17.3	4.5	White-Banded Vein
16.9	4.7	White-Banded Vein
17.0	4.6	White-Banded Vein
17.2	4.5	White-Banded Vein
16.9	4.6	White-Banded Vein
16.9	4.6	White-Banded Vein
17.6	4.5	White-Banded Vein
17.5	4.9	White-Banded Vein
17.6	4.8	White-Banded Vein
17.4	5.0	White-Banded Vein
17.5	4.8	White-Banded Vein

Ancient Travertine 2 (continued)

$\delta^{18}O$	$\delta^{13}C$	Lithofacies
17.5	4.7	White-Banded Vein
17.5	4.9	White-Banded Vein
17.2	4.8	White-Banded Vein
18.0	5.6	White-Banded Vein
18.5	5.6	White-Banded Vein
18.5	5.8	White-Banded Vein
17.2	5.2	White-Banded Vein
18.1	5.8	White-Banded Vein
17.3	4.9	White-Banded Vein
17.6	5.0	White-Banded Vein
17.7	5.3	White-Banded Vein
18.1	6.0	White-Banded Vein
18.3	5.9	White-Banded Vein
18.4	6.1	White-Banded Vein
17.6	5.2	White-Banded Vein
17.6	5.0	White-Banded Vein
17.4	5.1	White-Banded Vein
17.9	6.2	White-Banded Vein
17.7	5.8	White-Banded Vein
16.9	5.1	White-Banded Vein
18.0	5.7	White-Banded Vein
15.4	4.9	White-Banded Vein
17.2	5.8	White-Banded Vein
18.5	5.8	White-Banded Vein
18.6	5.6	White-Banded Vein
17.4	5.5	White-Banded Vein
18.6	5.9	Brown-Banded Vein
17.5	5.1	Brown-Banded Vein
18.8	5.1	Layered Carbonate Mat
19.4	5.2	Layered Carbonate Mat
18.9	6.1	Layered Carbonate Mat
18.7	5.6	Layered Carbonate Mat
18.9	6.1	Layered Carbonate Mat
18.9	6.1	Layered Carbonate Mat
18.7	6.1	Layered Carbonate Mat
20.7	5.5	Layered Carbonate Mat
21.4	5.4	Layered Carbonate Mat
18.8	6.3	Layered Carbonate Mat
18.6	5.9	Layered Carbonate Mat
18.7	6.8	Layered Carbonate Mat
18.1	5.2	Layered Carbonate Mat
18.7	4.5	Layered Carbonate Mat
19.2	5.3	Layered Carbonate Mat
19.0	4.2	Layered Carbonate Mat
19.3	3.3	Conglomerate

Ancient Travertine 2 (continued)

$\delta^{18}O$	$\delta^{13}C$	Lithofacies
19.4	3.9	Conglomerate
19.3	3.4	Conglomerate
22.7	2.7	Host Rock (Summerville)
20.2	3.8	Host Rock (Summerville)
20.1	3.6	Host Rock (Summerville)
19.9	3.3	Host Rock (Summerville)

Ancient Travertine 3

$\delta^{18}O$	$\delta^{13}C$	Lithofacies
17.7	4.0	White-Banded Vein
19.0	5.8	White-Banded Vein
18.9	5.6	White-Banded Vein
18.0	6.3	White-Banded Vein
18.1	5.8	White-Banded Vein
18.2	5.5	White-Banded Vein
17.7	5.6	White-Banded Vein
18.2	5.6	White-Banded Vein
18.5	5.6	White-Banded Vein
17.8	5.2	White-Banded Vein
18.6	5.8	White-Banded Vein
18.9	5.9	White-Banded Vein
17.6	5.8	White-Banded Vein
19.4	5.6	Layered Carbonate Mat
19.2	5.8	Layered Carbonate Mat
21.7	5.2	Layered Carbonate Mat
17.3	5.4	Layered Carbonate Mat
19.2	7.3	Layered Carbonate Mat
18.7	6.6	Layered Carbonate Mat
18.5	4.4	Conglomerate
18.8	4.7	Conglomerate
19.2	4.0	Conglomerate
18.4	-0.4	Host Rock (Summerville)

Ancient Travertine 4

$\delta^{18}O$	$\delta^{13}C$	Lithofacies
19.1	5.7	White-Banded Vein
19.6	5.8	White-Banded Vein
19.7	5.7	White-Banded Vein
20.0	5.6	White-Banded Vein
20.0	5.7	White-Banded Vein
19.2	5.9	White-Banded Vein
19.8	5.7	White-Banded Vein
26.3	5.0	White-Banded Vein
19.6	5.5	White-Banded Vein
19.3	5.4	White-Banded Vein
19.4	5.8	White-Banded Vein
19.5	5.6	White-Banded Vein
19.1	5.3	White-Banded Vein
19.6	5.4	White-Banded Vein
19.6	5.4	White-Banded Vein
19.6	5.8	White-Banded Vein
19.2	5.7	White-Banded Vein
19.7	5.9	White-Banded Vein
16.9	5.5	White-Banded Vein
19.8	5.5	White-Banded Vein
19.6	5.5	White-Banded Vein
19.4	5.4	White-Banded Vein
19.1	6.2	Layered Carbonate Mat
19.8	6.4	Layered Carbonate Mat
22.6	5.0	Conglomerate
19.1	4.1	Conglomerate
20.3	4.9	Conglomerate
23.5	4.9	Conglomerate
25.6	4.6	Conglomerate
19.0	1.7	Conglomerate
18.5	6.2	Conglomerate
23.9	-2.0	Host Rock (Brushy Basin)
18.4	2.9	Host Rock (Brushy Basin)
19.8	4.9	Host Rock (Brushy Basin)
18.6	-1.6	Host Rock (Brushy Basin)
16.8	-2.6	Host Rock (Brushy Basin)
17.3	-2.4	Host Rock (Brushy Basin)

Ancient Travertine 5

$\delta^{18}O$	$\delta^{13}C$	Lithofacies
19.4	6.0	White-Banded Vein
18.3	5.0	White-Banded Vein
18.6	4.9	White-Banded Vein
17.9	4.6	White-Banded Vein
18.0	4.7	White-Banded Vein
19.4	5.5	White-Banded Vein
20.4	4.4	White-Banded Vein
19.3	5.4	White-Banded Vein
18.2	5.4	White-Banded Vein
18.8	5.0	White-Banded Vein
21.4	4.7	White-Banded Vein
18.8	5.3	White-Banded Vein
19.9	4.7	White-Banded Vein
20.7	3.9	Conglomerate
21.3	4.5	Conglomerate
24.8	5.4	Conglomerate
14.9	6.0	Conglomerate
22.6	3.7	Conglomerate
20.3	-3.9	Host Rock (Entrada)
20.2	-3.3	Host Rock (Entrada)
21.1	-3.5	Host Rock (Entrada)

Ancient Travertine 6

$\delta^{18}O$	$\delta^{13}C$	Lithofacies [1]
18.5	5.1	White-Banded Vein 1
18.6	5.1	White-Banded Vein 1
18.1	5.1	White-Banded Vein 1
21.0	4.4	Conglomerate 1
20.9	3.3	Host Rock (Entrada) 1
18.8	5.6	White-Banded Vein 2
18.5	5.6	White-Banded Vein 2
18.4	6.1	White-Banded Vein 2
18.8	4.8	White-Banded Vein 2
18.3	5.1	White-Banded Vein 2
18.2	5.0	White-Banded Vein 2
18.8	5.3	White-Banded Vein 2
17.7	4.3	White-Banded Vein 2
16.9	6.0	White-Banded Vein 2
18.7	5.4	White-Banded Vein 2
18.6	5.1	White-Banded Vein 2
17.1	5.1	White-Banded Vein 2
19.1	5.3	White-Banded Vein 2

1- Number indicates area sampled from deposit (see Fig. 4.24)

Ancient Travertine 6 (continued)

$\delta^{18}O$	$\delta^{13}C$	Lithofacies [1]
19.4	5.3	Layered Carbonate Mat 2
19.9	6.3	Layered Carbonate Mat 2
21.4	5.0	Layered Carbonate Mat 2
22.3	5.7	Layered Carbonate Mat 2
18.8	5.9	Layered Carbonate Mat 2
18.6	6.3	Layered Carbonate Mat 2
19.6	6.5	Layered Carbonate Mat 2
21.8	6.5	Layered Carbonate Mat 2
22.3	2.5	Layered Carbonate Mat 2
20.3	5.9	Layered Carbonate Mat 2
22.3	5.0	Layered Carbonate Mat 2
21.7	5.3	Layered Carbonate Mat 2
19.0	5.7	Conglomerate 2
20.8	6.3	Conglomerate 2
19.1	4.1	Conglomerate 2
19.2	4.0	Conglomerate 2
19.4	4.3	Conglomerate 2
19.8	7.8	Conglomerate 2
21.0	4.8	Conglomerate 2
20.3	5.7	Conglomerate 2
21.7	5.2	Conglomerate 2
21.0	3.7	Host Rock (Entrada) 2
20.9	4.5	Host Rock (Entrada) 2
19.9	3.7	Host Rock (Entrada) 2
20.3	4.0	Host Rock (Entrada) 2
17.8	6.1	White-Banded Vein 3
20.0	6.0	White-Banded Vein 3
17.2	4.5	White-Banded Vein 3
19.0	5.3	White-Banded Vein 3
18.9	5.1	White-Banded Vein 3
19.1	5.8	White-Banded Vein 3
20.1	5.6	White-Banded Vein 3
20.1	5.8	White-Banded Vein 3
24.2	4.5	Layered Carbonate Mat 3
25.1	5.3	Layered Carbonate Mat 3
21.4	5.3	Conglomerate 3
20.1	4.4	Conglomerate 3
20.1	4.4	Conglomerate 3
20.0	2.3	Host Rock (Entrada) 3
19.2	2.3	Host Rock (Entrada) 3
20.1	2.3	Host Rock (Entrada) 3
20.2	2.3	Host Rock (Entrada) 3
19.5	2.1	Host Rock (Entrada) 3

1- Number indicates area sampled from deposit (see Fig. 4.24)

Ancient Travertine 7

$\delta^{18}O$	$\delta^{13}C$	Lithofacies
19.0	5.6	White-Banded Vein
18.9	6.3	White-Banded Vein
18.8	5.6	White-Banded Vein
19.1	6.6	White-Banded Vein
18.5	5.5	White-Banded Vein
18.5	5.9	White-Banded Vein
18.7	6.0	White-Banded Vein
18.9	5.6	White-Banded Vein
18.7	5.5	White-Banded Vein
19.0	5.5	White-Banded Vein

Non-Travertine Carbonate Veins

$\delta^{18}O$	$\delta^{13}C$	Fault [1]	Setting
15.0	-7.1	nSWG	Fault Zone
18.6	-5.6	nSWG	Hanging Wall
18.4	-8.1	nSWG	Hanging Wall
15.9	-5.5	nSWG	Hanging Wall
18.3	1.6	LGWF	Hanging Wall
18.6	1.6	LGWF	Hanging Wall
18.5	1.5	LGWF	Hanging Wall
18.4	1.7	LGWF	Hanging Wall
17.3	-5.9	LGWF	Hanging Wall
16.9	0.7	LGWF	Hanging Wall
16.6	0.4	LGWF	Hanging Wall
22.3	-0.1	LGWF	Hanging Wall

1- nSWG = northern fault of the Salt Wash Graben; LGWF = Little Grand Wash Fault

Traverse of a Reduction Halo Around Fracture

$\delta^{18}O$	$\delta^{13}C$	Description	Distance (m)[1]
18.3	5.0	Carbonate Infill	0
21.5	-2.4	Bleached Entrada	0.02
19.7	-2.8	Bleached Entrada	0.05
23.6	-2.6	Bleached Entrada	0.09
22.5	-2.2	Red Entrada	0.11
21.8	-2.8	Red Entrada	0.2
23.4	-2.3	Red Entrada	0.5
22.2	-2.0	Red Entrada	1.05
21.3	-2.7	Red Entrada	2.85
23.1	-1.5	Red Entrada	7.3

1 - Perpendicular distance from centre of fracture

Active Travertines

$\delta^{18}O$	$\delta^{13}C$	Travertine[1]	Distance (m)[2]
19.6	9.5	Crystal Geyser 1	4.3
19.1	9.4	Crystal Geyser 1	8.8
18.0	5.6	Crystal Geyser 1	13.1
18.1	5.7	Crystal Geyser 1	17.0
18.9	6.8	Crystal Geyser 1	21.0
18.9	5.8	Crystal Geyser 1	22.8
18.8	6.3	Crystal Geyser 1	27.1
18.7	6.2	Crystal Geyser 1	31.0
18.4	6.0	Crystal Geyser 1	35.0
18.6	6.4	Crystal Geyser 1	39.1
18.6	6.5	Crystal Geyser 1	42.9
18.7	6.5	Crystal Geyser 1	47.0
18.8	6.5	Crystal Geyser 1	50.1
19.0	6.4	Crystal Geyser 1	51.6
18.7	6.2	Crystal Geyser 1	53.9
18.5	6.7	Crystal Geyser 1	57.9
18.4	5.9	Crystal Geyser 1	62.2
18.3	6.1	Crystal Geyser 1	66.0
18.7	6.1	Crystal Geyser 1	69.7
19.3	7.9	Crystal Geyser 2	4.0
19.2	6.8	Crystal Geyser 2	8.0
19.2	7.2	Crystal Geyser 2	12.2
19.4	7.0	Crystal Geyser 2	16.2
19.2	6.5	Crystal Geyser 2	20.2
19.2	6.8	Crystal Geyser 2	24.1
19.3	6.5	Crystal Geyser 2	28.2
19.2	5.9	Crystal Geyser 2	31.6
18.9	5.5	Crystal Geyser 2	36.0
18.7	5.9	Crystal Geyser 2	36.9
18.5	5.6	Crystal Geyser 2	40.0
18.6	5.2	Crystal Geyser 2	44.0
18.4	5.4	Crystal Geyser 2	48.1
18.4	6.0	Crystal Geyser 2	52.3
18.9	5.7	Crystal Geyser 2	55.7

1 - Number indicates flow path for Fig. 4.14.
2 - Horizontal distance from geyser or spring vent.

Active Travertines (continued)

$\delta^{18}O$	$\delta^{13}C$	Travertine[1]	Distance (m)[2]
21.9	9.2	Ten Mile Geyser	2
21.1	8.7	Ten Mile Geyser	4
21.0	7.8	Ten Mile Geyser	4.9
20.8	8.9	Ten Mile Geyser	5.7
22.2	10.2	Ten Mile Geyser	7.9
19.2	6.8	Eastern Bubbling Spring (Three Sisters)	5
18.8	5.7	Eastern Bubbling Spring (Three Sisters)	10
20.1	8.4	Northern Bubbling Spring (Three Sisters)	At Vent
20.3	11.3	Southern Bubbling Spring (Three Sisters)	At Vent
19.9	6.5	Torrey Spring	0.2
20.1	8.3	Torrey Spring	7.5

1 - Number indicates flow path for Fig. 4.14.

2 - Horizontal distance from geyser or spring vent.

APPENDIX V

METHODOLOGY FOR U-TH DATING OF TRAVERTINES

Separation of Uranium and Thorium from Carbonate Samples

1. Samples are crushed to less than 1mm.
2. 'Dirty' samples are inspected under a binocular microscope and altered, weathered or stained pieces are removed.
3. 3-4 grams of sample weighed into a teflon beaker.
4. 3ml of Milli-Q H_2O added, then 3-4ml of concentrated HNO_3, 200µl at a time.
5. The beaker is placed on a hotplate at 120°C overnight.
6. The solution is spiked with ^{229}Th and ^{236}U.
7. Back on hotplate at 130°C for 2-3 hours.
8. Evaporate HNO_3 to dryness, add 10-15ml of H_2O_2 (5ml at a time) to eliminate any organic material. Flux on hotplate at 150°C for 1-2 hours then evaporate to dryness after each addition of H_2O_2 until reaction with residue upon adding H_2O_2 ceases.
9. Add enough 4M HNO_3 to get residue into solution, flux on hotplate at 130°C for 1-2 hours, then centrifuge to separate out any undissolved material. Pipette off solution into original beaker, then rinse residue into separate beaker and repeat dissolution procedure.
10. After centrifuging residue fraction pipette solution into original beaker, dry down the 4M HNO_3, then add enough 4M HNO_3 to put residue into solution again (approximately 5ml). Samples are now ready for column chemistry.
11. The column chemistry follows the first step of the two step separation procedure for U and Th of Yokoyama et al. (1999) with blanks of U = .007µg and Th = 10pg.

Determining Uranium and Thorium Concentrations and Ages

1. An aliquot of the separated U is taken and diluted to approximately 50 $ng.g^{-1}$ in 5% HNO_3. Solutions are introduced to a Micromass Isoprobe multiple collector ICP-MS through an Elementary Scientific Inc. Apex nebulizer system operating at 50 $\mu l.min^{-1}$. ^{234}U is measured using a Daly-photomultiplier detector located behind a Wide-Angle Retarding Potential filter which supplies an abundance sensitivity of approximately 200 ppm, thereby eliminating tailing from adjacent peaks. ^{235}U, ^{236}U (spike) and ^{238}U are measured simultaneously on Faraday detectors. Zeros are measured on peak in blank 5% HNO_3 for 60s prior to each analysis and U isotope ratios are measured in 5 blocks of 20 5x1s integrations. Each analysis consumes approximately 20ng U. $^{234}U/^{238}U$ and $^{236}U/^{238}U$ are corrected for instrumental mass bias assuming natural $^{235}U/^{238}U$ = 0.0072527 and an exponential fractionation law. Samples are bracketed between solutions of the NBL112-A standard which are used to determine the relative gain of the Daly-photomultiplier detector relative to Faraday detectors assuming that inaccuracy in the mass bias corrected $^{234}U/^{238}U$ reflects the Daly gain (typically 0.97-0.99).

2. An aliquot of the separated Th is taken up in 1ml of 5% HNO_3 and mixed with an aliquot of the U separated from that sample to give 50 $ng.g^{-1}$ U. Using identical instrumental conditions to those described for U, Th isotope ratios are measured in static multi-collection mode using the Daly-photomultiplier for ^{230}Th and Faraday detectors for ^{229}Th (spike) and ^{232}Th. ^{235}U and ^{238}U are also measured simultaneously on Faraday detectors and used to correct mass bias using the exponential fractionation law. Zeros are measured on peak in blank 5% HNO_3 for 60s prior to each analysis. Ratios are measured in 2 blocks of 20 5x1s integrations. Bracketing NBL112-A standards are used to correct Daly-photomultiplier gain in a similar fashion to that applied for U.

3. ^{230}Th and ^{238}U concentrations are calculated using standard isotope dilution calculations and $^{234}U/^{238}U$ is corrected for spike contribution, and its effect on the mass bias correction, using an iterative procedure and the exponential fractionation law.

4. Ages are calculated using Isoplot/Ex rev. 2.49 (Ludwig, 2001)